Individual and collective behaviour of bacteria under oxidative stress

Divya Choudhary

A thesis submitted for the degree of
Doctor of Philosophy

Somerville College,
University of Oxford
Michaelmas Term 2023

Statement of Originality

I declare that the work presented in this thesis is a compilation of the work performed by me under the supervision of Stephan Uphoff and Kevin Foster. The work in this thesis as part of my dissertation has not been submitted or is being currently submitted for any degree, diploma or other qualifications at the University of Oxford or any other institution except as mentioned in the preface. Stephan Uphoff and Kevin Foster edited the text in results chapters described in Chapters 3, 4 and 5.

List of publications contributed to during my thesis:

1. Choudhary, D.*, and Cassaro, J. C.* (2021). Digging deeper in the biofilm. *Nature Reviews Microbiology* 19.8
2. Choudhary, D., Lagage, V., Foster, K. R., & Uphoff, S.* (2023). Phenotypic heterogeneity in the bacterial oxidative stress response is driven by cell-cell interactions. *Cell Reports*, *42*(3). [as Chapter 3 in this thesis]
3. Choudhary, D., Foster, K. R.*, & Uphoff, S.* (2023). Chaos in a bacterial stress response. *Current Biology*, 33. [as Chapter 4 in this thesis]
4. Choudhary, D., Foster, K. R.*, & Uphoff, S.* (2024). A simple regulatory network coordinates a bacterial stress response in space and time. *Biorxiv*. [as Chapter 5 in this thesis]

* = corresponding author

Divya Choudhary
December 2023

Acknowledgements

I express immense gratitude to my supervisors, Stephan Uphoff and Kevin Foster, for their unwavering support, valuable discussions, constructive feedback, mentorship, and shared excitement for science. Thank you to David Sherratt, whose insights were consistently beneficial to the project. The supportive and very talented members of the Uphoff and Foster group played a vital role in down-regulating my stress response and amplifying my joy for experiments throughout my DPhil. Special thank you to Valentine, Maxence, Amy, and Fiona, who were instrumental in this journey, and to Tay and Matt, who were outstanding students to mentor. Thank you to Joe and Chloe for their contributions to helpful lab discussions.

I am very grateful to Valentine and Amy for guiding me through the start of my DPhil and for being unwavering pillars of support, and to Valentine for sharing a passion for bacterial oxidative stress response. To Fiona, thank you for always ensuring my sugar and energy levels are consistently high in the lab. Special thank you to Maxence for imparting his knowledge in microbiology, science discussions (including our weekly journal club), and being an exceptional mentor, both inside and outside the lab. I extend my gratitude to Somerville College and Oxford India Center for Sustainable Development (OICSD) for funding, with special thank you to Siddharth, Gaurav, and Vinita for their support and mentorship.

A heartfelt thank you to my Oxford family who played a crucial role in my journey, and I genuinely would not be here without them. Nina and Aditi, in particular, have been the best friends one could ask for, offering unwavering support and unconditional friendship. I am incredibly thankful to Sophie and Saran for always supporting, inspiring, and for all the adventures. A massive thanks to Carl, Sean, and Linda for their caring and supportive presence. Thanks to Miguel for our walks and numerous scientific discussions. To Rory, Christos, Agrima and Bushra, thanks for your love and support. To Sarthak, Satyam, Piyush, and Jasleen, thanks for supporting me from afar and patiently listening to my endless lab and science conversations. Special thank you to Vivekanandan Perumal and Marzia Cescon, whose encouragement motivated my scientific journey.

Lastly, incredibly thankful to my inspirational parents - Maa and Papa - for trusting and encouraging me throughout this journey. आपके समर्थन के बिना मैं यह हासिल नहीं कर पाती।
To Didi and Bhai for their support and laughter that helped me navigate the years of my DPhil, thank you from the bottom of my heart.

Contents

Contents **iv**

List of Figures **viii**

Abstract **x**

1. Introduction **1**

1.1 Gene regulation in bacteria under stress 1
1.2 Cells in a population commonly differ in their responses to stress 3
1.2.1 Sources of cell-cell variability 3
1.2.1.1 Intrinsic and extrinsic noise 3
1.2.1.2 Growth rates 5
1.2.1.3 Environmental variation 5
1.2.1.4 Determinism in 'noise-like' observations 7
1.2.2 Why does cell-cell variability emerge in a bacterial population under stress? 8
1.2.2.1 Bet-hedging under stress 8
1.2.2.2 Heterogeneity as a by-product of gene regulation 9
1.2.2.3 Division of labour 10
1.3 Bacteria under oxidative stress 12
1.3.1 Biochemistry of ROS 12
1.3.2 ROS toxicity 12
1.3.3 ROS sources 16
1.3.3.1 Endogenous sources 16
1.3.3.2 Exogenous sources 17
1.4 Protection from ROS 19
1.4.1 Protection from superoxide stress 19
1.4.2 Protection from H_2O_2 stress 19
1.4.2.1 Oxidative stress response regulation in *E. coli* 19
1.4.2.2 H_2O_2 stress response at the population level 22
1.5 Measuring variability in single cell gene expression heterogeneity 24
1.5.1 Snap-shot and time-lapse imaging of cells on agarose pads 25
1.5.2 Microfluidic devices complemented with real-time imaging 26
1.6 Thesis aims 26

2. Material and methods **29**
2.1 Strains and plasmids 30
2.2 Media and growth conditions 31
2.3 Microfluidics experimental setup 32
2.3.1 Microfluidic chip preparation 32
2.3.1.1 Mother machine chip preparation 32
2.3.1.2 Microcolony chip preparation 33
2.3.2 Mother machine setup 34
2.4 Microscopy 35
2.4.1 Time-lapse microscopy for mother-machine 35
2.4.2 Imaging of microcolonies 35
2.5 Live dead staining 36
2.6 Cell fixation 36
2.7 Microscopy data processing and analysis 36
2.7.1 Mother machine data processing 37
2.7.2 MutL-mYPet foci detection 37
2.7.3 Microcolony image analysis 38
2.8 Calibration of H_2O_2 concentration inside growth trenches 38
2.9 Quantification of parameters of cells 38
2.10 Alive vs dead and Deterministic vs stochastic categorisation 42
2.11 Chaos decision tree algorithm 42
2.12 Correlation analysis 43
2.12.1 Cross-correlation analysis 43
2.12.2 Autocorrelation analysis 43
2.13 Machine learning algorithm 44
2.14 Correlation Dimension to discriminate deterministic and stochastic processes 48
2.15 Lyapunov exponent computation 49
2.16 Linear regression analysis 50
2.17 Model parametrisation 50
2.17.1 Growth model parametrisation 50
2.17.2 Cell-cell interaction model parametrisation 51
2.17.3 Oxidative stress response model parametrisation 51
2.17.4 General stress response model parametrisation 52
2.18 Simulation visualization 53

3. Phenotypic heterogeneity in the bacterial oxidative stress response is driven by cell-cell interactions **54**

3.1 Summary 55
3.2 Introduction 55
3.3 Strong cell-cell variability is observed in the H_2O_2 stress response 56
3.4 A machine learning model is able to predict single-cell responses to H_2O_2 61
3.5 The properties of neighbouring cells drive oxidative stress response heterogeneity 65
3.6 Intracellular scavenging enzymes create a local H_2O_2 gradient 68
3.7 Barrier cells obtain high H_2O_2 tolerance via gradual adaptation 75
3.8 A rapid response to the environment overwrites cellular memory 78
3.9 Spatial gradients in H_2O_2 lead to cellular heterogeneity in mutagenesis 81
3.10 Discussion 83

4. Chaos in a bacterial stress response 89
4.1 Summary 90
4.2 Introduction 90
4.3 Quantitative model of the oxidative stress response in a bacterial population 92
    4.3.1 Cell growth model 94
    4.3.2 Cell-cell interaction model 96
    4.3.3 Oxidative stress response model 98
    4.3.4 Simulation procedure 101
    4.3.5 Simulation input 102
4.4 Chaos is predicted in a bacterial stress response 102
4.5 General stress response model 106
4.6 Observational data also suggest chaos 109
4.7 Experimental tests make or break chaos 115
4.8 A simple deterministic process explains chaotic oxidative stress response fluctuations 120
4.9 Discussion 130

5. A simple regulatory network coordinates a stress response in space and time to protect bacterial groups 134
5.1 Summary 135
5.2 Introduction 136
5.3 Expression dynamics of genes across the OxyR regulon 138
5.4 Transient growth inhibition causes a genome-wide expression pulse during stress 143
5.5 Upregulated genes exhibit pulsatile or gradual induction dynamics 145
5.6 Modelling explains the different regulation patterns 145

5.7 Model predictions suggest functional differences between pulsatile and gradually induced genes 149
5.8 Pulsatile genes show higher cell-to-cell expression heterogeneity 153
5.9 Downregulated, pulsatile, and gradually induced genes show different spatial patterns in cell populations 157
5.10 Discussion 158

6. Discussion 162
6.1 Bacterial stress responses: random or deterministic? 163
6.2 Deterministic chaos in cellular response 166
6.3 Gene regulation coordination in bacterial oxidative stress response 169
6.4 Outlook 171

Bibliography 173

Appendix 190

List of figures

1.1 Heterogeneity in stress response
1.2 Sources of heterogeneous stress response
1.3 Biochemistry of reactive oxygen species
1.4 Biochemistry of Fenton reaction
1.5 Bacteria under oxidative stress
1.6 Superoxide stress response
1.7 Transcriptional regulation by OxyR
1.8 Biochemistry of H_2O_2 scavenging by peroxidase and catalase
1.9 Stress response of *E. coli* to hydrogen peroxide
1.10 Iron regulation under H_2O_2
1.11 Population response of *E. coli* to hydrogen peroxide
1.12 Microfluidic devices for imaging single cells
3.1 Spatial gradient in oxidative stress response
3.2 Oxidative stress response characterised in microfluidic experiment
3.3 Growth effects on gene expression dynamics
3.4 Cells with Δ*oxyR* deletion do not survive 100 µM H_2O_2
3.5 Cell-cell variation in gene expression dynamics before and after H_2O_2 treatment
3.6 Machine learning predicts single cell response heterogeneity
3.7 Machine learning models to predict oxidative stress response heterogeneity and H_2O_2 treatment concentrations
3.8 Variation in the number of barrier cells per growth trench increases response heterogeneity across mother cells
3.9 Variation in the spatial structure of the micro-environment explains response fluctuations
3.10 Exponential decay of H_2O_2 in growth trenches as predicted by the calibration curve
3.11 Intracellular scavenging enzymes create short-range local H_2O_2 gradients
3.12 Δ*oxyR* cells do not provide cross protection against H_2O_2 stress
3.13 Metabolically inactive cells do not provide cross protection against H_2O_2 stress
3.14 Growth inhibition in the absence of cellular cross-protection
3.15 Local environmental variation determines divergent cell fates after H_2O_2 treatment
3.16 Cell death under 500 µM H_2O_2 treatment visualised using propidium iodide staining
3.17 Spatio-temporal response dynamics overwrite cell lineage-associated memory
3.18 Effect of cell movement on P*grxA*-CFP expression in a spatial H_2O_2 gradient
3.19 Exponential response decay after H_2O_2 removal
3.20 Response of sister cells diverge under 100 µM H_2O_2 treatment
3.21 Cells become more correlated with closer lineage relation and increasing barrier lengths
3.22 Cell memory in response to H_2O_2 treatment
3.23 Spatial heterogeneity in H_2O_2 concentration causes cell-to-cell variation in mutagenesis
4.1 Modelling the oxidative stress response in bacterial populations

4.2 Illustration of the iterative procedure for simulating the inter-dependent growth, stress response, and cell-cell interaction models
4.3 Illustration of model simulation with and without H_2O_2 treatment
4.4 The model predicts chaos in the stress response
4.5 Chaotic divergence of simulated stress response trajectories with small differences in initial conditions
4.6 Chaos emerges in a general model of stress responses in cell populations
4.7 Calibrating experimental versus modeling parameters
4.8 Cellular dynamics in model and experiments under low doses of H_2O_2
4.9 Experiments on the oxidative stress response in *E. coli* reveal a good fit with the modelling predictions
4.10 Mother cells display deterministic stress response dynamics under a wide range of H_2O_2 treatment and growth conditions in experiments
4.11 Measurements of stress response dynamics *in E. coli* are consistent with chaos
4.12 Stress response is negatively correlated with changes in number of barrier cells
4.13 Bacterial colonies in experiments exhibit oxidative stress response fluctuations consistent with chaos
4.14 Chaotic dynamics require strong coupling between cell-cell interactions and stress response
4.15 Chaotic dynamics require strong coupling between growth rate and stress response.
4.16 Predicted perturbations make or break chaos in experiments
4.17 Stress response and elongation rate dynamics with different growth and H_2O_2 treatment conditions
4.18 Deterministic chaos in oxidative stress response fluctuations at single cell level.
4.19 Phase diagrams for stochastic and deterministic traces of oxidative stress response.
4.20 Response fluctuations are not driven by noise
4.21 Correlation dimension analysis using Grassberger–Procaccia algorithm indicates that observed fluctuations are deterministic
5.1 Gene expression dynamics across the OxyR regulon under H_2O_2 treatment
5.2 Gene expression level changes in our study compared to the bulk mRNA level changes, reported by Roth *et al*., under H_2O_2 stress
5.3 Oxidative stress response genes show a range of different expression dynamics during constant H_2O_2 stress
5.4 Positively-regulated promoters show either pulsatile or gradual induction dynamics
5.5 Single cell expression traces of oxidative stress response genes display the cell-cell variability
5.6 A model of the oxidative stress response predicts the molecular basis of the different categories of gene regulation
5.7 Pulsatile genes exhibit higher expression sensitivity to H_2O_2 stress intensity
5.8 Pulsatile genes respond quickly to bridge the adaptation lag after H_2O_2 treatment
5.9 Cell-cell variability in gene expression magnitude for oxidative stress response genes in different regulation categories
5.10 Model to account for differences in reporters to follow gene expression dynamics
5.11 Coordination of pulsatile and gradual gene regulation in single cells
5.12 Spatio-temporal expression patterns across the OxyR regulon

Abstract

Bacteria, the most abundant organisms supporting life on Earth, inhabit various niches, from soil and aquatic life, to residing in hosts. Bacteria frequently experience oxidative stress during aerobic growth, host immune attack, microbiome interactions, and under antibiotic treatment. Here, we study bacteria under hydrogen peroxide (H_2O_2) and observe that individual cells exhibit variability in their oxidative stress response. Such diversification of cellular phenotype is often observed in response to changing environments, but the underlying causes of cell-cell variability and its implications for cellular function in the context of stress adaptation remain unclear. Cellular response variability is typically attributed to stochasticity in biochemical reactions inside a cell. Our machine learning algorithm reveals that the variability in cellular response is not stochastic but determined by the precise response of cells to dynamic levels of H_2O_2, created by short-ranged cell-cell interactions. We complement single-cell time-lapse imaging with mathematical modeling to probe the consequences of single-cell variability on population adaptation. We find that the H_2O_2 scavenging activity of cells creates strong H_2O_2 gradients, thereby protecting a large proportion of the population. We show that the gene expression fluctuations of individual cells during constant H_2O_2 treatment are in fact driven by chaos. Although it has been suggested that chaos may play a role in many biological phenomena, it has remained challenging to disentangle chaos from noise as a source of variability in biological data. The close correspondence between our experiments and model allowed us to show that chaos emerges from deterministic feedbacks between cells and their environment. These feedbacks amplify small differences in initial conditions, resulting in diverging stress response dynamics that lead to seemingly random phenotypic variability. Next, we investigate how individual cells manage to regulate the levels of many diverse genes that encode oxidative stress tolerance factors. We find that the dynamics of over two dozen genes create a diversity of spatiotemporal expression patterns that benefit the stress adaptation of a cell population. Overall, we show that bacterial stress responses can generate variability under stress via deterministic factors without noise. Our work provides a general approach for uncovering the hidden variables that drive variability in cellular responses to environmental changes and for probing the regulatory mechanisms from molecular, single-cell, and population perspectives.

Chapter 1

Introduction

1.1 Gene regulation in bacteria under stress

Bacteria surround us everywhere and colonise different niches, from soil to our gut. Survival in any habitat depends on how a bacterium can withstand the stress posed by environmental fluctuations, for example, by changes in temperature, pH, or exposure to toxins, radiation, antibiotics, etc. In response to external threats, bacteria rely on sensing the stress and activating responses to relieve the deleterious effects[1]. Bacterial stress responses involve a cascade of genes that are upregulated or downregulated to defend a bacterium against the incoming stress[1]. In general, genes regulated by stress responses code for enzymes with a variety of functions, *e.g.* repairing damaged macromolecules, removing or detoxifying stress agents from the cell[2], shutting down stress-sensitive or energetically costly processes such as DNA replication or protein translation[3,4], modifying metabolism[5], controlling cell motility and biofilm formation[6], and combatting aggressors (such as immune cells, competing bacteria, or phages).

Bacterial genomes contain thousands of different genes. mRNAs are transcribed from these genes which are translated into proteins to perform various functions. Gene regulation occurs at different levels, primarily during transcription in bacteria, when regulatory factors control transcription of a gene into mRNA by RNA polymerase[7,8]. Repressors inhibit transcription by binding an operator region that overlaps with the polymerase binding site (promoter) while activators up regulate the transcription by binding enhancer region near promoter and enhancing RNA polymerase binding to the promoter[9]. The promoter site has sequences that can code for the regulation of the gene(s) downstream. Whilst some genes like those essential for cellular growth are constitutively transcribed, the degree of regulation of other genes can vary in response to stress[1,8].

1.2 Cells in a population commonly differ in their responses to stress

Clonal populations of cells often exhibit variability in their phenotypes and gene expression levels, even under the same external environment [Figure 1.1][10,11]. Phenotypic heterogeneity was observed in 1957, when Novick and Weiner found the activity of beta-galactosidase enzyme to be induced at variable levels for single cells of the same bacterial culture[12]. Because of the small size of a bacterium, proteins are present in lower numbers inside individual cells compared to larger eukaryotic cells[13], rendering biochemical reactions, in which they are involved, more stochastic[10]. This variability has been implied in various studies for non-genetic individuality (where cells with identical genetic content vary in their protein expression levels and phenotypes)[14–16].

With technological advancements, studies at single-cell resolution have been performed and it has become clear that the stochastic nature of the underlying molecular processes can in some cases drive heterogeneity in the responses between individual cells[10,14,17–19]. To understand the consequences of heterogeneous responses, the first step is to understand the origin of the observed fluctuations[20,21].

1.2.1 Sources of cell-cell variability

1.2.1.1 Intrinsic and extrinsic noise

Cell-cell variation observed in gene expression dynamics can be a consequence of noisy regulation[22][Figure 1.1]. The ubiquity of phenotypic heterogeneity during stress can be attributed to the inherent noise present in gene expression[11,22–25][Figure 1.2A]. Intrinsic noise

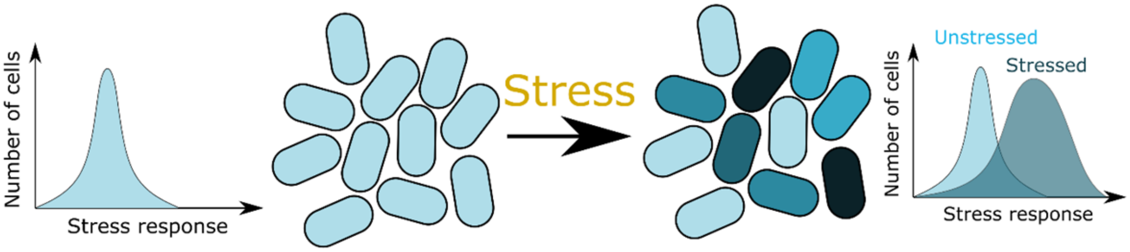

Figure 1.1 Heterogeneity in stress response:
A clonal population of cells exhibits variability in stress response phenotype under stressed conditions.

is a product of randomness due to collisions between small numbers of molecules in a bacterium that lead to various biochemical reactions. These collisions can regulate different pathways. For example, transcriptional regulation of stress responses to switch a gene 'on' or 'off' would be affected by the probabilistic collisions between the few copies of transcription factors and their binding sites on DNA[26,27]. Similarly, collisions between RNA polymerases with the active or switched 'on' gene promoters, and between ribonucleases and transcripts, will also be probabilistic, thus resulting in noisy fluctuations in the protein production rates of a given gene[19]. Azpeitia *et al.* showed that the residence time of transcription factor on DNA can affect noise in gene expression, with a shorter residence time reducing the noise in gene expression for lower levels of induction[28]. Mathematically, intrinsic noise is different than extrinsic noise. For extrinsic noise, the observed fluctuations of a gene will correlate with that of another gene in a cell, thus differentiating it from intrinsic noise. The temporal changes in the concentration of RNA polymerases, ribosomes, *etc.* contribute to extrinsic sources of noise. Extrinsic properties may also vary from cell to cell, leading to variation in gene expression. Furthermore, as a bacterial cell grows and divides, the differences in the size of daughter cells and unequal partitioning of molecules can lead to variability in the number of molecules inherited on division[27,29]. Kaern *et al.* showed that reduction in cell size can increase gene expression heterogeneity[14].

1.2.1.2 Growth rates

The concentration of molecules may vary with changing growth rates. On reduction of growth rate, the dilution of molecules in a cell is slowed down and results in an overall increased concentration inside a cell [Figure 1.2B]. Growth dependent heterogeneity has previously been implicated in SOS response[30], oxidative stress[31], and other stress response regulator dynamics[32]. Single cell gene expression dynamics observed by Sampaio *et al.* revealed temporal variability in different stress response genes (for resistance against acid stress, oxidative stress, heat shock, and other stresses) that were correlated with cellular growth dynamics [32]. Patange *et al.* studied *E. coli* in mother machine microfluidic devices under a short dose of high hydrogen peroxide and observed heterogeneous behaviour of the general stress response regulator, RpoS[31]. They found that the pulsatile behaviour of RpoS in individual cells was anti-correlated with their growth, allowing survival under stress. Martino *et al.* observed the induction of *dps*, which is important for nucleoid organisation under a starved state, in *E. coli* growing on agarose pads under oxidative stress[33]. They observed heterogeneity in single cell response traces that were dependent on the kinetics of cellular growth.

1.2.1.3 Environmental variation

Another potential source of cell-cell variability is the memory of past conditions[34–36][Figure 1.2C]. The duration of memory is generally set by the cellular growth rate, which determines the overall balance between the production and dilution of molecules as cells elongate and divide[32,37]. Because stress conditions affect growth rates, complex feedbacks can arise between the stress level and gene expression dynamics. Variation in cell growth and morphology can also affect the influx, dilution, and reaction-diffusion dynamics of stressor molecules[32,38–40]. Furthermore, cells in a population can interact and modulate their environment in response to stress[41–43]. Van Vliet *et al.* showed that cellular responses are spatially correlated, demonstrating how the response of a focal cell is affected by the response activity of neighbouring cells[44]. Cells are often under dynamic environments, coupled with imbalances in the levels of nutrients and the presence of stressors in the environment[10]. Growing in spatially structured populations, bacteria continuously consume and release compounds to their surroundings, creating long ranged or micrometre-sized short ranged interactions[45]. These interactions lead to phenotypic variations within a clonal population, which has been demonstrated in cross-feeding[46,47] and antibiotic tolerance[48]. While sponging up of nutrients creates a stressful niche within a population, sponging up of stressor molecules can relieve the stress for cells. These local environment variations create gene expression changes spatially, allowing for population level survival[49,50]. Zoheir *et al.* visualised different stress responses *i.e.* genotoxicity, cytotoxicity, and physiological stress simultaneously in a growing biofilm and found spatially stratified populations expressing heterogeneous stress response levels[50]. Bacteria often possess multiple stress resistance systems, *e.g.* acid stress in *E. coli* whose function depends on the level of acidity in the cellular environment. Hence, the stratification of pH levels in bacterial population would result in varied expression levels of different acid resistance system, as seen by Brameyer *et al* [51].

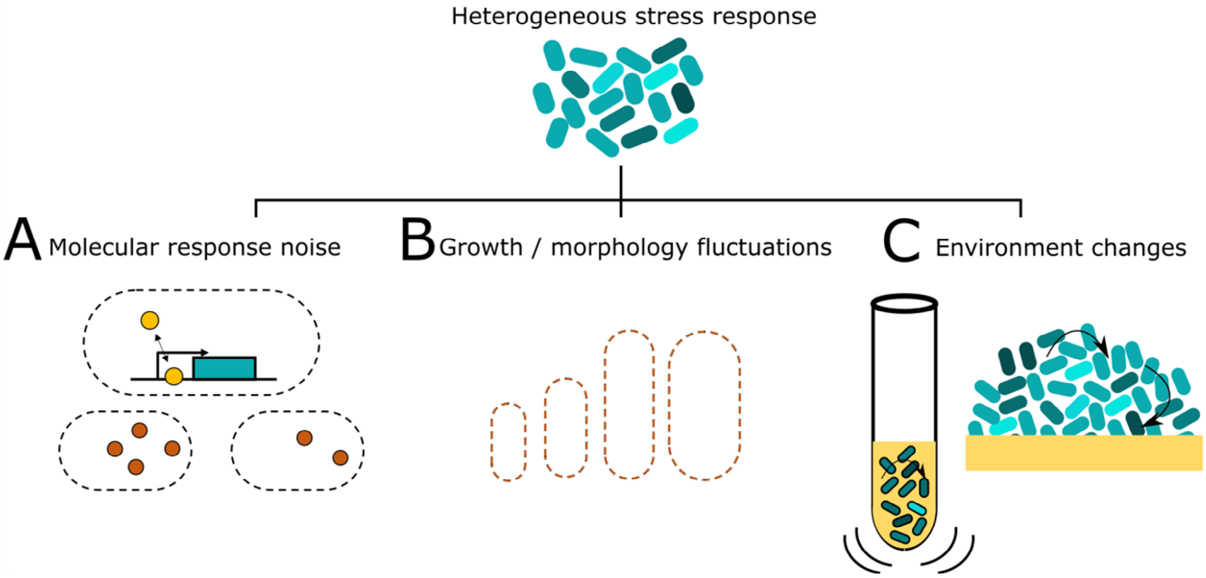

Figure 1.2 Sources of heterogeneous stress response:
*Individual cells exhibit variability in stress response due to (**A**) molecular response noise, (**B**) changes in cellular growth rates and morphology and/or (**C**) cell-cell interactions coupled with environment changes.*

Exploring the intersection of noisy stress responses, metabolism changes, and growth rates [Figure 1.2] can provide insights into population adaptations and an understanding of phenotype diversifications[31,37,52].

1.2.1.4 Determinism in ‘noise-like’ observations

As such, it is notoriously difficult to disentangle the primary stochastic sources of phenotypic heterogeneity from deterministic effects. This has been exemplified in studies that revisited the phage lysogenic switch, and discovered that its apparent stochastic behaviour can, at least partly, be explained by previously unobserved deterministic processes of the host cell[53–55]. Another study by Lavi *et al.* showed that the complex movement patterns of *Dictyostelium* and other migrating cells were an effect of the coupling of factors in the underlying machinery, that introduces instability in the system. The resulting 'noise-like' behavior[56] was observed and previously explained as random walks. Rossi *et al.* explored the non-uniform timing of cell death under antibiotic treatment and found cell-cell variation to be strongly linked to cell survival[57]. Another recent study by Yang *et al.* showed that deterministic dynamics appeared while studying cell death under stress, where noise initially played a role in erasing the effect of different cell states at the time of stress treatment[58]. These studies point to the idea that experimentally observed cell-cell variability may not always arise from noise or randomness. Heterogeneity may arise without the stochastic molecular noise, but due to underlying deterministic mechanisms that might be unknown and yet to be discovered. The understanding of how the cell-cell variability arises is then important to probe its implications and evolution.

1.2.2 Why does cell-cell variability emerge in a bacterial population under stress?

1.2.2.1 Bet-hedging under stress

Bacteria rely on sensory and gene regulatory systems to respond to changes in the conditions of their immediate environment[1]. When the environment around cells is perturbed and made stressful, cell-cell variability in growth rate[37] or gene expression may arise in response[10,14,32,59]. The phenotypic variability is often explained as a 'bet-hedging' mechanism where a subpopulation of cells compromises fitness for an increased adaptation capacity of the whole population[60]. Cells can utilise such variability to create diversity in a population without genetic modifications, thereby switching individual cells to different states which can increase survival probabilities under stress[14,59,61,62]. Against changing environments, cells induce specific stress responses that can lead to an adaptation lag before the response activation has been fully achieved against the threat[63]. Under such conditions, especially against unpredictable changes in the local environment of a cell, the bet-hedging strategy has been proposed to be useful, which works by generating subpopulations of cells with a range of induction of stress response genes, compromising on fitness but allowing long term survival[64]. For bacteria living in populations where they experience dynamic local environments of nutrients, stressors, and metabolites, such a strategy could serve as an evolutionary adaptative way to counter changing external conditions. The bet-hedging strategy has been widely studied for bacteria under antibiotic treatments, where cells can switch randomly into a dormant state, and these dormant cells can survive under stress. On removal of the antibiotic exposure, dormant cells that persisted in stressful conditions are able to regrow[64]. Mammar *et al.* studied the effect of noise in ComK gene, which is responsible for DNA uptake ability in *Bacillus subtilis*, and suggested that noise in genes can be under evolutionary pressure. They showed that a subpopulation of desirable phenotype in a heterogeneous population is achieved by changing the basal gene levels of cells by modulating the mean and variance of expression [65].

1.2.2.2 Heterogeneity as a by-product of gene expression regulation

Genes associated with stress responses appear to show particularly high levels of cell-cell variation[23,66], which may have evolved to enhance the survival of a genotype[36,67–69]. Hence, even though most cells do not maximise their fitness[70], cellular heterogeneity is advantageous for survival under stresses[71] such as alkylating stress[72], oxidative stress[31], antimicrobials[32,67,73] and acid stress[74].

Transcription factors modulate gene regulation under stress and studies have shown that noise in gene expression levels can be modulated by transcription factors[75,76]. Transcription factors regulate the induction rate of genes, and, it was observed that slower rates of gene induction are related to a intrinsically noisier expression[25,77,78]. These noisy gene expressions, under the control of a stress response transcription factor, can result in a heterogeneous cellular behaviour under stress. In bacteria, the number of molecules involved in sensing stresses and regulating gene expressions is often very small, such that stochastic fluctuations are unavoidable. It may even be highly improbable, if not impossible, for any stress response to be both fast and accurate at the same time[79]. Hence, when the speed of gene induction is crucial for survival, noise in the response amplitude may be an inevitable by-product of the underlying molecular network. While many studies have observed the advantageous effect of cell-cell heterogeneity, noise in gene expression can have negative consequences if the variability limits the accuracy of the stress response[20,71]. The inaccurate regulation of genes responsible for protecting microbes under stress can have deleterious effects on their growth and fitness[10,32,80–82](*e.g.* overexpression of certain stress response genes can be harmful as expressing them may be energetically costly for cells). Wolf *et al.* evolved de-novo *E. coli* promoters and demonstrated that all promoters exhibited basal levels of noise and highly regulated promoters were acted upon to exhibit higher noise levels. This noise is observed in expression of targets from regulators which in fact mediates a more accurate regulation[83].

1.2.2.3 Division of labor

Cells have multiple genes that can perform similar functions for protection under stress, for *e.g.* scavenging enzymes that degrade high amounts of reactive oxygen species. Mishra *et al.*

reviewed the role of scavengers in bacteria under oxidative stress. They suggested that scavenging enzymes with different kinetics, stability of proteins, and specificity to substrates are required by cells to tackle a more precise resistance to incoming oxidative stress[84]. While catalases protect *E. coli* cells at higher concentrations of hydrogen peroxide, peroxidases target multiple substrates and scavenge lower concentrations of hydrogen peroxide[85]. Cells in a population, as a result, may exhibit different levels of these enzymes for protection under diverse and dynamic levels of oxidative stress. *E. coli* also has multiple stress resistance systems, *e.g.* acid stress whose function depends on the level of acidity in the cellular environment. Hence, varying pH levels in bacterial populations would result in dynamic expression of a given acid resistance system, as suggested by Brameyer *et al* [51]. Such division of labor strategies can also allow cells to survive a broad range of stresses, *e.g.* pH levels. Overall, bet-hedging and division of labor contribute to explaining the adaptive benefits of phenotypic heterogeneity under stress. Moreover, the noise levels in gene expression are regulated to optimize population response under stress [86].

In this thesis, we explore the causes and consequences of cell-cell heterogeneity under oxidative stress, which is one of the major stresses experienced by bacteria, as a consequence of growing in aerobic conditions[2] and accumulation of high levels of reactive oxygen species (ROS) [87–89]. In particular, we study *E. coli* under hydrogen peroxide stress. Within a population exposed to H_2O_2, individual cells exhibit a heterogeneous behaviour whose underpinning mechanisms remain elusive. While the adaptation to H_2O_2 at the population level has been explored [90–92], its consequences at the single cell level have not been studied[85,90,91,93–96].

1.3 Bacteria under oxidative stress

1.3.1 Biochemistry of ROS

As a double-edged sword, molecular oxygen (O_2) plays a vital role in cellular functions, including respiration, but can also get converted into lethal ROS[97]. ROS such as superoxide (O_2^-) and hydrogen peroxide (H_2O_2), are formed in the cell when molecular oxygen adventitiously acquires one and two electron(s), respectively, from redox active flavoenzymes[98,99] [Figure 1.3]. Short-lived singlet oxygen species can also be formed through absorption of energy by O_2 which can photodynamically inactivate bacteria[100]. On absorption of electrons, molecular oxygen converts into the superoxide radical which on further reduction forms H_2O_2 [Figure 1.3]. O_2^- can also spontaneously dismutate into H_2O_2 and O_2, catalysed by the presence of superoxide dismutase (SOD) enzyme in a pH- and concentration dependent reaction[101][Figure 1.3]. Oxidation of ferrous iron (Fe^{2+}) by H_2O_2 results in the production of highly reactive hydroxyl radicals ($\cdot OH$) through Fenton[102] and Haber-Weiss[103] reactions [Figure 1.4]. An imbalance between the formation and detoxification rates of ROS[104] inside a living cell increases ROS concentrations causing cellular dysfunction and oxidative stress[105,106]. Almost every organism has evolved defense and repair mechanisms to survive the ubiquitous formation of ROS under aerobic conditions and these mechanisms are conserved through evolution from bacteria to eukaryotes[107–109].

1.3.2 ROS toxicity

The benefits of O_2 are limited by its toxicity to different components of a cell[106]. Oxidative stress can inactivate proteins, cause DNA damage, and lead to peroxidation of lipids, thereby

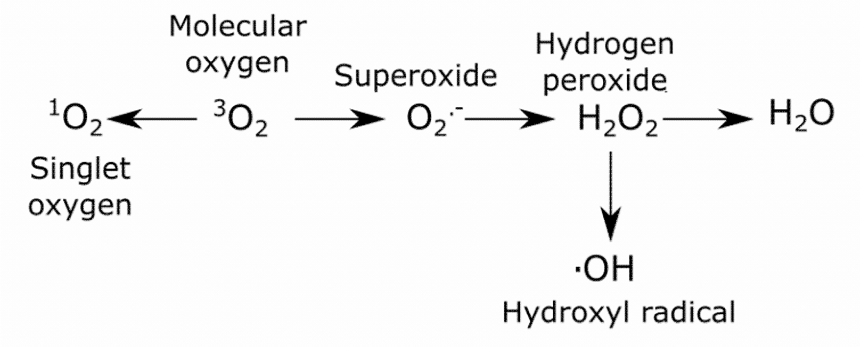

Figure 1.3 Biochemistry of reactive oxygen species:
Stepwise reduction of molecular oxygen leads to the formation of superoxide, hydrogen peroxide and water. Hydroxyl radicals are produced when H_2O_2 reacts with free iron via the Fenton reaction.

causing lethality[110]. Studies have shown that anaerobes can suffer from molecular oxygen itself due to the inactivation of enzymes, as it can form adducts to glycyl-radical enzymes leading to polypeptide cleavage[111]. Superoxide damages multiple targets in a cell, and more importantly, its scavenging by SOD releases H_2O_2, which on subsequent conversion to hydroxyl radicals is lethal to cells [Figure 1.5]. In 1986, Carlioz and Touati, constructed mutant strains of *E. coli* that were SOD deficient and exhibited growth defects when grown aerobically[112]. They observed poisoning of only a few vital processes required for cell growth including high rate of mutagenesis and branched-chain amino acid auxotrophy[112]. Besides those effects, auxotrophy of aromatic and sulphur-containing amino acids was later reported[106,113]. Superoxide also damages iron sulphur clusters since they are attracted to the catalytic iron ion of the enzyme. This binding event oxidises the Fe-S cluster making it unstable, and eventually, the iron ion is lost, which inactivates the enzyme[114]. This reaction also releases H_2O_2 as a by-product. The superoxide radical can react with a proton[115] to form perhydroxyl radicals that can damage polyunsaturated fatty acids[116].

Hydrogen peroxide (H_2O_2) is a small uncharged molecule that is degraded rapidly inside the cell with the action of catalases and peroxidases[85]. Despite high reduction potential, the oxidation action of H_2O_2 is slower than that of superoxide because of the activation barrier to break the dioxygen bond. However, d-orbital transition metals interacting with H_2O_2 experience weakened bond strength, and can hence oxidise the Fe-S clusters attacked by O_2^- [114]. H_2O_2 leads to the formation of hydroxyl radical which has one unpaired electron and can readily abstract electrons from substrates like iron [Figure 1.3]. Therefore, OH· radicals damage essential biomolecules inside bacterial cells by oxidising double bond and sulfhydryl groups in lipids, proteins, and cellular membrane surfaces[117] [Figure 1.5]. While lipid peroxidation is an inevitable result of oxidative stress for eukaryotic cells, it is less likely for bacteria because bacterial lipids are composed of saturated or monosaturated fatty acids that are less prone to oxidation[2].

Winterbourn *et al.* demonstrated that neither H_2O_2 nor O_2^- can directly damage DNA[118], however, mutants lacking SODs and catalases show high mutation rates[119,120], which can be explained by the production of lethal ·OH radicals via the Fenton reaction[102] [Figure 1.4]. The ·OH oxidises organics biomolecules at very fast diffusion-limited rates[121] and is the only ROS that directly damages most of the biomolecules in a cell, viz. RNA, DNA, protein, and lipids[97][Figure 1.5]. The most prominent effects of such damages are seen in DNA lesions that can result in high rates of mutagenesis and DNA strand breaks, killing most bacterial cells[122].

The DNA lesions include damage to nitrogenous DNA bases, cross-linking between DNA strands (inter- and intra-), adducts of protein with DNA which are formed on reaction of 2-deoxyribose or the nucleobases with ROS, in particular singlet oxygen, hydroxyl radicals[123].

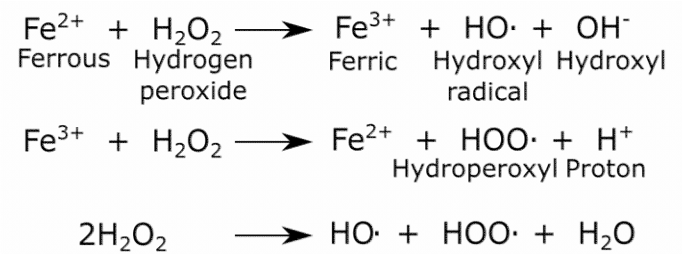

Figure 1.4 Biochemistry of Fenton reaction:
Equations depicting the stepwise reaction of hydrogen peroxide with ferrous iron to produce hydroxyl radicals that damage cellular components.

Singlet oxygen can also damage DNA directly by interacting with guanine (containing electron rich double bonds), unlike OH· radicals that target all nucleobases[124]. Guanine has a lower potential of reduction compared to other DNA bases, allowing the transfer of electrons to nearby oxidised bases, hence repairing them[125]. The commonly observed product of oxidised guanine is 8-oxo-7,8-dihydroguanosine (8-oxo-G)[126,127], which has the potential to pair with adenine or cytosine base, hence disturbing DNA coding[128]. Hsu *et al.* showed that proof reading by DNA polymerase is ineffective under these conditions. They showed that 8-oxoG: cytosine behaves as a mismatch (canonical in theory) and 8-oxoG: adenine pair recognises as a cognate, which finally leads to a G: T pairing in the resulting DNA strand post replication[129]. They also observed cases of inversion of mismatch recognition. Overall, the 8-oxo-G mismatch is either repaired or fixed as a G: T base pair mutation. Liu *et al.* found that on treating *E. coli* with a burst of H_2O_2, 8-oxo-G levels were higher in RNA than DNA, showing that peroxide stress has a more detrimental effect on RNA[130]. Other oxidative lesions modified under oxidative stress include oxidized cytosine 5-hydroxycytosine (5-HO-C), oxidized adenosine 8-oxo-7,8-dihydroadenosine (8-oxo-A), and oxidized uridine 5-hydroxyuridine (5-HO-U).[131] Other studies have demonstrated inhibition of translation under oxidative stress[3,124].

ROS exposure also causes protein damage in cells, where such damage can lead to a covalent change in proteins. In particular, amino acids methionine (Met) and cysteine (Cys) have higher oxidation sensitivity because they possess an electron rich sulphur atom [110]. Oxidative damages inactivate or destabilise proteins, rendering them non-functional, and this impaired function sometimes leads to cell death. Studies have observed oxidation in cysteinyl and methionyl residues of cell-extracts. However, such damages have not been documented for mutants of SOD or catalases/peroxidases[2]. Under very high levels of H_2O_2 (of the order of a few micromolar), di-sulphide bond formation in proteins has been detected in *E. coli*[132]. These H_2O_2 concentrations are many folds higher than physiologically relevant doses, demonstrating that proteins are not targeted by oxidants at doses of physiological importance[2]. However, several thiol redoxins, regulated by the H_2O_2 sensing transcription factor OxyR, show a rapid reduction of disulphide bonds including glutaredoxin-1 which converts oxidised OxyR back to its reduced form[2].

1.3.3 ROS sources:

1.3.3.1 Endogenous sources

The production of ROS inside cells due to aerobic metabolism was demonstrated by Imlay's group who showed that scavenging mutants of *E. coli* exhibit growth defects when grown aerobically[85,108]. Measurements with mutants allowed estimation of ROS generation in air-saturated *E. coli* showing production of 14 µM/s H_2O_2 during exponential growth in glucose medium and 5-10 µM/s O_2^- [85]. For aerobes, flavoproteins not involved in respiration are responsible for the production of high H_2O_2 as they increase the chances of an adventitious transfer of electrons to O_2[99]. Under high levels of oxygen in surroundings, cells can have

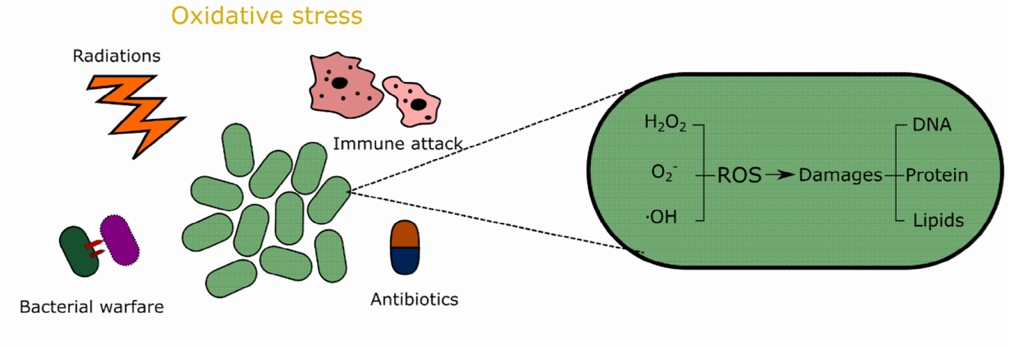

Figure 1.5 Bacteria under oxidative stress:
Bacteria are exposed to high amounts of reactive oxygen species (ROS) in the environment, for example, from radiations, antibiotics, host immune defences, and competing bacterial species. High concentrations of ROS such as hydrogen peroxide (H_2O_2), superoxide (O_2^-), and hydroxyl radical (·OH) can lead to redox imbalance in cells, causing damage to DNA, proteins, and lipids.

higher amounts of aberrant electron transfers to O_2 than redox enzymes, increasing the endogenous ROS[107].

1.3.3.2 Exogenous sources

As the oxygen levels increased on earth over billions of years, organisms evolved to tolerate oxygen and evolved responses to tackle high doses of oxidative stress[133]. Even though cells have advanced their oxidative stress mechanism and have evolved ways to survive aerobically, they continuously face high oxidative stress conditions [Figure 1.5]. Cyclic organic compounds like paraquat or quinones can enter cells and abstract electrons from redox enzymes, transfer them to O_2, and hence produce toxic amounts of O_2^- [134]. In oceanic and fresh waters H_2O_2 levels can rise up to millimolar ranges, enough to cause stress to bacteria[135]. Organic compounds including chromophores in water get excited by UV rays from the sun, transferring electrons from reductants to O_2[136] , which negatively affects the bacterial growth. Other abiotic sources found near the oxic-anoxic interfaces in hydrothermal

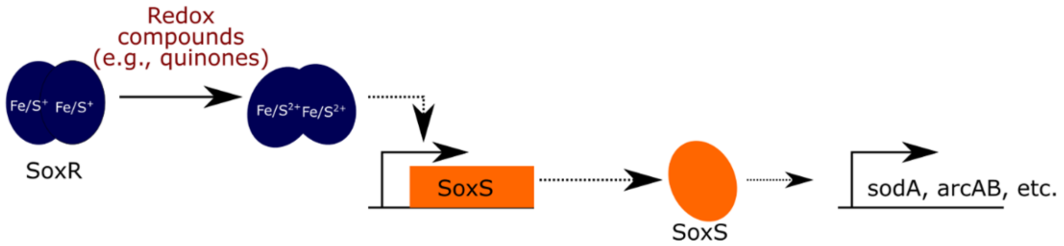

Figure 1.6 Superoxide stress response:
Under high superoxide concentrations in a cell, SoxRS transcription factor induces repair enzymes such as superoxide dismutase (sodA), multi-drug efflux pumps (acrAB).

vents or soil can produce ROS in the inhabiting microbes as a result of the collision of high-low potential fluids[137]. Bacteria residing in the large intestine can experience ROS toxicity due to the production of H_2O_2 by the reaction of oxygen with sulphide at the microoxic interface[138]. H_2O_2 in the gut can also be produced by the metabolism of lactic acid bacteria or by the action of phagocytic cells at the intestinal lining[89]. ROS produced by lactic-acid metabolism or lethal attacks by viral or bacterial species can be harnessed by bacteria to fight off competing species[139,140]. Plants and mammals also utilise ROS to inhibit bacterial growth by oxidative bursts generated via the immune response[95,141,142]. During inflammation and surgeries, infusion of ROS has led to lower infection rates[143]. However, the mechanism by which phagocytic H_2O_2 and/or O_2^- inhibits microbial growth is not clear[89,141]. Redox-cycling compounds like pyocyanin secreted by *Pseudomonas aeruginosa* and quinone found in plant competitors have been shown to impose intracellular O_2^- stress, although alternate functions of these compounds have been proposed in literature as well[89]. It has been suggested by Collin and Walker labs that clinical antibiotics show a common killing mechanism via ROS production[5,144,145], which has been a topic of debate and discussion. Other groups have shown contrary data[146–148], however, a lot of studies now support that the interactions between antibiotics and their targets lead to perturbations in metabolism that cause lethality via ROS generation or accumulation of other damaging molecules[5].

1.4 Protection from ROS

1.4.1 Protection from superoxide stress

O_2^-, being a charged species, cannot cross cellular membranes and penetrate bacterial cells. Therefore, superoxide stress is generally produced internally[149,150]. Superoxide dismutase (SOD) keeps the endogenous production of O_2^- low[2]. SoxRS transcription factors enable adaptation to these stresses [Figure 1.6]. SoxR is a protein dimer that senses redox-active molecules inside a cell by oxidation of Fe-S cluster in each of its monomers and induces SoxS, which acts as a secondary transcription factor, activating repair genes in its regulon including superoxide dismutase (sodA), multi-drug efflux pumps (acrAB), *etc*[151][Figure 1.6]. Unlike O_2^-, H_2O_2 very readily crosses membranes at rates similar to water by virtue of being very small, non-polar, and uncharged[85]. Hence, H_2O_2 serves as an ideal weapon to harm bacteria[151]. Various abiotic and biotic sources, as mentioned in the previous section, can lead to an increased amount of peroxide stress in the environment. H_2O_2 diffuses passively through membranes making it difficult for the target cell to exclude it from flowing into the cell[85,152].

1.4.2 Protection from H_2O_2 stress

1.4.2.1 Oxidative stress response regulation in E. coli

The transcription factor OxyR is the major stress response regulator activated by H_2O_2, inducing expression of H_2O_2 scavenging and enzymes to repair redox damage under stressful concentrations of H_2O_2[2,97,151][Figure 1.7, 1.9]. On entering a cell, H_2O_2 reduces the glutathione (GSH) to oxidised glutathione (GSSG) ratio inside the cell, consequently increasing the overall redox potential. The redox potential of *E. coli* is -260 mV to -280 mV. When the redox potential reaches around -185 mV, the transcription factor OxyR senses an overabundance of H_2O_2 by oxidizing its hyperreactive thiol (Cys199) to a sulfenic acid at a rate of 10^5 $M^{-1}s^{-1}$, thereby detecting micromolar concentrations of H_2O_2 within seconds[153]. The sulfenic acid subsequently forms a disulphide bond with Cys208[154,155]. This oxidised form of OxyR cooperatively binds the DNA to regulate gene expression [Figure 1.7]. OxyR can bind DNA as a dimer or tetramer where monomers bind to adjacent parts of DNA via helix-turn-helix binding[156] [Figure 1.7]. This results in an overall lack of conservation of the sequence of bases where OxyR binds the DNA and results in many degenerate homologies. Toledano *et al*. showed that OxyR, in its oxidised state, can recognise the sequence of ATAG nucleotides spaced by 10 base pairs in four major grooves [157], whereas reduced OxyR associates with 2 pair of major grooves separated by a helix turn [Figure 1.7]. OxyR differentially regulates gene activity, where it can bind promoters of some genes in oxidised form and others in both oxidised and reduced forms[158]. Generally, the reduced form is inactive and does not activate transcription. OxyR stimulates transcription of about two dozen genes, including H_2O_2 scavenging enzymes *i.e.,* catalase (KatG) and NADH peroxidase (AhpCF), which have high catalytic efficiency[85] [Figure 1.8]. Oxidised OxyR induces several enzymes for disulphide reduction (gorA, grxA, trxC, dsbG), one of which, grxA, reduces OxyR, thereby enabling deactivation of the response[97,159]. OxyR, in its reduced form, binds to its own gene promoter, having an auto- inhibitory action[160]. OxyR, in its oxidised form, induces an array of genes [Figure 1.9] that are involved in regulating the

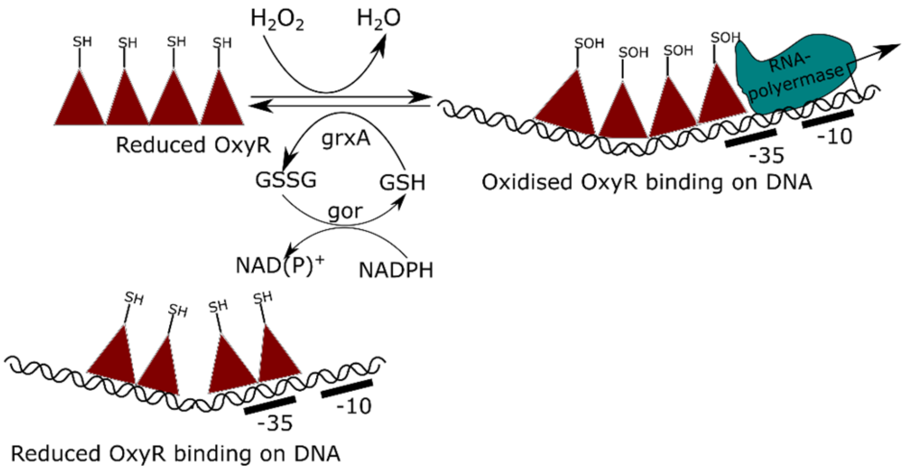

Figure 1.7 Transcriptional regulation by OxyR:
The figure shows the redox reaction of OxyR under high H_2O_2 concentrations inside a cell. The schematic depicts the binding of OxyR on DNA in its oxidised and reduced forms. The DNA strand is annotated with -10 and -35 positions relative to the promoter region. The reduced form of OxyR binds two major grooves separated by one DNA helix, whereas oxidised OxyR associates in four adjacent grooves, regulating the transcription of genes in its regulon.

metabolic production of ROS (oxyS)[161], and iron metabolism (dps, fur, sufA-E, hemH, mntH)[84]. OxyS also facilitates cell cycle arrest suggested to help in DNA repair.[162] The miniferretin dps sequesters iron[163] and, with the help of other iron metabolism genes (yaaA[164], fur), avoids the Fenton reaction [Figure 1.4]. To balance iron sequestration by dps, cells induce ClpSA, which subsequently allows iron sulfur clusters to be repaired[165] [Figure 1.10]. Under normal growth conditions, cells synthesise their iron sulfur clusters using the housekeeping Isc system. Since Isc does not work well in low iron conditions, induction of Suf enzymes allows cells to repair Fe-S clusters which would otherwise be repaired by Isc [166][Figure 1.10]. Cells also shift towards utilising manganese, instead of iron, as a divalent mononuclear enzyme cofactor, which is unreactive with H_2O_2[167]. Heme synthesis in biosynthetic pathways is sustained by hemH and hemF in iron scarce conditions[168][Figure 1.10]. OxyR induced stress response regulation in *E. coli* is widely conserved in different

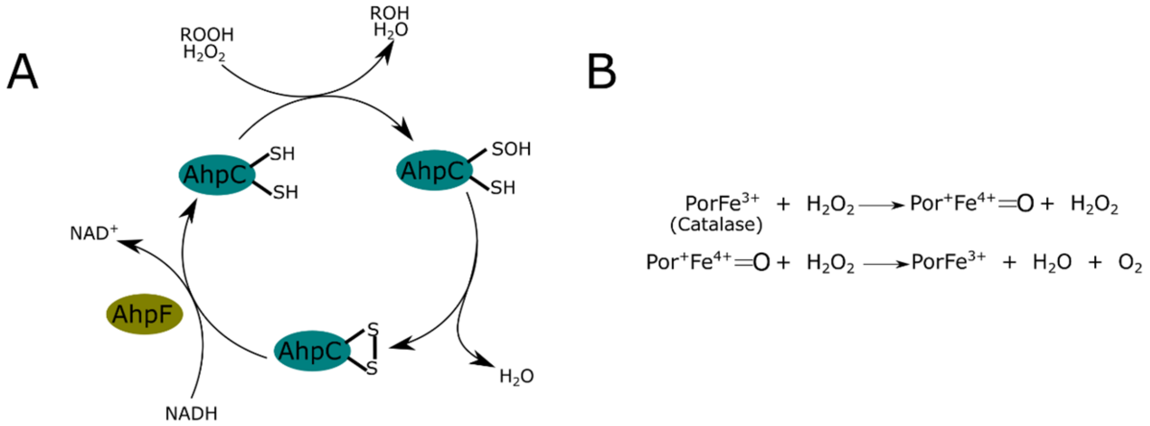

Figure 1.8 Biochemistry of H_2O_2 scavenging by peroxidase and catalase:
*The equations show the degradation of H_2O_2 into water by (**A**) AhpCF (alkyl hydroxy peroxidase) and (**B**) KatG (catalase).*

bacterial species[109]. While *E. coli* uses OxyR to respond quickly to sub micromolar concentrations of H_2O_2, *Vibrio vulnificus* uses two OxyR proteins that are sensitive to different ranges of H_2O_2[169]. Gram positive bacteria often have a different H_2O_2 sensor, namely PerR, which are dimeric proteins belonging to the Fur family of metal binding transcriptional factors[151].

1.4.2.2 H_2O_2 stress response at the population level

Oxidative stress under H_2O_2 exposure has been of interest for a long time and has been characterised thoroughly at the population level for planktonic cultures and colonies [Figure 1.11]. Treating cells with a low dose of H_2O_2 was found to increase their tolerance to a subsequent challenging dose[119]. Many groups studied the protection effect under oxidative stress and found that the density of bacterial cell culture affected its stress sensitivity. Low density cultures were more sensitive to H_2O_2 stress and to competition with other ROS-

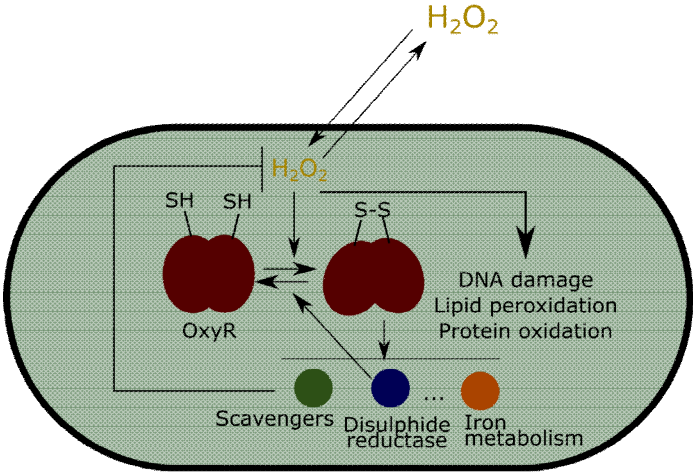

Figure 1.9 Stress response of E. coli to hydrogen peroxide:
H_2O_2 passively enters E. coli through the cell membrane. Higher cellular concentrations of H_2O_2 oxidise OxyR, which then undergoes a conformational change. The oxidised OxyR induces an array of stress response genes including scavenging enzymes, disulphide reductases, and iron metabolism genes. Scavenging enzymes reduce the amount of intracellular H_2O_2, and grxA (glutaredoxin-1) converts the OxyR back to its reduced form.

producing bacteria[90,170]. For bacteria interacting with plant cells, it was found that the initial H_2O_2 scavenging rate of the invading bacteria was proportional to the bacterial density[95][Figure 1.11]. The activation of OxyR, was also found to be a function of cell density[153]. Cochran *et al.* found that the outer surface of *P. aeruginosa* biofilms blocked H_2O_2 penetration because H_2O_2 neutralisation by KatG enzyme was much faster than the diffusion of H_2O_2 through the biofilm[91][Figure 1.11]. Seaver *et al.* modelled H_2O_2 fluxes in individual cells and their compartmentalisation in *E. coli*, and found that the rate limiting step of H_2O_2 detoxification was the entry of H_2O_2 into cells[85]. Despite the H_2O_2 adaptation at the population level being sensitive to cell density as evidenced by aforementioned observations [90–92], its consequences at the single cell level have not been studied[85,90,91,93–96]. The role of spatial organisation of cells in protecting a population from oxidative stress remains unknown. Are all cells uniformly contributing to this phenomenon, or is a subpopulation of

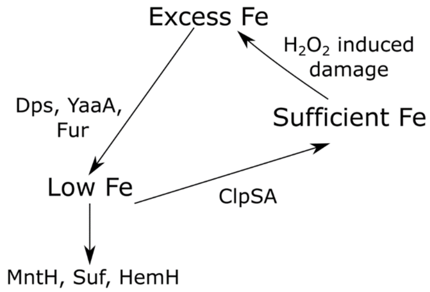

Figure 1.10 Iron regulation under H_2O_2:
The figure shows the different genes involved in maintaining sufficient levels of iron in cells treated with H_2O_2.

cells carrying this burden via ‘bet-hedging’[60]? Another mechanism could be that the phenotypic variations are a result of cell-cell growth variability[32,37]. The cells on the outside of a bacterial population protect the cells further away from H_2O_2 by sponging it up [Figure 1.11], which leads to variability in concentrations of H_2O_2 in the local environment across a spatial scale. It remains unclear how these environmental changes would affect cellular response to oxidative stress and provide cross-protection at a population level. A single cell analysis of gene expression dynamics is indeed needed to answer such questions.

1.5 Measuring variability in single cell gene expression heterogeneity

A clonal population consists of genetically identical cells. With changes in transcriptome, genes in individual cells can be uniquely activated or repressed, hence, diversifying the phenotype without permanent changes in the genome. RNA sequencing[171] has been widely used to quantify changes in gene expression under various stressed conditions[172], for example, H_2O_2[173] and antibiotics[174]. While this technique only gives the fold change in the number of RNA transcripts in a population[175,176], the single cell resolution can be achieved

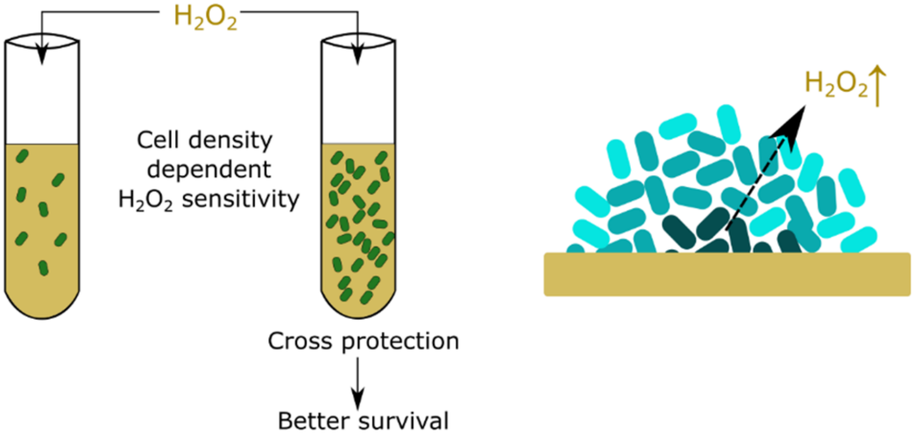

Figure 1.11 Population response of E. coli to hydrogen peroxide:
(left) Stress response of E. coli to H_2O_2 *in planktonic culture is dependent on cell density, with a higher density of cells resulting in better survival due to cross protection. (right)* H_2O_2 *gradients are observed in biofilms, where outer cells of a biofilm sponge up hydrogen peroxide, thereby protecting the cells located further inside.*

using advanced methods but has several technical challenges for analysing bacteria transcriptome changes[175,177]. Other methods involve constructing transcriptional fluorescent reporters of genes of interest wherein a fluorescent protein can be genetically inserted next to the promoter of interest. On activation of the promoter, the fluorescent protein would be translated and the fluorescence, thus produced, can be visualised at a single-cell level using microscopy or flow cytometry[178].

1.5.1 Snap-shot and time-lapse imaging of cells on agarose pads

The dynamics of gene expression can be measured by single-cell imaging of bacteria tagged with fluorescent reporters[179]. In these studies, cells are loaded onto agarose pads which allow growth of cells and a clear background against which cells can be imaged [Figure 1.12A]. Recent studies have also incorporated continuous flow systems alongside, allowing for a

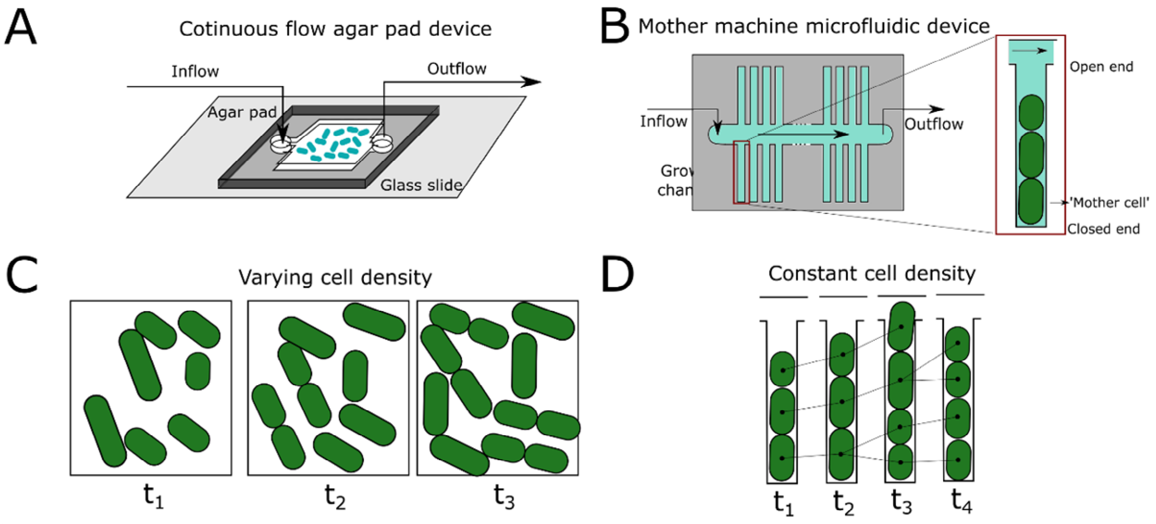

Figure 1.12 Microfluidic devices for imaging single cells:
*(**A**) Representation of cells sandwiched between agarose pad mounted on a glass slide under continuous inflow of growth media with or without a stressor. (**B**) Representation of a 'mother-machine' microfluidic device, with continuous in- and out- flow. An enlarged growth trench, open on one end, is shown on the right. (**C**) Kymograph of cells growing on agar pad depicting that cell density varies over time. (**D**) Kymograph of cells growing in channels of microfluidic device where cell density is maintained over time.*

constant stress treatment[180] [Figure 1.12]. BiofilmQ[181] and Delta2.0[182] software allow for data analysis on such images for cells growing in 3-D biofilms and 2-D microcolonies, respectively. The analysis tracks individual bacteria as they grow in these structured populations [Figure 1.12D]. The fluorescence and other morphological parameters of individual cells are quantified to study cell behaviour fluctuations. The growth of bacterial colonies on a surface create gradients of metabolites, oxygen, and nutrients which can lead to the varying environment for individual cells[44,45,183]. However, since the gradients are dynamic over time, it limits the reliability of the measurement of stress response dynamics. Moreover, microscopy analysis may fail when cells grow perpendicular to the imaging plane at higher densities[19].

1.5.2 Microfluidic devices complemented with real-time imaging

The aforementioned problems have been partially mitigated by the use of microfluidic devices that maintain a monolayer of cells and can image cells for a very long time[19]. These devices act as chemostats with a continuous in- and out- flow of growth media for cells with or without a desired stress treatment [Figure 1.12]. There have been various designs with 2D or 1D growth of cells, with both open or closed channel ends[184–186][Figure 1.12B]. Channels closed at one end allow for measuring a single cell that sits at the bottom of the channel (mother cell) for longer durations (called 'mother machines'), while the one open at both ends allows to keeps cell age distribution more uniform[19].

1.6 Thesis aims

This thesis is organized as follows. In the Chapter 2, we describe the materials and methods used in the following results chapters. In the Chapter 3, we aim to understand the cause and consequences of bacterial cell-cell variability under H_2O_2 stress. We experimentally study *E. coli* in mother machine microfluidic devices and surprisingly observe H_2O_2 concentration gradients on the micro-meter scale that lead to variable expression of the oxidative stress response across cells. Motivated by this observation, we disentangle the effects of environmental versus cell-intrinsic sources of phenotypic variability, both spatially and temporally. Using a machine learning model trained on experimental data, we show that the origin of cell-cell variability is deterministic. Using the model to pin-point the sources affecting single-cell variability under continuous H_2O_2 stress, we experimentally show that cell-cell interactions drive the stress response of an individual cell. We further study the consequences of heterogeneity on cellular growth rate, mutation rate, and survival under H_2O_2 stress. Lastly, we perform experiments in micro-colonies to explore the effect of cell-cell variability in conditions relevant to biofilms. Taken together, our study challenges the common notion of cellular variability being driven by molecular noise under stress. Instead, we show that the apparent heterogeneity stems, on the contrary, from a very precise response of individual cells to local environmental variation that is generated by the surrounding cells. In the Chapter 4, we aim to understand the source of cell-cell variability in the oxidative stress response under continuous treatment. Specifically, we explore why the response is variable across cells when the underlying mechanisms are actually deterministic. Combining experiments and mathematical modelling, we show that the bacterial stress response to H_2O_2 is chaotic, i.e., a deterministic system that is sensitive to small perturbations. We show that fluctuations in stress response arise from a completely deterministic model without the requirement of noise. The mathematical model predicts regimes of cellular growth rate, H_2O_2 concentration, and cell-cell interactions that make or break chaos under H_2O_2 stress. Our results imply chaotic gene regulation as a mechanism for diversifying bacterial response under stress, offering functional benefits. In Chapter 5, we aim to understand how the transcription factor OxyR controls tens of genes, each exhibiting a unique induction timing and magnitude. We investigate the transcription of over thirty genes implicated in H_2O_2 stress tolerance. We observe that while some genes show transient regulation upon H_2O_2 stress, others are up- or down-regulated throughout the continuous treatment. Among the up-regulated category, we identify that genes are either gradually induced, maintaining a high level over time, or pulse and decay upon H_2O_2 exposure. Although, the expression dynamics of these gradual and pulsatile genes are correlated in individual cells during steady state, they transiently diverge after H_2O_2 treatment. Our model suggests that the binding dissociation constant of OxyR and the promoters, the gene induction rate, and the cellular growth dynamics explain the observed gene regulation patterns. We find that the pulsatile genes show a higher sensitivity to H_2O_2, enabling a rapid defense against sudden stress. Cells exhibit higher variability in pulsatile gene expression level. Conversely, gradually and negatively regulated genes display a more consistent response. The varied sensitivity of genes to H_2O_2 also influences the spatial organisation of gene expression. Pulsatile genes are predominantly expressed by a small fraction of cells near the H_2O_2 source, while gradual and down-regulated genes involve more cells to protect the population against stress. Altogether, our results establish that rather than just being an 'on-off' switch, OxyR binding orchestrates a defined expression program with distinct spatio-temporal dynamics and noise profiles for genes in the regulon. This coordinated response contributes to population-wide protection under oxidative stress.

Chapter 2

Materials and methods

2.1 Strains and plasmids

We used strains derived from *E. coli* K12 AB1157 for our experiments. All the strains had a constitutively expressed P_{RNAI}-mKate2 marker aiding the segmentation of cells during microscopy and *flhD* deletion to stop the cells from escaping out of the microfluidic growth channels during time-lapse microscopy. The reporter plasmids for genes reported in this thesis were obtained from the Zaslaver transcriptional reporter library of PSC101 plasmids[178]. The reporter plasmids comprised of GFPmut2 fluorescence protein after the promoter region of a given gene or operon and had a kanamycin resistance marker. GFPmut2 was replaced with SCFP3A fluorescent protein for P*katG*, P*ahpC*, and P*grxA* using Gibson Assembly (NEB). The reporter plasmids were mini-prepped and transformed in our AB1157 background strain. Strains were selected on 25 µg/mL kanamycin resistance LB agarose plates and checked for fluorescence signal by microscopy snapshots. These strains also carried an endogenous MutL-mYPet fusion for the detection of DNA mismatches[187]. The chromosomal reporter for P*grxA*- SCFP3A was constructed by inserting P*grxA*- SCFP3A - kanamycin in endogenous loci (*aslA*) on the chromosome of DH5α strain expressing pKD46-ampicillin on plasmid using λ-red recombination. The successful colonies were selected by growing them overnight on kanamycin plates and subsequently re-streaking again on kanamycin selective plates at 37˚C to get rid of the temperature sensitive pKD46 plasmid. Then, the insert was moved into our strain of interest that had P_{RNAI}-mKate2 marker and *flhD* deletion, using P1-phage transduction. The successful colonies were selected on kanamycin plates and tested for the insert using colony PCR, after which, the colonies were restreaked and grown overnight thrice to get rid of the phage. Colony PCR was again performed before storing the strain at -80˚C. P*grxA*-mYPet and P*katG*-mYPet plasmids with ampicillin resistance marker were obtained by genetically editing P*grxA*- SCFP3A -kanamycin and P*katG*- SCFP3A -kanamycin plasmids using Gibson assembly. We first replaced CFP with mYPet fluorescent protein and the resultant plasmid was edited again using Gibson assembly to replace the kanamycin with an ampicillin resistance marker. The final strain was checked by colony PCR, microscopy snapshot, and re-streaking on 100 µg/mL ampicillin plates. Finally, the P*grxA*-mYPet-ampicillin and P*katG*-mYPet-ampicillin plasmids were transformed in the P*grxA*-SCFP3A-kanamycin chromosomal fluorescent reporter strain to construct the dual reporter strain. The strain was imaged to test for dual fluorescence using microscopy snapshots and selected on plates supplemented with 25 µg/mL kanamycin and 100 µg/mL ampicillin. The strain SU802 with a Δ*oxyR*::kan deletion was described in Lagage *et al*[188]. The strain 882 with a Δ*oxyR*::kan deletion carried a pUC18 plasmid constitutively expressing mYPet as a fluorescent marker to distinguish Δ*oxyR* cells from wild-type cells in the experiments with a mixture of the two strains, as described in Chapter 3.

The strain list is mentioned in Appendix A.8.

2.2 Media and growth conditions

Strain construction was performed in LB or LB supplemented with antibiotics at 37˚C. 4 mL cultures were grown at 200 rpm in 10 mL culture tubes. Successfully constructed strains were stored in glycerol stocks at -80˚C. For experiments, strains were streaked from these glycerol stocks on LB agarose plates with appropriate antibiotic selection. A single colony was picked and then grown overnight in M9 minimal media. M9 minimal media was prepared by adding M9 salts (15 g/L KH_2PO_4, 64 g/L Na_2HPO_4, 2.5 g/L NaCl, and 5.0 g/L NH_4Cl), 2 mM

$MgSO_4$, 0.1 mM $CaCl_2$, 0.5 mg/mL thiamine, MEM amino acids, 0.1 mg/mL L-proline, and 0.2% glucose (or glycerol) to water. The next day, overnight culture was diluted 1:50 and grown to OD_{600} ~0.3 in M9 minimal media. 10% LB media was prepared by mixing 10% LB(V/V) with M9 glucose minimal media. For loading cells in microfluidic chips, 0.85 mg/mL Pluronic F127 was added to the media to avoid cell aggregation. For experiments done under hydrogen peroxide treatment, the specified concentration of H_2O_2 was added to the growth media immediately before the start of the experiment and the treatment was provided to the cells at the time mentioned in each experiment.

The list of reagents used in this thesis is mentioned in Appendix A.9.

2.3 Microfluidics experimental setup

2.3.1 Microfluidic chip preparation

2.3.1.1 Mother machine chip preparation

Single-cell imaging was performed using the 'mother machine' microfluidic device as described in Lagage *et al.*, Uphoff *et al*[185,188]. The chip has a main channel for the flow of media, branching into perpendicular growth trenches (also called 'growth channels') of dimension 1.2 µm width, 1.2 µm height, and 25 µm length. The chips were made of polydimethylsiloxane (PDMS, Dow Corning Sylgard 184 kit) polymer using a silicon wafer mold (Conscience). A 1:10 solution of polymerising agent and PDMS monomer were rigorously mixed and then poured onto the silicon wafer. This was placed in a vacuum chamber and pressurised to remove air bubbles. The device was then heated at 65˚C in an oven for 2 hours to polymerise. For each experiment, one chip was cut out using a scalpel, and holes for the inlet and outlet were punched using a 0.75 mm biopsy puncher. The device was cleaned using 100% ethanol and dried with nitrogen gas. The cleaning protocol was repeated 3 times. The PDMS chip was bonded on a glass coverslip (thickness No 1.5). These coverslips were first cleaned by sonication with acetone for 20 mins and then by isopropanol for 20 min, and finally dried with nitrogen gas. The cleaned coverslip and PDMS chip were exposed to air plasma for 2 min and bonded at 95˚C for 30 min.

For shorter growth channel experiments, a different silicon wafer was used to generate mother machine chips of shorter trenches of 10 µm length, 1.2 µm width, and 1.2 µm height. Here a “negative” mould was prepared first using PDMS as an intermediate from a silicon wafer (by mixing monomer and curing agent 1:5) that was then used to prepare the “positive” chips using the method explained above.

2.3.1.2 Microcolony chip preparation

Cells were streaked on LB plates with antibiotics (25 µg/mL kanamycin and 100 µg/mL ampicillin) and grown overnight at 37˚C. A colony was picked and grown overnight in 4 mL LB at 37˚C in a shaking culture. For colony experiments performed in Chapter 3, 2 µl spots of overnight culture were dropped on an LB agarose plate without letting the pipette tip touch the agar surface and grown for 2 hours at 37˚C. Using a scalpel, the agarose was cut surrounding a spot (1 cm by 1 cm). 8 µl of 10 mM H_2O_2 solution in LB was dropped close to the spot and left to dry for ~3 minutes. The agarose pad was then flipped onto a clean glass slide and then covered with a cap of a culture tube that was sealed with tape. For colony experiments performed in Chapter 4, *E. coli* microcolonies were grown on 1% agarose pads prepared with M9 glucose + 10% LB media. Melted agarose solution was poured onto the top of an empty 50 mL syringe plunger head wrapped with adhesive tape to act like a container. A glass cover slip was then placed on top of the taped cylinder. After the agarose was set, the cover slip was removed and 1 µl spots of overnight culture were dropped on the flat agarose surface and grown for 2 hours at 37˚C. After 2 hours, the agarose was removed from the plunger head, thus leaving a conical dip in the agarose that acted as a reservoir for adding H_2O_2 treatment solution. The agarose pad was inverted to sandwich the cells between the agarose and a cover slip for imaging. A needle was inserted through the adhesive tape to continuously flow in the growth medium with H_2O_2 using syringe pumps. The medium dripped onto the conical dip and diffused through the agarose to reach the cells below. The microfluidic setups were subsequently mounted on the microscope for time-lapse imaging.

2.3.2 Mother machine setup

1 mL of exponentially grown cells were spun down for 2 min at 6000 rpm. These cells were then resuspended in 100 µL of the supernatant and loaded in the microfluidic chips by pipetting through the inlet. For experiments with a lower and variable number of cells per trench, as described in Chapter 3, the cells were centrifuged and resuspended in 500 µL of supernatant before being loaded into the chip. The chip was then inserted into a custom-built centrifuge holder and spun at 5000 rpm for 10 min to aid the loading of cells into the growth trenches. 50 mL syringes were filled with growth media (as mentioned in experiments) containing Pluronic F127 and H_2O_2 as indicated. The syringes were attached to silicon tubing (Tygon) and loaded onto syringe pumps (NewEra SyringePumpPro) to deliver media into chips at a constant flow rate of 2.5 mL per hour. Cells were initially grown without H_2O_2 for ~3 hours before switching the inlet media to a syringe containing H_2O_2 using a Y-junction attached to the inlet of the chip.

2.4 Microscopy

2.4.1 Time-lapse microscopy for mother-machine

Time lapse imaging was performed using a Nikon Ti-E inverted fluorescence microscope equipped with 100x NA 1.40 immersion oil objective, motorized stage, sCMOS camera (Hamamatsu Flash 4), LED excitation source (Lumencor SpectraX), and operated with a perfect focus system. Exposure times were 100 ms for P_{RNAI}-mKate2 ($\lambda = 555$ nm), 75 ms for CFP reporters ($\lambda = 440$ nm), and 300 ms for MutL-mYPet ($\lambda = 508$ nm) using 50% of maximal LED excitation intensities. The excitation and emission lights were separated using a triband dichroic and individual emission filters. The microscope chamber (Okolabs) was maintained at 37˚C throughout the experiments. Images were captured every 3 min for the 3 emission channels. On average, 45 to 50 fields of view (FOV) were captured per experiment with each FOV containing 26 growth trenches. This yielded ~1200 independent growth trenches each containing a single mother cell and its progeny. With 8 cells per growth trench, on average ~10,000 cells were captured in total per time point. For cross correlation analysis experiments in Chapter 3, we imaged P_{RNAI}-mKate2 for cell segmentation at 50 ms and CFP channel at 50 ms exposure times every 45 seconds. Since this was a shorter time duration between cycles, we could capture around 18 to 20 FOV which yielded ~500 cells per time point.

2.4.2 Imaging of microcolonies

Time lapse imaging was performed on a Nikon Ti-E microscope equipped with a 100x NA 1.45 oil immersion objective, motorised stage, sCMOS camera (Photometrics Prime95B), LED excitation source (Lumencor SpectraX), and perfect focus system. Exposure times were

100 ms for P_{RNAI}-mKate2 (λ = 555 nm), 75 ms for CFP reporters (λ = 440 nm), and 300ms for MutL-mYPet (λ = 508 nm) using 50% of maximal LED excitation intensities. The microscope chamber (Okolabs) was maintained at 37˚C throughout the experiments. Images were captured every 3 minutes for brightfield and the 3 fluorescence channels. On average, 10 to 20 fields of view (FOV) were recorded per experiment with each FOV capturing a section of the microcolony.

2.5 Live dead staining

1mg/mL solution of propidium iodide was prepared from the stock. 1/1000 dilution was added in PBS buffer solution and flown into the mother machine 11.5 hours after treatment removal, images of which were captured in the RFP channel.

2.6 Cell fixation

Inert cells were prepared by chemical fixation. Cells were pelleted and resuspended in 4% formaldehyde and then stored at room temperature for 30 minutes for inactivation before mixing with live WT cells for imaging.

2.7 Microscopy data processing and analysis

2.7.1 Mother machine data processing

Time lapse microscopy data were saved as .nd2 files and visualized in Fiji. The data were processed using the BACMMAN plugin in Fiji as described in Ollion *et al.*[189] and further analysed using custom Python scripts. Images were first pre-processed by BACMMAN using the P_{RNAI}-mKate2 fluorescence channel to stack all individual growth trenches and correct for experimental drift in x-y coordinates and image rotation. The outlines of cells in the growth trenches were then jointly segmented and tracked over time based on the P_{RNAI}-mKate2 fluorescence signal. The traces were visually inspected and manually corrected for errors in segmentation or lineage tracing using the BACMMAN software. The CFP, GFP and mYPet fluorescence of the different reporter plasmids was extracted by overlaying the cell masks from the P_{RNAI}-mKate2 channel onto the CFP channel and computing the mean intensity over the cell area. BACMMAN software was also used to detect foci of the MutL-mYPet reporter for DNA mismatches within the cell masks. BACMMAN generated output in separate Excel files containing cell growth characteristics, P_{RNAI}-mKate2 segmentation marker intensity data, intensity data of fluorescence reporter for stress response, and MutL-mYPet foci detections. These files were then further analysed using a custom Python pipeline as described in the following sections.

2.7.2 MutL-mYPet foci detection

For MutL-mYPet foci detection carried out by BACMMAN, images were band pass filtered between within 1 to 400 pixels. Next, the image was gaussian smoothed with a scale of 2 pixels, and the spot segmentation was performed using a Seed Laplacian threshold of 0.8, propagation threshold of 1.5, and seed threshold of 1.7. Foci that were detected in multiple consecutive frames within the same cell were counted only once in the first frame. The mismatch rate was calculated by dividing the total number of foci by the total number of cells per frame.

2.7.3 Microcolony image analysis

Segmentation of cells growing in microcolonies was performed based on the P_{RNAI}-mKate2 fluorescence signal and using the MicrobeTracker tool in MATLAB [190] followed by manual correction of the segmentation masks. These outlines were then applied to the CFP channel and a MATLAB script was used to quantify the average intensity per cell area. Cell lineage tracing was performed manually and custom python code was used to plot CFP intensity traces.

2.8 Calibration of H_2O_2 concentration inside microfluidic growth trenches

We estimated the local H_2O_2 concentration in the growth trenches from the P*grxA*-CFP reporter intensities of cells located at different positions. We calibrated the analysis using the reporter intensities of the cells located at the open end of the growth trenches that were exposed to defined H_2O_2 concentrations (12.5 µM, 25 µM, 37.5 µM, 50 µM, 62.5 µM, 75 µM, and 100 µM). The fluorescence intensities at steady-state (1- 3 hours after start of treatment) showed a linear relation with the external H_2O_2 concentration. This was used to obtain the conversion factor for computing the H_2O_2 concentration from the reporter intensity of cells at any position in the trenches.

2.9 Quantification of cellular parameters

Cell length (L): The cell length was computed from the maximum distance between the points on the cell masks.

Cell area (A): The cell area was computed from the total area covered by the cell mask.

Estimated cell surface area to volume ratio: This ratio was empirically calculated as $\rho = \frac{24L\ (L^2+A)}{A(3L^2-A)}$

A cell is considered a cylinder capped with 2 hemispheres with the total length as L and radius as r.

$$\frac{SA}{V} = \rho = \frac{2\pi r(L-2r) + 4\pi r^2}{\pi r^2(L-2r) + \frac{4\pi r^3}{3}}$$

Simplifying the above equation and approximating $A = 2rL$. Here A is the cell area output from BACMMAN.

$$\rho = \frac{24L\ (L^2 + A)}{A(3L^2 - A)}$$

Elongation Rate: The instantaneous elongation rate was calculated based on the log-difference in cell length between consecutive frames as $\frac{\log(L_t) - \log(L_{t-\Delta t})}{\Delta t}$. For calculating the elongation rates of cells at different positions in the growth trench, cells were tracked according to their initial position until the number of barrier cells decreased by 2.

Generation time: The time difference between two consecutive cell divisions.

Division Rate: The inverse of the cell generation time.

Gene expression: The reporter fluorescence intensity values were averaged over the area of each cell.

Length Growth Rate: This was calculated as the coefficient of a linear fit (β) to the logarithm of cell length over each cell cycle. $L = L_0 e^{\beta t}$, where L_0 is the length at birth. Since it is calculated over the whole lineage duration, we cannot capture the instantaneous changes in elongation rate.

Fate of a cell: A mother cell was defined dead if the length growth rate was less than 0.012 min^{-1} for >10 hours after stress removal.

Barrier cell: Cells that are located between the open end of a trench and the focal cell being analysed.

Number of barrier cells: The number of cells that are located between the open end of a trench and the focal cell being analysed.

Cumulative barrier length: The sum of lengths of barrier cells.

Cumulative barrier area: The total area covered by the barrier cells.

Cumulative barrier surface area to volume: The total estimated surface area to volume ratio of all barrier cells.

Lineage annotation: The identity of cells was obtained from BACMMAN to define their lineage relations as sisters, cousins, or non-related.

Response peak intensity: The oxidative stress response reporters showed an initial peak in intensity and then reached a lower steady-state level. The initial peak intensities for each mother cell were detected using the PeakUtils module in Python with a normalised threshold of 0.15 and minimum distance between peaks of 2 frames. This absolute response peak value was subtracted by the mean reporter intensity without H_2O_2 treatment.

Response induction time: The time at which a mother cell crosses an intensity threshold of 20% of the steady state intensity value (i.e. 1480 a.u. for P*grxA*-SCFP3) after the start of H_2O_2 treatment.

Response peak time: The time at which a mother cell reaches its response peak intensity after the start of H_2O_2 treatment.

Coefficient of variation: The CV values were calculated as the standard deviation divided by the mean for the response induction time, peak time, and peak intensity. CVs of steady state intensities were calculated for mother cells or all cells from 90 minutes post treatment until 6 hours post treatment after subtracting the mean intensity for each cell before H_2O_2 treatment.

Promoter activity: The instantaneous promoter activity at time t was calculated as the cell averaged rate of change of total fluorescence intensity of a cell. It was computed as:

$\frac{1}{A}\frac{d(I.A)}{dt} = I\frac{1}{A}\frac{dA}{dt} + \frac{dI}{dt}$ where I is the mean fluorescent intensity of cell and A is the cell area. Here, $\frac{1}{A}\frac{dA}{dt}$ was given by the instantaneous elongation rate of the cell. For calculating the promoter activity values of cells at different positions in the growth trench, cells were tracked according to their initial position until the number of barrier cells decreased by 2.

Expression Rate: The instantaneous expression rate at time t was calculated based on the difference in cell intensity I_t at time between consecutive frames as $\frac{I_t - I_{t-\Delta t}}{\Delta t}$. For calculating the elongation rates of cells at different positions in the growth trench, cells were tracked according to their initial position until the number of barrier cells decreased by 2.

Peaky expression: 90th percentile of the mean fluorescence intensities from 12 to 90 minutes post H_2O_2 treatment. This value was subtracted by the mean fluorescence intensity without H_2O_2 treatment i.e. basal fluorescence intensity.

Steady expression: Average gene expression from 150 minutes post H_2O_2 treatment. This value was subtracted by the mean fluorescence intensity without H_2O_2 treatment i.e. basal fluorescence intensity.

Time to peak expression for single cells: Time until 100 minutes post H_2O_2 when individual cells show maximum fluorescence intensity.

Relative expression in spatial dimension: Expression intensity of cells with at least 1 barrier cell divided by the intensity of the outermost cell (i.e. cell with no barrier cells) was computed per growth channel at steady state (>150 minutes post H_2O_2 treatment) and transient state (0 to 90 minutes post H_2O_2 treatment).

2.10 Alive vs dead and Deterministic vs stochastic categorisation

The MATLAB code described in Toker *et al.*[191] was used to categorise P*grxA*-SCFP3 traces of individual mother cells as showing deterministic or stochastic fluctuations. Traces were analysed at steady-state from 1-hour after the start of H_2O_2 treatment. The traces were pre-processed with a moving-mean filter using a window of 3 time points (i.e. 9 min) twice. The rationale for this is that we are principally interested in the large-scale response fluctuations on the time-scale of the cell cycle (~50 to 100 min, depending on conditions). Only traces with at least 5.5 hours of data were included in this analysis (length of data required for entropy calculation in the pipeline). P*grxA*-SCFP3 traces were further categorised as originating from live or dead mother cells. A cell was considered dead if the elongation rate as computed by BACMMAN was below 0.0024 min^{-1} for at least 4.5 hours after the start of treatment.

2.11 Chaos decision tree algorithm

To categorise if the fluctuations in P*grxA*-SCFP3 traces of individual mother cells are deterministic or stochastic in Chapter 4, we applied the 'Chaos decision tree algorithm' as described by Toker *et al*[191]. The pipeline is available as MATLAB code. Briefly, the algorithm tests for stochasticity by computing the permutation entropy using the cyclic phase permutation algorithm. The permutation entropy quantifies the extent to which the values in a trace are ordered or random in time. The value of the permutation entropy for the original trace is compared to many randomly shuffled versions of the same trace in which the temporal order of the data points is removed while the mean and standard deviation are maintained. If the fluctuations are stochastic, then the permutation entropy is similar for the original and shuffled traces; otherwise, the fluctuations are classified as deterministic. The chaos decision tree further tests for stationarity. i.e. whether statistical properties like the mean and standard deviation of a trace do not change over time; else the trace is classified as non-stationary.

2.12 Correlation analysis

2.12.1 Cross-correlation analysis

The temporal cross-correlation between the P*grxA*-SCFP3 reporter intensity traces of mother cells and the number of barrier cells per trench was computed using the statsmodel library in Python. Correlation values from individual growth trenches were then averaged over all observed growth trenches for different lag times. The minimum of the cross-correlation curve was obtained using the argrelextrema function in Python to obtain the lag time of the reporter intensity in response to changes in the number of barrier cells.

2.12.2 Autocorrelation analysis

Autocorrelation analysis was performed to distinguish between periodic and chaotic fluctuations of the P*grxA*-SCFP3 traces of individual mother cells in Chapter 4. Traces with at least 2-hours of data were analysed at steady-state from 1-hour after the start of H_2O_2 treatment. The traces were pre-processed with a moving-mean filter using a window of 3 frames (i.e. 9 min) twice. Due to the slower growth of cells in M9 glycerol media, a window of 6 frames was used and traces were analysed at steady-state from 2-hours after the start of H_2O_2 treatment. ACF curves were computed from the DPgrxA difference signal, which was calculated by subtracting the P*grxA*-SCFP3 values of consecutive frames. The Python stattools.acf function from the statsmodel library was used to output the autocorrelation value over a range of lag times. Mean ACF curves were computed by averaging the ACF values from the single-cell traces at each lag time. A peak finding algorithm was applied to the mean ACF curves to quantify the period of non-chaotic P*grxA*-SCFP3 traces. This was done in Python using the find_peaks function in the scipy.signal library with a prominence of 0.2. ACF curves for simulated GrxA traces were computed during steady-state from 700 to 5200 min after the start of H_2O_2 treatment at t = 50 min. The analysis was done as explained for experimental data but without moving-mean filtering.

2.13 Machine learning algorithm

In Chapter 3, we trained a random forest regressor model to predict the initial peak intensity of the P*grxA*-CFP reporter for each mother cell. A separate random forest classifier model was trained to predict the external H_2O_2 concentration. A list of features (shown below) was calculated from the output data provided by BACMMAN. Data from multiple experiments (as indicated in figure captions) were combined into one dataset for model training and testing. Feature values for each mother cell and its environment were stored in separate CSV files which served as input to the Python-based Machine learning model. The following Python libraries/packages were used: pandas; numpy; peakutils; matplotlib; stats, from scipy; preprocessing, utils, shuffle, metrics, model_selection, ensemble from sklearn, ststamodel.api.

126 features were extracted from each mother cell and labelled with the output value i.e. the P*grxA*-CFP peak intensity for each cell. The data was then split 80:20 into training and test data using train_test_split module from sklearn. The training and test data were then individually shuffled using the shuffle library in sklearn.

Utilising the supervised learning method, a random forest model is an ensemble technique that can predict the output numerical value or classification class, for regressor and classifier respectively, based on the combined outputs generated by multiple decision trees that each process a random subset of the data with a random subset of the available features[192].

For the regression model, the decision trees compute numerical values at each tree node. The feature values were extracted from a subset of training data at each decision node that were randomly drawn from the feature list. Prediction was then performed for multiple trees and mean squared error was calculated for every predictor and minimized by bootstrapping. The final output numerical value for the P*grxA*-CFP peak intensity per cell is the average of these predictions.

The classification model generates probabilistic predictions of labelled outputs of the given data set, whose decision is based on bootstrapping results from a collection of randomized trees. Here, the different H_2O_2 treatment concentrations were considered as separate classes for each mother cell. The decision trees making up the forest were trained with the input data as an independent classifier. These independent trees are formed using random subsets from training data sets and the randomized feature set that was extracted. The label that is selected by the majority of the trees is output as the class. We used 100 trees and a forest depth of 3000 for bootstrap samples in both of the above-mentioned algorithms.

After the models had been trained, the test data were used to evaluate the model accuracy based on the normalized difference between the predicted and observed P*grxA*-CFP peak intensity per cell, and averaged over all cells in the test dataset. We report the model accuracy accordingly:

$$A = 1 - \frac{1}{n} . \sum_{s=1}^{s=n} \left| \frac{pred_s - exp_s}{exp_s} \right|$$

The accuracy of the classification model was evaluated using a confusion matrix to quantify the frequency of true positive and true negative predictions. To assess the relative importance of the different feature types for the predictive power of the model, we used the mean decrease impurity test in the scikit-learn package in Python[192].

We performed cross-validation on the regressor and classification models by splitting the data into 5 sets and evaluating the performance of the trained model. In Chapter 3 we report the mean and standard deviation of the scores obtained from these models. We report Mean Absolute Percentage Error (MAPE) for the regressor model and the accuracy score for the classification model.

Machine Learning Features:

$$GrxA_{peak} = \ \{GrxA|_{t_p<t<t_q}\}_{peak} - \frac{\sum_{t=-treatment}^{t=0} GrxA}{treatment} \ ; t_p = 0 \ , t_q = 60 \ minutes$$

1. Kurtosis = $Y_{kurt} = (t_2 - t_1) * \frac{\sum_{t=t_1}^{t=t_2}\left(Y_t - \frac{\sum_{t=t_1}^{t=t_2} Y_t}{t_2 - t_1}\right)}{\left(\sum_{t=t_1}^{t=t_2}\left(\left(Y_t - \frac{\sum_{t=t_1}^{t=t_2} Y_t}{t_2 - t_1}\right)^2\right)\right)^2}$

2. Skewness = $Y_{skew} = (t_2 - t_1) * \frac{\frac{\sum_{t=t_1}^{t=t_2} Y_t}{t_2 - t_1} - Median(Y_t \forall t_1 < t < t_2)}{\left(\frac{\sum_{t=t_1}^{t=t_2}\left(Y_t - \frac{\sum_{t=t_1}^{t=t_2} Y_t}{t_2 - t_1}\right)^2}{t_2 - t_1}\right)^{0.5}}$

3. Median = $Y_{median} = Median(Y_t \forall t_1 < t < t_2)$

4. Mean or average = $Y_{mean} = \frac{\sum_{t=t_1}^{t=t_2} Y_t}{t_2 - t_1}$

5. Minimum = $Y_{min} = Minima(Y_t \forall t_1 < t < t_2)$

6. Maximum = $Y_{max} = Maxima(Y_t \forall t_1 < t < t_2)$

7. Range of magnitude = $Y_{range} = Y_{max} - Y_{min}$

All the above features were calculated for 'mother cells' where Y_t =:

1. Cell length at time point t = l_t

2. Cell area at time point t = A_t

3. Instantaneous cell elongation rate at time point t = $\beta_t = \frac{l_t - l_{t-1}}{1}$

4. Instantaneous cell area increase rate at time point t = $\rho_t = \frac{A_t - A_{t-1}}{1}$

5. Estimated cell surface area to volume ratio at time point t = $\alpha_t = \frac{l_t}{A_t - (\frac{2{A_t}^2}{3{l_t}^2})}$

6. Number of barrier cells at time point t =$B_t = Maxima(Idx_{cell,t}) - 1$

7. Total length of barrier cells =$l_{t,barrier} = (\sum_{i=0}^{i=B_t} l_i)_t$

8. Total area of barrier cells = $A_{t,barrier} = \left(\sum_{i=0}^{i=B_t} A_i\right)_t$

9. Cumulative 3D surface area to volume ratio of barrier cells = $\alpha_{t,barrier} = \left(\sum_{i=0}^{i=B_t} \frac{l_i}{A_i - \left(\frac{2A_i^2}{3l_i^2}\right)}\right)_t$

For accounting for different conditions, the following time-point series were analysed:

1. Untreated: $t_2 = \text{treatment}\, , t_1 = \text{treatment} - 135 \text{ minutes}$
2. Hydrogen peroxide treated: $t_2 = \text{treatment} + 135 \text{ minutes}\, , t_1 = \text{treatment}$

Total number of input features = 7*9*2 = 126 + 1 output variable = 127 features

2.14 Correlation Dimension to discriminate deterministic and stochastic processes

We used the Grassberger-Procaccia algorithm[193] to estimate the correlation dimension (D_{corr}) of the GrxA response dynamics, which can be understood as the effective number of dynamic variables that generate the response fluctuations. A large number implies a stochastic process whereas a low number results from a deterministic process[194].

To compute the correlation dimension, we followed the procedure described in Sandler *et al*[194]**.** For a given trace of {GrxA_n} where n is any time point, the algorithm constructs a vector {GrxA_n , GrxA_{n+1} , GrxA_{n+2} ,…, GrxA_{n+E-2} , GrxA_{n+E-1}} considering them in E-dimensional space (E is also called embedding dimension). For a data set with N data points in an embedding dimension E, the correlation sum $C(r)$ is quantified to then compute d_{corr}:

$$C(E,r) = \frac{2}{N(N-1)} \sum_{i=1}^{N} \sum_{j=i+1}^{N} \Theta\left(r - |x_i - x_j|\right)$$

The Heaviside step function $\Theta(x)$ ($\Theta(x) = 1$ if $x > 0$ and $\Theta(x) = 0$ if $x \leq 0$) is used to compute the fraction of data points x_i and x_j that are within a distance r of each other. The values of r were evenly spaced in log scale from 0.01σ to 3σ, where σ is the standard deviation of the fluctuation of the given GrxA trace.

The correlation dimension $C(r)$ follows a power law for small r, such that $C(r)\ \alpha\ r^{D_{corr}}$. Therefore, D_{corr} can be estimated from the slope of a log-log plot of $C(r)$ versus r. $C(r)$ grows monotonically with r.

The D_{corr} obtained for different values of E is plotted against E. For a deterministic process, the D_{corr} vs E plot saturates and the saturating value of D_{corr} corresponds to the effective dimension of the dynamic process, i.e. the number of dynamic variables that determine the response dynamics. In contrast, a truly stochastic process yields a straight line for D_{corr} vs E, with $E = D_{corr}$ for any value of dimension E, implying that the process is determined by an infinite number of dynamic variables.

We applied a moving-average filter with a filtering window of 3 time points (i.e. 9 minutes) to smooth experimental P*grxA*-SCFP3 traces before applying the Grassberger – Procaccia algorithm. The rationale for this is that we are principally interested in the large-scale response fluctuations on the time-scale of the cell cycle (~50 to 100 min, depending on conditions). Nevertheless, applying the Grassberger – Procaccia algorithm to experimental data without smoothing also produced a low correlation dimension, consistent with the dynamics being overall deterministic.

2.15 Lyapunov exponent computation

Lyapunov exponent was computed for simulated oxidative stress response (GrxA) traces of mother cells (positioned at the closed end of growth trenches) during steady-state from 700 to 5200 min after the start of H_2O_2 treatment at t = 50 min. The traces were normalized in MATLAB using the “normalise” function. The Lyapunov exponent was computed in MATLAB using the “phaseSpaceReconstruction” function and “lyapunovExponent” function with fs = 10.

2.16 Linear regression analysis

The linear regression analysis was performed in Python using the stats.linregress function in scipy library which computes the least square regression for a linear fit between two sets of data points.

2.17 Model parametrisation

The parameterisation of models described in Chapter 4 was performed as follows:

2.17.1 Growth model parametrisation

Under the experimental conditions of our study, the mean elongation rates of *E. coli* cells growing without H_2O_2 in M9 glycerol, M9 glucose and M9 glucose + 10% LB media are $g_0 = 0.025$ min^{-1}, 0.042 min^{-1}, and 0.065 min^{-1} respectively. For the sigmoidal function describing the sensitivity of elongation rate to H_2O_2, the growth rate reduces to half when $[H_2O_2]_{cell} = c_2 = 10^{-4}$ μM, with growth stalling at $[H_2O_2]_{cell} \sim 2c_2$. The value c_2 was chosen in the sub-nanomolar range as *E. coli* cells can tolerate up to nanomolar

$[H_2O_2]_{cell}$ in the absence of exogenous H_2O_2 [85]. The steepness of the sigmoidal decay is given by parameter c_1 and was refined to match the variation of elongation rates for cells at different positions in a growth trench under H_2O_2 treatment observed in the mother machine experiments. To this end, we varied c_1 over five order of magnitude from 200 μM^{-1} and minimized the value of mean absolute error (MAE) between g_{model} and $g_{experimental}$. For a given value of c_1, the MAE was estimated for steady-state elongation rate values obtained for cells at different positions in trenches growing in M9 glucose and treated with various concentrations of H_2O_2 (12.5 µM, 25 µM, 37.5 µM, 50 µM, 62.5 µM, 75 µM, 82.5 µM, 100 µM, and 500 µM).

$$MAE = \left| \frac{g_{model,i,cell\_position} - g_{experimental,i,cell\_position}}{g_{experimental,i,cell\_position}} \right|$$

Where i denotes the different H_2O_2 concentrations and $cell\_position$ denotes the position of cells in the trench from the open end. The MAE plotted against different values of c_1 showed a minimum at $2 \cdot 10^4$ μM^{-1}.

2.17.2 Cell-cell interaction model parametrisation

The reaction-diffusion equation was solved with a cell radius of R_c= 0.575 µm and growth trench width W = 1.2 µm. The diffusion coefficient of H_2O_2 in water is $D = 10^{-9}$ m^2/s. The H_2O_2 absorption rate [85] is $k_{abs} = 1.6 \cdot 10^{-5}$ m/s.

2.17.3 Oxidative stress response model parametrisation

The model was parametrised using the following literature values[85,195,196]: $K_{Ahpc} = 660\ s^{-1}$,$h_{AhpC} = 1.2\ \mu\mathrm{M}$,$K_{KatG} = 490000\ \mathrm{s}^{-1}$,$h_{KatG} = 5900\ \mu\mathrm{M}$,$R_{H_2O_2,basal} = 0.02\ \ \mu\mathrm{M\ min}^{-1}$,$K_{ox} = 0.1\ \mu\mathrm{M}^{-1}\ \mathrm{s}^{-1}$,$K_{red} = 8\ \mu\mathrm{M\ s}^{-1}$,$h_{OxyR} = 2583\ \mu\mathrm{M}$, $[OxyR]_{total} = 1\ \mu\mathrm{M}$.

The gene regulatory parameters were matched to the experimental data presented in Chapters 3 and 4: $h_{AhpC,act} = 0.1\ \mu\mathrm{M}$, $h_{KatG,act} = 0.18\ \mu\mathrm{M}$, $h_{GrxA,act} = 0.1\ \mu\mathrm{M}$, $K_{AhpC,act} = 0.2\ \mu\mathrm{M\ min}^{-1}$, $K_{KatG,act}\ = 0.15\ \mu\mathrm{M\ min}^{-1}$, $K_{GrxA,act}\ = 0.1\ \mu\mathrm{M\ min}^{-1}$, $R_{grxA,basal}\ = 0\ \mu\mathrm{M\ min}^{-1}$, $R_{katG,basal}\ = 0\ \mu\mathrm{M\ min}^{-1}$, $R_{aphC,basal}\ = 0.01\ \mu\mathrm{M\ min}^{-1}$, $R_{influx} = 1\ \mathrm{min}^{-1}$.

We estimated the calibration factor $k_{GrxA,calibration}$ which allowed to compare the P*grxA-SCFP3* intensity from experiments to the GrxA concentrations in the model simulations, such that $GrxA_{model,calibrated} = k_{GrxA,calibration} \cdot GrxA_{model} = GrxA_{experimental}$. We varied $k_{GrxA,calibration}$ from 0 to 2500 with steps of 50 and minimized the MAE between $GrxA_{model,calibrated}$ and $GrxA_{experimental}$. For a given value of $k_{GrxA,calibration}$, the MAE was estimated from the P*grxA*-SCFP3 intensity values of the cells at the open end of the growth trenches in M9 glucose media at steady-state treated with various concentrations of H_2O_2 (12.5 µM , 25 µM , 37.5 µM , 50 µM , 62.5 µM , 75 µM , 82.5 µM , 100 µM and 500 µM).

$MAE = \left|\frac{GrxA_{experimental,i} - GrxA_{model,calibrated,i}}{GrxA_{experimental,i}}\right|$, *i* denotes the different H_2O_2 concentrations.

The MAE plotted against $k_{GrxA,calibration}$ showed a minimum at 1150.

2.17.4 General stress response model parametrisation

We used the following parameter values to solve the general stress response model:

$h_E = 1\ \mathrm{a.u.}$, $K_{act} = 0.1\ \mathrm{a.u.\,min^{-1}}$, $h_{act} = 1\ a.u.$, K_{cat} was varied between 0 to $20\ \mathrm{min^{-1}}$, $R_{influx} =\ 1\ \mathrm{min^{-1}}$, $[Toxin]_{external}$ was varied between 0 to 200 a.u.

The parameters used in the growth model and cell-cell interaction model were the same as for the H_2O_2 stress response model.

2.18 Simulation visualization

We generated videos to visualise the simulation results in Chapter 4 using custom Python code and the following libraries: Image, ImageDraw from PIL, tifffile. We drew rows of rod-shaped cells according to the outputs of the growth model and the intensity of each cell was given by a linear grayscale conversion of the [GrxA] value from the stress response model. Simulations with multiple growth trenches were combined into the same image and converted into tiff files. The tiff files were concatenated over time into videos using Fiji[197].

Chapter 3

Phenotypic heterogeneity in the bacterial oxidative stress response is driven by cell-cell interactions

3.1 Summary

Genetically-identical bacterial cells commonly display different phenotypes. This phenotypic heterogeneity is well known for stress responses where it is often explained as bet hedging against unpredictable environmental threats. Here, we explore phenotypic heterogeneity in a major stress response of *Escherichia coli* and find it has a fundamentally different basis. We characterise the response of cells exposed to hydrogen peroxide (H_2O_2) stress in a microfluidic device under constant growth conditions. A machine-learning model reveals that phenotypic heterogeneity arises from a precise and rapid feedback between each cell and its immediate environment. Moreover, we find that the heterogeneity rests upon cell-cell interaction, whereby cells shield each other from H_2O_2 via their individual stress responses. Our work shows how phenotypic heterogeneity in bacterial stress responses can emerge from short-range cell-cell interaction and result in a collective phenotype that protects a large proportion of the population.

3.2 Introduction

In this chapter, we study the basis of cell-cell variability in the oxidative stress response of *E. coli* to hydrogen peroxide. Exposure to ROS is rapidly lethal [2,90,162]. Thus, genes of ROS scavenging enzymes are induced within minutes after H_2O_2 treatment [153,188]. If there is a strong trade-off between response speed and accuracy, then it would be expected that these genes exhibit particularly noisy expression, and this was indeed observed in several studies with different types of ROS treatments [31,33,74,188]. However, whether phenotypic variation during oxidative stress is truly the result of unavoidable molecular fluctuations, a population bet-hedging strategy, or caused by other factors is unknown. In addition to uncertainty about the functional consequences of phenotypic heterogeneity, its molecular origins are also complex and incompletely understood. To address this, we devised a strategy to understand the sources and consequences of oxidative stress response heterogeneity, based upon analysing the responses at the single-cell level as bacteria grow in a microfluidic device. Our work reveals that striking phenotypic heterogeneity in the oxidative stress response can emerge without the need for stochastic molecular noise but via cell-cell interactions.

3.3 Strong cell-cell variability is observed in the H_2O_2 stress response

We studied the oxidative stress response of cells in the "mother machine" microfluidic device for single-cell fluorescence imaging under constant growth conditions[185]. The device consisted of an array of 25 µm long and 1.2 µm wide growth trenches that open to a perpendicular channel with constant medium flow [Figure 3.1A]. Each trench contained 8 ± 2 cells with an average length of 2.6 ± 0.7 µm per cell (± std) [Figure 3.2A]. We used a strain with a transcriptional reporter for the OxyR response on a low copy-number plasmid (P*grxA*-CFP) [178]. A constitutively expressed P_{RNAI}-mKate2 fluorescent protein served as a cytoplasmic label for automated cell segmentation and detection of cell division events. After a period of unperturbed growth, the growth medium flow was changed to medium containing 100 µM H_2O_2. Cells activated the OxyR response after a delay of 12.4 ± 2.1 min following the onset of treatment. P*grxA*-CFP expression peaked after 38 ± 10.8 min and subsequently stabilised at a lower steady-state expression level that was sustained by the constant flow of fresh medium with H_2O_2 into the growth trenches [Figure 3.1B]. Other transcriptional reporters regulated by OxyR, P*katG*-CFP and P*ahpC*-CFP, showed qualitatively similar expression dynamics [Figure 3.2B-D]. As expected, the promoter activity (expression rate)

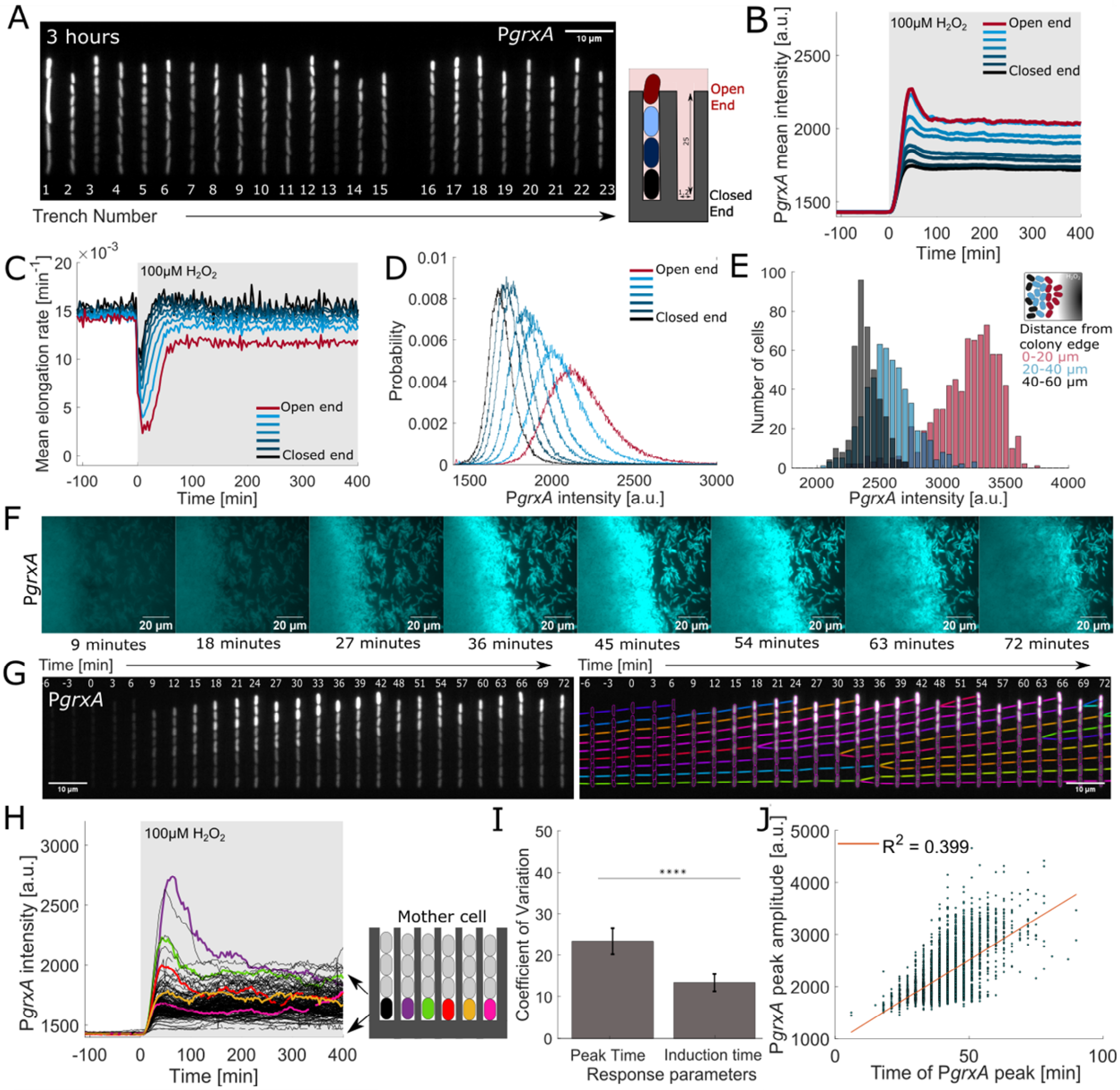

Figure 3.1 Spatial gradient in oxidative stress response:

*(**A**) Snapshot of E. coli cells with transcriptional reporter PgrxA-CFP in growth trenches after 3 hours of 100 µM H_2O_2 treatment. (**B**) PgrxA-CFP intensities with continuous 100 µM H_2O_2 treatment added at time 0 min (shaded area) averaged across cells at specific positions in the growth trench (black line: mother cells at closed end; red line: cells at open end, 3 experimental repeats). (**C**) Mean log elongation rate for cells at different positions in the growth trench with 100 µM H_2O_2 treatment added at 0 min (black line: mother cells at closed end; red line: cells at open end, 3 experimental repeats). (**D**) Distribution of PgrxA-CFP intensities of cells with different number of barrier cells computed for 3 to 6 hours after start of 100 µM H_2O_2 treatment (black line: mother cells at closed end; red line: cells at open end) (~180,000 data points for steady state histograms, 3 experimental repeats). (**E**) Histograms of PgrxA-CFP intensity for cells at different positions in a microcolony after 30 min of 10 mM H_2O_2 treatment. (**F**) PgrxA-CFP snapshots of a microcolony under 10 mM H_2O_2*

*treatment (Time post treatment annotated in the figures). (**G**) Kymograph of one growth trench with PgrxA-CFP intensities and lineage tracing of cells over time with 100 µM H_2O_2 treatment added at time 0 min. (**H**) PgrxA-CFP intensities of individual mother cells over time (example cells highlighted in colour). (**I**) Temporal variation of the oxidative stress response across mother cells. Coefficient of Variation (CV, standard deviation/mean) of the response induction time after 100 µM H_2O_2 treatment and the time to reach the PgrxA-CFP peak intensity. CV was computed for all mother cells in a single experiment and collated for different repeats. (bar chart represents the mean and standard deviation, **** $p<0.0001$, 3 experimental repeats). (**J**) Correlation between PgrxA-CFP peak amplitude and peak time (each dot represents one mother cell) (~3200 cells, 3 experimental repeats). Orange line represents the linear regression fit with $R^2 = 0.399$.*

of cytoplasmic label P_{RNAI}-mKate2 compared to that of P*grxA*-CFP stayed constant during treatment, but the overall intensity increased transiently [Figure 3.3]. This could be explained by a reduction in cell growth rate causing accumulation of cytoplasmic proteins. Indeed, treatment with 100 µM H_2O_2 caused an instantaneous drop in the rate of cell elongation [Figure 3.1C]. However, following OxyR activation, most cells (91.86 ± 0.87 %) recovered growth to pre-treatment rates, indicating complete adaptation to 100 µM H_2O_2, whereas cells with a *ΔoxyR* deletion are unable to induce the stress response and failed to recover [Figure 3.4]. This assay, therefore, provides a way to investigate phenotypic heterogeneity under conditions where the stress response is both essential and effective. In addition, we later explore the impact of higher H_2O_2 concentrations on heterogeneity in cell fates (below).

The magnitude of the oxidative stress response was highly variable across all cells present in the microfluidic trenches [Figure 3.1D]. The mother machine device is popular for studies of cellular heterogeneity because the environmental conditions are believed to be so uniform that any phenotypic variation can be attributed to intracellular noise sources[31,32,72,198]. However, this assumption is rarely tested rigorously. Here, we noticed that cells at the open end of the trenches exhibited higher OxyR reporter expression compared to cells located at

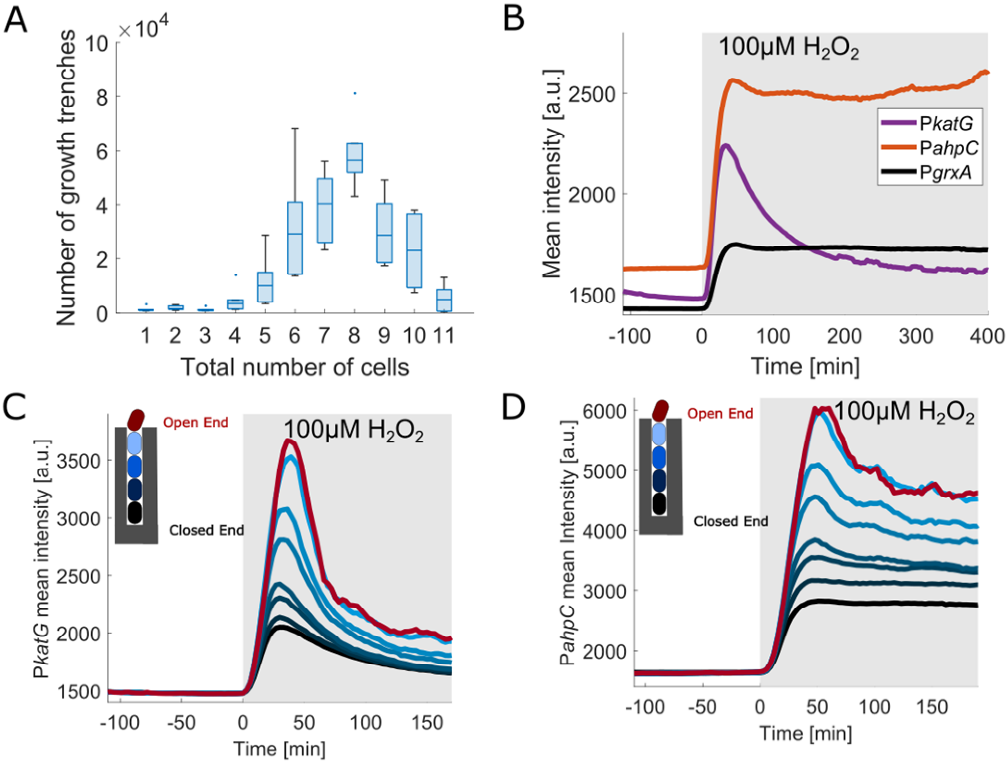

Figure 3.2 Oxidative stress response characterised in microfluidic experiment:
*(**A**) Distribution of number of cells per growth trench at the time of 100 μM H_2O_2 treatment (3 experimental repeats). (**B**) Mean CFP intensity for mother cells under 100 μM H_2O_2 treatment added at time 0 min (shaded area) for the transcriptional reporters of PkatG and PahpC and PgrxA (≥ 2 experimental repeats each). (**C**) PkatG-CFP intensities with continuous 100 μM H_2O_2 treatment added at time 0 min (shaded area) averaged across cells at specific positions in the growth trench (2 experimental repeats, black line: mother cells at closed end; red line: cells at open end). (**D**) PahpC-CFP plot similar to panel C (2 experimental repeats).*

the closed end during H_2O_2 treatment [Figure 3.1A-B, D]. By analysing cells according to their position in the trenches, we found that the average magnitude of the OxyR response decreased from the open to the closed end of the trench. The effect of H_2O_2 treatment on cell elongation was also reduced with increasing distance from the open end [Figure 3.1C]. These observations suggested that the oxidative stress response is very sensitive to a cell's local environment, wherein the stress level decays on a scale of a few micrometres away from the

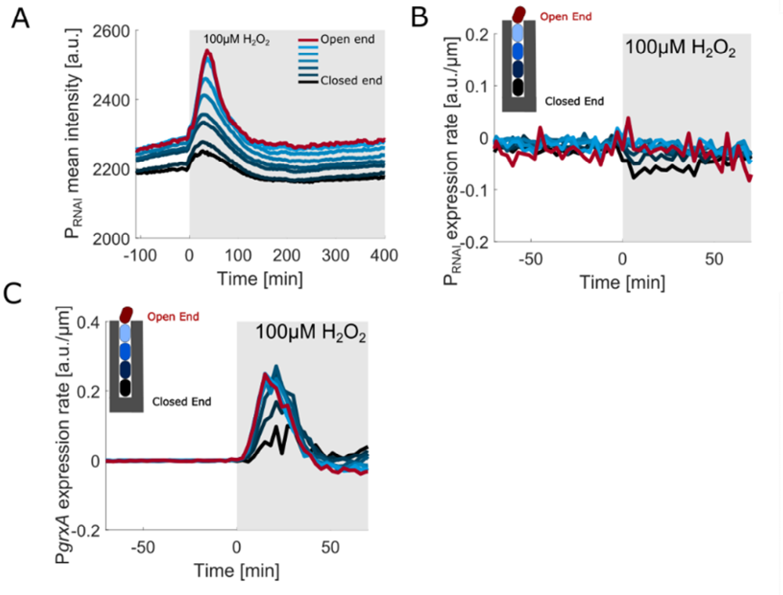

Figure 3.3 Growth effects on gene expression dynamics:
*(**A**) P_{RNAI}-mKate2 intensities with continuous 100 µM H_2O_2 treatment added at time 0 min (shaded area) averaged across cells at specific positions in the growth trench (3 experimental repeats, black line: mother cells at closed end; red line: cells at open end). (**B**) P_{RNAI}-mKate2 expression rate (promoter activity) with continuous 100 µM H_2O_2 treatment added at time 0 min (shaded area) averaged across cells at specific positions in the growth trench (3 experimental repeats, black line: mother cells at closed end; red line: cells at open end). (**C**) PgrxA-CFP expression rate (promoter activity) similar to panel B (3 experimental repeats).*

source of treatment. To test the relevance of this steep gradient in bacterial microcolonies, we applied 10 mM H_2O_2 treatment (higher concentration than microfluidics to account for cell density dependent protection effect) onto a colony grown on agarose pads. This resulted in a higher P*grxA*-CFP response along the edge of the colony compared to the interior, which is consistent with the patterns in the mother machine [Figure 3.1E-F].

3.4 A machine learning model is able to predict single-cell responses to H_2O_2

Although a cell's position in a trench accounted for a part of the observed phenotypic

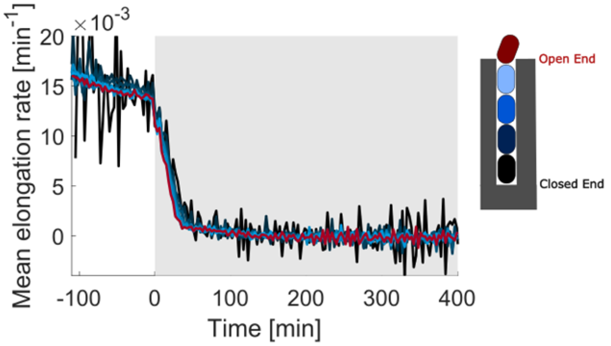

Figure 3.4 Cells with ΔoxyR deletion do not survive 100 µM H_2O_2:
Mean elongation rate for ΔoxyR cells at different positions in the growth trench with 100 µM H_2O_2 treatment (shaded area; black line: mother cells at closed end; red line: cells at open end) (3 experimental repeats).

heterogeneity, we found that the magnitude of the stress response was variable even between individual cells located at the same position in the trenches, such as the “mother cells" positioned at the closed ends [Figure 3.1G-H]. Notably, the basal expression of P*grxA*-CFP without H_2O_2 treatment was uniform across cells, showing that the variation is indeed a consequence of environmental stress [Figure 3.5A]. The magnitude of the initial P*grxA*-CFP response peak shortly after H_2O_2 treatment showed even higher cell-cell variation than the fluctuations of the response at steady-state during prolonged treatment [Figure 3.5B]. However, the activation time of the response after the start of treatment was much more uniform across mother cells, whereas the time to reach the expression peak was variable and correlated with the peak response magnitude of each cell (Pearson’s R = 0.399, $p = 10^{-15}$) [Figure 3.5]. This indicates that while cells can reliably sense the onset of H_2O_2 stress and respond rapidly, the response magnitude depends on an unidentified factor that varies substantially between cells.

This heterogeneity could be caused by a variety of mechanisms, including molecular stochasticity in the specific regulatory circuits or general gene expression machinery [25,27], cell-to-cell variation in growth or morphology [32,38,39], variable cell-to-cell interactions [41–43], or differences in the local environment of cells [43,44]. To pinpoint the mechanisms, we designed a machine learning model using random forest regression [Figure 3.6 A]. We computed 126 features based on the time-series data of cell size, shape, and growth rates for each mother cell as well as the other cells present in the same trench [Appendix A.2]. The model was trained to predict the peak intensity values of the P*grxA*-CFP reporter after the onset of H_2O_2 treatment from 80% of the observed mother cells and tested on the remaining 20% of mother cells (790, unseen during model training). The model predicted the magnitude of the oxidative stress response for individual cells with a mean accuracy of ~70% [Figure 3.6B, Appendix A.1]. The performance of the model was validated through cross-validation, testing on complementary subsets of the data, yielding an accuracy of 70.8 ± 1 %.

We evaluated the distribution of P*grxA* intensities of cells at different positions in the growth channel for each experiment, which did not reflect day-to-day variations [Figure 3.5C]. To investigate whether day-to-day variations affected the predictive performance of our machine learning model, we compared the outputs of the analysis conducted on individual experiments with those obtained when all experiments were combined. This analysis focused on cells treated with 100uM H_2O_2, resulting in accuracies of 77.98%, 77.78%, and 79% for ~200 unseen cells in individual experiments, and an accuracy of 77.93% when considering all experiments together. The accuracies were remarkably consistent, suggesting that day-to-day variation had minimal impact on the predictive power of the model.

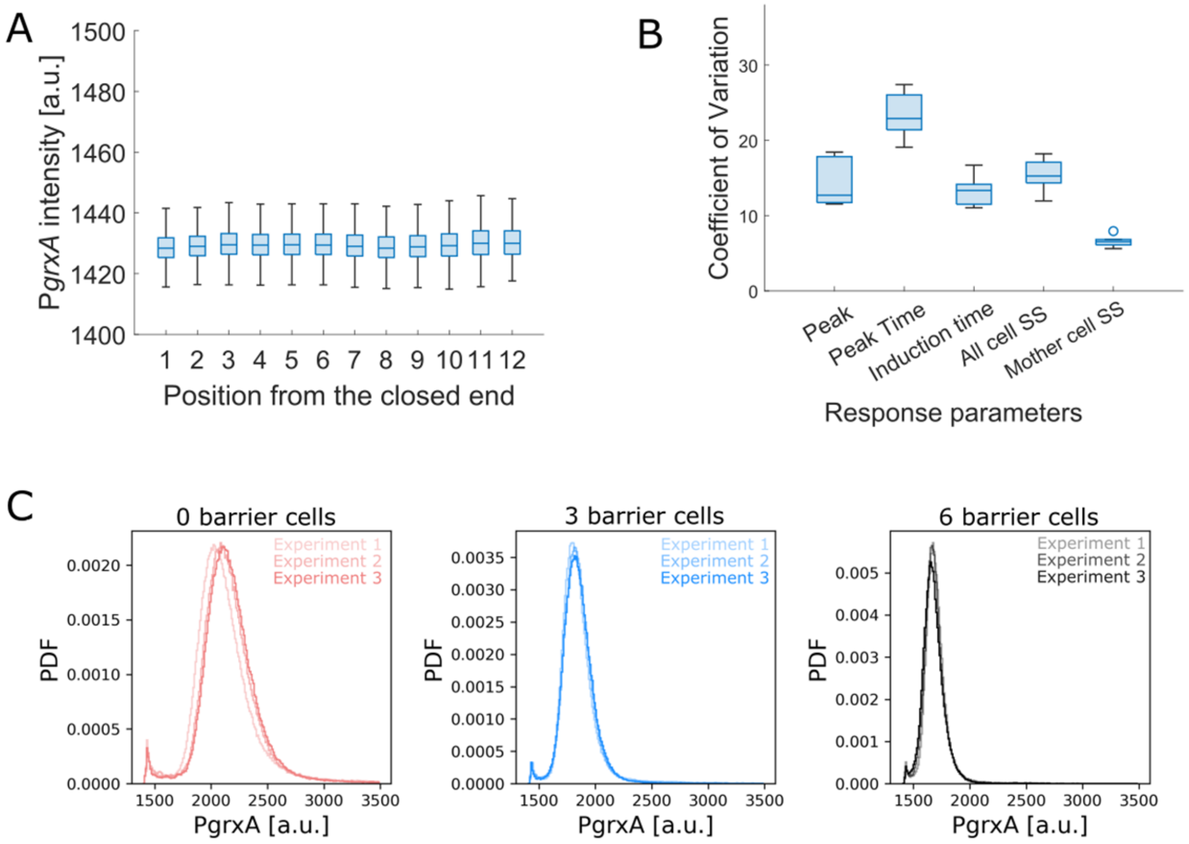

Figure 3.5 Cell-cell variation in gene expression dynamics before and after H_2O_2 treatment:
*(**A**) PgrxA-CFP intensities for cells at different positions in the growth trench before treatment (3 experimental repeats, box plots with median 25th and 75th percentile). (**B**) Variation of the oxidative stress response across mother cells with 100 µM H_2O_2 treatment. Coefficient of Variation (standard deviation/mean) for the peak amplitude (Peak), the time to reach the PgrxA-CFP peak intensity (Peak Time), the response induction time (time until PgrxA-CFP > 1480 a.u.) and PgrxA-CFP intensity from 2 hours post treatment (SS: steady-state) for all cells in growth trenches and for all mother cells (3 experimental repeats, box plots with median 25th and 75th percentile).(**C**) Distribution of PgrxA-CFP intensities of cells with 0 (left), 3(middle) and 6(right) barrier cells under 100 µM H_2O_2 treatment for individual experiments (different shades show different experiments).*

Importantly, by its nature, the machine learning model lacks the ability to predict cell-cell variability that arises stochastically. The power of the model, therefore, suggests that the primary cause of cell-cell variability is not driven by unpredictable molecular fluctuations. Rather, it has a deterministic origin. Further testament to the power of the model is that it was able to predict P*grxA*-CFP responses for cells treated with a range of H_2O_2 concentrations (37.5 – 100 µM) although the concentration itself was unknown to the model. After cross-validation, the model achieved an accuracy of 83.4 ± 1.3%. Hence, the features extracted from cell growth characteristics and morphology were sufficient to deduce the underlying H_2O_2 concentration [Figure 3.7A, Appendix A.3-A.4].

The machine learning model also provides information on the sources of cellular heterogeneity. The features that contributed the most to the predictive power (~66%) of the model related to the characteristics of what we term "barrier cells", i.e. the cells located between the mother cell and the open end of each trench [Figure 3.6C]. The two strongest features accounting for ~53.5% of the total predictive power were (i) the cumulative length of the barrier cells in a trench, and (ii) the combined surface area-to-volume ratio of the barrier cells in a trench. In fact, a model that contained only features of the barrier cells and no features of the mother cell was still able to predict mother cell responses with high accuracy [Figure 3.7B, Appendix A.5-A.6]. Moreover, when cross-validated, this model achieved an accuracy of 69.86 ± 0.1%. Hence, it appears that an individual cell's stress response magnitude does not depend on its own characteristics or location but can be accurately predicted from the number and morphology of its neighbours. That is, the model suggests that the cell-cell variability rests primarily upon the effects of other cells on a focal cell. We next explored the mechanism by which the type and geometry of these intercellular interactions determine an individual cell's stress response.

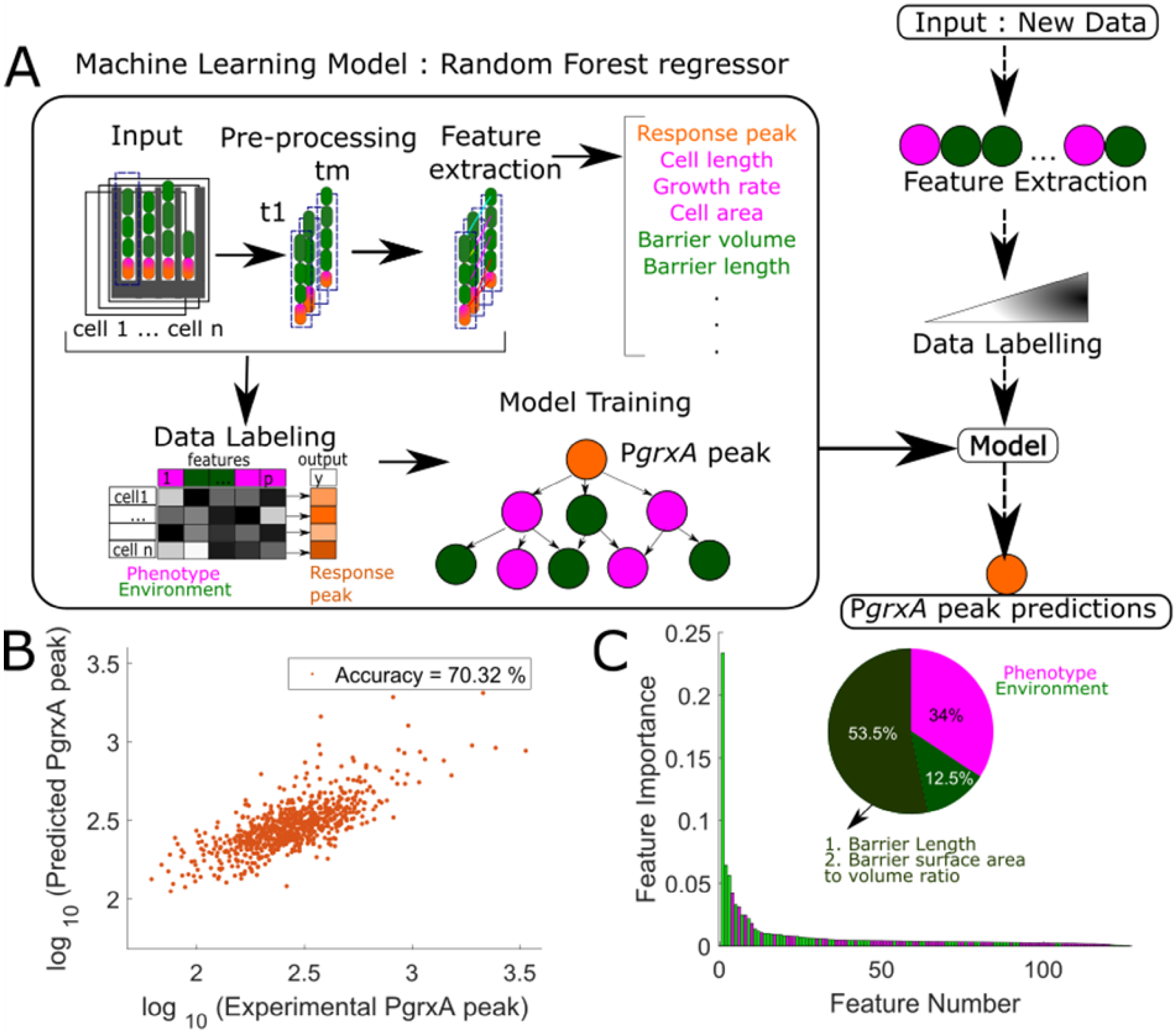

Figure 3.6 Machine learning predicts single cell response heterogeneity:
*(**A**) A random forest machine learning model predicts PgrxA-CFP peak intensities of ~789 mother cells (orange). It uses features that describe the phenotypic characteristics of the mother cell (magenta) and the other cells in the local environment of each trench (barrier cells, green). (**B**) PgrxA-CFP peak predicted by the model plotted against the experimentally measured PgrxA-CFP peak (each dot represents one mother cell) (data in* Appendix *A.1). (**C**) Feature importance plots show the relative contribution of the 126 input features to the predictive power of the model (feature names in Appendix A.2). Barrier cell features (green) are more important than the mother cell features (pink). The two most important features are highlighted and account for 53.5% of the predictive power*

3.5 The properties of neighbouring cells drive oxidative stress response heterogeneity

To further test the apparent role of cell-cell interactions, we designed a microfluidic experiment with a variable number of cells per trench at the time of treatment (5 ± 2 cells) [Figure 3.8A], instead of filling all growth trenches completely. The cells do not show variation in their response and elongation rate in untreated conditions after being loaded into the microfluidic device [Figure 3.8B]. Consequently, there are no significant confounding effects from memory retained from the planktonic culture that may influence the results of experiments performed under low-loading conditions, where the treatment is provided within few minutes of loading the chips. Under these low-loading conditions, the magnitude of the oxidative stress response of the mother cells became even more variable [Figure 3.8C-D]. Notably, P*grxA*-CFP intensities of mother cells decreased when an increasing number of barrier cells was present, suggesting that these are protecting the mother cell from H_2O_2 [Figure 3.9A-B]. The number of barrier cells fluctuates as cells divide and are pushed out of the open end of the trenches. Although the cell-average reporter expression was stable during constant H_2O_2 treatment, individual mother cells showed dynamic fluctuations at steady-state [Figure 3.9C].

Cross-correlation analysis showed that these expression fluctuations were negatively correlated with the variation in the number of barrier cells in the same trench [Figure 3.9D]. The negative cross-correlation peaked at a lag time of 4.5 ± 1.5 min, showing that fluctuations in the number of barrier cells preceded changes in P*grxA*-CFP expression. These rapid changes in fluorescence signal are driven by dynamics in expression rate due to OxyR signalling as well as changes in cell growth rate that affect the rate of fluorescent protein

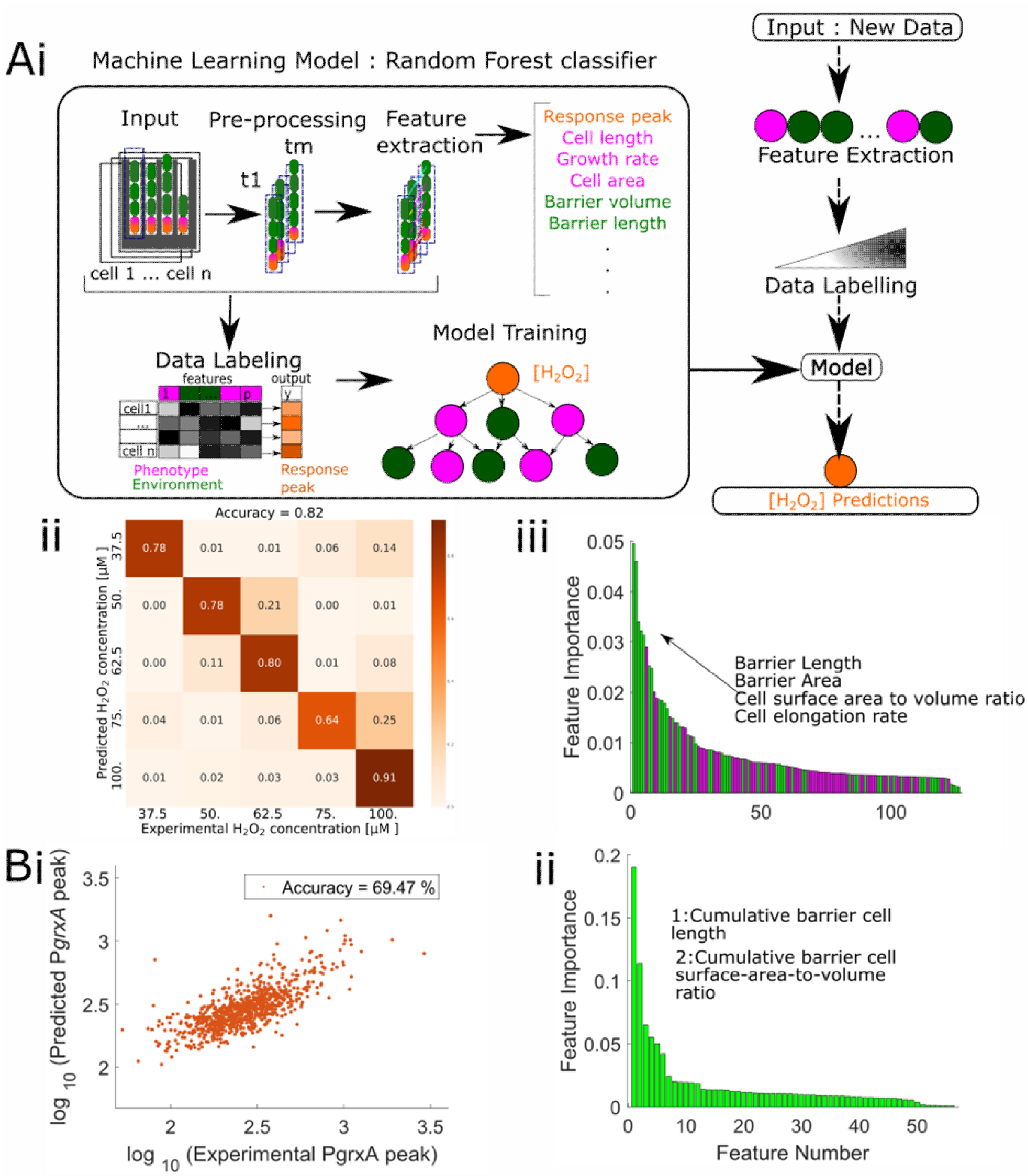

Figure 3.7 Machine learning models to predict oxidative stress response heterogeneity and H_2O_2 treatment concentrations:

(A) Machine learning classifier model predicts external H_2O_2 concentration(orange). (i) It uses features that describe the phenotypic characteristics of the mother cell (magenta) and the other cells in the local environment of each trench (barrier cells, green). (ii) Confusion matrix of predicted [H_2O_2] against the experimental [H_2O_2] for ~900 mother cells (unseen by training data). (iii) Feature

*importance plot shows the relative contribution of the 126 input features to the predictive power of the model. Mother cell features shown in magenta and local environment features (relating to the barrier cells) in green. The features whose mathematical derivatives are in the top 10 most important features are highlighted. Whereas the prediction of PgrxA-CFP peak intensities relied on only a few important features relating to the barrier cells, prediction of [H_2O_2] uses a broader range of different features relating to the mother cell and barrier cells. (**B**) Machine learning model trained only on barrier cells predicts mother cell response heterogeneity: A random forest machine learning model predicts PgrxA-CFP peak intensities of ~850 mother cells (orange). It uses features that describe the other cells in the local environment of each trench (barrier cells, green), and no features for the mother cells themselves. (i) PgrxA-CFP peak predicted by that model plotted against the experimentally measured PgrxA-CFP peak (each dot represents one mother cell). (ii) Feature importance plot shows the relative contribution of the 54 input features to the predictive power of the model. The features of the two most important environmental characteristics accounting for ~73.5% importance is highlighted.*

dilution. Hence, the OxyR response is exquisitely sensitive and rapidly responds to very subtle changes in a cell's micro-environment, such as the division or disappearance of a single cell in the vicinity. Based on calibration experiments with different H_2O_2 concentrations [Figure 3.10A-B], we inferred the local extracellular H_2O_2 concentration from the P*grxA*-CFP intensity of a cell. This showed an exponential decrease of H_2O_2 concentration from the open end of the trench and each barrier cell decreased the local H_2O_2 concentration by 32.3 ± 4.6% [Figure 3.10C]. The response variation persisted even when restricting the analysis to mother cells with a fixed number of barrier cells, especially when that number was small [Figure 3.9E].

Indeed, the Machine Learning model pointed to the surface area-to-volume ratio of the barrier cells as an important feature that determines mother cell responses, in addition to the total volume of the barrier cells. To test this directly, we reasoned that an increased number of barrier cells at a constant total volume would result in a larger total surface area-to-volume ratio. As predicted, we found that the P*grxA*-CFP magnitude decreased with increasing

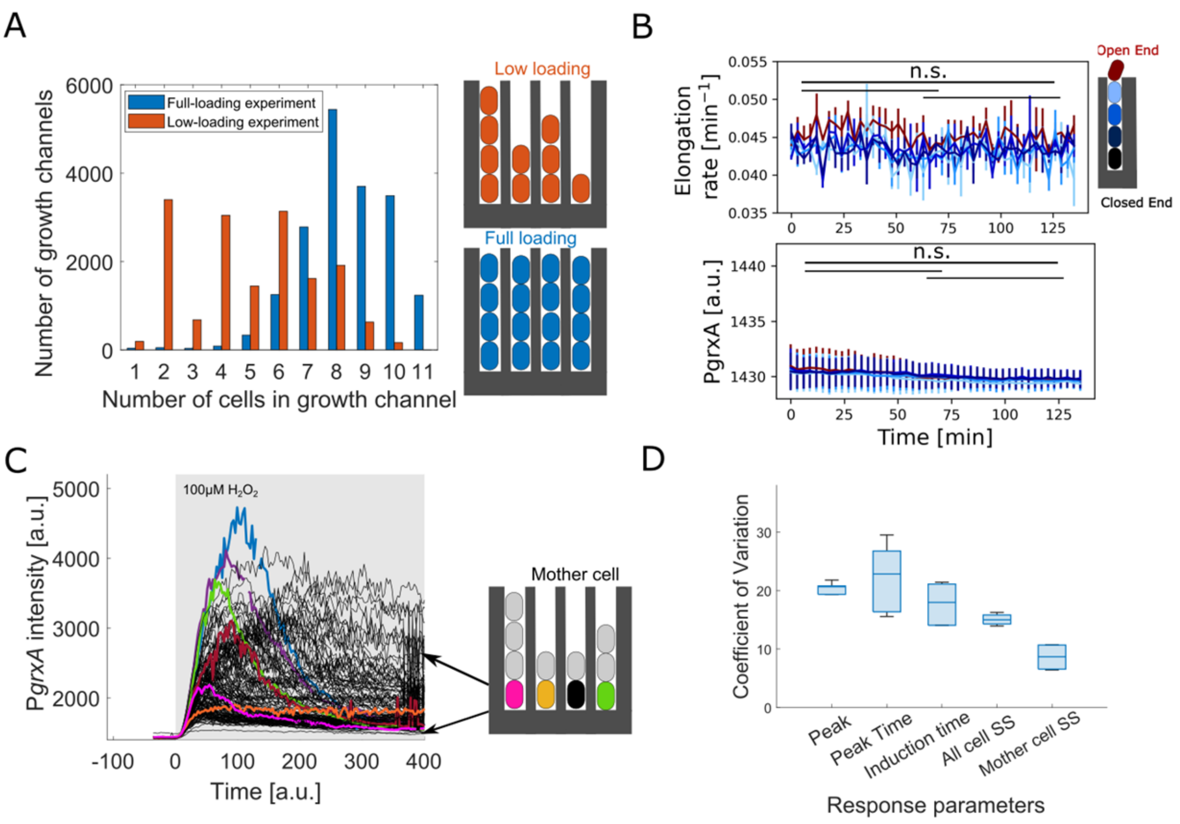

Figure 3.8 Variation in the number of barrier cells per growth trench increases response heterogeneity across mother cells*:*

*(**A**) Distribution of number of cells per trench at the beginning of treatment for experiments with partially filled trenches (low-loading, orange) versus completely filled trenches (full-loading, blue) (3 experimental repeats each). (**B**) Mean elongation rate (top) and PgrxA intensity (bottom) for cells at different positions in the growth trench in untreated growth conditions after loading the chip at t= 0 min (black line: mother cells at closed end; red line: cells at open end) (3 experimental repeats). (**C**) PgrxA-CFP intensities of individual mother cells (6 example cells highlighted in colour) over time treated with 100 µM H_2O_2 (added at time 0 min, shaded area) (~300 traces). (**D**) Variation of the oxidative stress response across mother cells for low-loading experiment after 100 µM H_2O_2 treatment. Coefficient of Variation (standard deviation/mean) for the peak amplitude (Peak), the time to reach the PgrxA-CFP peak intensity (Peak Time), the response induction time (time until PgrxA-CFP > 1480 a.u.) and PgrxA-CFP intensity from 2 hours post treatment (SS i.e. steady state) for all cells in growth trenches and for all mother cells (3 experimental repeats, box plots with median 25th and 75th percentile).*

surface area-to-volume ratio of barrier cells when their total volume was kept constant in the analysis [Figure 3.9F]. Therefore, these measurements confirm the predictions of the

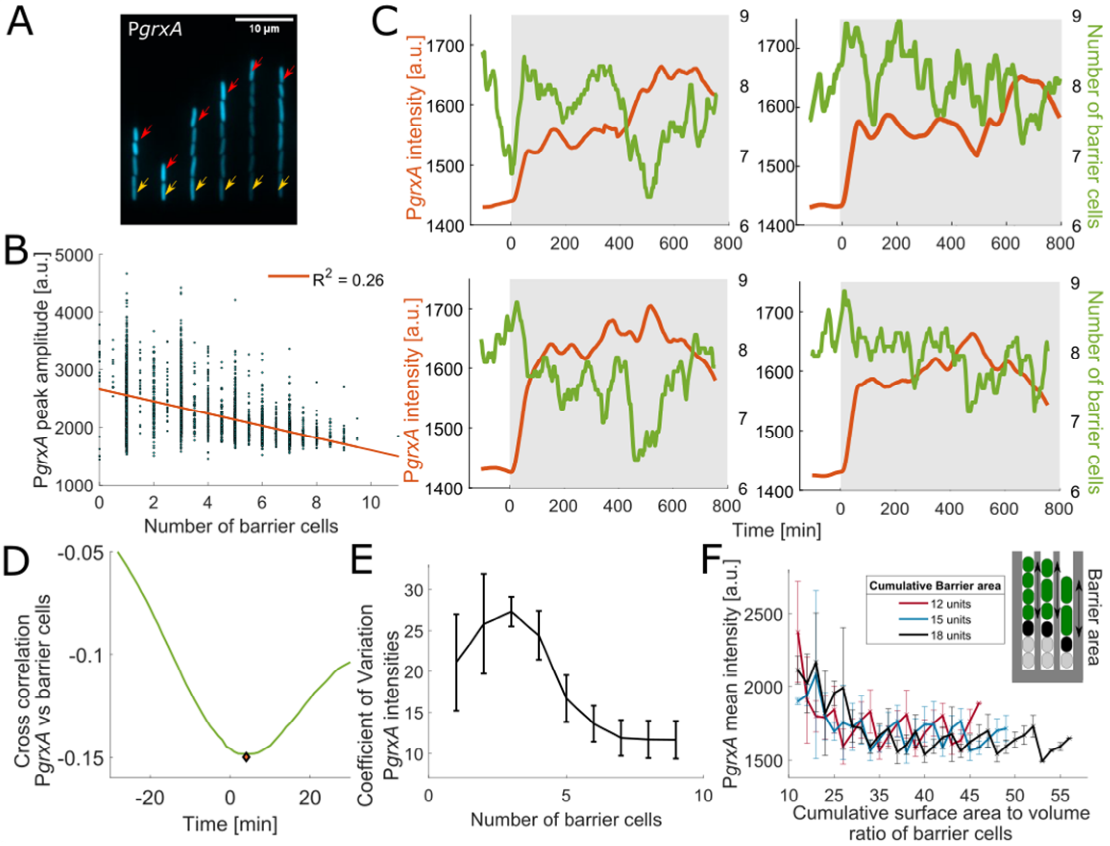

Figure 3.9 Variation in the spatial structure of the micro-environment explains response fluctuations:

*(**A**) Snapshot of PgrxA-CFP under 100 µM H_2O_2 treatment for growth trenches with variable number of cells (mother cells marked with yellow arrow, outermost cells with red arrow). (**B**) PgrxA-CFP peak intensity amplitude under 100 µM H_2O_2 treatment plotted against the average number of barrier cells around the time of treatment (± 9 min; each dot represents one mother cell) (~3250 cells, 3 experimental repeats). (**C**) Example time-traces of PgrxA-CFP intensity (orange) for mother cells and the number of barrier cells in the same trench (green) with 100 µM H_2O_2 treatment added at 0 min (shaded area). Curves were smoothed using a moving mean filter with 45 min window. Note that barrier cell numbers fluctuate between 6-10 cells per trench during steady-state growth. (**D**) Mean temporal cross correlation for PgrxA-CFP of mother cells against the number of barrier cells per trench (example time traces shown in panel C), when mean PgrxA-CFP intensity has reached steady-state from 2 hours after start of 100 µM H_2O_2 treatment until end of experiment (~11 hours) (~950 cells, 2 experimental repeats). Minima is represented by the orange diamond. (**E**) Coefficient of Variation for PgrxA-CFP intensity of mother cells with different number of barrier cells (CV: std/mean was computed for all mother cells in a single experiment, error bars represent std across experiments). (**F**) PgrxA-CFP intensity for cells with the same total area of barrier cells (18, 15 or 12 units) plotted against the cumulative surface area to volume ratio of the barrier cells (3 experimental repeats).*

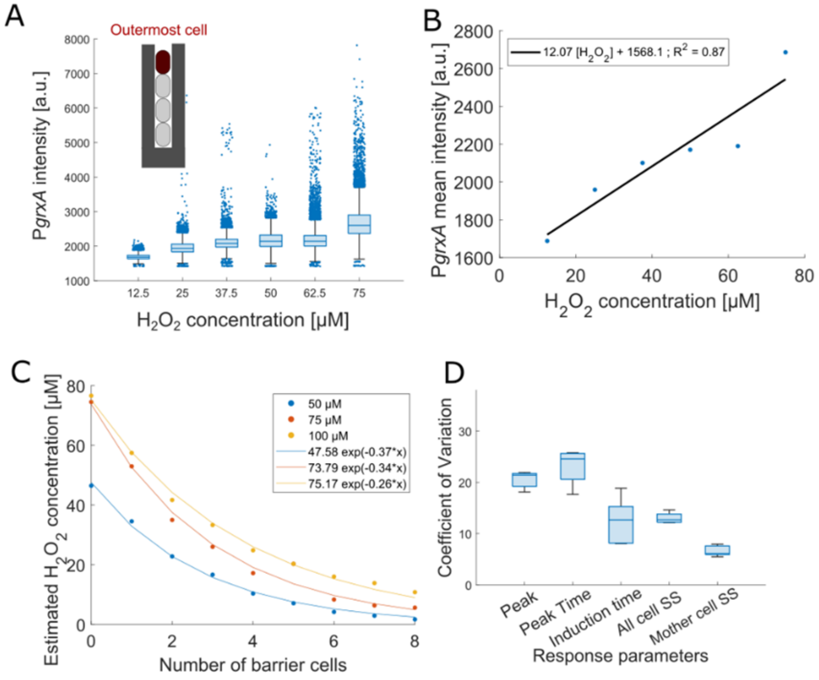

Figure 3.10 Exponential decay of H_2O_2 in growth trenches as predicted by the calibration curve: *(**A**) PgrxA-CFP intensities for these outermost cells 2 hours after the start of treatment for different H_2O_2 concentrations. (~107500 data points with 17921 ± 1960 data-points for each concentration, box plots with median 25th and 75th percentile) (**B**) A linear regression fit of the mean values in panel A gave the calibration equation for intensity changes for different H_2O_2 concentrations as $I = 12.07 \cdot [H_2O_2] + 1568.1$ with $R^2=0.87$. (**C**) Estimated concentration along the growth trench with mean intensities for varying number of barrier cells based on the PgrxA-CFP intensity according to the calibration curve from panel B. Single exponential fits are shown. (**D**) Variation of the oxidative stress response across mother cells in 1.4 µm wide growth trenches after 100 µM H_2O_2 treatment. Coefficient of Variation (standard deviation/mean) for the peak amplitude (Peak), the time to reach the PgrxA-CFP peak intensity (Peak Time), the response induction time (time until PgrxA-CFP > 1480 a.u.) and PgrxA-CFP intensity from 2 hours post treatment (SS: steady-state) for all cells in growth trenches and for all mother cells (3 experimental repeats, box plots with median 25th and 75th percentile).*

machine learning model that the number, size, and morphology of neighbouring cells determine a cell's dynamic response to H_2O_2.

3.6 Intracellular scavenging enzymes create a local H_2O_2 gradient

We next sought to understand the mechanistic basis for the cell-cell interactions underlying

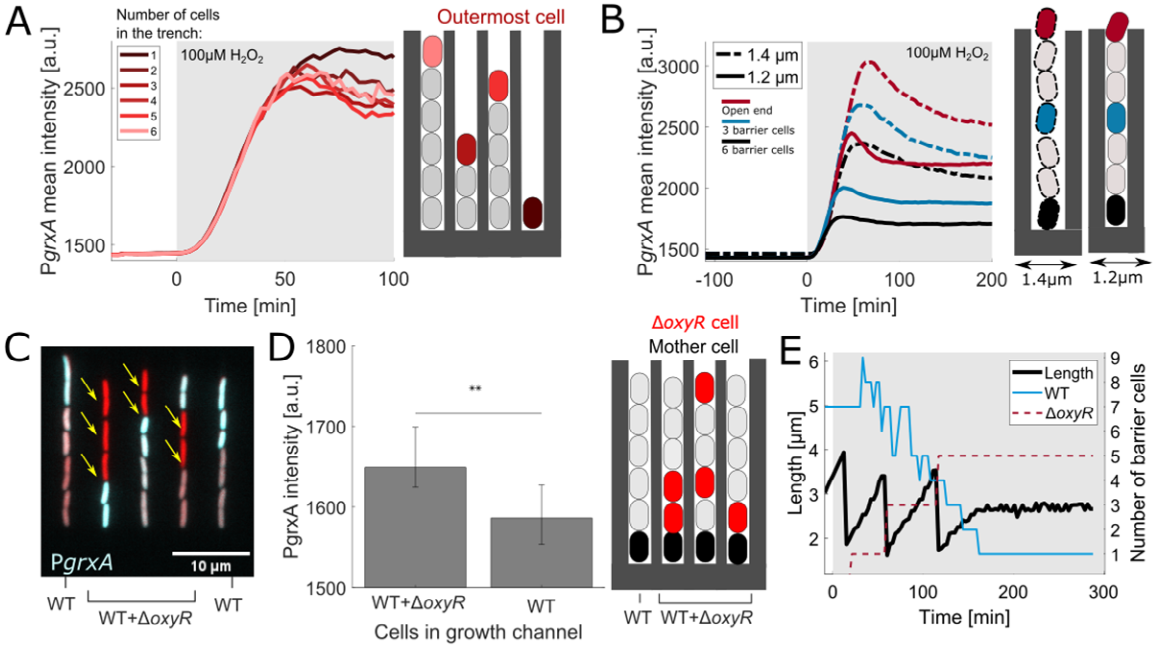

Figure 3.11 Intracellular scavenging enzymes create short-range local H_2O_2 gradients: *(**A**) Mean PgrxA-CFP intensity for outermost cells in growth trenches (marked by red arrows in Figure 3.9A with total number of cells per trench ranging from 1 to 6). 100 µM H_2O_2 treatment added at 0 min (shaded area) (4 experimental repeats). Figure 3.8A shows the number of cells per curve. (**B**) PgrxA-CFP mean intensities for trenches with widths of 1.2 µm (solid lines) and 1.4 µm (dashed lines) for cells with 0 (red), 3 (blue) and 6 (black) barrier cells (3 experimental repeats each). (**C**) Snapshot of merged PgrxA-CFP (cyan) and mKate2 cell marker (red) intensity for trenches with a mix of WT and ΔoxyR strain under 100 µM H_2O_2 treatment (ΔoxyR cells marked with arrow, separate channel images in Figure 3.12B). (**D**) Mean PgrxA-CFP intensity for WT mother cells in growth trenches containing a mix of barrier cells with at least one ΔoxyR cell or purely WT barrier cells (~1600 mother cells, 3 experimental repeats, error bars represent 25th and 75th percentile, ** $p<0.01$). (**E**) Example time-trace of length of a ΔoxyR cell situated at the closed end of a trench (black), and the number of WT (blue) and ΔoxyR cells (red dashed) in the same trench. Number of WT cells decreases as the ΔoxyR cells grow in the trenches and push them out, demonstrating that a ΔoxyR cell can only grow when protected by WT cells.*

phenotypic heterogeneity. We again used microfluidic chips in which the trenches were only partially filled with cells. The outermost cells in each growth trench exhibited the same level of stress response irrespective of their distance from the open end, showing that the geometry of the trenches itself does not restrict H_2O_2 diffusion [Figure 3.9A, 3.11A]. Importantly, this demonstrates that the microfluidic device itself does not create gradients in the stressor that could explain cell-cell differences in the responses. If the cells themselves are indeed generating the observed patterns, this suggests that changes in cell-density will impact the cell-cell variability. To test the effects of cell-density, we next designed a variation on our mother machine device that had wider trenches, increasing them from 1.2 µm to 1.4 µm. As again predicted by the importance of cell-cell effects, this local reduction in cell density reduced both the barrier effect [Figure 3.11B] and cell-cell variation [Figure 3.10D]. Hence, a decrease in cell density permits a higher and more uniform H_2O_2 flux. However, this effect could be caused by the cell mass passively blocking H_2O_2 diffusion, or by active degradation of H_2O_2 by the barrier cells.

We hypothesised that a role for active degradation was likely because H_2O_2 is rapidly scavenged by catalase which is induced by the OxyR response. The Damköhler number (a dimensionless quantity that relates the reaction rate to the rate of diffusion) is $\sim 4 \cdot 10^3$ for the ratio of the catalase scavenging rate ($5.4 \cdot 10^4$ s^{-1} [84]) to the diffusion of H_2O_2 across the *E. coli* cell envelope ($1.6 \cdot 10^{-5}$ m/s, [85]). Hence, the scavenging rate is limited by the diffusion into cells, which is consistent with our finding that the protective effect of the barrier cells was determined to a large extent by their surface area. To experimentally test for the importance of H_2O_2 scavenging in creating the observed exponential stress gradient along the trenches in the device, we loaded trenches with a mix of a Δ*oxyR* strain and a wild-type strain with P*grxA*-CFP reporter [Figure 3.11C]. Δ*oxyR* cells cannot induce catalase and other oxidative stress response genes, which limits their ability to degrade high amounts of H_2O_2 coming in from the environment. As expected if H_2O_2 scavenging is important, we observed that the gradient in P*grxA*-CFP reporter intensity was disrupted by the presence of Δ*oxyR* cells [Figure 3.11C]. Moreover, wild-type cells positioned behind Δ*oxyR* cells showed elevated

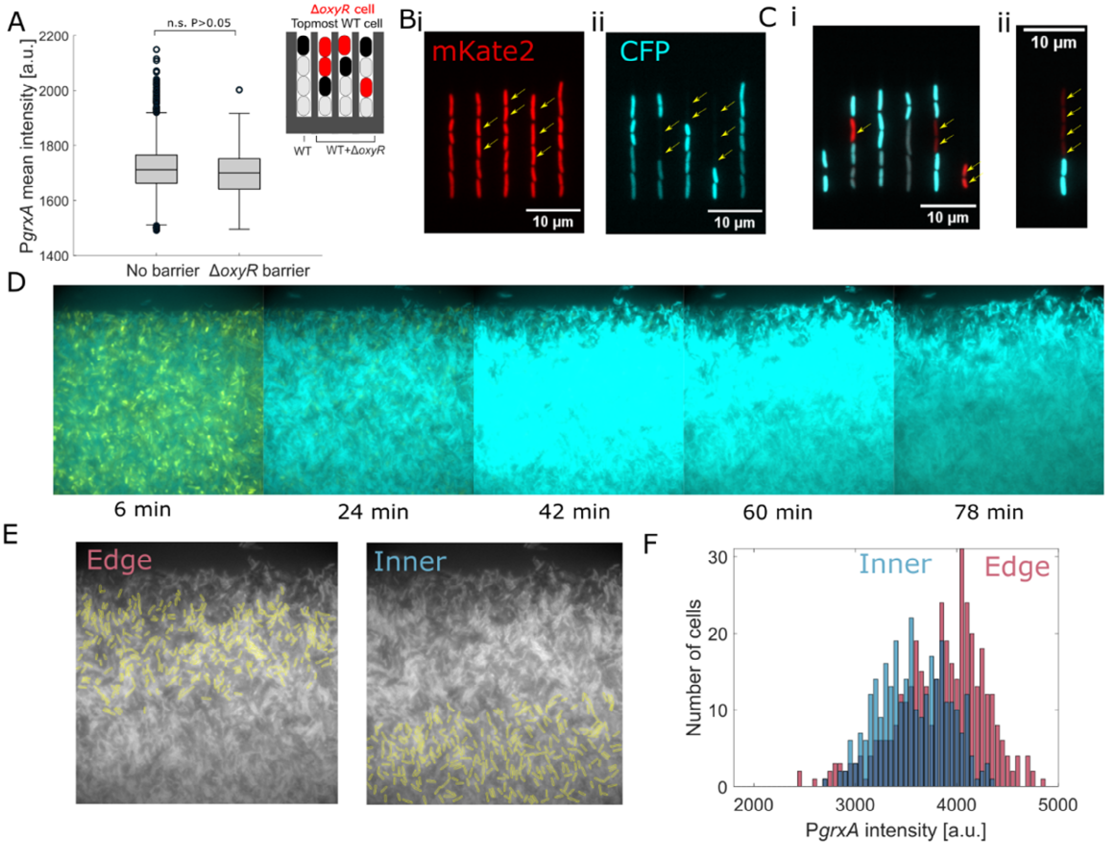

Figure 3.12 ΔoxyR cells do not provide cross protection against H_2O_2 stress:
*(**A**) PgrxA-CFP intensity ~20 min post 100 µM H_2O_2 treatment for top-most WT cells (shown as black in the schematic) in trenches that have either no barrier or barrier of ΔoxyR cells. (3 experimental repeats, box plots with median 25th and 75th percentile). (**B**) Snapshot of PgrxA-CFP (cyan) and mKate2 cell marker (red) intensity for trenches with a mix of WT and ΔoxyR strain under 100 µM H_2O_2 treatment (ΔoxyR cells marked with arrow). (**C**) Merged snapshot PgrxA-CFP (cyan) and mKate2 cell marker (red) intensity for trenches with a mix of WT and ΔoxyR strain under 100 µM H_2O_2 treatment (ΔoxyR cells marked with arrow). (**D**) PgrxA-CFP snapshots of a microcolony of WT mixed with ΔoxyR cells (yellow) under 10 mM H_2O_2 treatment. (**E**) Segmented WT cells on the edge (left) or interior (right) of the microcolony. (**F**) Histograms of PgrxA-CFP intensity for WT cells at the edge (red) or interior (blue) of a microcolony after 30 min of 10 mM H_2O_2 treatment.*

stress responses [Figure 3.11D, 3.12A-C]. Δ*oxyR* barrier cells caused no reduction in local H_2O_2 concentration [Figure 3.12A-C] unlike the ~30% reduction by wild-type barrier cells [Figure 3.10C]. In fact, wild-type cells had a marked protective effect on Δ*oxyR* cells,

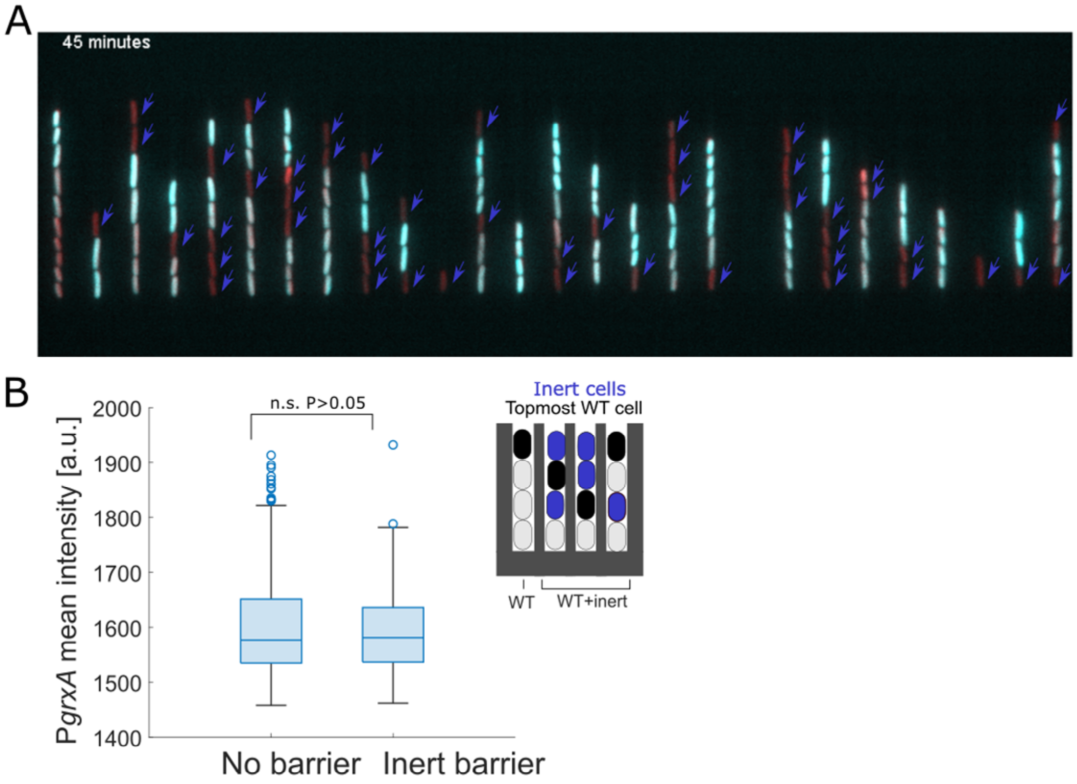

Figure 3.13 Metabolically inert cells do not provide cross protection against H_2O_2 stress:
*(**A**) Snapshot of PgrxA-CFP (cyan) and mKate2 cell marker (red) intensity for trenches with a mix of live WT cells and inert (chemically fixed) cells under 100 µM H_2O_2 treatment (inert cells marked with arrow). (**B**) PgrxA-CFP intensity ~20 min post 100 µM H_2O_2 treatment for top-most WT cells (shown as black in the schematic) in trenches that have either no barrier or barrier of inert cells. (4 experimental repeats, box plots with median 25th and 75th percentile).*

consistent with bulk culture measurements [90]. On their own, Δ*oxyR* cells were unable to grow during 100 µM H_2O_2 treatment [Figure 3.4], but with wild-type cells acting as a barrier, Δ*oxyR* cells were able to grow until the wild-type cells exited the trench [Figure 3.11E]. We also studied the effect of Δ*oxyR* cells in a bacterial colony, by again mixing them with wild-type strain carrying the P*grxA*-CFP reporter. Here, we observed a stronger stress response than in a clonal wild-type colony and no longer saw a steep spatial gradient from the edge to the interior [Figure 3.12D-F]. This is again consistent with the importance of H_2O_2 scavenging rather than cells passively blocking H_2O_2. To explore if cell mass had any protective effect, we loaded trenches with a mixture of wild-type cells and inert cells that had been chemically fixed. Like Δ*oxyR* cells, inert cells caused no reduction in the stress level of neighbouring cells [Figure 3.13].

3.7 Barrier cells obtain high H_2O_2 tolerance via gradual adaptation

We next sought to understand how the cells at the top of the trench are able to survive and provide protection for other cells in the face of high concentrations of H_2O_2. Elongation rates of the outermost cells in the trenches show that >50 µM H_2O_2 will lead to growth inhibition in the absence of cellular cross-protection [Figure 3.14]. Consistent with this, the onset of our standard 100 µM H_2O_2 treatment completely halted the growth and division of ~1- 2 outermost barrier cells per trench. However, the cells in the interior of the trenches only transiently slowed in growth and quickly recovered unperturbed elongation and division rates despite ongoing H_2O_2 treatment [Figure 3.1C]. These surviving interior cells divide and push live progeny towards the stress source and thereby replace the barrier cells that had been stalled growth by the sudden onset of treatment. This suggests that the barrier cells that persist are those that are given time to adapt to a gradual increase in H_2O_2 concentration. Such gradual adaptation is known to enhance survival of higher stress levels [188,199,200].

To test if this “priming” effect underlies the high stress tolerance of the barrier cells, we compared the impact of the sudden onset of high levels of H_2O_2 with a gradual onset [Figure 3.15A]. A sudden 1-hour pulse with 500 µM H_2O_2 concentration stalled the growth of 99%

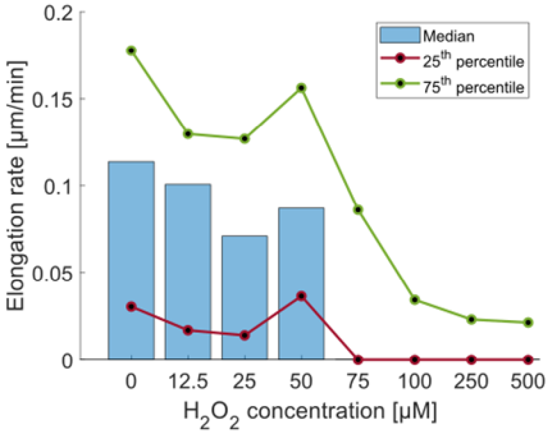

Figure 3.14 Growth inhibition in the absence of cellular cross-protection:
Elongation rate for outermost cells in the trenches traced from time of treatment until 30 minutes post treatment for different H_2O_2 *concentrations.*

of mother cells [Figure 3.15B], and only 13% of mother cells subsequently recovered growth [Figure 3.16]. Consistent with our observations of cross protection at 100 µM H_2O_2, these individuals were protected by more barrier cells than those that irreversibly stopped growth [Figure 3.15B]. Furthermore, the delay before the surviving cells started to regrow after treatment removal was variable and negatively correlated with the number of barrier cells [Figure 3.15A, C]. When a gradual increase of H_2O_2 concentration was applied, again reaching up to 500 µM in 18 minutes and then kept constant for an hour, many more of the cells survived [Figure 3.15B]. The result is consistent with the importance of priming for generating a subpopulation of stress-tolerant barrier cells. However, the actual adaptation process of the barrier cells during continuous treatment is more complex, because it involves both a temporal and a spatial gradient in stress level.

To understand the spatio-temporal dynamics of adaptation, we tracked individual cells as they moved from birth at the closed end of the trench until they exited the open end [Figure 3.17A]. P*gxrA*-CFP expression increased rapidly over time as cells traverse the spatial H_2O_2

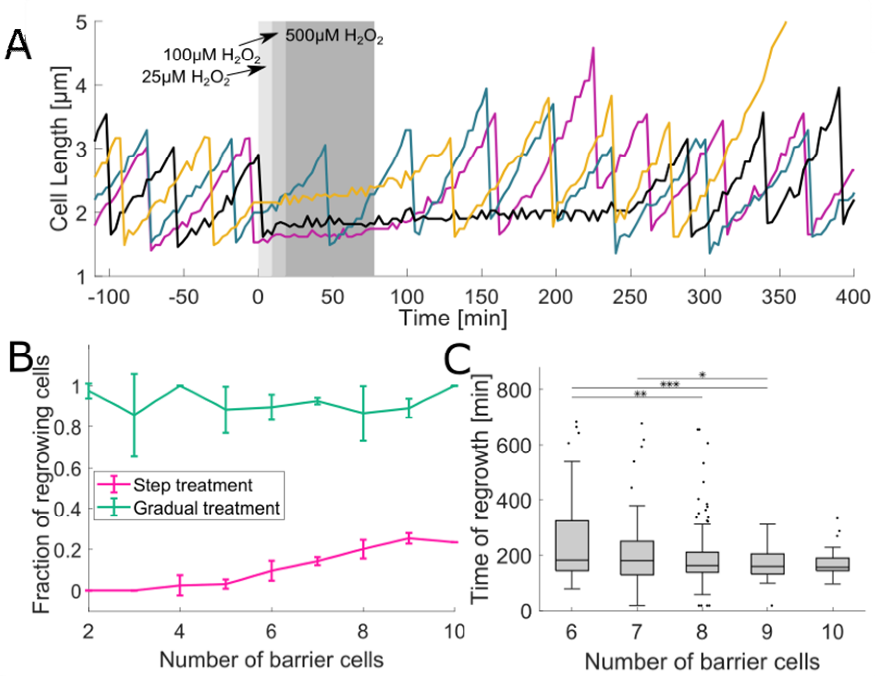

Figure 3.15 Local environmental variation determines divergent cell fates after H_2O_2 treatment: *(**A**) Individual mother cell length traces with gradual increase in H_2O_2 concentration from 25 µM to 100 µM to 500 µM (shaded area), followed by recovery without treatment. (**B**) Proportion of mother cells that recover growth within ~11 hours after the removal of 500 µM H_2O_2 treatment that was applied in a single step (pink) or gradually (green, as illustrated in panel A) plotted against number of barrier cells at the time of treatment (≥3 experimental repeats each; line plot with mean and standard deviation). (**C**) Time of regrowth of mother cells after step 500 µM H_2O_2 treatment plotted against number of barrier cells at the time of treatment. (~300 cells; boxplot with median, 25th and 75th percentile; *$p<0.05$, ** $p<0.01$, *** $p<0.001$).*

gradient [Figure 3.17B, 3.18]. This observation can be explained by two effects; first, the exponential increase in H_2O_2 concentration along the length of the trench, and second, the increasing speed of movement as cells are pushed by exponentially growing cells located deeper in the trench. The speed of movement varies between cells due to fluctuations in elongation rates and the number of cells per trench [Figure 3.17C]. Cells that had the same number of barrier cells and moved faster to the trench opening showed a steeper response than slower moving cells [Figure 3.17D]. When mobile cells experience a gradient of H_2O_2 in space and time, successful adaptation requires that the induction rate of scavenging

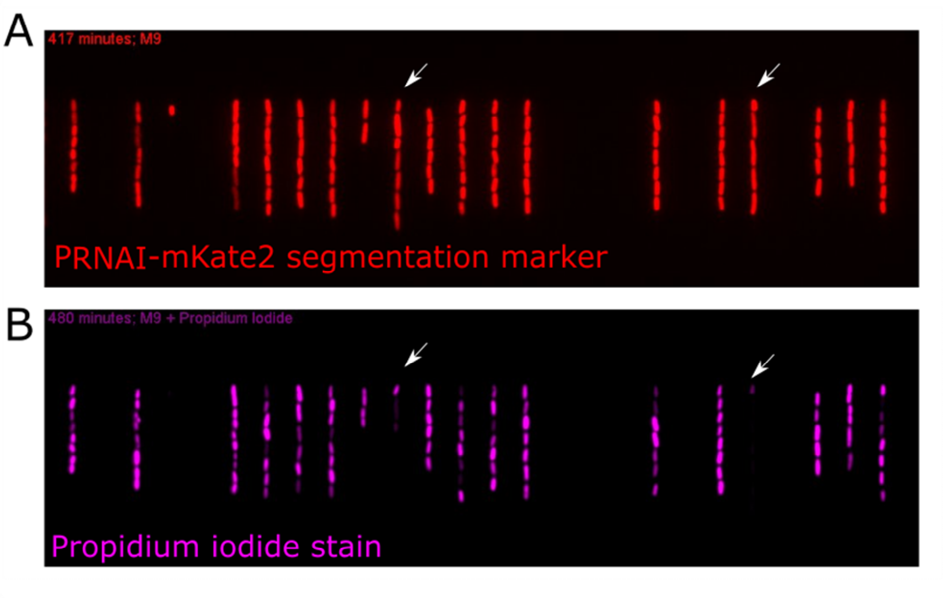

Figure 3.16 Cell death under 500 µM H_2O_2 treatment visualised using propidium iodide staining: *(**A**) Snapshot of E. coli cells with segmentation marker* P_{RNAI}-mKate2 *in growth trenches 360 minutes (~6 hours) post removal of 500 µM H_2O_2 treatment. The 2 growth trenches marked with white arrows regrew after treatment removal. (**B**) Snapshot of E. coli cells stained with propidium iodide as an indicator of cell death.*

enzymes matches the increasing influx of H_2O_2. Indeed, movement speed and the response induction rate were correlated in individual cells (Pearson correlation coefficients = 0.76) [Figure 3.17E]. Next, in order to isolate the effect of the spatial gradient on the response induction rate, we analysed cells that moved with similar speed. In this case, cells with fewer barrier cells had a higher response induction rate because they experience a steeper spatial H_2O_2 gradient [Figure 3.17F]. Together, the multiplicative effects of accelerated movement and increasing stress gradient lead to a rapid induction of the response as cells are pushed towards the trench opening.

3.8 A rapid response to the environment overwrites cellular memory

In principle, a cell's gene expression level is shaped by its immediate response to the current local environment as well as its memory of past stress exposure [34]. We thus explored if any of the response heterogeneity that we observe can be traced back to a cell's lineage history. When H_2O_2 treatment was stopped, reporter intensities started to drop quickly and decayed exponentially with a half-life that matched the cell doubling time, confirming that CFP is a stable protein and diluted by cell division [Figure 3.19]. If oxidative stress impacted the stability of CFP, the decay rate of reporter intensity would be higher than the cell doubling rate, factoring for protein degradation. However, in our experiments, the decay rate of CFP matches the doubling time, confirming the photostability of CFP under H_2O_2 treatment. The P*grxA*-CFP decay rate was variable across cells but closely correlated with the growth rate, which explained the observed cell-cell variation in the response deactivation [Figure 3.17G]. Cytoplasmic proteins are randomly equipartitioned at cell division, so the CFP intensities of sister cells were closely correlated immediately after birth [Figure 3.20]. However, during constant H_2O_2 treatment the intensity of the cell located closer to the open end of the trench quickly diverged from the sister [Figure 3.17F, 3.20]. Specifically, the intensity difference between the two sisters increased exponentially over time because the cell closer to the open end of the trench experiences a higher H_2O_2 concentration and itself acts as a barrier for the cell located below. This effect was much less pronounced for sisters born with a larger number of barrier cells because they move more slowly in a shallower H_2O_2 gradient. These patterns suggest that any stress response memory is erased quickly for cells that move rapidly up the H_2O_2 gradient at the open end of the trenches. However, cells that experience more uniform conditions could in principle maintain memory across generations.

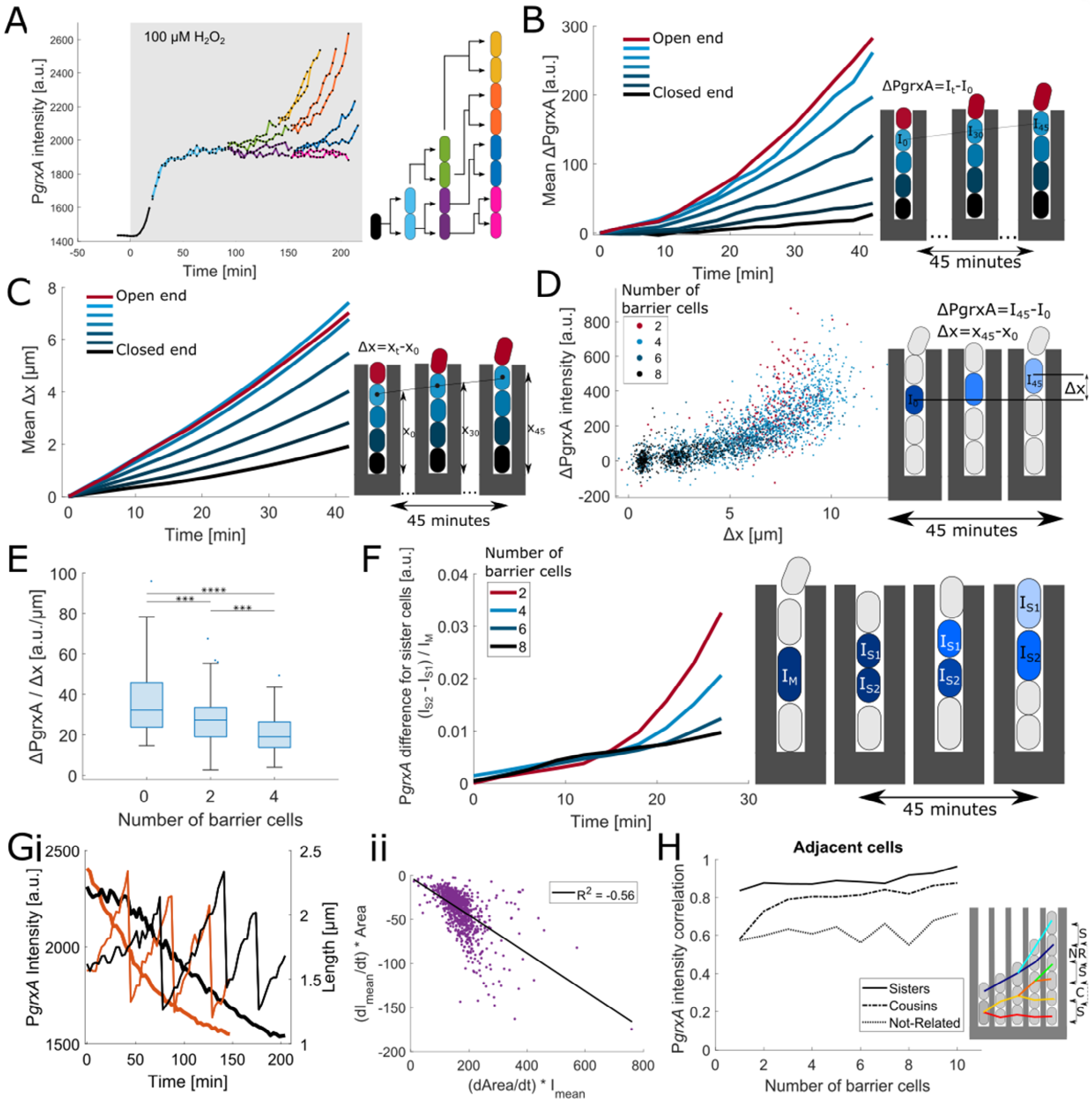

Figure 3.17 Spatio-temporal response dynamics overwrite cell lineage-associated memory:
*(**A**) PgrxA-CFP intensities for a representative mother cell and its progeny that move towards the opening of the growth trench. 100 µM H_2O_2 treatment added at 0 min (shaded area). (**B**) Effect of cell movement on PgrxA-CFP expression in a spatial H_2O_2 gradient: Mean increase in PgrxA-CFP intensity (ΔPgrxA) over time when the population response has reached steady-state (from 2 hours after start of 100 µM H_2O_2 treatment until end of experiment ~11 hours). Each curve represents cells moving towards the trench opening from a different starting position (black line: mother cells at closed end; red line: cells at open end) (3 experimental repeats). (**C**) Effect of cell position in the growth trench on the movement speed: Each curve shows the mean movement Δx towards the trench*

*opening of cells with different starting position (black line: mother cells at closed end; red line: cells at open end) (3 experimental repeats). (**D**) Response induction rate depends on the cell movement speed: Each point represents the total increase in PgrxA-CFP and total movement of a single cell traced for 45 min. Colours represent the starting position according to the number of barrier cells (~2800 total number of cells, 3 experimental repeats). (**E**) Response induction rate depends on cell position in the growth trench: Relative increase in PgrxA-CFP per distance for cells that move 7 ± 0.2 μm in 45 min. Number of barrier cells represents the starting position (~200 total number of cells, 3 experimental repeat, *** $p<0.001$, **** $p<0.0001$). (**F**) Responses of sister cells diverge over time: PgrxA-CFP intensity difference between sister cells (S1 and S2) followed for 30 minutes post division when the response has reached steady-state. Intensity differences were normalised by the intensity of the cell they arose from. Number of barrier cells represents the starting position at the time of cell division (~5400 pairs, 3 experimental repeats). (**G**) Heterogeneous growth rates explain variability in the deactivation rate of the response: (i) PgrxA-CFP intensity (thick lines) and cell lengths (thin lines) of 2 representative mother cells (black and orange plots respectively) after removal of 500 μM H_2O_2 at time 0 min, showing that faster growth leads to a faster decay. (ii) Correlation between PgrxA-CFP intensity decay (dI_{mean}/dt) and cell growth rate (dArea/dt) after removal of 500 μM H_2O_2 (~1000 mother cells). (**H**) Effect of cell position on response memory: Pearson's correlation coefficient for PgrxA-CFP intensities of adjacent cell pairs with variable number of barrier cells, related as sisters (S, solid), cousins (C, dash-dotted) or not related (NR, dotted) (3 experimental repeats).*

To test this, we quantified the difference in CFP reporter intensities between adjacent cells in the same trench that were either related as sisters (separated 1 generation before), cousins (2 generations separated), or not related (>2 generation separated). Sister pairs were more correlated than cousins, and cousins were more correlated than distantly related cell pairs [Figure 3.17H, 3.21A], confirming the presence of cross-generational response memory. However, the correlation between cousins dropped to the level of unrelated cells when the number of barrier cells was small [Figure 3.17H, 3.21B]. We further tested cell memory using repeated short pulses of H_2O_2 treatment to understand whether a past response affected a subsequent response. We saw a low level (~25%) of correlation in the response intensities between subsequent pulses of the same mother cell [Figure 3.22]. Therefore, oxidative stress response memory can persist over generations when the environment is constant, but

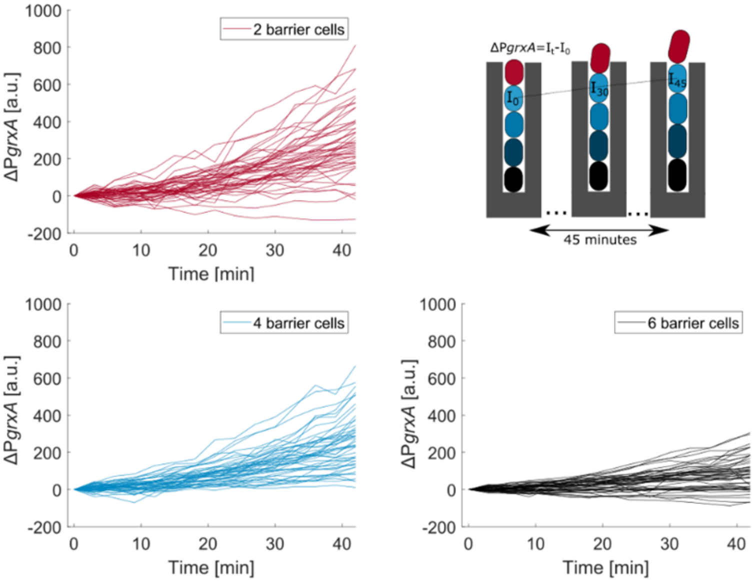

Figure 3.18 Effect of cell movement on PgrxA-CFP expression in a spatial H_2O_2 gradient: *Increase in PgrxA-CFP intensity for single cells (ΔPgrxA) over time when the response has reached steady-state (from 2 hours after start of 100 µM H_2O_2 treatment until end of experiment ~11 hours). Each curve represents a single cell moving towards the trench opening from a different starting position. (red line: cells with 2 barriers; blue line: cells with 4 barriers; black line: cells with 6 barriers; 45 traces shown for each case).*

changing environmental conditions dictate the instantaneous response level and effectively overwrite cell lineage memory.

3.9 Spatial gradients in H_2O_2 lead to cellular heterogeneity in mutagenesis

It has been shown that variation in the timing [72,201] or magnitude of a stress response [202] can cause cell-to-cell variation in mutation rates. We were therefore interested whether the phenotypic heterogeneity driven by cell-cell interaction in our experiments could also lead to mutational heterogeneity. Lagage *et al*. reported that H_2O_2 treatment causes a burst of mutations prior to induction of the oxidative stress response in *E. coli* [188]. Here, we used the

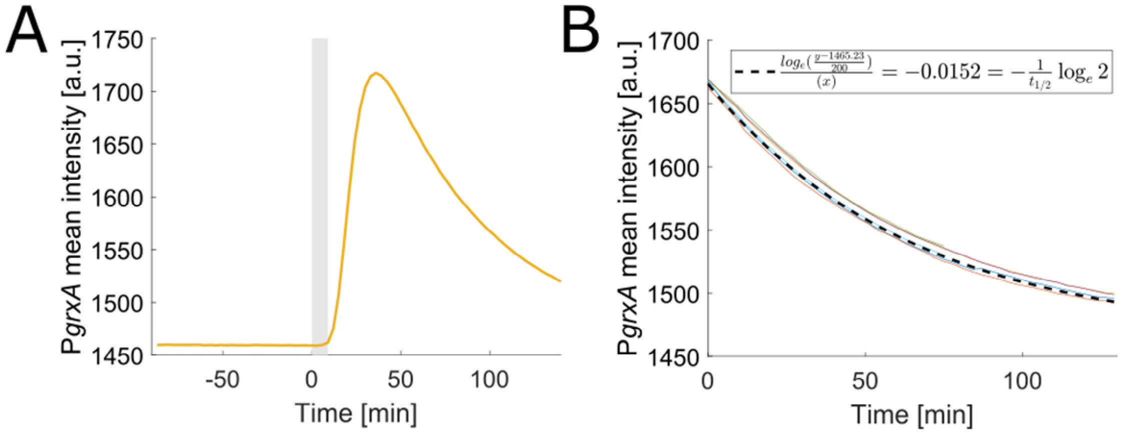

Figure 3.19 Exponential response decay after H_2O_2 removal:
*(**A**) Mean PgrxA-CFP intensity for 100 µM H_2O_2 treatment from 0 to 9 minutes (shaded). (**B**) Exponential fit to the decay of intensity after treatment removal of data shown in panel A, $t_{1/2}$ = 45.6 min as expected for the generation time of ~45 min (thin lines show curve of different dilution traces and bold dashed line indicates the fit, 6 repeats). This shows that sCFP3 is stable and diluted by cell growth.*

same approach with a MutL- mYPet fusion (which forms foci at sites of DNA mismatches) to monitor the occurrence of DNA replication errors in single cells [187,203]. Cells showed a burst of DNA replication errors immediately after the onset of treatment [Figure 3.23A-B], and the magnitude of this burst decreased steeply with increasing number of barrier cells [Figure 3.23C]. Moreover, the spatial gradient in mutagenesis was lost when we grew cells in wider trenches [Figure 3.23C], consistent with the uniform stress response observed under these conditions. Finally, bacterial colonies with 10 mM H_2O_2 treatment exhibited a higher frequency of DNA mismatch foci along the edge of the colony compared to the interior. Therefore, mutational heterogeneity can arise when local cellular interactions generate cell-cell variability in stress response expression.

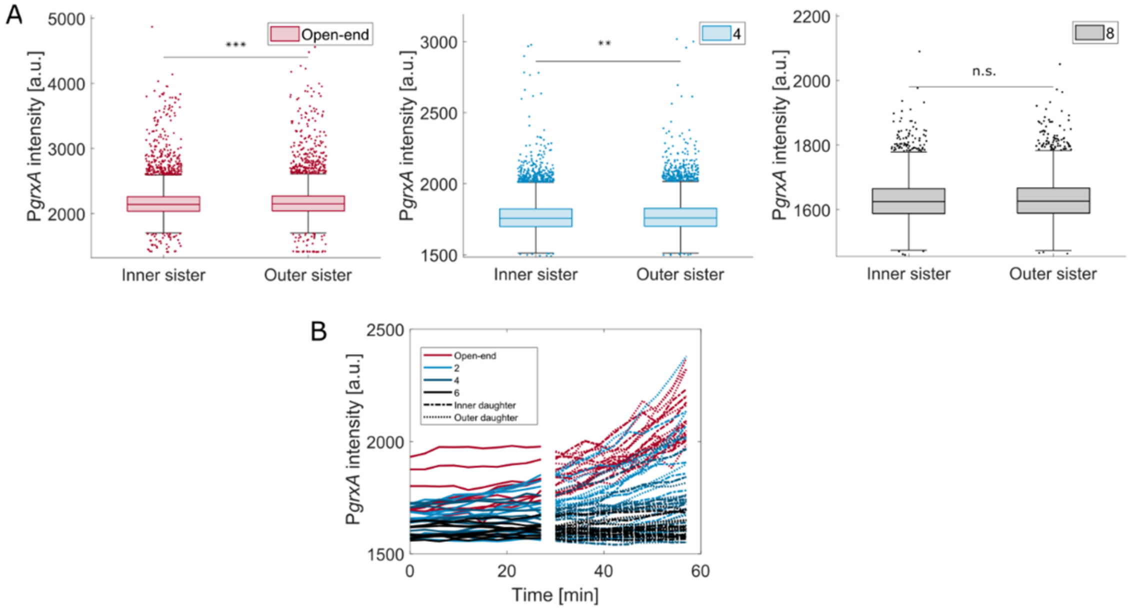

Figure 3.20 Response of sister cells diverge under 100 µM H_2O_2 treatment:
*(**A**) PgrxA-CFP intensity at the time of division for sister cells at steady state with 100 µM H_2O_2 treatment. (Outer sister: closer to the open end). Pairs with outer sister having 0 (maroon), 4 (blue) and 8 (black) barrier cells are displayed (~ 34000 sister cell pairs, 3 experimental repeats, box plots with median 25th and 75th percentile; *** p<0.001, ** p<0.01 and n.s. for p>0.05). (**B**) Single-cell traces for the data shown in Figure 3.17F. PgrxA-CFP intensity traces for sister cells (outer: dashed, inner: dash-dotted), and their progenitor cells (time of division ± 27 minutes). Colour code based on number of barrier cells at the time of division (10 mother-daughter pairs for each case plotted).*

3.10 Discussion

Phenotypic heterogeneity within bacterial populations has been well documented but its origins are difficult to pinpoint and its purpose is debated. This cell-cell variability is often attributed to bet-hedging, but could also arise due to unavoidable biochemical noise or an underlying deterministic process that appears random because it has not been thoroughly characterised. These scenarios are not necessarily mutually exclusive, and a part of the apparent heterogeneity may also stem from non-biological measurement noise. Studies of the oxidative stress response in bacteria have revealed characteristics that partially support each

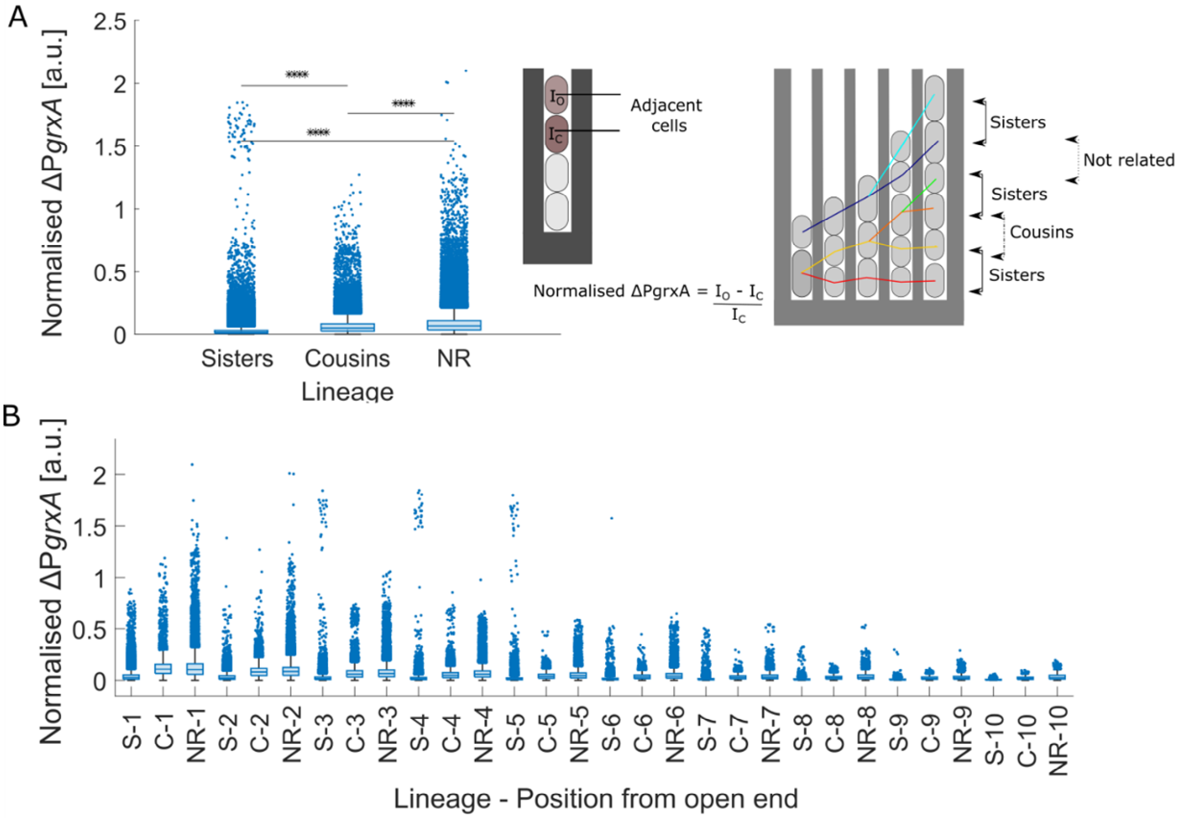

Figure 3.21 Cells become more correlated with closer lineage relation and increasing barrier lengths:

*(**A**) Normalised PgrxA-CFP intensity difference for adjacent cell pairs related as sister (S), cousins (C), or not related (NR) under 100 µM H_2O_2 (box plots with median 25th and 75th percentile, **** $p<0.0001$, 3 experimental repeats). (**B**) Normalised PgrxA-CFP intensity differences for adjacent cells at different positions from the open end and separated by lineage identity (e.g. S-1 shows the intensity difference between sisters at position 1 from the open end etc; 3 experimental repeats, box plots with median 25th and 75th percentile). In general, unrelated cells have higher intensity differences than cousins or sisters, and intensity differences decrease with increasing number of barrier cells.*

of these models [31–33,91,204]. To help resolve this uncertainty, here we have characterized the spatio-temporal behaviour of single *E. coli* cells growing in a defined environment under a constant treatment of H_2O_2. In contrast to the expectation from a stochastic process, we find

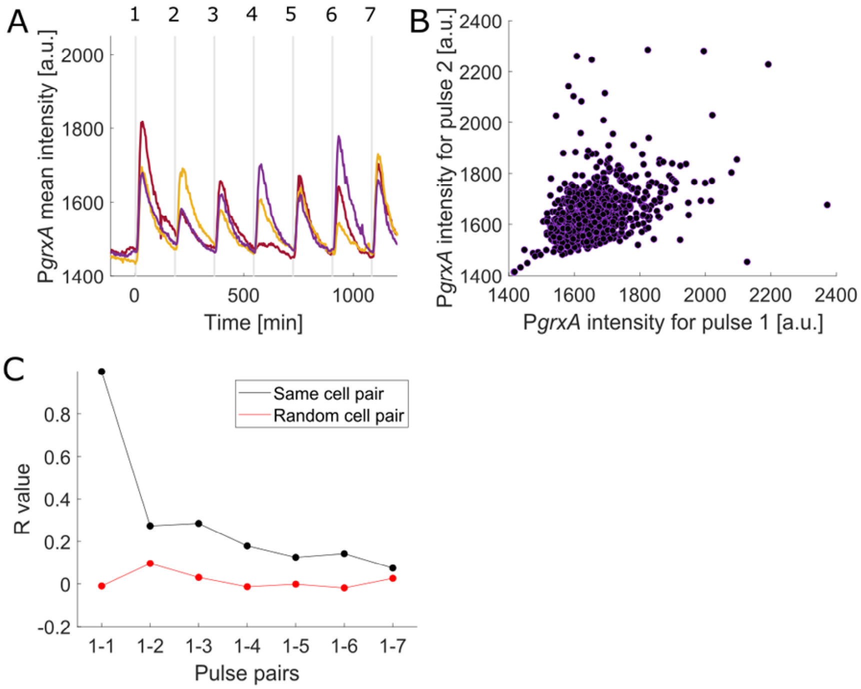

Figure 3.22 Cell memory in response to H_2O_2 treatment:
*(**A**) Testing for response memory with repeated short pulses of H_2O_2 treatment. Example PgrxA-CFP traces of 3 mother cells experiencing 9 minutes of 100 µM H_2O_2 treatment every 3 hours (treatment times indicated in grey). (**B**) Scatter plot of PgrxA-CFP intensity values of mother cells 60 minutes post treatment for the first and second pulse of treatment, showing ~25% correlation indicative of a low level of response memory between successive pulses (~800 cells, 2 experimental repeats). (**C**) Correlation R values for PgrxA-CFP intensity values for pairs of pulses of the same mother cell or for pulses of randomly paired cells as negative control (~800 cells, 2 experimental repeats). Intensities were measured at 60 minutes after each treatment pulse. Response memory decays over time from ~25% correlation between successive pulses (pulse pairs 1-2) close to the random level for pulse pairs 1-7. Residual long-lived correlation may reflect permanent intensity differences across cells e.g. due to position in the microscopy field of view.*

that individual cells modulate their gene expression extremely precisely to the local H_2O_2 concentration. Moreover, the induction of scavenging enzymes generates steep H_2O_2 gradients, with each cell contributing to a ~30% reduction of H_2O_2 in its vicinity. The gradient is expected to be more pronounced in a 2D or 3D microcolony where a focal cell is shielded by neighboring cells across multiple spatial dimensions, as opposed to 1D growth channels in microfluidics. The result is that the response of a focal cell is defined by the

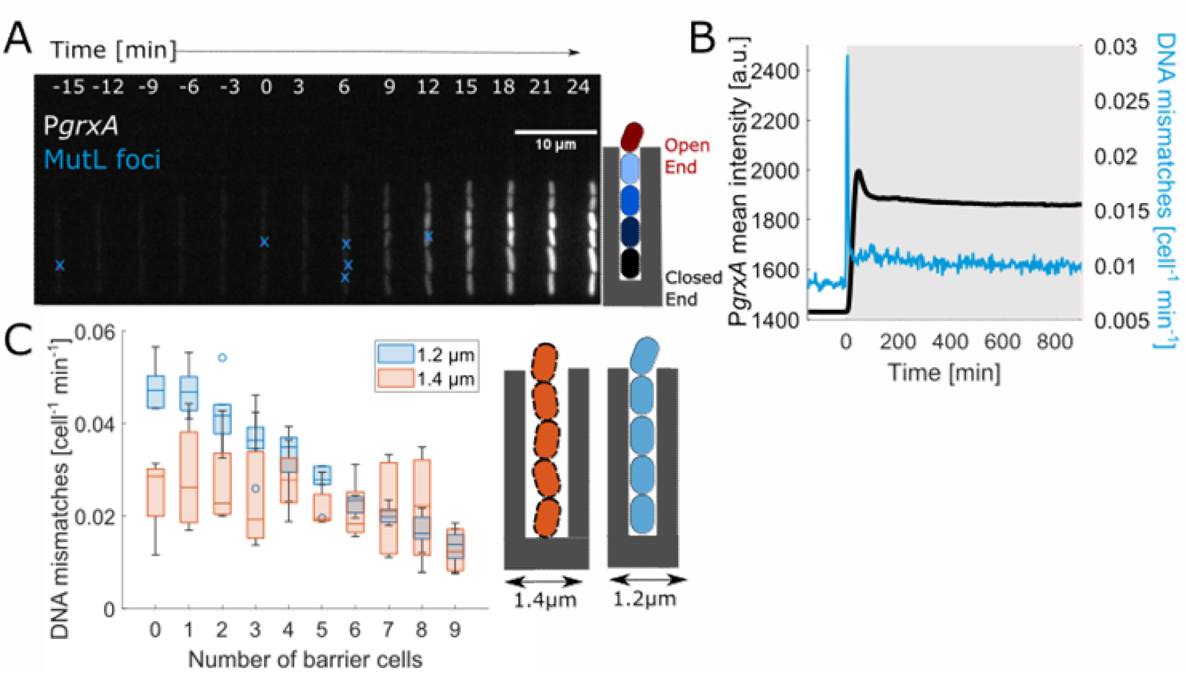

Figure 3.23 Spatial heterogeneity in H_2O_2 concentration causes cell-to-cell variation in mutagenesis:

*(**A**) Kymograph of one growth trench with PgrxA-CFP intensities under 100 µM H_2O_2 treatment added at time 0 min. Blue crosses represent MutL-mYPet mismatch foci. (**B**) Mean rate of DNA mismatch foci (per cell per minute, blue) and PgrxA-CFP mean intensity (black) for all cells in the growth trenches (3 experimental repeats). (**C**) Dependence of the mismatch rate on cell position: Amplitude of the DNA mismatch rate peak for cells with different number of barrier cells under 100 µM H_2O_2 treatment for growth in 1.2 µm (blue) and 1.4 µm (orange) wide trenches (3 experimental repeats each).*

properties of its neighbours, which generates striking phenotypic heterogeneity via cell-cell interactions. Our work does not exclude the possibility that stochastic processes become important for phenotypic heterogeneity in the oxidative stress response under lethal conditions, where the heterogeneity in fate of the cells can be a result of stochastic biological events like DNA damage not explored in detail in this study. Nevertheless, our findings make clear that striking cell-cell variability can emerge without the need for such stochastic underpinnings. The accuracy of the response to the local environment is likely based on the rapid uptake of H_2O_2 together with its high reactivity and specificity towards OxyR[205].

Induction of scavenging enzymes and GrxA reductase lowers the intracellular H_2O_2 concentration and deactivates OxyR in a negative feedback loop, which increases response speed and accuracy in general [206]. Because oxidative stress is mutagenic, the emergent gradients in H_2O_2 concentration also caused spatial variation in the frequency of DNA replication errors across cells. This process can thereby diversify mutation rates among cells growing in a structured population. Indeed, our observation that H_2O_2-induced mutation rates decrease with increasing cell density matches results obtained in liquid bulk culture [207,208]. We find that individual cells can rapidly modulate their oxidative stress response according to the ROS levels in their immediate environment, which improves their chances of survival [Figure 3.11, 3.14, 3.15, 3.16]. However, this individual response can also result in the emergence of a collective behaviour whereby cells that are closest to a stressor protect those that are further away. While sudden exposure to high H_2O_2 concentrations can kill cells on the outside of a dense population, the initial H_2O_2 gradient created by these cells allows the survivors in the interior to regrow and re-establish the protective gradient. This collective response, therefore, also has temporal component by allowing a subpopulation of cells to experience a gradual increase in stress and obtain high tolerance via priming. This all suggests that there can be both an individual and group benefit to the generation of this phenotypic heterogeneity.

A limitation we encountered in our study is the difficulty to account for the effects of cell death during H_2O_2 treatment. The fluorescence intensity of a transcriptional reporter (*e.g.* P*grxA*-CFP) provides a readout for the H_2O_2 level in live cells only. Our time-lapse measurements can distinguish live and dead cells based on the growth rate. We confirmed using propidium iodide staining that mother cells which stopped growing for multiple hours during H_2O_2 treatment are indeed dead [Figure 3.16]. However, it was not possible to reliably distinguish live and dead barrier cells from the growth rate because the observation time is limited as these cells are quickly pushed out of the trenches. Hence, we were unable to characterise quantitatively how the death of barrier cells affects the H_2O_2 gradient. Other indicators for cell viability and/or reporters for the H_2O_2 level in cells could resolve this issue in future studies. Another limitation related to the use of a transcriptional CFP reporter protein is that it can only indirectly inform about response memory. Further insight could be gained by measuring the levels of the native stress response proteins using translational fluorescent fusions or biochemical quantification techniques.

Chapter 4

Chaos in a bacterial stress response

4.1 Summary

Cellular responses to environmental changes are often highly heterogeneous and exhibit seemingly random dynamics. The astonishing insight of chaos theory is that such unpredictable patterns can in principle arise without the need for any random processes i.e., purely deterministically without noise. However, while chaos is well understood in mathematics and physics, its role in cell biology remains unclear because the complexity and noisiness of biological systems make testing difficult. Here, we show that chaos explains the heterogeneous response of *Escherichia coli* cells to oxidative stress. We developed a theoretical model of the gene expression dynamics and demonstrate that chaotic behaviour arises from rapid molecular feedbacks that are coupled with cell growth dynamics and cell-cell interactions. Based on theoretical predictions, we then designed single-cell experiments to show we can shift gene expression from periodic oscillations to chaos on demand. Our work suggests that chaotic gene regulation can be employed by cell populations to generate strong and variable responses to changing environments.

4.2 Introduction

The birth of chaos theory was highly significant because it made clear that unpredictable patterns in nature can arise without stochasticity i.e. purely deterministically [209]. Many seemingly noisy systems were subject to reanalysis and reinterpreted as chaotic rather than stochastic, including examples from biology such as ecological dynamics [210–215], gene expression [216,217], immune system dynamics [218,219], neural signal dynamics [220–223], circadian rhythms [224,225] and heart beats [226]. However, the underlying causes of dynamics in biological systems are not as well understood as in the physical or chemical sciences [227,228]. As a result, the inference of chaos in biology often rests upon mathematical models alone [211,212,220,229–232], which is not sufficient to demonstrate that chaos actually occurs in the biological system itself.

Empirically, chaotic dynamics have been inferred in biological data by statistical detection tools [210,221,233,234]. However, it is challenging to distinguish chaotic from stochastic causes in this manner because the inference methods are highly sensitive to measurement noise and random fluctuations that are inherent to all biological processes [235]. This problem was recently illustrated by Toker *et al.*, who applied new analysis tools to both physical and biological systems [191]. While they found evidence for chaos in physical and simulated biological data, they concluded that measured heart rate data is stochastic, in spite of a large number of papers having previously concluded it is chaotic [226]. Chaos then has proved much more difficult to evidence in biological systems than in physical ones, leaving the importance of chaotic dynamics for biology in doubt.

In response to environmental threats, bacteria have evolved stress responses that drive rapid physiological adaptation [236]. Stress responses are intensively studied because they are central to the ways that bacteria survive environmental threats and diverse treatments, including antibiotics [2,17,237,238]. We serendipitously discovered chaotic behaviour in a theoretical model of one of the major bacterial stress responses, specifically the oxidative stress response of the model species *E. coli*. This discovery allowed us to leverage the detailed understanding and tractability of *E. coli* to overcome the typical challenges faced when studying chaos in biological systems. Under high hydrogen peroxide stress, a cell will strongly induce the expression of proteins that remove H_2O_2 both within the cell and thereby lower the concentration of H_2O_2 in its vicinity. Our works shows that this response, in combination with the responses of surrounding cells, perturbs the regular periodicity of cell growth, driving the stress response dynamics from periodic oscillations to chaotic fluctuations. By identifying the drivers of chaos, we are able to predict the conditions when it will be present and when it will be lost, and we validate these predictions empirically. In this way, we provide clear experimental evidence of chaos in a living system. Our results further suggest that chaotic gene regulation could be common in the bacterial responses to diverse types of stresses and offer functional benefits.

4.3 Quantitative model of the oxidative stress response in a bacterial population

Genetically-identical bacteria often display considerable cell-to-cell variability in their responses to the environment [239] [Figure 4.1A]. Stress responses can be particularly variable [23], and it is often assumed that this variability results from stochastic processes inside the cell. Noisy as well as oscillatory response patterns have been observed in bacteria exposed to reactive oxygen and nitrogen species[31,33,74,240]. Such behaviour could arise when the induction of detoxifying enzymes reduces the local concentration of stressor molecules[90], leading to dynamic feedbacks. Indeed, in Chapter 3, we found that cellular heterogeneity in the response of *E. coli* to oxidative stress by hydrogen peroxide is driven by cell-cell interactions rather than intracellular noise, where the response of each cell is determined by the hydrogen peroxide scavenging activity of its neighbours. This project began with the

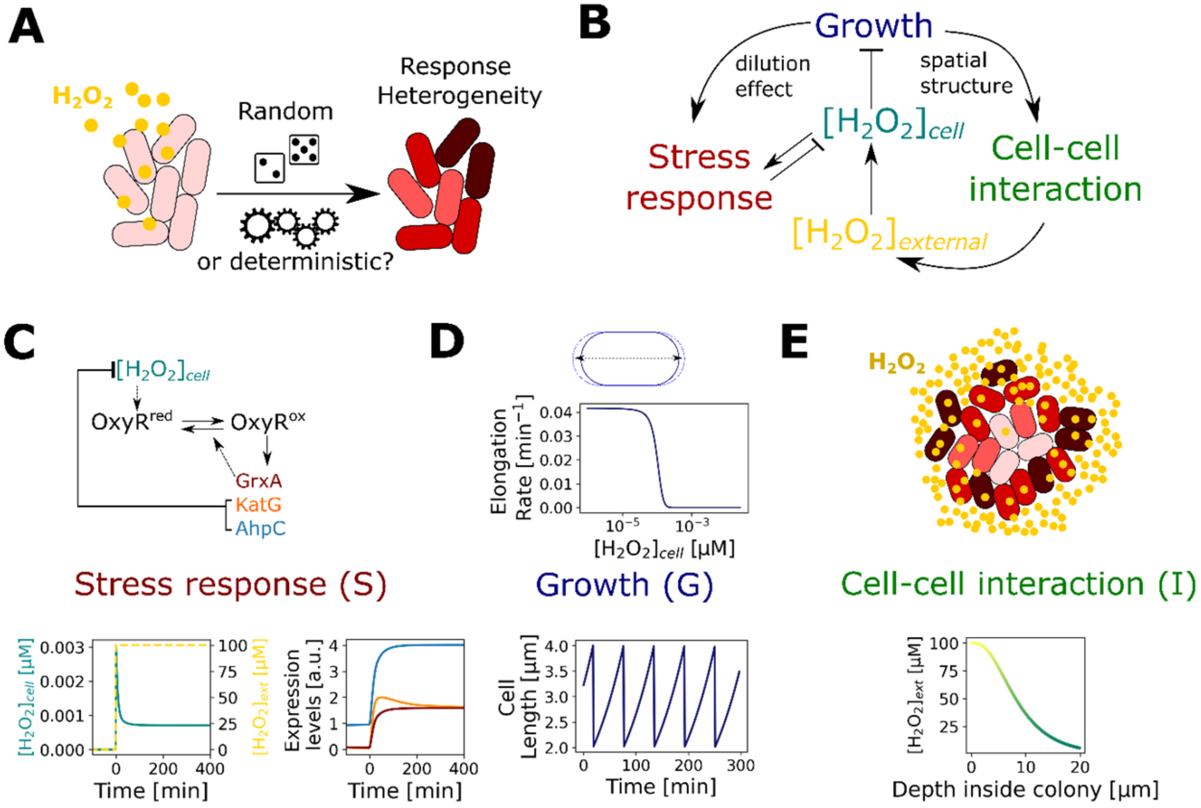

Figure 4.1 Modelling the oxidative stress response in bacterial populations:
*(**A**) Environmental stress, such as H_2O_2 exposure, induces heterogeneous responses in bacterial populations, which could be caused by stochastic or deterministic mechanisms. (**B**) H_2O_2 affects cell growth rates (G), and triggers an intracellular stress response (S) that creates stressor gradients by cell-cell interactions (I). S-G-I feedback modulates H_2O_2 concentration in space and time, both outside and inside the bacteria ($[H_2O_2]_{external}$, $[H_2O_2]_{cell}$ respectively). (**C**) Schematic of the core OxyR gene regulatory circuit corresponding to the stress response component of the model. It predicts the expression dynamics of proteins that scavenge intracellular H_2O_2 (KatG, AhpCF) and control OxyR oxidation status (GrxA). Model output illustrated for constant $[H_2O_2]_{external}$ exposure from 0 min. (**D**) The growth model describes the inhibition of cell elongation by H_2O_2. In turn, the growth dynamics feed into the stress response model by determining the dilution rate of enzymes. Top: Cell elongation rate as a function of intracellular H_2O_2. Bottom: Exponential growth and division cycles of a single cell without H_2O_2 treatment. (**E**) Cell-cell interactions are described by a reaction-diffusion model where intracellular scavenging of H_2O_2 creates a stress gradient from the edge to the interior of a cell population. Changes in the number and arrangement of cells in the population are determined by the growth model.*

goal of better understanding the impact of this response on cell-to-cell variability via a numerical model [Figure 4.1, 4.2]. The model captures three coupled processes [Figure 4.1B, 4.2]. First is the dynamics of the intracellular stress response (named S in the model). In *E. coli*, these occur when H_2O_2 oxidises the transcription factor OxyR, which induces expression of H_2O_2 scavenging enzymes AhpCF and KatG, and the glutaredoxin-1 GrxA that converts oxidised OxyR back to its reduced form[2,153] [Figure 4.1C]. Second is the inhibitory effect of H_2O_2 on the growth rate of the cells (named G in the model) [Figure 4.1D] and, finally, there is the impact of cell-cell interactions (named I in the model) [Figure 4.1E]. These cell-cell interactions arise because the uptake of H_2O_2 by one cell can lower the concentration of H_2O_2 for surrounding cells. The individual models are formulated as follows and their parameterisation is described in Chapter 2.

4.3.1 Cell growth model

The growth of rod-shaped *E. coli* cells is described by an adder model with equal length added to the cell over time between successive division events [241]. The elongation rate g determines the increase in cell length l from time t to $t+1$:

$$l_{t+1} = l_t \cdot (1 + g) \qquad \text{\{Eq 4.1\}}$$

The cell divides into 2 daughter cells of equal length when the total cell length added from the birth length exceeds 2 µm. We model the inhibition of the cell elongation rate by H_2O_2 as a sigmoidal decay:

$$g([H_2O_2]_{cell}) = g_0 \cdot \left(1 - \frac{1}{1 + 10^{-c_1([H_2O_2]_{cell} - c_2)}}\right) \qquad \text{\{Eq 4.2\}}$$

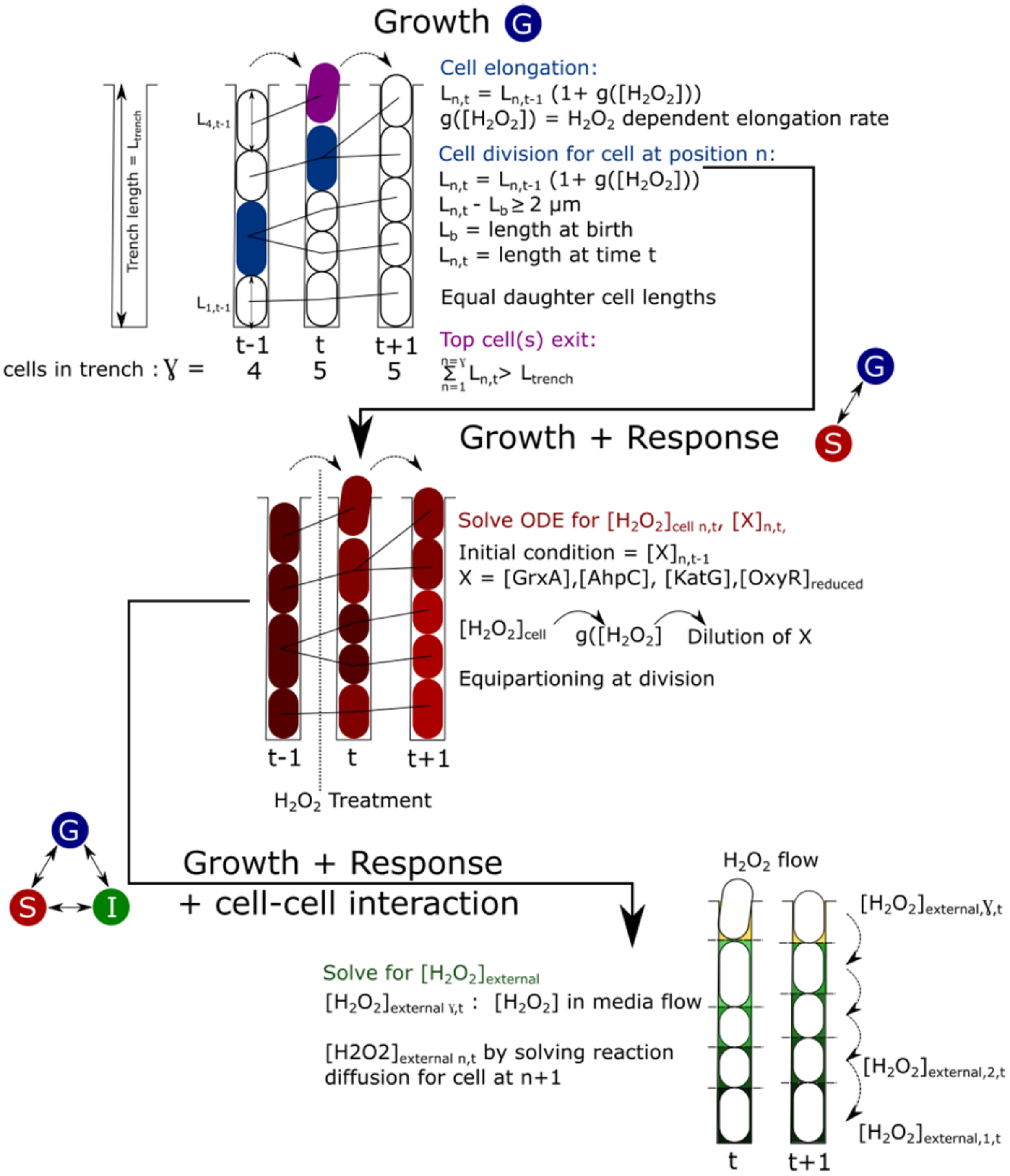

Figure 4.2 Illustration of the iterative procedure for simulating the inter-dependent growth, stress response, and cell-cell interaction models:

The growth model predicts the changes in the number, size, and positions of the cells in the 1-dimensional cell population for the next time point in the simulation. The output of the growth model *feeds into the stress response model, which predicts for each cell the changes in the intracellular concentration of* H_2O_2*, concentration of reduced regulator* $OxyR^{red}$*, and concentrations of the stress response enzymes (GrxA, KatG, AhpCF) for the next time point. The cell elongation rate from the growth model predicts the dilution rate of enzymes. At steady-state, the average enzyme production rates and* H_2O_2 *influx rate are balanced with the respective average dilution rates. Temporary unbalance between production and dilution rates leads to fluctuations in concentrations in single cells. The cell-cell interaction model predicts the external* H_2O_2 *concentration that each cell is exposed to. A reaction-diffusion equation is solved for the uptake of* H_2O_2 *by the outermost cell first which is exposed to the fixed concentration of* H_2O_2 *in the growth media. This leads to a reduced external* H_2O_2 *concentration for the cell located immediately beneath the outermost cell. The procedure is repeated to predict the external* H_2O_2 *concentration from one cell to the next until the mother cell is reached at the bottom of the population. The outputs of the interdependent models at one time point are used as input conditions for the next time point. The simulation runs for a set number of time points.*

where g_0 is the elongation rate without treatment, $[H_2O_2]_{cell}$ is the intracellular H_2O_2 concentration, and the sigmoidal decay factors $c_1,\ c_2$ determine the sensitivity of the elongation rate to $[H_2O_2]_{cell}$.

4.3.2 Cell-cell interaction model

Scavenging of H_2O_2 results in concentration gradients that are determined by the spatial arrangement of cells and the diffusion of H_2O_2 with diffusion coefficient D. Hence, $[H_2O_2]_{external}$ is a function of a cell's position x along the length of the growth trench. The spatial arrangement was modelled as a one-dimensional colony of rod-shaped cells with radius R_C in cuboid growth trenches with square cross section W^2. This is analogous to the growth trenches in a mother machine device, as described in Chapter 3, with H_2O_2 treatment entering through the open end of the trench (where $x = 0$). The scavenging rate of H_2O_2 is limited by the absorption of H_2O_2 across the cell envelope, as shown in Chapter 3, with absorption rate constant k_{abs}. We modelled the spatial profile of $[H_2O_2]_{external}$ based on the reaction-diffusion equation, using a similar approach as described in Yang *et al.* [242]:

$$\frac{\partial [H_2O_2]_{external}}{\partial t} = (W^2 - \pi R_c^2)\, D \frac{\partial^2 [H_2O_2]_{external}}{\partial x^2} - 2\pi R_c k_{abs} [H_2O_2]_{external} \qquad \{\text{Eq 4.3}\}$$

We first consider the profile of $[H_2O_2]_{external}$ along the length of a single cylinder-shaped cell of length l_t (the hemispherical caps at the cell poles will be considered below). At each position x, $(W^2 - \pi R_c^2)$ corresponds to the area around the cell where H_2O_2 diffuses through the trench. The circular perimeter of the cell where H_2O_2 is absorbed is $2\pi R_c$. At steady-state, $\frac{\partial [H_2O_2]_{external}}{\partial t} = 0$. Therefore, the reaction-diffusion equation becomes:

$$(W^2 - \pi R_c^2)\, D \frac{\partial^2 [H_2O_2]_{external}}{\partial x^2} = 2\pi R_c k_{abs} [H_2O_2]_{external} \qquad \{\text{Eq 4.4}\}$$

To solve this equation for $[H_2O_2]_{external}$, we introduce the coefficient λ:

$$\frac{\partial^2 [H_2O_2]_{external}}{\partial x^2} = \frac{1}{\lambda^2} [H_2O_2]_{external} \qquad \{\text{Eq 4.5}\}$$

with $\lambda = \sqrt{\frac{(W^2 - \pi R_c^2)\, D}{2\pi R_c k_{abs}}}$

We assume the non-adsorbing boundary condition at x = l_t.

The solution to this equation is: $[H_2O_2]_{external}(x) = [H_2O_2]_{external,0} \frac{cosh(\frac{x-l_t}{\lambda})}{cosh(\frac{l_t}{\lambda})}$ {Eq 4.6}

Here, $[H_2O_2]_{external,0}$ is the concentration at $x = 0$.

We modify the above equations to account for the shape of *E. coli* cells as cylinders capped with hemispheres. First, we multiply equation 4.4 by the cell length l_t:

$$(W^2 - \pi R_c^2) \cdot l_t \cdot D \cdot \frac{\partial^2 [H_2O_2]_{external}}{\partial x^2} = 2\pi R_c \cdot k_{abs} \cdot l_t \cdot [H_2O_2]_{external} \qquad \{\text{Eq 4.7}\}$$

Compared to the cylinder geometry, the free volume in the trench through which H_2O_2 diffuses increases by $2\pi R_c^3 - \frac{4}{3}\pi R_c^3$ due to the two hemispherical caps. The surface area for H_2O_2 absorption is unchanged. Hence:

$$\left(W^2 l_t - \pi R_c^2 l_t + \left(2\pi R_c^3 - \frac{4}{3}\pi R_c^3\right)\right) \cdot D \cdot \frac{\partial^2 [H_2O_2]_{external}}{\partial x^2} = 2\pi R_c \cdot k_{abs} \cdot l_t \cdot [H_2O_2]_{external} \qquad \{\text{Eq 4.8}\}$$

The solution to the equation is $[H_2O_2]_{external} = [H_2O_2]_{external,0} \frac{cosh(\frac{x-l_t}{\lambda\prime})}{cosh(\frac{l_t}{\lambda\prime})}$ {Eq 4.9}

Where, $\lambda' = \sqrt{\frac{\left(W^2 l_t - \pi R_c^2 l_t + (\frac{2}{3}\pi R_c^3)\right)D}{2\pi R_c k_{abs} l_t}}$

4.3.3 Oxidative stress response model

The oxidative stress response was modelled based on mass action kinetics using a set of 5 coupled ordinary differential equations (ODEs) to predict the dynamics of gene expression and intracellular H_2O_2 concentration ($[H_2O_2]_{cell}$) for a given external H_2O_2 concentration ($[H_2O_2]_{external}$). $[H_2O_2]_{cell}$ oxidises the transcription factor OxyR from its reduced to oxidised form, where K_{ox} is the 2nd-order oxidation rate constant. The total OxyR concentration was assumed constant, such that $[OxyR]_{Ox} = [OxyR]_{total} - [OxyR]_{Red}$. Oxidised OxyR is reduced by GrxA with Michaelis-Menten kinetics where K_{red} is the catalytic rate constant and h_{OxyR} is the Michaelis constant. Hence:

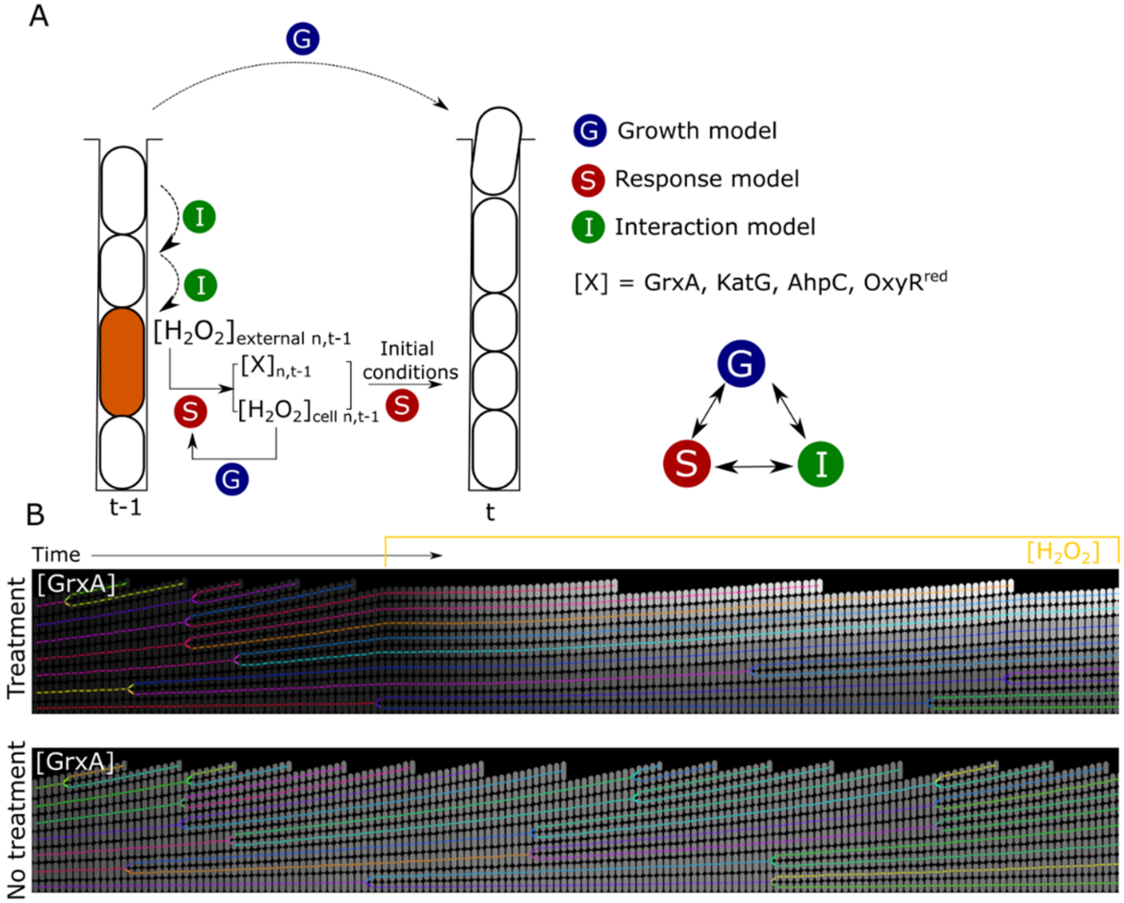

Figure 4.3 Illustration of model simulation with and without H_2O_2 treatment:
*(**A**) Schematic representation for solving the growth (G), response (S) and cell-cell interaction (I) models simultaneously for a representative focal cell shown in orange. (I) computes the $[H_2O_2]_{external}$ for the focal cell. This feeds into (S) solving for the concentrations of different enzymes [X] that are regulated by OxyR (e.g. GrxA, KatG, AhpC, $OxyR^{red}$) and $[H_2O_2]_{cell}$. $[H_2O_2]_{cell}$ is used as input for (G) to modulate the elongation rate of cell. The outputs serve as initial condition for the next time point. (**B**) Representative kymographs produced by the model for a single 1-dimensional cell population tracked over time. Greyscale shows GrxA concentration with constant 260 µM H_2O_2 treatment (top; duration of treatment marked in yellow) and without treatment (bottom).*

$$\frac{d[OxyR]_{Red}}{dt} = -K_{ox} \cdot [OxyR_{Red}] \cdot [H_2O_2]_{cell} + K_{red} \cdot [GrxA] \cdot$$

$$\left(\frac{[OxyR]_{total} - [OxyR]_{Red}}{([OxyR]_{total} - [OxyR]_{Red}) + h_{OxyR}}\right) \qquad \{Eq\ 4.10\}$$

The OxyR regulon includes numerous genes involved in various aspects of oxidative stress tolerance. We reduced this system to the two key H_2O_2 scavenging enzyme genes *katG* and *ahpC*, and the glutaredoxin-1 *grxA*. Each gene has a basal expression rate ($R_{grxA,basal}$, $R_{katG,basal}$, $R_{ahpC,basal}$) and an inducible expression rate that depends on the concentration of oxidised OxyR ($[OxyR]_{total} - [OxyR]_{Red}$). The maximal induced-expression rates are given by $K_{grxA,act}$, $K_{katG,act}$, $K_{ahpC,act}$. The parameters $h_{GrxA,act}$, $h_{katG,act}$, $h_{ahpC,act}$ define the concentrations of $[OxyR]_{Ox}$ that give half-maximal induction of each gene. Gene expression is counteracted by dilution due to cell growth with rate g, given by the growth model (Eq 4.2). The gene expression dynamics follow:

$$\frac{d[GrxA]}{dt} = R_{grxA,basal} + K_{grxA,act} \cdot \left(\frac{[OxyR]_{total} - [OxyR]_{Red}}{([OxyR]_{total} - [OxyR]_{Red}) + h_{grxA,act}}\right) - g \cdot [GrxA]$$

{Eq 4.11}

$$\frac{d[KatG]}{dt} = R_{katG,basal} + K_{katG,act} \cdot \left(\frac{[OxyR]_{total} - [OxyR]_{Red}}{([OxyR]_{total} - [OxyR]_{Red}) + h_{katG,act}}\right) - g \cdot [KatG]$$

{Eq 4.12}

$$\frac{d[AhpC]}{dt} = R_{aphC,basal} + K_{ahpC,act} \cdot \left(\frac{[OxyR]_{total} - [OxyR]_{Red}}{([OxyR]_{total} - [OxyR]_{Red}) + h_{ahpC,act}}\right) - g \cdot [AhpC]$$

{Eq 4.13}

The intracellular H_2O_2 concentration is determined by the influx of external H_2O_2 with rate $R_{influx} \cdot [H_2O_2]_{external}$, a basal endogenous production rate $R_{H_2O_2,basal}$, and scavenging by catalase and peroxidase enzymes with Michaelis-Menten kinetics where K_{AhpC}, K_{KatG} are the catalytic rate constants and h_{AhpC}, h_{KatG} are the Michaelis constants:

$$\frac{d[H_2O_2]_{cell}}{dt} = R_{influx} \cdot [H_2O_2]_{external} + R_{H_2O_2,basal} - K_{Ahpc} \cdot [\text{AhpC}] \cdot \left(\frac{[H_2O_2]_{cell}}{[H_2O_2]_{cell} + h_{AhpC}}\right) - K_{KatG} \cdot [\text{KatG}] \cdot \left(\frac{[H_2O_2]_{cell}}{[H_2O_2]_{cell} + h_{KatG}}\right) \quad \{\text{Eq } 4.14\}$$

Simulating the interlinked cell-cell interaction model (I), stress response model (S), and growth model (G) required discretisation in space and time. The simulation procedure is explained in the following section and depicted schematically in Figures 4.2 and 4.3.

4.3.4 Simulation procedure

First, the cell-cell interaction model predicts the external $[H_2O_2]_{external}$ concentration that each cell is exposed to according to its position in the growth trench. The reaction-diffusion equation (Eq. 4.9) is solved for the uptake of $[H_2O_2]_{external}$ by the outermost cell first which is exposed to the fixed concentration of $[H_2O_2]_{external}$ in the growth media. This leads to a reduced external $[H_2O_2]_{external}$ concentration for the cell located immediately beneath the outermost cell. The procedure is repeated to predict the external $[H_2O_2]_{external}$ concentration from one barrier cell to the next until the mother cell is reached at the bottom of the population.

Secondly, the stress response model predicts for each cell the changes in the intracellular $[H_2O_2]_{cell}$ concentration, concentration of reduced regulator OxyR^{red}, and concentrations of the stress response enzymes (GrxA, KatG, AhpCF) for the next time point (Eq. 4.10-4.14). It uses the external $[H_2O_2]_{external}$ concentration from the cell-cell interaction model and the cell elongation rate g (Eq. 4.2) from the growth model as inputs for each cell.

Thirdly, the growth model uses the intracellular $[H_2O_2]_{cell}$ concentration from the stress response model as input to compute the cell elongation rate g for each cell (Eq. 4.2), and changes the number, size, and positions of all the cells for the next time point (Eq. 4.1). Cell elongation and division pushes cells towards the open end of the trench. If the summed cell lengths exceed the trench length then the outermost cell is removed at the next time point.

The outputs of the interdependent models at one time point are used as input conditions for the next time point. The simulation runs for a set number of time points. Parallel growth trenches are treated as independent simulation runs. Simulations of the model were performed using custom-written Python code.

4.3.5 Simulation input

Simulation runs were initialised by specifying the user-defined parameters: number of time points T, time step duration Δt (1 min), $[H_2O_2]_{external}$, time of H_2O_2 treatment (time point 50, unless mentioned otherwise), number of growth trenches (n_g), length of growth trenches (L_{trench}), initial cell lengths at t_0. Unless otherwise specified, the initial cell lengths were drawn from a random distribution to match experimental conditions where cells are loaded into growth trenches from an unsynchronised culture. Cells are positioned in a straight row with their poles touching. The values used for simulations are mentioned in the Appendix A.7.

4.4 Chaos is predicted in a bacterial stress response

We began by solving a 1-dimensional version of the model, where cells are exposed to a

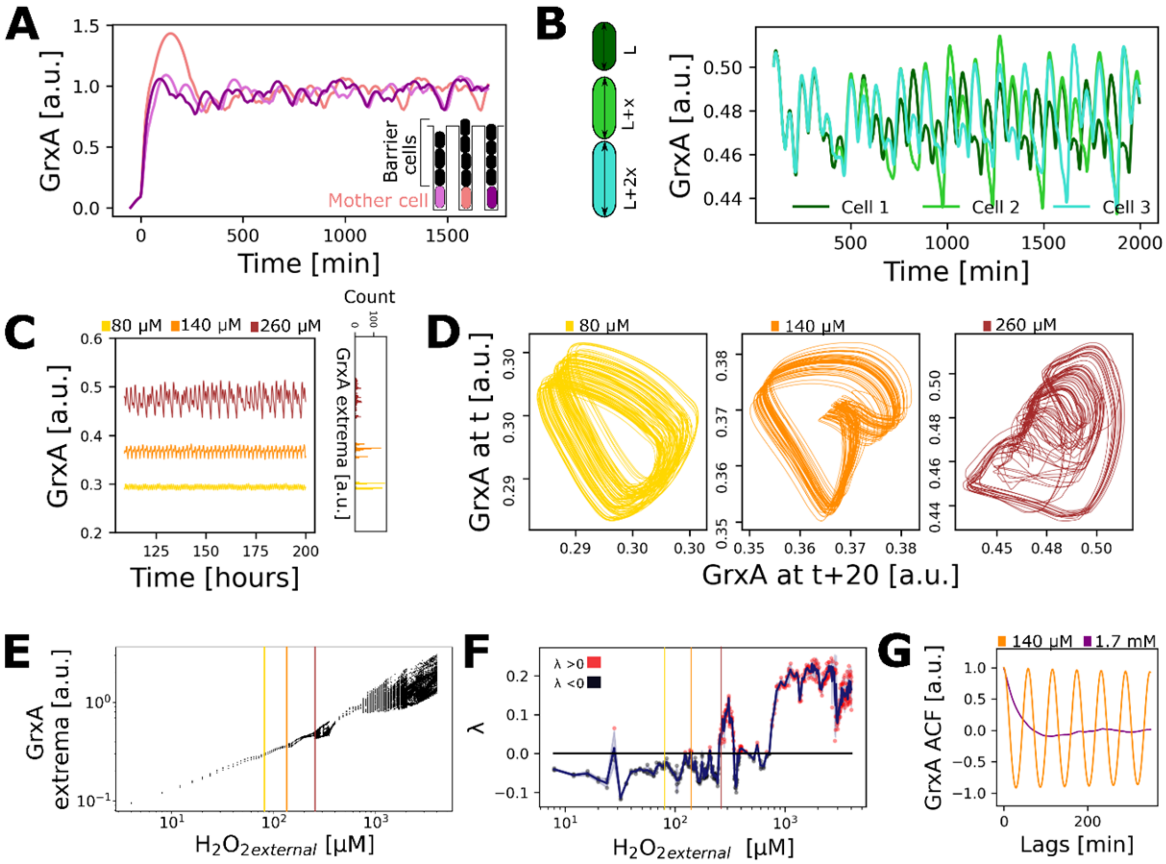

Figure 4.4 The model predicts chaos in the stress response:
*(**A**) Oxidative stress response fluctuations in individual 'mother cells' at the base of a 1-dimensional population with 'barrier cells' positioned closer to the H_2O_2 source. The model produces seemingly random dynamics of GrxA protein expression level during continuous H_2O_2 treatment from t=0 min. The curves represent three independent simulation runs starting with unsynchronised cells at random points in the cell cycles. (**B**) Stress response fluctuations diverge greatly over time even if the differences in initial conditions are very small; here shown by the GrxA dynamics for 3 mother cells that differ very slightly in their initial stage of the cell cycle ($2.5 \cdot 10^{-4}$ % and $5 \cdot 10^{-4}$ % length differences). (**C**) (left) Representative GrxA dynamics for a mother cell with continuous treatment at different H_2O_2 concentrations (80, 140, 260 μM). (right) Histogram of counts of extrema detected for 3 mother cells for different H_2O_2 concentrations. (**D**) Phase diagrams for the GrxA dynamics of the mother cells presented in panel C displaying limit cycle (80 μM) and, multistable periodic oscillations (140 μM) and chaotic fluctuations (260 μM). (**E**) Bifurcation plot of the GrxA extrema values over a range of H_2O_2 concentrations (n = 3 simulations per concentration). Vertical lines represent example traces in panels C and D. (**F**) A positive Lyapunov exponent (λ) shows chaotic divergence from initial conditions, computed for GrxA dynamics at different H_2O_2 concentrations. Individual points represent single mother cells with red dots for chaos ($\lambda > 0$) and black dots for periodicity ($\lambda \leq 0$). Blue line and shaded region show mean ± STD of n = 3 cells simulated per H_2O_2 concentration. (**G**) The*

autocorrelation function (ACF) distinguishes periodic and chaotic response fluctuations. Mean of ACF for GrxA of mother cells decreases steeply for chaotic traces under high H_2O_2 treatment (1.7 mM, purple) and shows regular peaks for periodic traces under low H_2O_2 treatment (140 µM, orange) (n = 3 simulations).

constant external H_2O_2 concentration from one direction [Figure 4.3]. This simple geometry allowed us to explore the behaviour of the system at steady-state and is highly amenable to empirical testing, via microfluidic growth trenches (called "mother machine") that are commonly used in experiments with bacteria[185]. We then followed the stress response (GrxA expression level) in so-called 'mother cells' located at the base of the cell group farthest from the source of treatment; the other cells are termed 'barrier cells' [Figure 4.4A]. Given that the model is purely deterministic, with no noise terms, we were surprised to observe seemingly random fluctuations in the stress response of individual mother cells [Figure 4.4]. Moreover, repeated runs of the model yielded highly variable stress response trajectories, which we initially found confusing because model parameters were identical throughout. The only source of variability was that each run of the model began with unsynchronised cells, i.e. at random points in the cell cycles. To explore if this was the source of the variation, we ran the model with synchronized barrier cells but shifted the initial cell cycle progression of only the mother cell by $2.5 \cdot 10^{-4}$% and $5 \cdot 10^{-4}$ %. The resulting three trajectories were initially indistinguishable but began to diverge significantly after ~6 hours post treatment with H_2O_2 [Figure 4.4B, 4.5]. Once diverged, the dynamics became completely different for the three model runs. This extreme sensitivity to small differences in initial conditions of a deterministic model suggests chaotic dynamics[191,243].

We next visualised response trajectories as phase diagrams across a range of H_2O_2 concentrations. These show the defined and closed orbits of periodic oscillations for lower

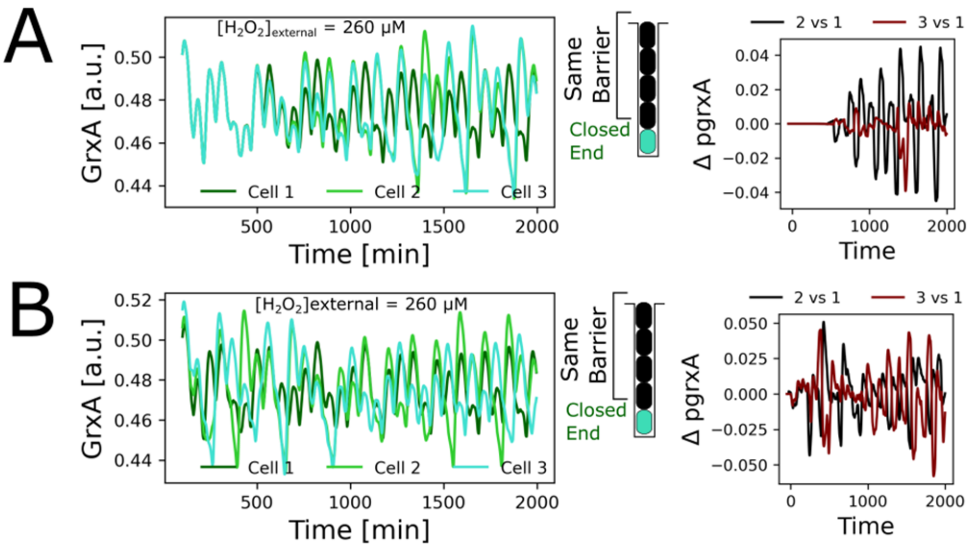

Figure 4.5 Chaotic divergence of simulated stress response trajectories with small differences in initial conditions:

*Left: Simulated trajectories of GrxA concentration in mother cells under constant 260 µM H_2O_2 treatment. The simulations were performed for mother cells that differ very slightly in their stage of the cell cycle at the start of the simulation. All other parameters and initial conditions were identical for the three simulations (including the number and sizes of the other cells in the population). (**A**) Mother cell length difference of +$2.5 \cdot 10^{-8}$ % (cell 2) and +$5 \cdot 10^{-8}$ % (cell 3). (**B**) Mother cell length difference of 2.5 % (cell 2) and 5% (cell 3). The plots on the right show the difference in GrxA concentration between mother cell pairs (cell 2 vs 1, cell 3 vs 1). The larger difference in initial conditions for panel B compared to panel A leads to a faster divergence of trajectories.*

H_2O_2 concentrations, but at higher H_2O_2, we observe the dense aperiodic orbits that are indicative of chaotic fluctuations [Figure 4.4C-D]. These fluctuations can also be seen in a bifurcation diagram, which shows the extrema values of the fluctuations for cells as a function of H_2O_2 concentration. The form of the resulting diagram is characteristic of a chaotic system that shifts from periodic to chaotic regimes as H_2O_2 concentration increases [Figure 4.4E]. To test formally for chaotic dynamics, we computed the Lyapunov exponent λ, which is positive for a chaotic system where a small perturbation in initial conditions leads to exponential divergence of the trajectories. As expected from the bifurcation diagram, cells in the model at higher H_2O_2 concentrations showed chaos ($\lambda > 0$), while lower concentrations caused predominantly periodic oscillations in responses ($\lambda < 0$) [Figure 4.4F]. Note that the frequent and abrupt transitions between periodic and chaotic behavior that we observe in our simulations are typical even for the simplest mathematical models of chaos[209]. An autocorrelation curve of the aperiodic traces also decreased quickly over time, again indicative of chaos, whereas periodic oscillations showed characteristic autocorrelation peaks [Figure 4.4G].

4.5 General stress response model

To explore the generality of our observations, we replaced the detailed model of the oxidative stress response with a simpler version for a generic stress response [Figure 4.6A]. We formulated a general model to study the emergence of chaos in the response to a generic toxin. Here, cells take up toxic molecules from their surroundings and protect themselves by producing enzymes that reduce intracellular toxin concentrations [Figure 4.6B-C]. The purpose of this model was to abstract as many of the molecular details as possible and explore if a simple gene regulatory circuit is still capable of producing chaotic dynamics when coupled with the growth model and the cell-cell interaction model described above.

In this stress response model, the intracellular toxin concentration $[Toxin]_{cell}$ is determined by the influx of external toxin with rate constant R_{influx}, and detoxification by an enzyme E where K_{cat} is the catalytic rate constant and h_E is the Michaelis constant:

$$\frac{d[Toxin]_{cell}}{dt} = R_{influx}[Toxin]_{external} - K_{cat}[\mathrm{E}]\left(\frac{[Toxin]_{cell}}{[Toxin]_{cell} + h_E}\right) \qquad \{\text{Eq 4.15}\}$$

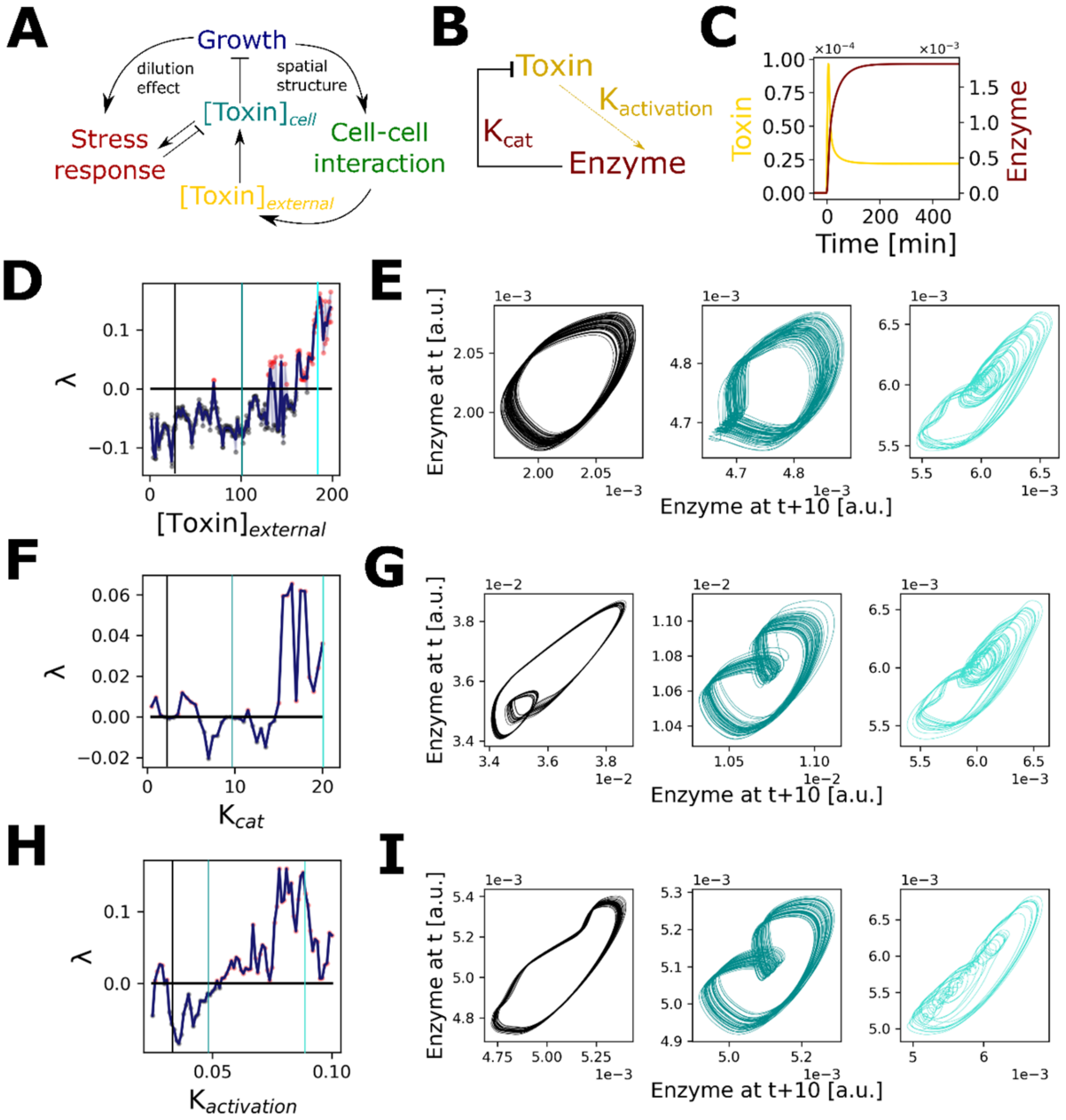

Figure 4.6 Chaos emerges in a general model of stress responses in cell populations:

*(**A**) Uptake of toxins reduces cell growth rates (G) and triggers an intracellular stress response (S) that creates toxin gradients by cell-cell interactions (I). S-G-I feedback modulates toxin concentration in space and time, both outside and inside the bacteria ([Toxin]$_{external}$, [Toxin]$_{cell}$ respectively). (**B**) Schematic of a generic stress response in which exposure to a toxin induces the expression of a detoxifying enzyme with rate $K_{activation}$ that removes toxin with rate K_{cat}. (**C**) Model output illustrates the expression dynamics of the enzyme (maroon) and the intracellular toxin concentration (yellow) for constant external toxin exposure from t=0 min without S-G-I feedback. (**D**) A positive Lyapunov exponent (λ) shows chaotic divergence from initial conditions, computed for enzyme expression*

dynamics over a range of toxin concentrations (n = 3 simulations per toxin concentration). Higher external toxin concentrations lead to chaos. ***(E)*** *Phase diagrams for the enzyme expression dynamics of a mother cell at toxin concentrations marked by vertical lines in panel D, displaying periodic oscillations and chaotic fluctuations.* ***(F)*** *Higher K_{cat} of the enzyme increases chaotic behaviour. Lyapunov exponent for enzyme expression dynamics over a range of K_{cat} values.* ***(G)*** *Phase diagrams for the enzyme expression dynamics of a mother cell at K_{cat} values marked in panel F, displaying periodic oscillations and chaotic fluctuations.* ***(H)*** *Higher expression rate $K_{activation}$ of the enzyme increases chaotic behaviour. Lyapunov exponent for enzyme expression dynamics over a range of $K_{activation}$ values.* ***(I)*** *Phase diagrams for the enzyme expression dynamics of a mother cell at $K_{activation}$ values marked in panel H, displaying periodic oscillations and chaotic fluctuations.*

The detoxifying enzyme is produced at an inducible expression rate that depends on the intracellular toxin concentration. The maximal induced-expression rate is K_{act} and h_{act} defines the toxin concentration that gives half-maximal gene induction. Enzyme expression is counteracted by dilution due to cell growth with rate g, given by the growth model (Eq 4.2).

$$\frac{d[E]}{dt} = K_{act}\left(\frac{[Toxin]_{cell}}{[Toxin]_{cell} + h_{act}}\right) - g[E] \qquad \{\text{Eq 4.16}\}$$

As for oxidative stress response model, the cell elongation rate depends on the intracellular toxin concentration:

$$g([Toxin]_{cell}) = g_0 \cdot (1 - \frac{1}{1 + 10^{c_1([Toxin]_{cell} - c_2)}}) \qquad \{\text{Eq 4.17}\}$$

Similar to the oxidative stress model, we observe that an increased toxin concentration leads to chaotic enzyme expression dynamics [Figure 4.6D-E]. Furthermore, the system becomes more prone to chaotic behaviour as the catalytic efficiency of the enzyme or its expression rate increase [Figure 4.6F-I].

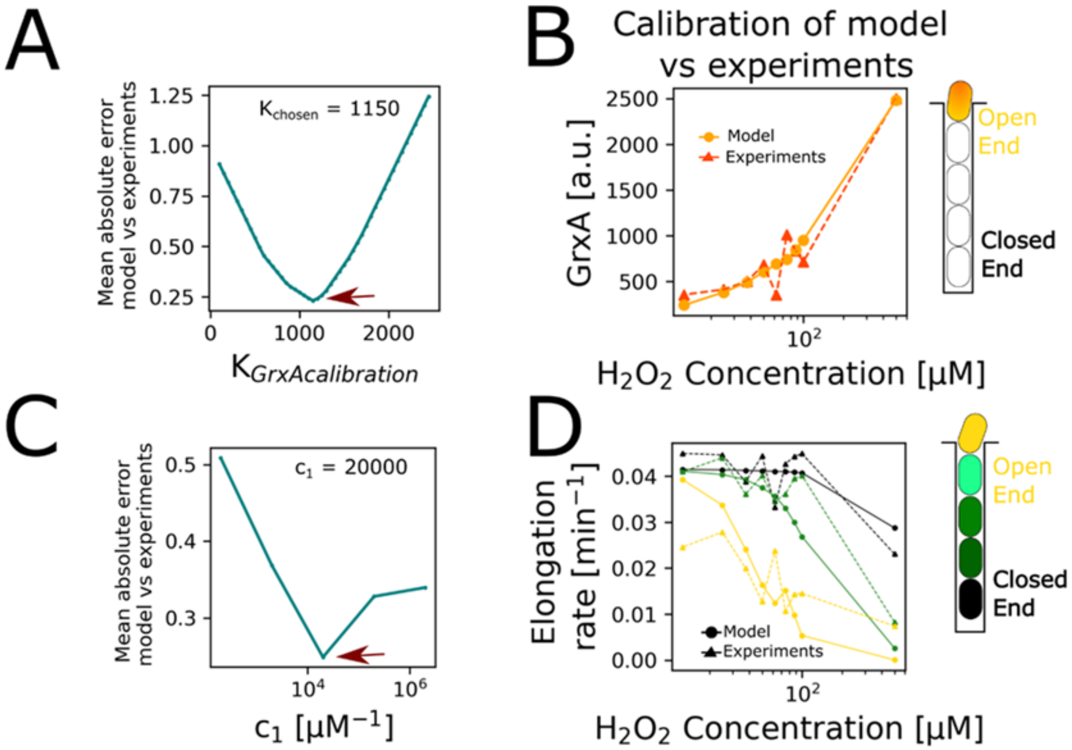

Figure 4.7 Calibrating experimental versus modeling parameters:
*(**A**) Mean absolute error for experimental PgrxA-SCFP3 intensities versus GrxA concentration in model simulations for different values of calibration factor* $\boldsymbol{k_{GrxA,calibration}}$*. The arrow indicates the minimum point of the curve that was chosen as the parameter for all other simulations. (**B**) Experimental mean PgrxA-SCFP3 (dashed dark orange; triangles) and calibrated GrxA values from the model (orange; circles) of cells at the open end of the trenches at steady-state for different* H_2O_2 *concentrations. (**C**) Mean absolute error of the cell elongation rate from experimental data versus model simulations for different values of calibration factor* $\boldsymbol{c_1}$*. The arrow indicates the minimum point of the curve that was used for parameter* $\boldsymbol{c_1}$*. (**D**) Mean cell elongation rates from model simulations (circles) and experiments (dashed; triangles) for cells at different positions in the trench over a range of* H_2O_2 *concentrations (yellow to black color represents cells from open to closed end of a growth trench).*

4.6 Observational data also suggest chaos

We next performed experiments on *E. coli* populations growing in mother machine chips under constant H_2O_2 treatment, where the stress response level is measured with a transcriptional P*grxA*-SCFP3 gene expression reporter and time-lapse fluorescence microscopy.

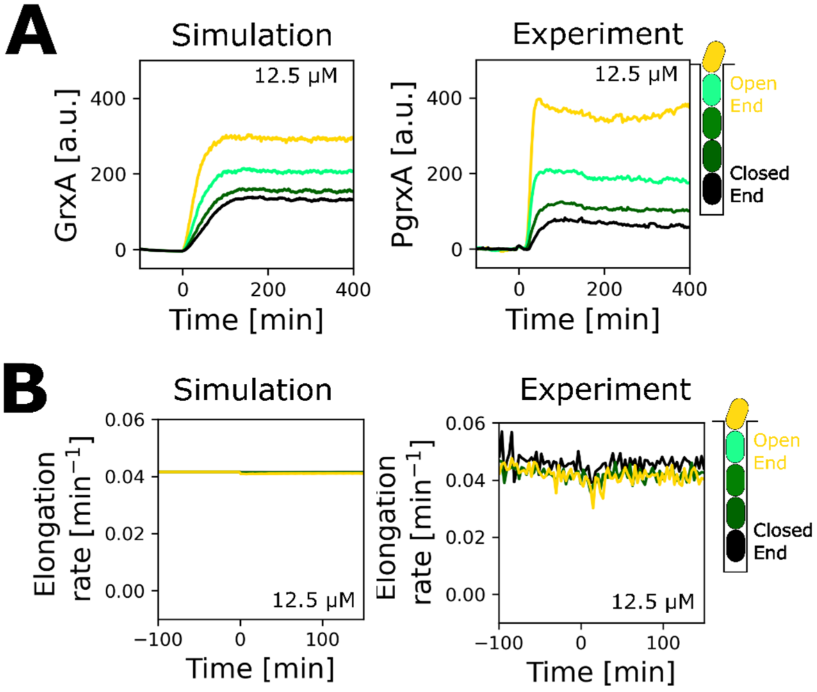

Figure 4.8 Cellular dynamics in model and experiments under low doses of H_2O_2:
*Modelling predictions (left) and experimental data (right) for (**A**) mean GrxA expression and (**B**) mean elongation rates under constant 12.5 μM H_2O_2 treatment in M9 glucose from t=0 min for cells at different positions in growth trench (n = 20 simulated trenches and 3 experimental repeats).*

We first tested the ability of the model to predict the general characteristics of the stress response. Adjusting model parameters to the measurement conditions [Figure 4.7] demonstrated an excellent quantitative agreement between our theory and the experiments [Figure 4.8, 4.9A-C]. Both showed similar spatio-temporal response dynamics and the same gradient in stress response level along the row of cells [Figure 4.9A]. There is discrepancy noted during the transient phase of the initial response to higher H_2O_2 concentrations [Figure 4.9B-C]. This arises because some cells die when confronted with sudden treatment, as outlined in Chapter 3. Following this, surviving cells recover growth and death rates drop to a low level after the adaptation delay. The model does not account for the impact of cell

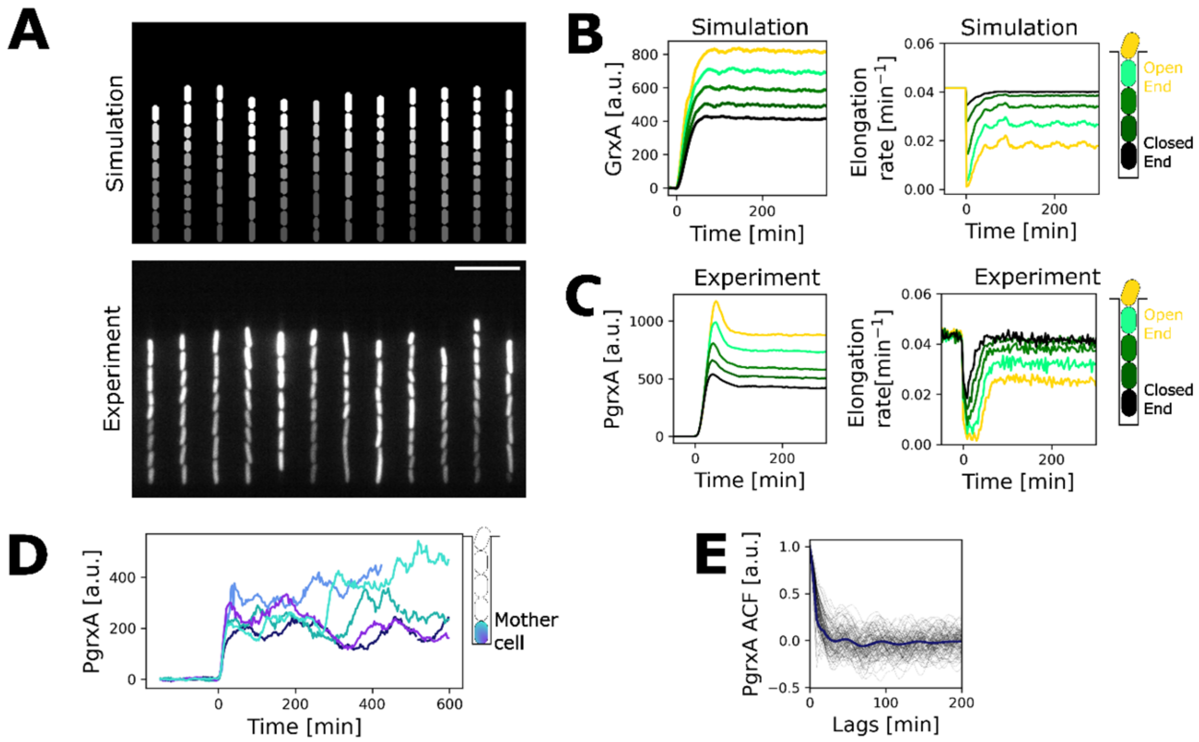

Figure 4.9 Experiments on the oxidative stress response in E. coli reveal a good fit with the modelling predictions:

*(**A**) Top: Model simulation snapshot of GrxA expression after 90 minutes of 100 µM H_2O_2 treatment. Bottom: Snapshot of experiment with E. coli cells growing in a 'mother machine' expressing PgrxA-SCFP3 after 90 minutes of 100 µM H_2O_2 treatment. Scale bar: 10 µm. (**B, C**) Model simulation predictions and experimental data for mean GrxA expression (left) and mean cell elongation rates (right) under constant 100 µM H_2O_2 treatment from t=0 min for cells at different positions in growth trench (n = 100 simulated trenches and 3 experimental repeats). (**D**) PgrxA-SCFP3 dynamics of individual cells diverge greatly over time under constant 100 µM H_2O_2 treatment from t=0 min in experiments (5 representative mother cells shown). (**E**) The steep decay of the autocorrelation function (ACF) of the response fluctuations is consistent with chaos. Mean of ACF for PgrxA-SCFP3 of mother cells with 100 µM H_2O_2 treatment (blue, 3 experimental repeats). ACF for individual cell traces shown in black (n = 100).*

death, resulting in disparities during the transient phase. Indeed, cell death is negligible for lower treatment concentration, such as 12.5 µM H_2O_2, thereby reducing the disparities between experimental observations and model predictions during the transient phase [Figure

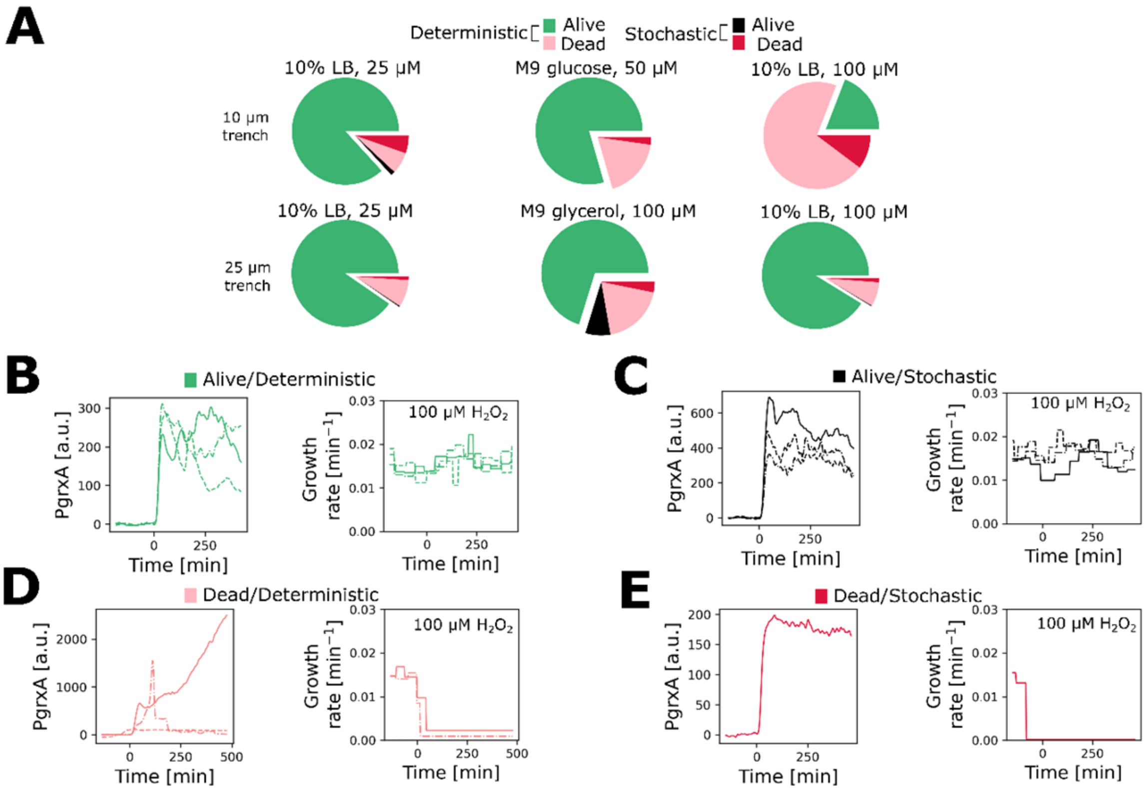

Figure 4.10 Mother cells display deterministic stress response dynamics under a wide range of H_2O_2 treatment and growth conditions in experiments:
*(**A**) Pie-charts indicate the fraction of dead (pink / red) and alive (green / black) mother cells classified as having deterministic (green / pink) or stochastic (black / red) stress response dynamics (based on PgrxA-SCFP3 signal) for t > 60 min after start of H_2O_2 treatment according to the chaos decision tree algorithm by Toker et al. Cells were grown in different media (M9 glucose + 10% LB, M9 glucose, M9 glycerol) inside long (25 µm) or short (10 µm) growth trenches, treated with low (25 µM) or high (100 µM) H_2O_2 (on average 1249 ± 457 cells (std) with n ≥ 3 experimental repeats per pie-chart). (**B-E**) Representative traces of PgrxA-SCFP3 (left) and growth rate (right) for mother cells in 25 µm growth trenches treated with 100 µM H_2O_2 at t = 0 min predicted as (**B**) alive and deterministic (green); (**C**) alive and stochastic (black); (**D**) dead and deterministic (pink); and (**E**) dead and stochastic (red). For traces predicted as dead, the time of cell death is when growth rate drops abruptly to zero.*

4.8]. Moreover, the model and experimental outcomes are fully consistent for the long-term dynamics at steady-state. All analyses of simulated and experimental data are conducted on response fluctuations at steady-state. Experiments also matched the theoretical prediction that sudden H_2O_2 treatment triggers an induction of stress response which coincides with a transient dip in the cell elongation rate followed by adaptation [Figure 4.8, 4.9B-C]. Importantly, like the model, the mother cells in experiments displayed large fluctuations in stress response level during constant H_2O_2 treatment [Figure 4.9D]. The autocorrelation curves from these traces decreased quickly over time indicating a lack of periodicity in the dynamics, consistent with chaotic behaviour [Figure 4.9E]. We further applied the 'Chaos decision tree algorithm' of Toker *et al.* [191], which is an analysis pipeline that uses the permutation entropy to categorise dynamics as stochastic or deterministic. The pipeline classified 92% of the measured stress response trajectories as deterministic [Figure 4.10, 4.11A-B], supporting the prediction of the model that the fluctuations are predominantly a consequence of deterministic chaos and not caused by noise. Most of the 8% of trajectories that were categorised as stochastic corresponded to cells that had died at the onset of H_2O_2 treatment [Figure 4.10, 4.11A-B]. Active growth dynamics are hence required for chaotic response behaviour.

As another test to distinguish deterministic chaos from noise, we applied the Grassberger - Procaccia algorithm[193]. This algorithm identifies the correlation dimension (or fractal dimension), which should be low when the response fluctuations are driven by a deterministic process with a small number of effective variables, but tends to infinity for a truly stochastic process[194]. We found a finite correlation dimension of ~2 for the GrxA dynamics in experiments and simulations, indicating determinism in the system [Figure 4.11C]. The analysis, therefore, is consistent with our model prediction that deterministic response fluctuations are generated by a simple cyclic cell growth pattern that generates oscillations

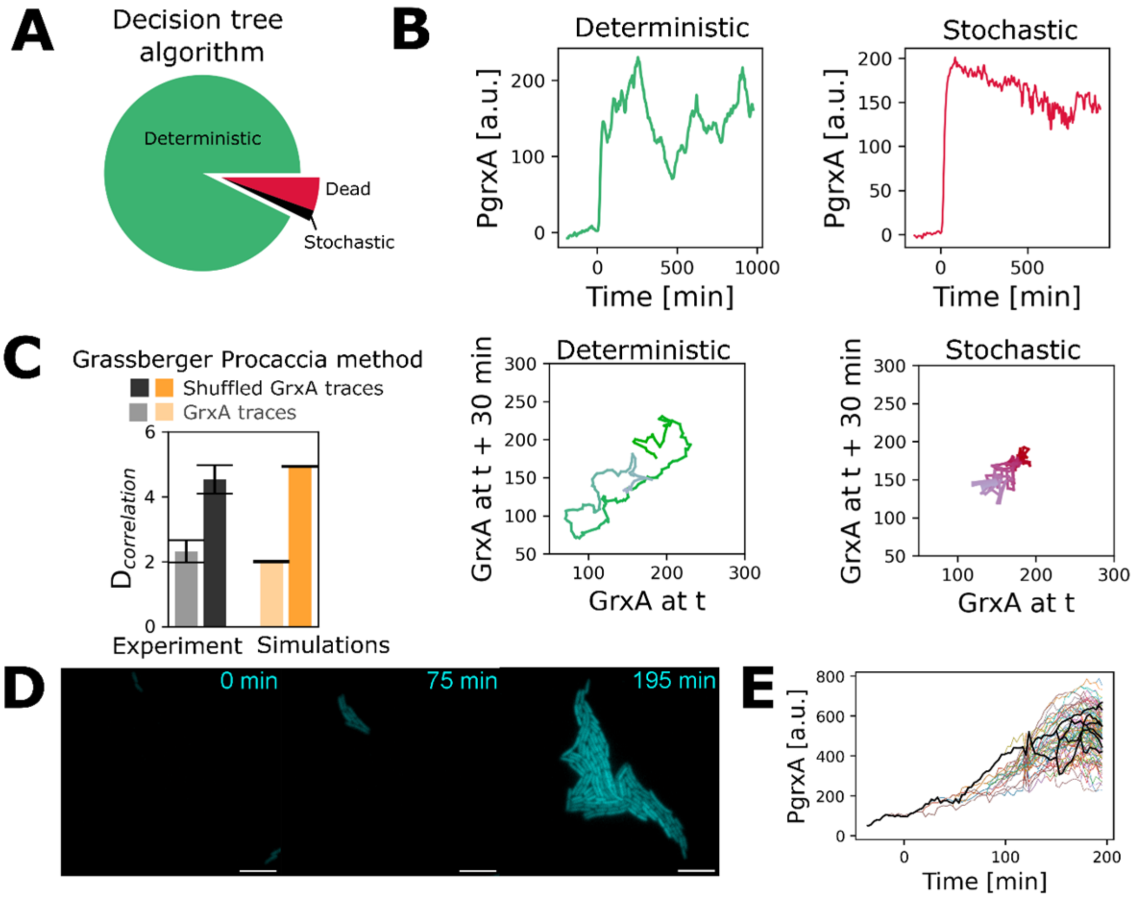

Figure 4.11 Measurements of stress response dynamics in E. coli are consistent with chaos: *(**A**) Decision tree algorithm by Toker et al.*[191] *suggests that most mother cells in experiments display deterministic and chaotic response dynamics under 100 µM H_2O_2. Pie-chart indicates the fraction of dead (red) and alive (green / black) mother cells detected as having stochastic (black / red) or deterministic (green) dynamics under 100 µM H_2O_2 (n = 3581 cells, 3 experimental repeats). (**B**) PgrxA traces (top) and their phase diagrams (bottom) for representative mother cell traces treated with 100 µM H_2O_2 treatment from t=0 min, which are classified as deterministic (green) or stochastic (red). (**C**) Bar plots show mean and standard deviation of maximal correlation dimension for experimental (black) and model (orange) GrxA traces of mother cell with (dark) or without shuffling (light) under 100 µM H_2O_2 treatment as computed by the Grassberger-Procaccia method. Random shuffling was performed as a control to remove temporal relation between data points. The low correlation dimension is consistent with determinism in experiments and simulations. (**D**) Stress response dynamics of cells growing in a colony are consistent with chaos. Snapshots of PgrxA-SCFP3 expression with 1 mM H_2O_2 treatment from t = 0 min show cell-cell variability (scale bar = 10 µm). (**E**) Single-cell trajectories from the colony experiment in panel D are consistent with chaotic divergence of stress response dynamics.*

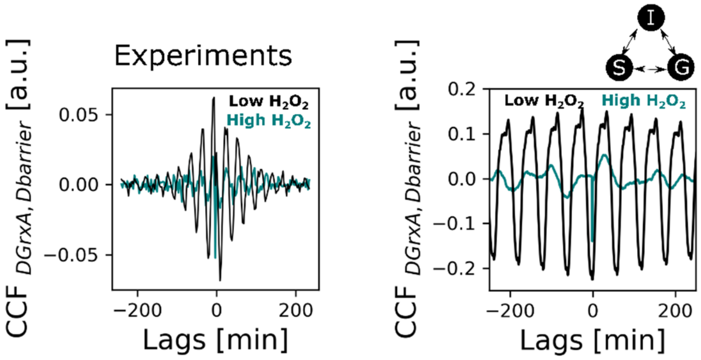

Figure 4.12 Stress response is negatively correlated with changes in number of barrier cells: *Response fluctuations are generated by a simple cyclic cell growth pattern that generates oscillations in the number of barrier cells. Fluctuations in GrxA traces for mother cells are anti-correlated with changes in the number of barrier cells over time. Mean cross-correlation between changes in GrxA (DgrxA) and number of barrier cells (Dbarrier) for mother cells in experiment (left) and model (right) for periodic (black, low* H_2O_2*) and chaotic (teal, high* H_2O_2*) conditions.*

in the number of barrier cells. Indeed, GrxA dynamics were negatively correlated with changes in the number of barrier cells in experiments, consistent with the expectation that an increase in the number of barrier cells reduces the local H_2O_2 concentration and thus the stress response level [Figure 4.12]. The use of the mother machine allowed us to follow cell trajectories over long periods, which is important for our ability to test the model's predictions. However, the 1D structure introduced by the mother machine is also potentially unrepresentative of the way that bacteria normally grow and respond to stresses. To study cells in a more realistic setting, we imaged 2D microcolonies with continuous H_2O_2 treatment [Figure 4.11D, 4.13A-B]. Although these experiments cannot monitor cells over long time, we again observed substantial heterogeneity in responses between individual cells, both within and across microcolonies, which is consistent with chaotic behaviour [Figure 4.11E, 4.13C-D]. Moreover, as the colony grows and expands, the stress response eventually decreases and becomes more uniform [Figure 4.13E]. This behaviour is predicted by the model: scavenging reduces the H_2O_2 concentration in a larger colony and, with this, the potential for chaotic responses is predicted to decrease [Figure 4.13F].

4.7 Experimental tests make or break chaos

Our model predicts the existence of chaotic behaviour in a biological system - the oxidative stress response of *E. coli* – and our observational data are consistent with chaos. Together, these two approaches lend support for chaotic behaviour and they reflect the typical standard of evidence in biological systems, where modelling predicts chaos and/or observation of seemingly chaotic dynamics are reported. However, there are problems with such evidence. Most obviously, a modelling prediction is just that; it does not demonstrate that chaos actually occurs in a biological system. Secondly, tests for chaos from observational data are challenging when the underlying causes of the dynamics are uncertain.

We, therefore, sought to leverage the tractability of our study system to provide strong evidence of chaos in a biological system via targeted perturbation. In particular, if the dynamics are indeed deterministic, then it should be possible to shift the responses away from the chaotic regime into the parameter space where periodic oscillations occur, whereas this should not be possible for stochastic fluctuations (*e.g.* caused by gene expression noise). To evaluate this prediction, we returned to our model to identify changes that remove the chaos from the dynamics and shift them to periodic oscillations. This analysis revealed that feedback between each of the three components of the model – cell growth (G), cell interactions (I) and stress response (S) [Figure 4.1B] - is required for the emergence of

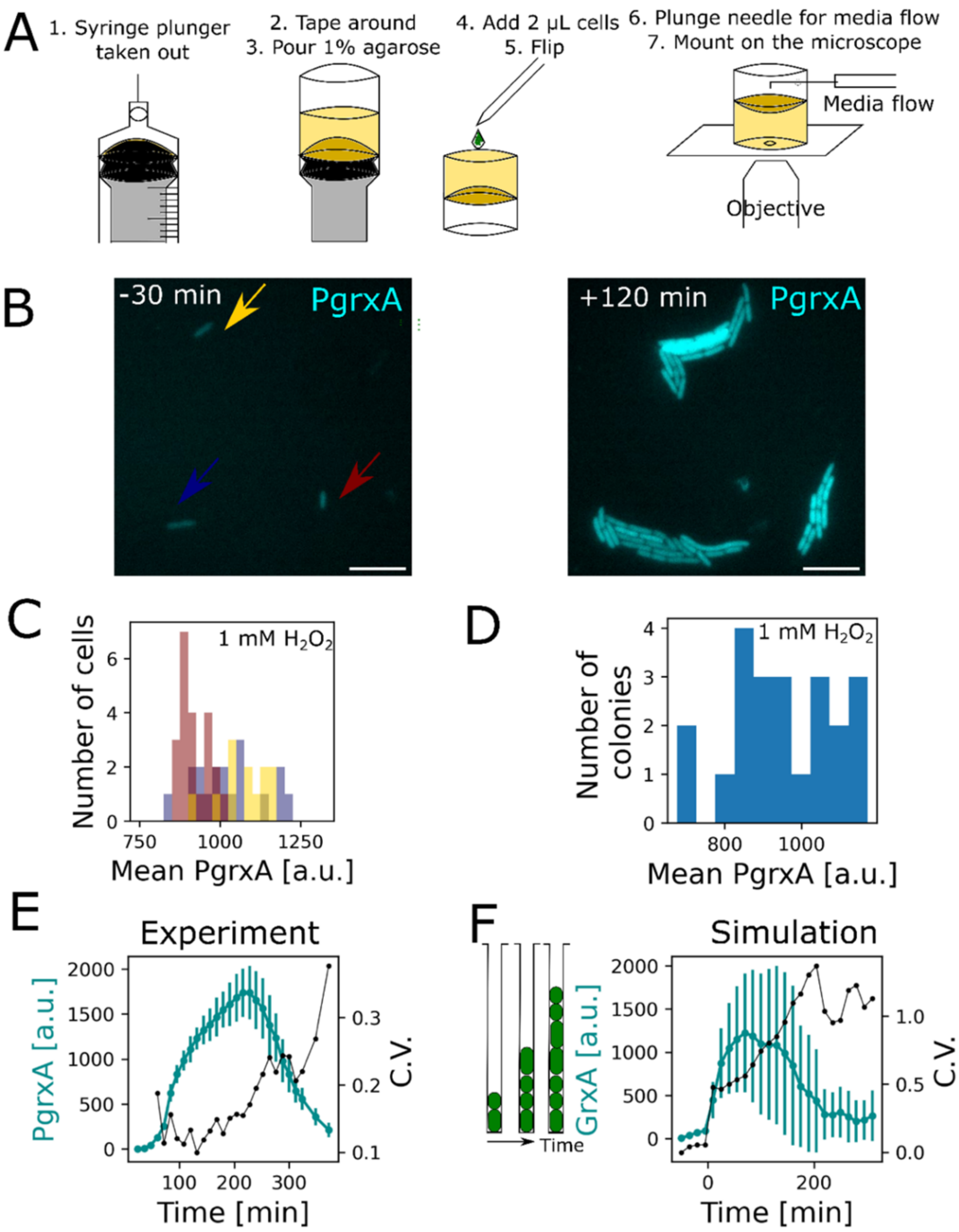

Figure 4.13 Bacterial colonies in experiments exhibit oxidative stress response fluctuations consistent with chaos:

*(**A**) Schematic describing the preparation of agarose pads for imaging bacterial microcolonies under continuous H_2O_2 infusion. (**B**) Snapshots of PgrxA-SCFP3 expression of microcolonies growing from 3 single cells under 1 mM H_2O_2 treatment (left; 30 mins before treatment, right; 120 mins after treatment). (**C**) Histograms of PgrxA-SCFP3 intensities of individual cells show heterogeneous*

*responses at 120 minutes after start of 1 mM H_2O_2 treatment (colours corresponding to microcolonies arising from cells marked with arrows in panel B, n=54 cells). (**D**) Histograms of mean PgrxA-SCFP3 intensities for entire colonies at 120 minutes after start of 1 mM H_2O_2 treatment showing variability in responses between different colonies (n = 22 colonies with 16 ± 12 cells per colony). (**E, F**) Oxidative stress response dynamics and cell-to-cell heterogeneity of microcolonies in experiments match model predictions. The GrxA expression (cyan lines, mean ± standard deviation across cells) initially increases upon constant 1 mM H_2O_2 treatment from t = 0 min but the average response of the whole population decreases again when a growing number of cells in the interior of the population becomes protected by the H_2O_2 scavenging activity of the cells at the edge of the colony. This divergence of the population causes an increase over time in the coefficient of variation (C.V., black lines) of GrxA expression across cells in the colony. (**E**) Experimental results for PgrxA-SCFP3 expression of all cells tracked in a microcolony over time (increasing from n = 2 to 737 cells over time). (**F**) Simulation of a one-dimensional population growing in a very long trench (100 µm) matches experimental results shown in panel E for microcolonies (n = 3 simulations).*

chaotic dynamics [Figure 4.14, 4.15]. Specifically, S is always required as it is the core of the stress response. Without the cell-cell interaction component of the model, no fluctuations were observed for the GrxA traces [Figure 4.14A]. When the cell growth component was uncoupled from the model, i.e. the growth rate was unaffected by the H_2O_2 treatment, then the response oscillations were no longer chaotic but periodic [Figure 4.15A].

From here, we identified parameter changes for each component of the model that are predicted to shift stress response dynamics from chaotic to periodic. These changes were as follows: i) reduce cell growth rate to slow down the oscillations in the number of cells per trench (G) [Figure 4.16A, 4.15], ii) reduce cell numbers to lower the effects of cell-cell interaction (I) [Figure 4.16B, 4.14], iii) reduce the stress response (S)[Figure 4.4, 4.16C]. For each case, we then devised a way to make this manipulation experimentally [Figure 4.16A-C, 4.17]: i) growth rates were reduced by switching to a less favoured carbon source for E. coli (from glucose to glycerol) [Figure 4.16A] ii) the protective effect of cell-cell interactions was reduced by manufacturing a modified mother machine with fewer cells in each growth channel [Figure 4.16B]; iii) the strength of the stress response was reduced by lowering the

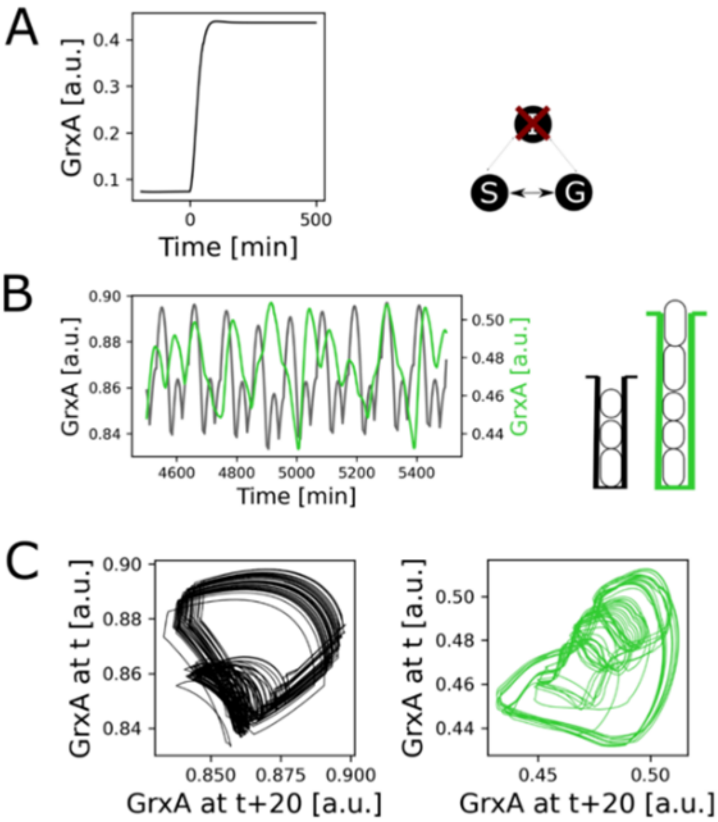

Figure 4.14 Chaotic dynamics require strong coupling between cell-cell interactions and stress response:
*(**A**) Response fluctuations are no longer chaotic if simulations are performed such that cell-cell interactions are absent. In this case, the concentration* $[H_2O_2]_{external}$ *is constant and identical for all cells in a trench. Plot shows steady GrxA expression for mother cell with 10 µM* H_2O_2 *treatment starting at t = 0 min. (**B**) Representative simulated GrxA traces of mother cells from the full S+G+I model (with cell-cell interactions causing* $[H_2O_2]_{external}$ *gradients). Periodic dynamics are seen for cells growing in a shorter growth trench with smaller population (15 µm, 2 – 4 cells, black) and chaotic dynamics for cells growing in a longer trench with larger population (25 µm, 5 – 7 cells, light green).(**C**) Phase diagrams of the GrxA traces in panel B showing closed orbits for periodic oscillations (left) but not for chaotic fluctuations (right).*

concentration of H_2O_2 [Figure 4.16C]. In each case, we followed the dynamics of the stress response in mother cells as before, and used autocorrelation analysis to test for chaos. If the dynamics are periodic, one will see a characteristic autocorrelation, which peaks at the frequency of the periodicity in the data. If the dynamics are chaotic, by contrast, no such peak

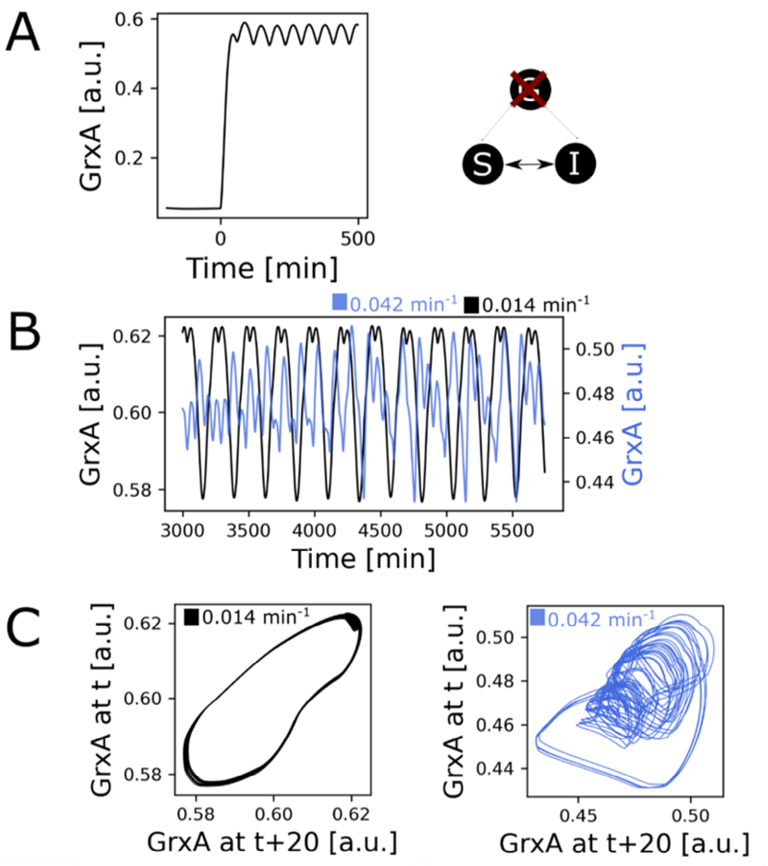

Figure 4.15 Chaotic dynamics require strong coupling between growth rate and stress response: *(**A**) Response fluctuations are no longer chaotic if simulations are performed such that growth rate is unaffected by H_2O_2 (g([H_2O_2]) is constant). This change uncouples the G model from the S and I models. Plot shows periodic oscillations in GrxA expression for mother cell with 400 µM H_2O_2 treatment starting at t = 0 min. (**B**) Representative simulated GrxA traces of mother cells from the full S-G-I model (with growth rate dependent on H_2O_2). Periodic dynamics are seen at low growth rate (0.014 min^{-1}, black) and chaotic dynamics at high growth rate (0.042 min^{-1}, light blue). (**C**) Phase diagrams of the GrxA traces in panel B showing closed orbits for periodic oscillations (left) but not for chaotic fluctuations (right).*

in the autocorrelation is seen. However, if the fluctuations are stochastic, then we should not observe autocorrelation peaks under any condition. As expected, applying this test revealed no peak in the autocorrelation function for experimental conditions that yield chaos [cyan traces in Figure 4.16A-C, 4.18A, C, E]. By contrast, in all three cases designed to remove chaos, we observe peaks in the autocorrelation function [black traces in Figure 4.16A-C, 4.18B, D, F]. In summary, we were able to identify three conditions that break the chaos in the model. We then demonstrate that making these manipulations in experiments also shifts cell responses away from chaotic to periodic oscillations.

4.8 A simple deterministic process explains chaotic oxidative stress response fluctuations

The above analyses all strongly support a deterministic origin to the response dynamics. However, this does not imply the responses are entirely devoid of any noise. The number of OxyR molecules and H_2O_2 scavenging enzymes per cell is expected to fluctuate randomly due to gene expression noise[244]. Might these fluctuations still be important for the response dynamics when combined with the deterministic causes? To investigate this, we added gene expression noise to our model by introducing a stochastic term in each molecular component of the stress response model (S*) and coupled it with the cell growth or cell interaction model components as before [Figure 4.19].

The stress response model was modified using the Langevin approach [245–247] to account for stochasticity in gene regulation. This approach involves adding a stochastic noise term to the set of differential equations (Eq 4.10-4.14). Specifically, for the deterministic differential equation of the form:

$$\frac{dX}{dt} = f(X) \qquad \{\text{Eq } 4.18\}$$

where $X = [OxyR]_{Red},\ [GrxA], [KatG], [AhpC]$,

we add a noise term η,

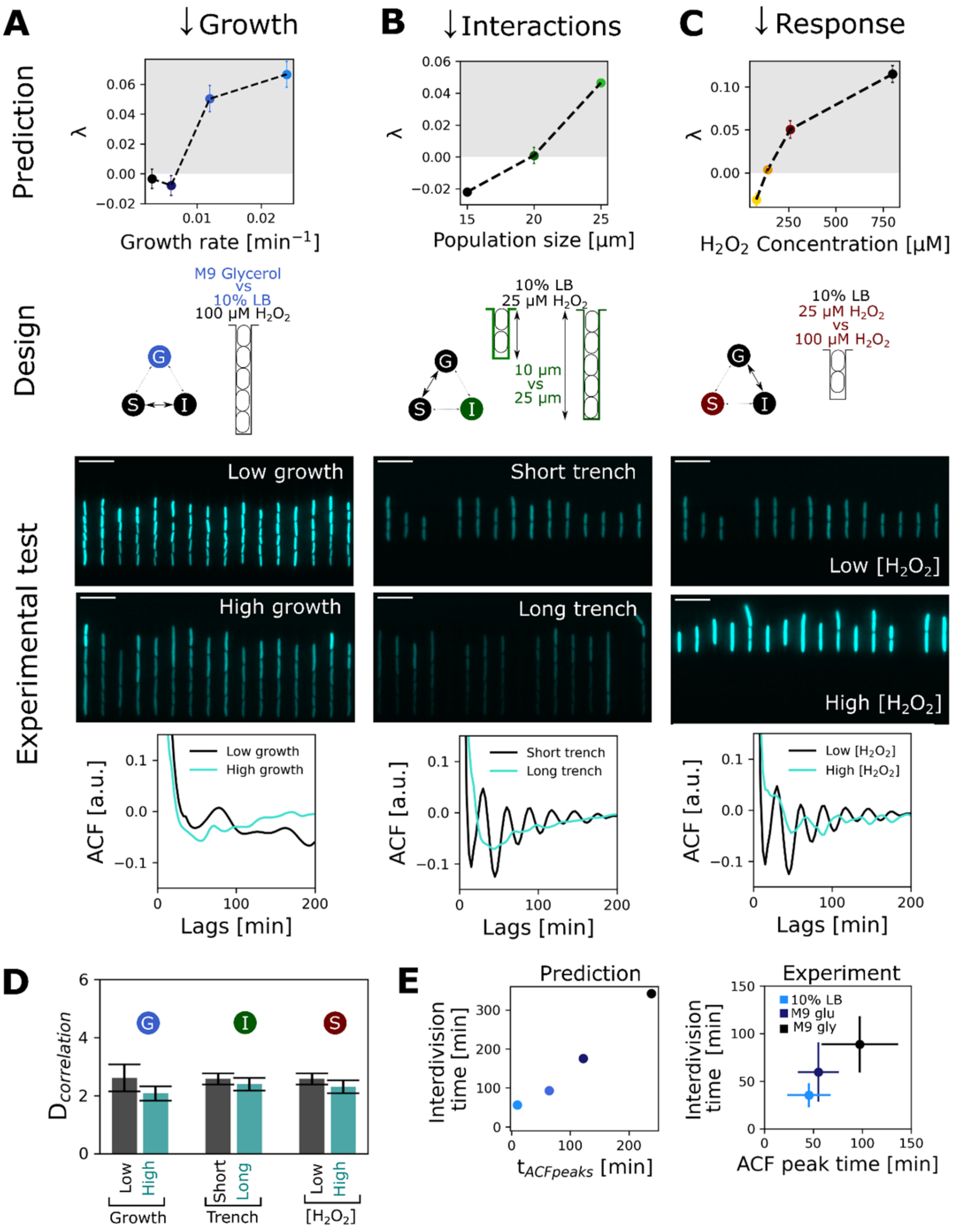
A
↓Growth
B
↓Interactions
C
↓Response
Prediction
λ
Growth rate [min^{-1}]
Population size [µm]
H_2O_2 Concentration [µM]
Design
M9 Glycerol
vs
10% LB
100 µM H_2O_2
10% LB
25 µM H_2O_2
10 µm
vs
25 µm
10% LB
25 µM H_2O_2
vs
100 µM H_2O_2
G
S
I
Experimental test
Low growth
High growth
Short trench
Long trench
Low [H_2O_2]
High [H_2O_2]
ACF [a.u.]
Lags [min]
D
$D_{correlation}$
Low
High
Growth
Short
Long
Trench
[H_2O_2]
E
Prediction
Interdivision time [min]
$t_{ACFpeaks}$ [min]
Experiment
10% LB
M9 glu
M9 gly
ACF peak time [min]

***Figure 4.16 Predicted perturbations make or break chaos in experiments**:*
*Model predicts that chaos no longer occurs for reduced strength of either of the model components (Growth: G, Interactions: I, or Response: S). Mean and standard deviation of Lyapunov exponent (λ) show a transition from deterministic (λ≤0) to chaotic (λ>0) GrxA dynamics in simulations of cells with increasing (**A**) growth rates, (**B**) population size, and (**C**) H_2O_2 concentration. Experimental designs to test model predictions by changing (A) growth media, (B) trench lengths, and (C) H_2O_2 concentrations. Snapshots (scale bars = 10 µm) of PgrxA-SCFP3 90 minutes after start of treatment for cells growing in (A) M9 glycerol (slow growth, top) or M9 glucose + 10% LB (fast growth, bottom) in 25 µm trenches treated with 100 µM H_2O_2. (B) M9 glucose + 10% LB in 10 µm (2-4 cells per trench, top) or 25 µm (5-7 cells per trench, bottom) trenches treated with 25 µM H_2O_2. (C) M9 glucose + 10% LB in 10 µm trenches treated with 25 µM H_2O_2 (top) or 100 µM H_2O_2 (bottom). Autocorrelation analysis demonstrates the predicted transitions from periodic to chaotic dynamics in experiments. ACF curves of PgrxA-SCFP3 dynamics show characteristic peaks for periodic oscillations (black); these peaks are absent for chaotic dynamics (teal) in the case of (A) growth rate perturbation (1806, 1991 cells respectively, n ≥ 3 repeats), (B) population size perturbation (1003, 1440 cells respectively, n ≥ 3 repeats), and (C) H_2O_2 concentration perturbation (1003, 1361 cells respectively, n ≥ 3 repeats). (**D**) Bar plots show mean and standard deviation of maximal correlation dimension for GrxA traces of mother cells in experimental conditions shown in panel A, B, C resulting in chaos (teal), or periodicity (black) as obtained from the Grassberger-Procaccia method. (**E**) The periods of non-chaotic oscillations correlate with cell cycle duration (interdivision time) over a range of growth rates in simulations and experiments. Mean and standard deviation of interdivision time and the time of the first ACF peak for simulated GrxA dynamics (left, n = 3 simulations per condition) and experiments (right) with 100 µM H_2O_2 in M9 glycerol in 25 µm trenches (black), 50 µM H_2O_2 in M9 glucose in 10 µm trenches (dark blue) and 25 µM H_2O_2 in M9 glucose + 10% LB in 10 µm trenches (light blue) (966, 397, 661 cells respectively; n ≥ 3 repeats).*

$$\frac{dX}{dt} = f(X) + \eta \qquad \{\text{Eq 4.19}\}$$

$$\eta = \sigma \frac{\mathrm{dW}}{\mathrm{dt}}$$

Where W is the variable of a Weiner process satisfying the condition that $W_t - W_0 \sim \mathcal{N}$ [248].

$\mathcal{N}$ is a normal distribution with mean of µ and variance of σ^2. Rearranging Eq 4.17 gives the stochastic differential equation (SDE) as follows:

$$dX = f(X)\,dt + \sigma dW \qquad \{\text{Eq 4.20}\}$$

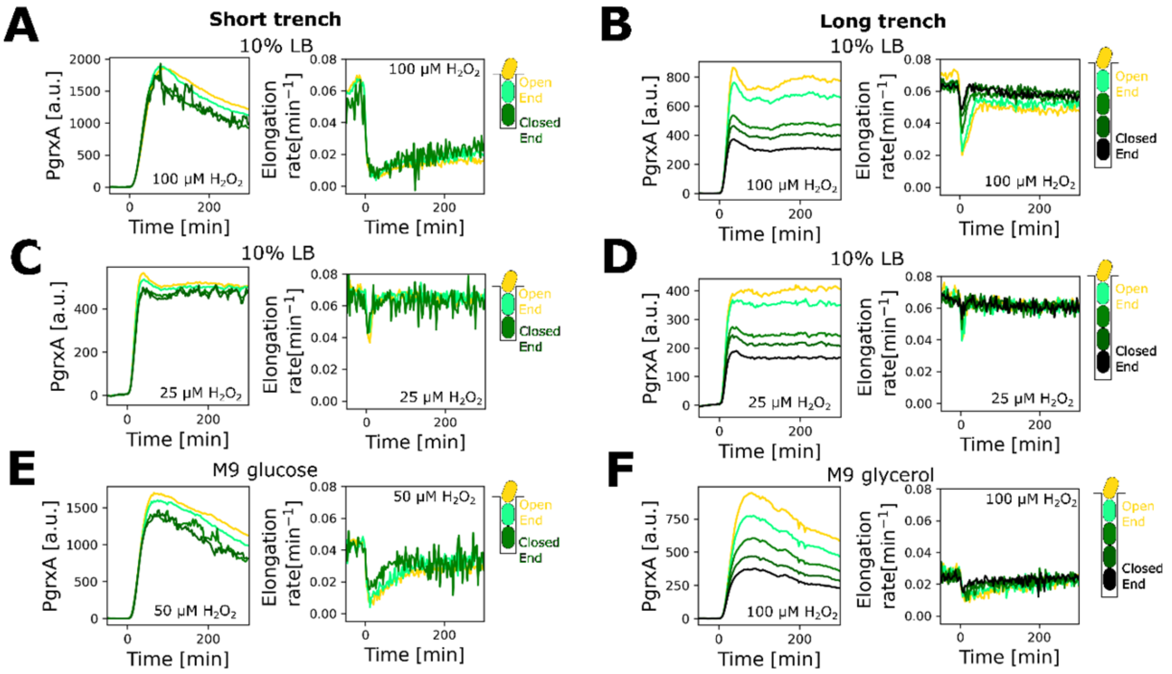

***Figure 4.17 Stress response and elongation rate dynamics with different growth and H_2O_2 treatment conditions**:*

*Summary of oxidative stress response dynamics in experiments with different growth and H_2O_2 treatment conditions. Cells growing in shorter trenches have reduced population size, increased stress response expression, and prolonged inhibition of growth with H_2O_2 treatment compared to cells in long trenches. Mean PgrxA-SCFP3 expression (left) and elongation rate (right) for cells growing in M9 glucose +10% LB in (**A**) 10 µm and (**B**) 25 µm trenches with 100 µM H_2O_2 treatment starting at t = 0 min (colour indicates cell position in the trench from yellow at open end to green/black at closed end of the trench, n = 3 experimental repeats). (**C, D**) Same as for panels A and B but with 25 µM H_2O_2 treatment starting at t = 0 min (n=3 experimental repeats). (**E, F**) Same as for panels A and B but with 50 µM H_2O_2 and 100 µM H_2O_2 treatment for cells growing in M9 glucose and M9 glycerol respectively (n = 3 experimental repeats).*

To solve Eq 4.20 numerically, we use the Euler-Maruyama method [249,250]. Let $\Delta t = t_{i+1} - t_i$ where i represents the iteration step from 0,1, … to N (number of iterations). Therefore, equation 4.20 can be rewritten as:

$$X_{i+1} = X_i + f(X_i)\Delta t + \sigma Z_i\sqrt{\Delta t} \qquad \{\text{Eq } 4.21\}$$

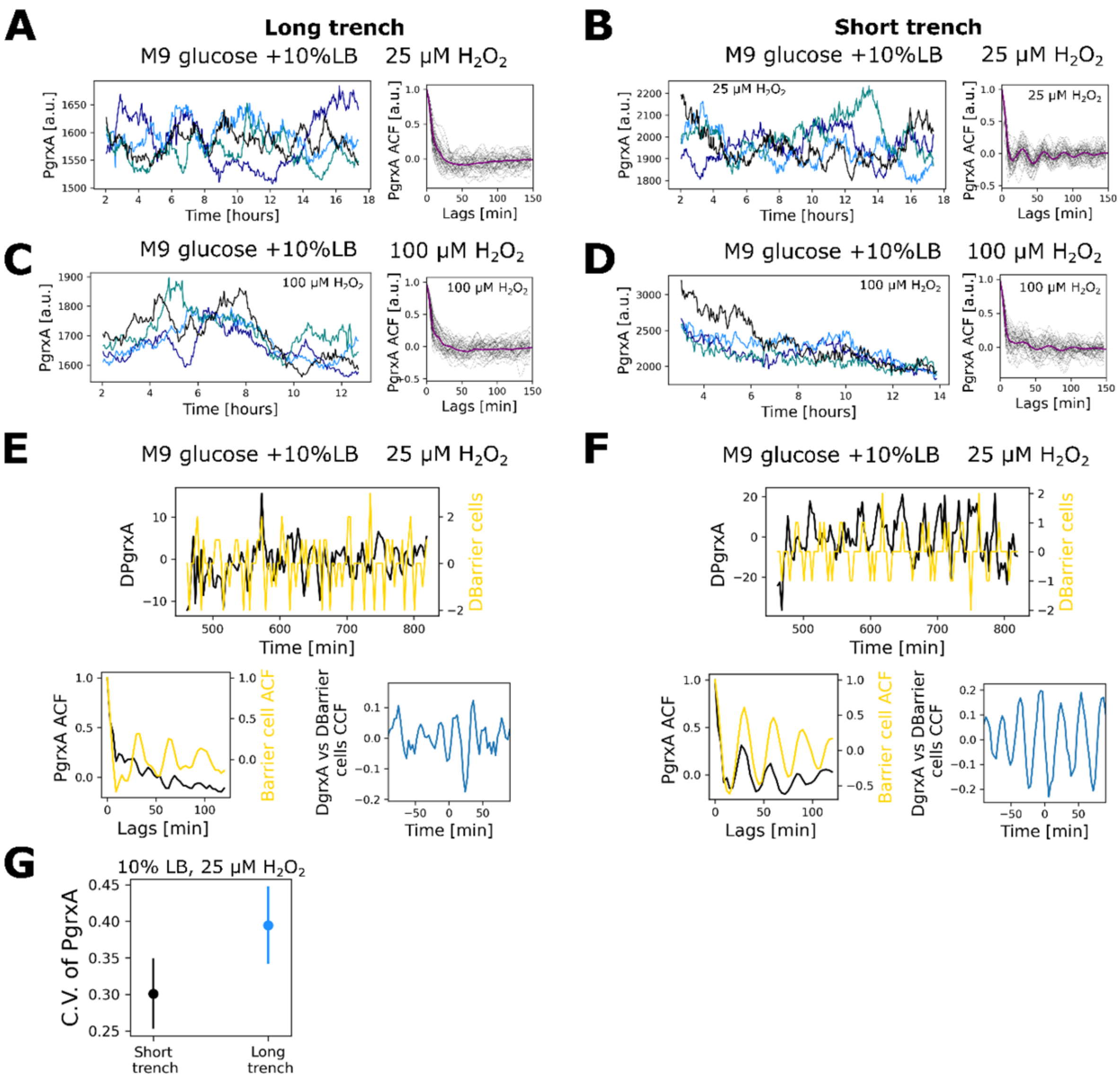

Figure 4.18 Deterministic chaos in oxidative stress response fluctuations at single cell level:
*Correlation analysis shows chaotic and periodic response dynamics at a single-cell level in experiments. (**A-D**) 5 representative PgrxA-SCFP3 expression traces and ACF curves for 50 individual mother cells (black) and cell-average curve (purple). (**A**) Chaotic dynamics: M9 glucose + 10% LB with 25 μM H_2O_2 in 25 μm trenches. (**B**) Periodic dynamics: M9 glucose + 10% LB with 25 μM H_2O_2 in 10 μm growth trenches. (**C**) Chaotic dynamics: M9 glucose + 10% LB with 100 μM H_2O_2 in 25 μm trenches. (**D**) Periodic dynamics: M9 glucose + 10% LB with 100 μM H_2O_2 in 10 μm growth trenches. (**E, F**) Representative mother cell traces showing cross-correlation between changes in PgrxA-SCFP3 expression (DpgrxA, black) and changes in barrier cell numbers (DBarrier cells, yellow). Corresponding autocorrelation of DpgrxA (ACF, left) and cross-correlation of DpgrxA vs Dbarrier cells (CCF, right) plots for the single mother cell traces above. Cells growing in M9*

*glucose + 10% LB and treated with 25 µM H_2O_2 in (**E**) 25 µm trenches (chaotic dynamics) and (**F**) 10 µm trenches (periodic dynamics). (**G**) Under chaotic conditions cell-cell variability increases. Coefficient of variation (C.V.) of PgrxA-SCFP3 expression for mother cells growing in M9 glucose + 10% LB and treated with 25 µM H_2O_2 in 25 µm (blue) and 10 µm trenches (black) (n= 3 experimental repeats).*

Where Z_i represents the normal distribution (Weiner process derivatives) with mean = 0 and variance = 1.

To solve the equations numerically, the equations were non-dimensionalised in time $t_{nd} = t \cdot g$, where g is the elongation rate. Then, noise term γ_{gene} was added to each equation, giving the following:

$$\frac{d[OxyR]_{Red}}{dt_{nd}} = \frac{1}{g}\Big(-K_{ox}[OxyR_{Red}][H_2O_2]_{cell} + K_{red}[GrxA]\big(\frac{[OxyR]_{total}-[OxyR]_{Red}}{([OxyR]_{total}-[OxyR]_{Red}) + h_{OxyR}}\big)\Big) + \gamma_{OxyR} \qquad \{\text{Eq } 4.22\}$$

$$\frac{d[GrxA]}{dt_{nd}} = \frac{1}{g}\Big(R_{grxA,basal} + K_{grxA,act}\Big(\frac{[OxyR]_{total}-[OxyR]_{Red}}{([OxyR]_{total}-[OxyR]_{Red})+ h_{grxA,act}}\Big) - g[GrxA]\Big) + \gamma_{GrxA} \qquad \{\text{Eq } 4.23\}$$

$$\frac{d[KatG]}{dt_{nd}} = \frac{1}{g}\Big(R_{katG,basal} + K_{katG,act}\Big(\frac{[OxyR]_{total}-[OxyR]_{Red}}{([OxyR]_{total}-[OxyR]_{Red})+ h_{katG,act}}\Big) - g[KatG]\Big) + \gamma_{KatG} \qquad \{\text{Eq } 4.24\}$$

$$\frac{d[AhpC]}{dt_{nd}} = \frac{1}{g}\Big(R_{aphC,basal} + K_{ahpC,act}\Big(\frac{[OxyR]_{total}-[OxyR]_{Red}}{([OxyR]_{total}-[OxyR]_{Red})+ h_{ahpC,act}}\Big) - g[AhpC]\Big) + \gamma_{AhpC} \qquad \{\text{Eq } 4.25\}$$

To solve the equations numerically using the Euler-Maruyama method, Eq 4.22-4.25 were converted to the form shown in Eq 4.18, giving the following:

$$[OxyR]_{Red_{i+1}} = [OxyR]_{Red_i} + \frac{\Delta t_{nd}}{g}\Bigg(- K_{ox}[OxyR]_{Red_i}[H_2O_2]_{cell_i} +$$

$$K_{red}[GrxA]_i\left(\frac{[OxyR]_{total}-[OxyR]_{Red_i}}{([OxyR]_{total}-[OxyR]_{Red_i})+ h_{OxyR}}\right)\Bigg) + \sigma_{oxyR}Z_i\sqrt{\Delta t_{nd}} \quad \text{\{Eq 4.26\}}$$

$$[GrxA]_{i+1} = [GrxA]_i + \frac{\Delta t_{nd}}{g}\Bigg(R_{grxA,basal} + K_{grxA,act}\left(\frac{[OxyR]_{total}-[OxyR]_{Red_i}}{([OxyR]_{total}-[OxyR]_{Red_i}) + h_{grxA,act}}\right) -$$

$$g[GrxA]_i\Bigg) + \sigma_{GrxA}Z_i\sqrt{\Delta t_{nd}} \qquad \text{\{Eq 4.27\}}$$

$$[KatG]_{i+1} = [KatG]_i + \frac{\Delta t_{nd}}{g}\Bigg(R_{katG,basal} + K_{katG,act}\left(\frac{[OxyR]_{total}-[OxyR]_{Red_i}}{([OxyR]_{total}-[OxyR]_{Red_i}) + h_{katG,act}}\right) -$$

$$g[KatG]_i\Bigg) + \sigma_{KatG}Z_i\sqrt{\Delta t_{nd}} \qquad \text{\{Eq 4.28\}}$$

$$[AhpC]_{i+1} = [AhpC]_i + \frac{\Delta t_{nd}}{g}\Bigg(R_{aphC,basal} +$$

$$K_{katG,act}\left(\frac{[OxyR]_{total}-[OxyR]_{Red_i}}{([OxyR]_{total}-[OxyR]_{Red_i}) + h_{ahpC,act}}\right) - g[AhpC]_i\Bigg) + \sigma_{AhpC}Z_i\sqrt{\Delta t_{nd}} \quad \text{\{Eq 4.29\}}$$

The noise term is added in the form $\gamma_{gene} = \sigma_{gene}Z_i\sqrt{\Delta t_{nd}}$

For our simulations $\Delta t_{nd} = 5 \cdot 10^{-6}\, min^{-1}$ and $\{\sigma_{OxyR}, \sigma_{GrxA}, \sigma_{KatG}, \sigma_{AhpC}\} = \{0.0002, 0.02, 0.02, 0.02\}$. We chose values of σ such that the magnitude of the fluctuations of the stochastic response model (S*) was similar to the magnitude of the chaotic fluctuations of the full deterministic model (S+G+I).

We compared the phase diagrams of stochastic and deterministic traces derived from experiments and modelling. These diagrams indicated that stochastic traces exhibit a random zig-zag pattern, whereas deterministic traces form distinct closed loops [Figure 4.19, 4.20].

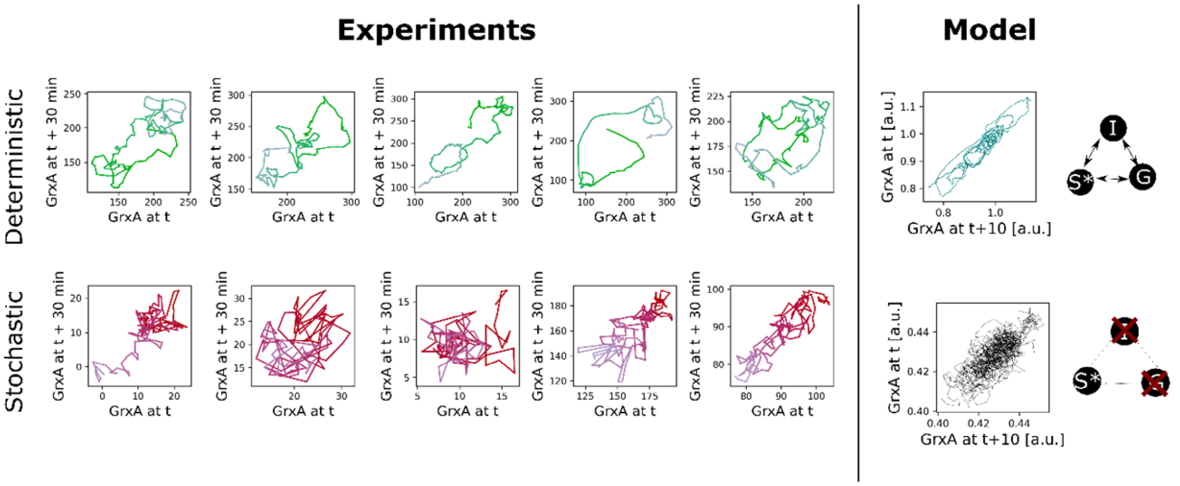

***Figure 4.19**: **Phase diagrams for stochastic and deterministic traces of oxidative stress response**. PgrxA phase diagrams (bottom) for representative mother cell traces treated with 100 µM H_2O_2 treatment from t=0 min, which are classified as deterministic (green, top), stochastic (red, bottom) in experiments (left) and model(right).*

Although the resulting response dynamics superficially match aspects of the experimental data, they disagreed with key features. Specifically, none of the noisy response models (S*, S*+I, S*+G) showed both (1) loss of autocorrelation peaks for higher H_2O_2 concentrations, and (2) negative cross-correlation between response fluctuations and the number of cells per trench [Figure 4.20]. These findings again support our conclusion that the fluctuations are predominantly deterministic. Only when we coupled the noisy response with the full model of growth and cell interactions (S*+G+I) did we recover the dynamics seen in experiments, but this was already the case for the model without noise. Therefore, the model can tolerate the addition of noise but does not require it for the generation of unpredictable response fluctuations. We find further evidence of the importance of deterministic processes over stochastic ones when we apply the Grassberger-Procaccia algorithm to the noisy response models. In all cases, the noisy models do not converge on a low correlation dimension,

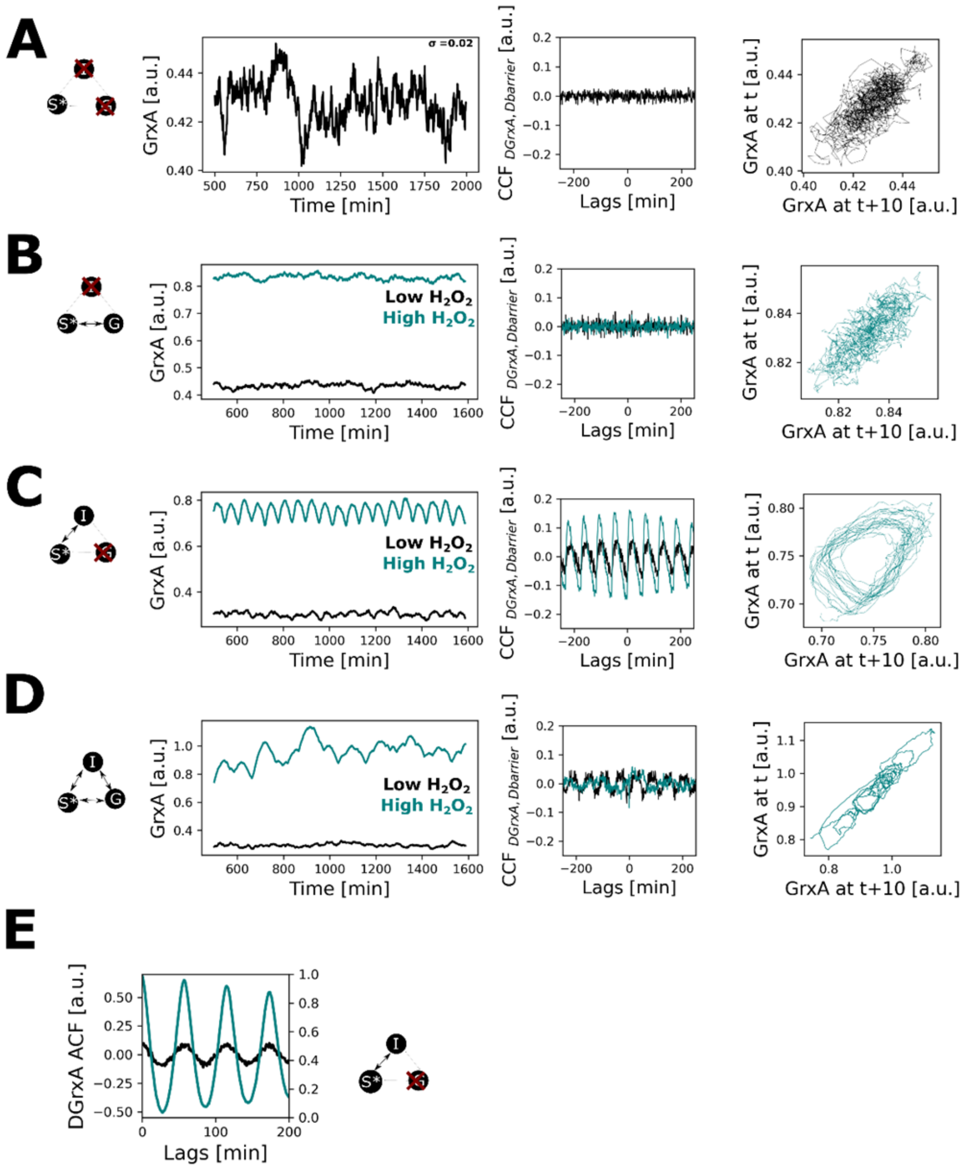

Figure 4.20 Response fluctuations are not driven by noise:

Simulations of the stress response model with gene expression noise (S) do not match experimental observations unless the response model (S*) is coupled with the growth (G) and cell-interactions (I) model components. Therefore, noise alone cannot explain the response fluctuations. (**A**) Noisy stress response model without growth and cell-interactions components does not show expected cross-correlations: Example simulated GrxA trace shows gene expression fluctuations (left), but no cross-correlation function (CCF) peaks are seen between changes in GrxA (DGrxA) and changes in barrier cells (Dbarrier) (middle), in disagreement with experiments (Figure 4.12). Corresponding phase diagram (right) does not show the characteristic extended orbits of periodic or chaotic fluctuations. (**B**) Coupling of the growth model with the noisy response model (S*+G) does not generate the expected cross-correlation and phase diagram orbits, neither for low (black) nor high (teal) H_2O_2*

*concentrations. (**C**) Coupling of the cell-interaction model with the noisy response model (S*+I) generates the expected cross-correlation and phase diagram orbits, but the autocorrelation of the dynamics for low (black) and high (teal) H_2O_2 concentrations is inconsistent with experiments (Figure 4.12). (**D**) Coupling of the growth and cell interaction models with the noisy response model (S*+G+I) generates the expected cross-correlation and phase diagram orbits for low (black) and high (teal) H_2O_2 concentrations. (**E**) For simulated traces of the S*+I model (panel C), the ACF shows periodic oscillations even at high H_2O_2 concentration (teal), in contrast to experiments where high H_2O_2 leads to chaos and loss of ACF peaks.*

whereas the deterministic model had a correlation dimension of ~2 [Figure 4.21]. This means that although the model includes multiple dynamic variables for each of the interacting cells in a trench, the response dynamics of one focal cell are actually driven by a deterministic process with only ~2 effective variables. Strikingly, the experimental data had the same effective correlation dimension of ~2 across all growth conditions used in our tests for chaos (varying growth rate, trench length, H_2O_2 concentration), irrespective of whether the dynamics were periodic or chaotic [Figure 4.16D, 4.21]. This finding suggests that one simple deterministic process is responsible for generating all the observed response dynamics in experiments, from periodic to chaotic. Moreover, both our model and experiments suggest the cause of this determinism is strongly linked to the cell cycle [Figure 4.12, 4.15]. Indeed, the timing of the peaks in the autocorrelation curves matches the cell cycle duration in each experimental condition, which is again predicted by the model [Figure 4.16E].

How does one process generate periodic oscillations under some conditions and chaotic fluctuations under others? Periodic oscillations occur at low stress levels when the cell growth rate is constant. Here, the number of cells in a given locality oscillates at regular intervals as cells grow and divide, leading to periodic changes in the H_2O_2 concentration around each cell. At higher stress treatments, the growth rate of each cell becomes sensitive to the H_2O_2 concentration. The cells then grow at variable rates and their local numbers

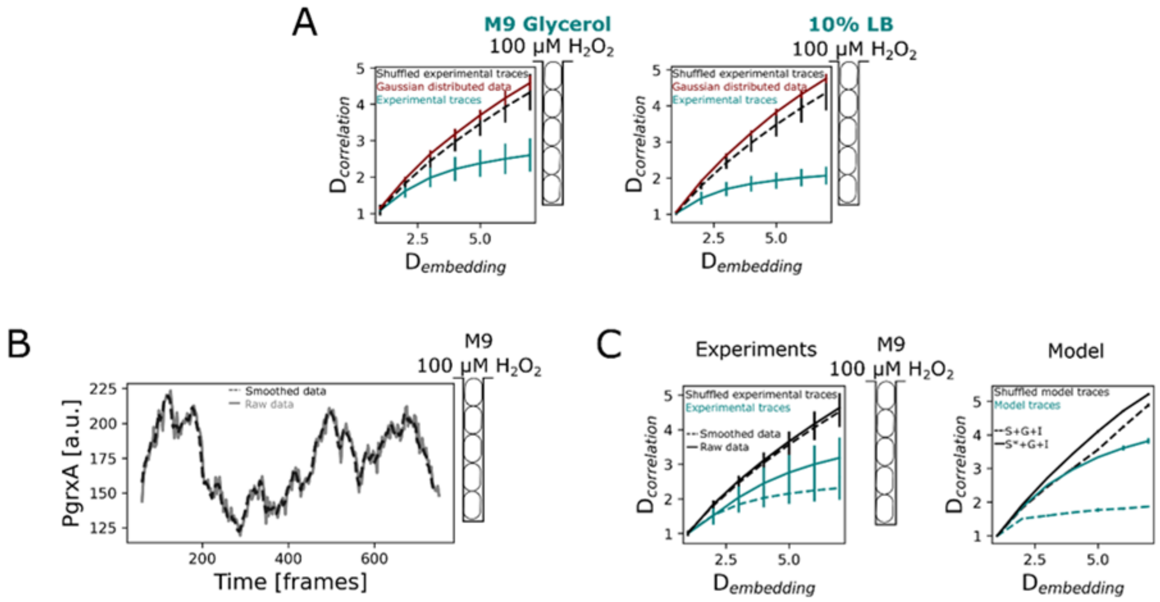

Figure 4.21 Correlation dimension analysis using Grassberger – Procaccia algorithm indicates that observed fluctuations are deterministic:

*(**A**) Curves show the correlation dimension as a function of the embedding dimension from PgrxA-SCFP3 traces of mother cells during H_2O_2 treatment at steady-state under the indicated measurement conditions. Curves for experimental traces (teal) are compared to experimental traces with randomly shuffled time points (dashed black) and to synthetic traces with data points drawn from a Gaussian distribution with the same mean and standard deviation as the experimental traces (maroon). The curves from experimental traces saturate at a finite correlation dimension of ~2 for all measurement conditions, consistent with deterministic dynamics, whereas the curves from the randomized controls do not saturate. (970, 733 traces for cells growing in M9 glycerol and M9 glucose + 10% LB respectively, curves represent mean values with error bars representing standard deviation). (**B**) Effect of moving-mean smoothing on correlation dimension analysis. (left) Example raw PgrxA-SCFP3 trace (grey) and after smoothing with a filter window of 9 minutes (black dashed). (right) Correlation dimension versus embedding dimension from PgrxA-SCFP3 traces as in panel A for raw data (solid lines) or with moving-mean smoothing (dashed lines). (**C**) Application of correlation analysis to simulated GrxA traces from the full deterministic model (S+G+I, dashed lines) and the full model with noisy stress response (S*+G+I, solid lines).*

change without a fixed period, leading to irregular oscillations in H_2O_2. In this way, the stress response dynamics transition to chaos.

4.9 Discussion

Our work has identified chaos in a bacterial stress response. This finding shows that seemingly random phenotypic heterogeneity can be generated by deterministic rather than stochastic processes. That is, regulatory circuits are able to generate unpredictable outputs, even when the underlying mechanisms are entirely deterministic. Such cases are called chaotic because they have the property of amplifying infinitesimally small differences in the initial conditions to an extent that forecasting the long-term behaviour is impossible no matter how accurately the initial conditions can be defined. While noise due to molecular fluctuations is certainly present in cells, our model and experiments show that phenotypic heterogeneity among cells can arise without the requirement for stochasticity. Moreover, our analyses suggest that the key driver of both the periodic oscillations and chaotic fluctuations is the determinism of the cell cycle [Figure 4.14, 4.15, 4.16].

We have focused here on the behavior of cells as they grow in lines in channels of the mother machine microfluidic device. The great advantage of this study system is that one can follow stress response dynamics of individual cells for relatively long periods in a bacterial population where cell-cell interactions are still preserved. These relatively long time series from single cells were important for our ability to both identify and describe chaos empirically. However, our work suggests that the chaotic behavior seen in this system also occurs in more complex and realistic growth conditions. When we study cells in two dimensional colonies, we also see unpredictable stress response dynamics, which are consistent with chaos [Figure 4.11D-E, 4.13]. It will be interesting to understand how chaotic processes are affected in even more complex growth environments, such as submerged biofilms. On the one hand, additional variation in the local density and arrangement of cells should increase the potential for chaos, while on the other the increasing capacity to scavenge H_2O_2 within larger communities may reduce stress levels and the duration of any chaotic dynamics.

Why have bacterial cells evolved to display such chaotic behaviour? Our work shows that multiple processes interact to generate chaos, including the cell cycle and changes in local cell density. Another important factor is the strength of the stress response itself: a high expression rate and high catalytic efficiency of scavenging enzymes are critical to the transition from periodic oscillations to chaos [Figure 4.6, 4.16]. The evolution of chaotic behaviour in the oxidative stress response, therefore, may lie in the benefits of a strong response for surviving stress, which is likely to provide a strong selective advantage to cells[2,205]. This importance of a strong response for chaos mirrors the classic theoretical results on chaos in population biology. There, models predict that high population growth rate is needed to generate chaotic dynamics [243], because this causes the population to overshoot equilibria and over-compensate [251].

Chaos also results in a variable response among cells. An intriguing possibility, therefore, is that chaotic responses could have the benefit of diversifying cell behaviour as a population bet-hedging strategy against unpredictable stresses[71]. Although microbes can harness intracellular molecular noise to generate phenotypic heterogeneity, deterministic chaos can achieve this without noise disturbing the response accuracy of each individual cell. In fact, our study showed that the conditions that lead to chaos are exactly those where bet-hedging is valuable in principle, namely at high stress levels and in cell populations but not in isolated cells. Although our work is based upon the detailed study of one bacterial stress response, the existence of chaotic behaviour may be widespread in cellular systems for related reasons [211,252]. Using a generalised model, we find that chaotic cell responses are possible whenever the absorbance of a stressor reduces a cell's growth rate and lowers the stressor concentration of the surrounding cells [Figure 4.6]. The feedback between these effects creates spatio-temporal dynamics that amplify small perturbations, leading to chaotic behavior. Hence, the survival strategies of bacteria and other cells exposed to stressors such as antibiotics, antimicrobial peptides, or reactive chemicals, all have the potential for deterministic chaos. Specifically, under the influence of dynamics external conditions, a high catalytic efficiency and high induction rates inside cells will lead to diffusion limitation, resulting in a periodic behavior as predicted by the S+I model [Figure 4.15]. Further, if, under such conditions, cellular growth rates are modulated, this could induce instability, driving the bacterial response towards chaos.

The study of chaos in biology has received considerable attention, and there are many potential examples where unpredictable dynamics have been observed that appear chaotic[191]. However, it remains challenging to identify chaos from either observational data or theoretical models alone. Here, we have presented a different strategy that rests on the ability to manipulate chaos. In addition to the prediction of chaos and observational experiments, our model also correctly predicts the conditions where chaotic dynamics are lost. This close fit between model and measurements provides clear evidence for the existence of chaos in the single-cell dynamics of bacterial stress responses.

Chapter 5

A simple regulatory network coordinates a stress response in space and time to protect bacterial groups

5.1 Summary

Bacteria employ diverse and elaborate regulatory networks to respond to their environment. While transcriptomics and proteomics show that these networks can shift strongly as conditions change, the underlying logic of regulatory networks often remains unclear in the face of such bulk measurements performed at discrete time points. Here we demonstrate the power of time-resolved single-cell imaging to explain the functioning of the *E. coli* oxidative stress response. We study the expression dynamics of over thirty genes in the regulon of the transcription factor OxyR. This work reveals a surprising diversity in the dynamics across the genes, with differences in the timing, magnitude, and up- vs down-regulation of expression. Nevertheless, there is an underlying simplicity to the regulon that explains these variable patterns. Firstly, all genes, including those not regulated by OxyR, exhibit a transient increase in their protein levels simply due to the slowing down of cell growth under stress. Genes that are genuinely upregulated by OxyR show either gradual induction or pulsatile expression that decays rapidly after its peak. The difference between the two forms of upregulation appears to result solely from changes in transcription factor binding dynamics that control stress sensitivity. Pulsatile genes are stress-sensitive and activate rapidly to transiently protect cells during the first moments of stress. In cell groups, this results in steep spatial gradients of gene expression such that cells that are close to the stressor protect those that are further away. Gradually upregulated genes are less sensitive and induce more evenly in space with less cell-to-cell heterogeneity, resulting in a larger number of cells investing in both individual and collective protection. Our study shows how a single transcription factor can create multiple expression patterns in space and time, which protect cell groups from stress.

5.2 Introduction

Bacterial stress response regulons are complex and typically comprise tens of genes that perform an array of functions crucial for survival under stress[253]. Remarkably, dynamic changes in the expression of stress response genes are controlled by only a small number of master transcriptional regulators. It is a fascinating question how one such transcription factor can convert a stress signal into a global response that orchestrates the timing and magnitude of transcriptional changes according to the specific functions of many individual genes. Bulk transcriptomic and proteomic studies show an association between stress tolerance and gene regulation under oxidative stress[173], osmotic stress[254], heat stress[254,255], pH stress[256], phage infection[257] , and antibiotic exposure[258]. Moreover, these methods often identify tens to hundreds of genes that shift in expression with stress treatments, which suggests a complex regulatory network underlying each response[172]. However, these methods are limited in their ability to link gene regulation with cellular phenotypes such as growth rate, because they typically comprise bulk population measurements, which lack single-cell resolution. In addition, due to cost and practicality, genome-wide gene expression data is typically recorded at only a few time points, meaning that temporal dynamics cannot be followed in any detail[259,260]. The use of such measurements can be limiting for understanding the effects of phenotypic heterogeneity displayed by bacteria, especially under stress, whereby individual cells display different responses in space and time[49,261,262]. The existence and potential importance of phenotypic heterogeneity have been shown by studies that follow the regulation of stress response genes using single-cell imaging methods[17,32,263].

Temporal order in the activation of different genes within a regulon has been demonstrated in the cellular response to environmental changes *e.g.* under DNA damage stress, antibiotic

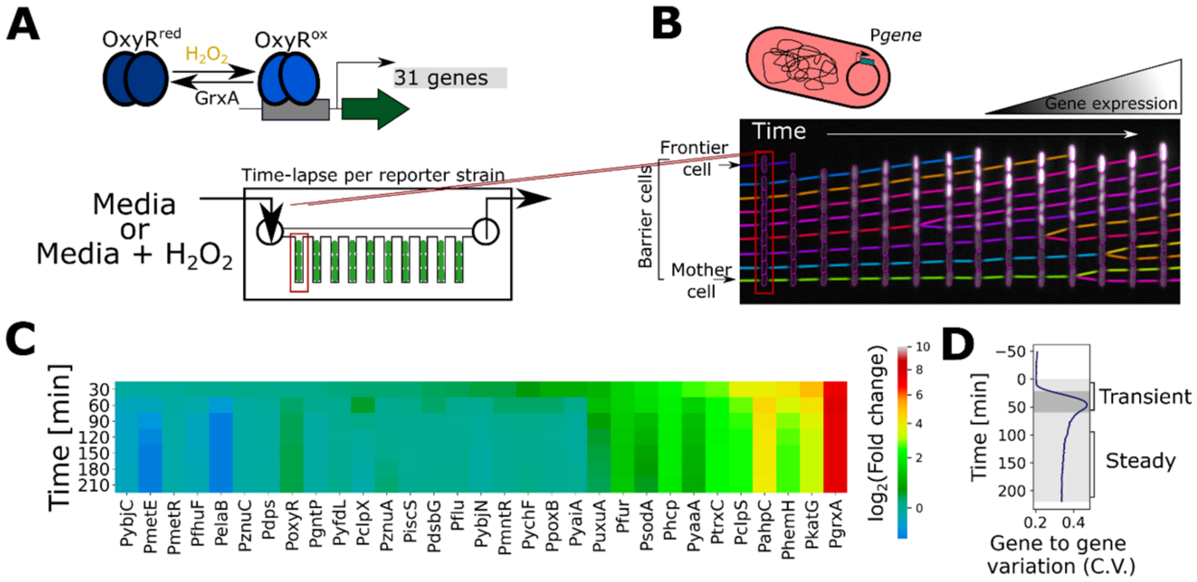

Figure 5.1 Gene expression dynamics across the OxyR regulon under H_2O_2 treatment:
*(**A**) Upon exposure to hydrogen peroxide, oxidation of OxyR leads to induction of a wide regulon of genes in E. coli. The schematic displays the microfluidics-based methodology to visualise the promoter activity of 31 fluorescently-tagged transcriptional reporters by time-lapse microscopy at single-cell resolution. (**B**) The kymograph represents cell growth over time in one of the representative growth channels with intensity of cells reporting gene expression levels. We define 'mother cells', 'barrier cells', and 'frontier cells' according to their position relative to the open end of the growth channel where H_2O_2 treatment is provided. (**C**) Heatmap represents mean log_2-fold change in gene expression relative to basal level of frontier cells for 31 transcriptional reporters at 30-minute intervals during continuous treatment with 100 µM H_2O_2 from t = 0 min (n ≥ 1000 cells and ≥2 repeats per gene). (**D**) Coefficient of variation (C.V.) for gene-to-gene expression variability across the 31 transcriptional reporters of frontier cells under 100 µM H_2O_2 treatment provided at t = 0 minutes. (Shaded region represents H_2O_2 treatment, with the darker shade representing the highly variable gene-gene expression post treatment; n ≥ 1000 cells and ≥ 2 repeats per gene).*

stress, flagellar biosynthesis, and metabolic pathways[74,206,262–267]. Moreover, gradients in the concentrations of stress agents or metabolic by-products within bacterial populations can stratify gene expression at local and global spatial scales[49,50,261]. One can observe these complex spatio-temporal gene expression patterns under stress due to the effect of cell-cell interactions, feedbacks between cell growth rate and gene expression [32,268,269], and environmental fluctuations[17,32,45]. However, to date, studies that characterised these patterns have tended to focus on a single reporter gene for a given stress. This leaves open the question of how the full regulon of a stress response is functionally coordinated in space and time.

Here, we leverage the recent advancements in single-cell imaging that allow cellular behaviour to be followed in a constantly controlled environment for long durations[17,32,263]. We focus on the oxidative stress response of *Escherichia coli* under H_2O_2 treatment, which is a major reactive oxygen species that causes damage to proteins, lipids, and DNA. H_2O_2 readily permeates cells[27] causing redox imbalance [85]. This stress leads to oxidation and a conformational change in the transcription factor OxyR[158,160]. OxyR acts as a sensor for intracellular H_2O_2 levels and regulates an array of more than two dozen genes in its regulon, involved in diverse functions to maintain cell survival under H_2O_2 stress[2,151,173,199,270], including iron homeostasis[164–166,168,271], H_2O_2 scavenging[84,85,108], and redox maintenance[97,159,272]. We characterise the changes in the transcription of 31 genes, which have been previously identified as part of the oxidative stress response[33,84,85,97,159,160,163–166,168,173,270–284] (Table 5.1), in microfluidic 'mother-machine' devices and employ mathematical modelling to explain the observed regulatory dynamics. Our work provides insight into how a single transcription factor can coordinate tens of genes with distinct expression patterns in space and time, which enables bacteria to protect themselves both individually and collectively.

5.3 Expression dynamics of genes across the OxyR regulon

We imaged gene expression dynamics using time-lapse microscopy of *E. coli* cells, each carrying one of 31 plasmid-based transcriptional reporters that have an OxyR-regulated

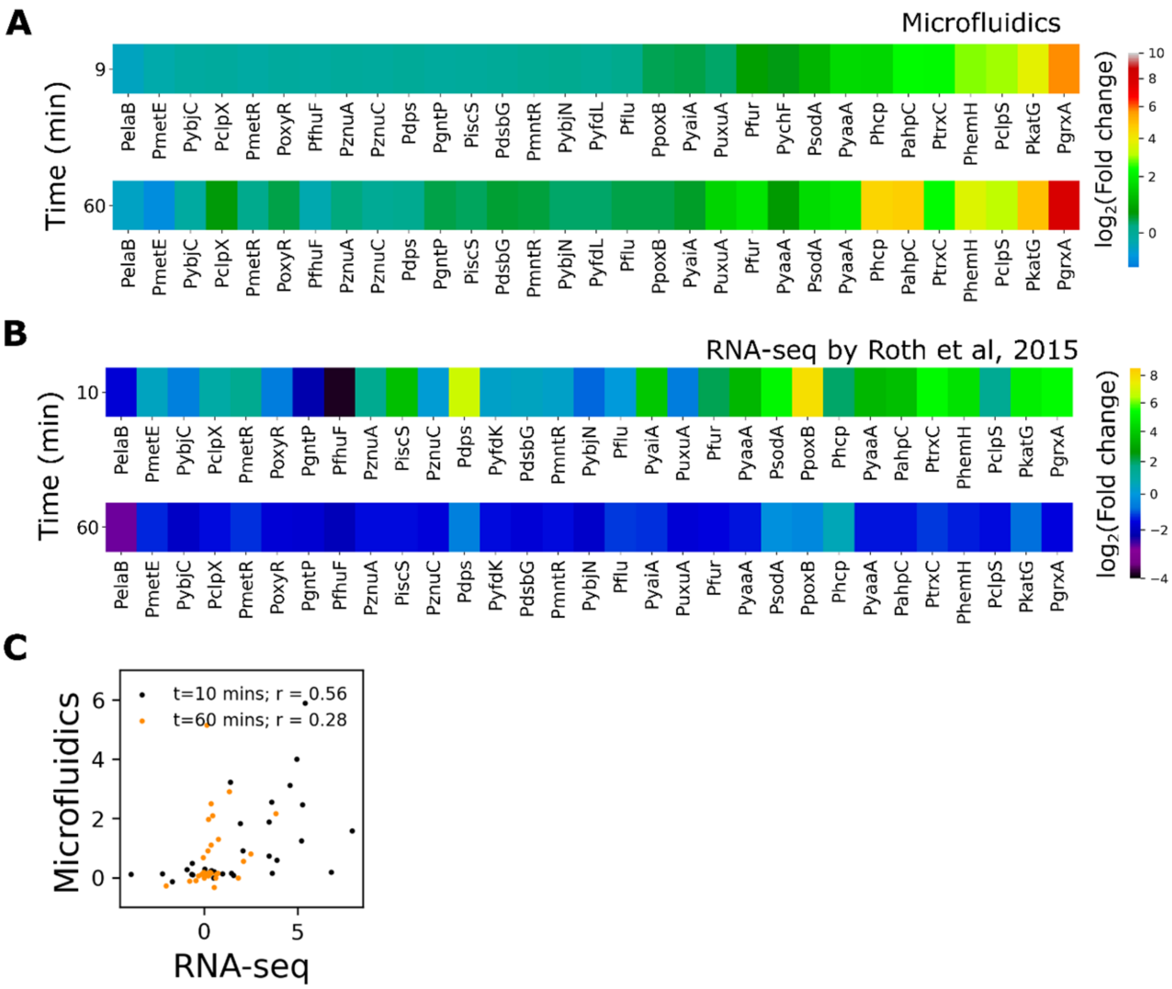

Figure 5.2 Gene expression level changes in our study compared to the bulk mRNA level changes, reported by Roth et al, under H_2O_2 stress:

*(**A**) Heatmap represents mean log₂-fold change in gene expression relative to basal level of frontier cells for 31 transcriptional reporters at 9 minutes (top) and 60 minutes (bottom) post treatment with 100 µM H_2O_2 (n ≥ 1000 cells and ≥2 repeats per gene). (**B**) Heatmap represents data collected by Roth et al.[173] showing mean log₂-fold change in mRNA levels of cells for 31 genes at 10 mins (top) and 60 mins (bottom) after treatment with 2.5 mM H_2O_2. (**C**) Comparison of log₂-fold change in gene expression levels from microfluidic single-cell imaging and mRNA levels in panel A and B at 10 min (black) and 60 minutes (orange) post H_2O_2 treatment. Pearson's coefficient (r) for linear fit between the data sets are indicated in the plot.*

promoter followed by a fast-maturing GFP[178] or sCFP3 (for P*katG*, P*ahpC* and P*grxA*). We collected data for ~10,000 individual cells growing inside mother machine trenches during

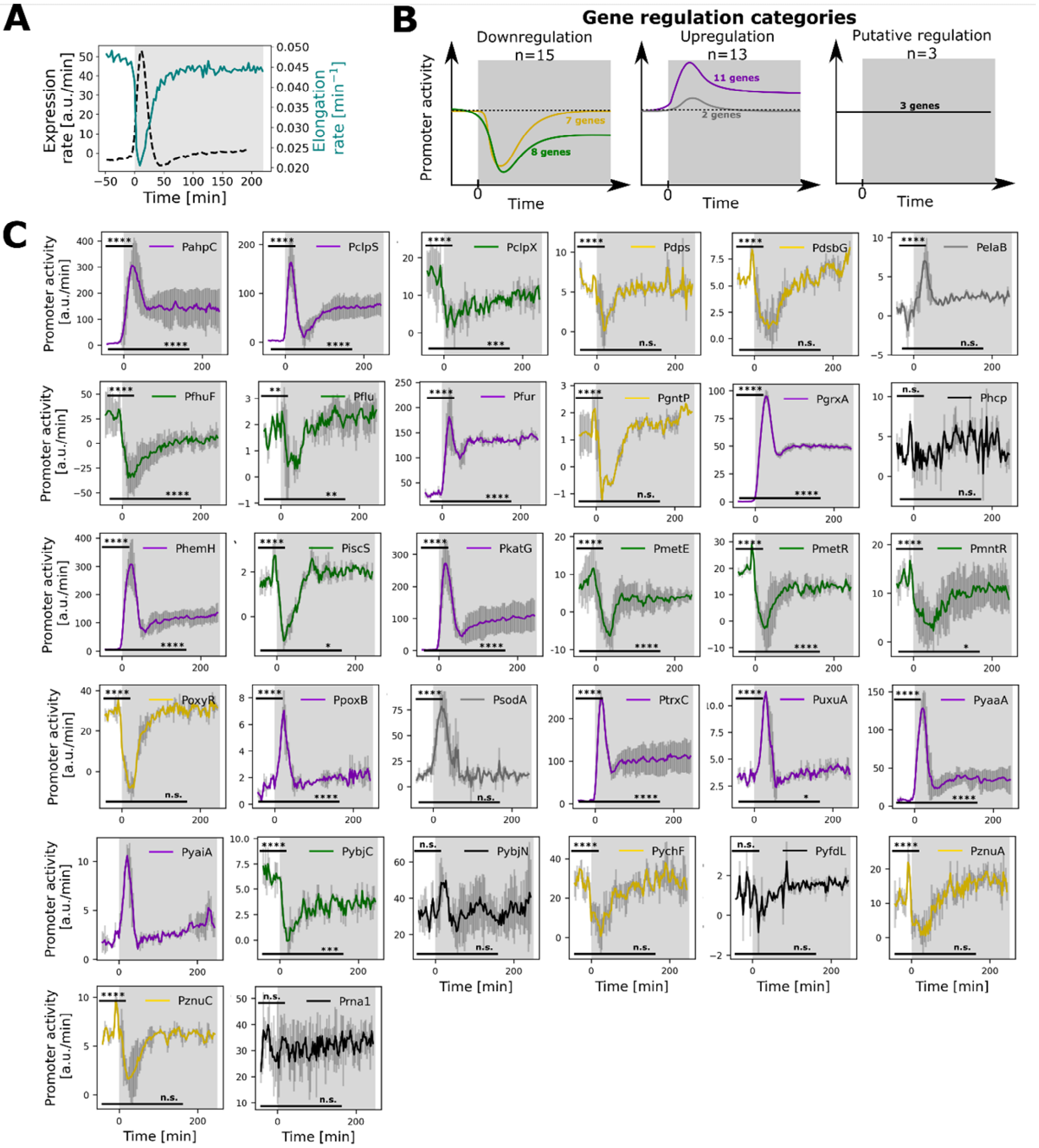

Figure 5.3 Oxidative stress response genes show a range of different expression dynamics during constant H_2O_2 stress:

*(**A**) Mean elongation rate (teal) and mean expression rate for all genes (black; dashed) of frontier cells treated with 100 µM H_2O_2 from t=0 min (shaded region). (**B**) Schematic illustrates the expression dynamics of the 5 gene regulation categories together with the number of genes in each category: (left) downregulation throughout the H_2O_2 treatment (green) or transient downregulation post treatment (gold); (middle) upregulation throughout the H_2O_2 treatment (purple) or transiently uptreatment (grey); (right) no significant change in promoter activity observed (black). Dashed lines represent the basal levels. (**C**) Mean promoter activity of frontier cells for 31 transcriptional reporters*

and the constitutively expressed promoter Prna1 with constant 100 µM H_2O_2 *treatment from t = 0 minutes (shaded region). Promoter activity shows the expression rate corrected for changes in cell growth rate. Non-parametric Mann-Whitney tests were used to indicate significant changes in promoter activity at the transient or steady-state relative to the basal level expression; where ****:* $p \leq 0.0001$*, ***:* $p \leq 0.001$*, **:* $p \leq 0.01$*, *:* $p \leq 0.05$*, n.s.:*$p > 0.05$*. Line colours correspond to the gene regulation categories as explained in panel B. Error bars represent standard deviation (*$n \geq 1000$ *cells and ≥ 2 repeats per gene).*

continuous H_2O_2 stress from ~2 hours before until 6 hours post treatment at 3-min time intervals, resulting in a rich dataset of ~200,000 expression measurements per reporter gene [Figure 5.1A]. The microfluidic chip provides an opportunity to disentangle genuine gene regulatory dynamics from environmental changes because the continuous inflow of fresh media with H_2O_2 keeps the treatment concentration constant despite changes in the scavenging capacities of cells [Figure 5.1B]. With this setup, we were able to observe that all 31 genes showed an initial expression pulse within 10 min after the start of treatment [Figure 5.1C, 5.2A]. Expression of different genes diverged after this initial pulse. After 90 min of continuous H_2O_2 treatment, most genes remained upregulated while others became downregulated relative to the untreated expression level [Figure 5.1C]. Our results are broadly consistent with previous RNAseq measurements[173] for time points shortly after the start of treatment, but differ at later time points [Figure 5.2]. The variations could be ascribed to the methodology used in our study. We analyse gene expression dynamics in an exponentially growing population of lower cell density continuously exposed to H_2O_2. This approach contrasts with bulk studies that examine gene expression in high cell density cultures after treatment with a single dose of H_2O_2. For RNA seq data, cells are exposed to a high dose of treatment to extract measurable levels of mRNA transcripts. However, in microfluidic experiments, we subjected cells to a lower concentration of stress. Because of these differences, we would not expect a precise alignment in terms of the overall magnitude.

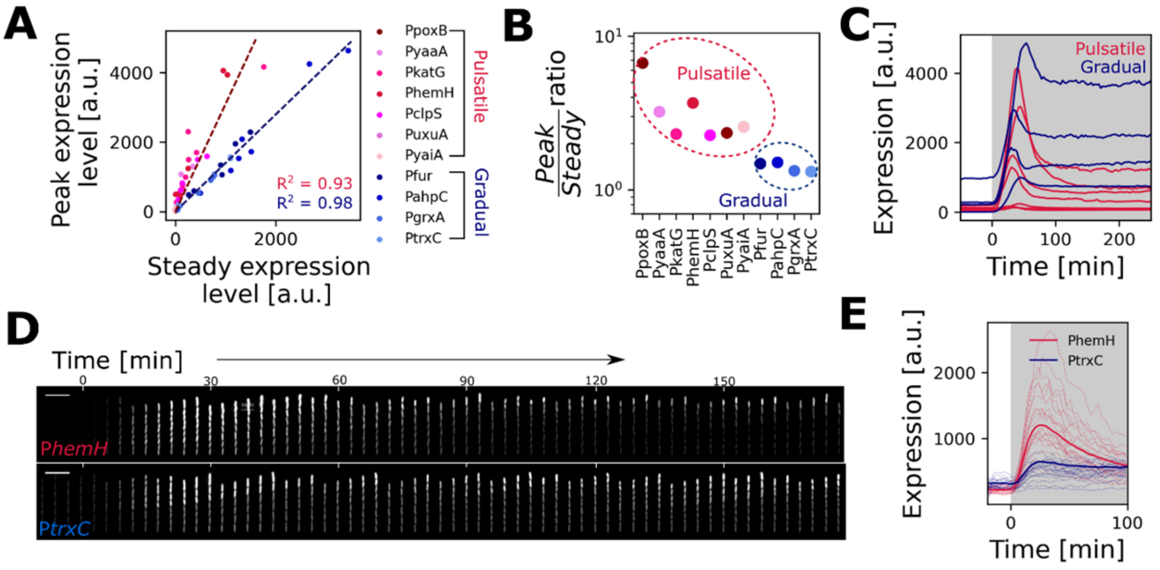

Figure 5.4 Positively-regulated promoters show either pulsatile or gradual induction dynamics: *(A) Plot of the peak expression level (during the transient phase) versus the expression level at steady-state of frontier cells relative to basal expression for the indicated transcriptional reporters with 25 µM, 50 µM and 100 µM H_2O_2 treatment. The pulsatile and gradual induced genes cluster on two distinct slopes, shown with linear fits (dashed lines). (**B**) Peak/steady ratio obtained by linear regression of values for individual genes shown in panel B (pink: pulsatile genes, blue: gradual induced genes, n≥3 repeats per gene). (**C**) Plot shows mean reporter expression levels of frontier cells for pulsatile and gradual genes under 100 µM H_2O_2 treatment provided at t = 0 min, (pink: pulsatile, blue: gradual, n ≥ 1500 and n≥3 repeats per gene. (**D**) Kymograph of PhemH and PtrxC transcription reporter expression representative of pulsatile and gradual induction with 100 µM H_2O_2, respectively. (**E**) Plot shows mean (bold) and single cell (thin) reporter expression levels of mother cells for PhemH (pink, pulsatile) and PtrxC (blue, gradual) under 100 µM H_2O_2 treatment provided at t = 0 min.*

Nevertheless, the transcriptional reporter data and RNA seq analysis would be qualitatively comparable at the start of the treatment. This allows for the identification of induced and repressed genes that vary dramatically in the magnitude of their expression levels. Moreover, we performed experiments using the AB1157 strain of *E. coli* that carries an amber mutation in RpoS[285]. This allowed us to isolate the role of OxyR in gene regulation without the influence of stationary phase regulation by RpoS, Consequently, there may be variations in the genes (co-)regulated by RpoS. To further characterise differences in the regulation between genes, we computed the coefficient of variation (CV, variance normalised by the mean) across the expression levels of the 31 genes. The gene-to-gene variation was low in untreated cells, greatest during the transient expression peak shortly after treatment, and intermediate during steady-state treatment [Figure 5.1D]. This suggested that the genes vary not only in expression magnitude but also show pronounced differences in induction timing and dynamics.

5.4 Transient growth inhibition causes a genome-wide expression pulse during stress

We are able to analyse cell growth dynamics in the microfluidic devices at the same time as gene expression level. Importantly, this analysis revealed that the expression pulse at the start of stress treatment precisely coincides with a period of transient growth inhibition [Figure 5.3A]. During normal growth, protein concentrations stay constant in a cell because the expression rate is balanced with the dilution of molecules due to cell growth and division. H_2O_2 stress is known to rapidly stall cell growth which is triggered by an OxyS-mediated cell cycle arrest[162]. To remove the effect of growth dynamics on genes in the OxyR regulon, we normalised changes in expression level by the growth rate, to give a measure of the promoter activity [262]. 31 genes were categorised as upregulated genes and downregulated genes if there was significant increase or decrease in promoter activity post H_2O_2 treatment. Surprisingly, 15 of the 31 genes that show an expression pulse after treatment actually display a significant reduction in promoter activity [Figure 5.3B, C] indicating down regulation. In other words, the transcription rate from these promoters is downregulated in response to H_2O_2, but the reduction in growth rate outweighs this effect, resulting in an effective accumulation of proteins and the illusion of gene upregulation. These conclusions are supported by studying the constitutively-expressed P*rna1* promoter that is not part of the OxyR regulon, which our

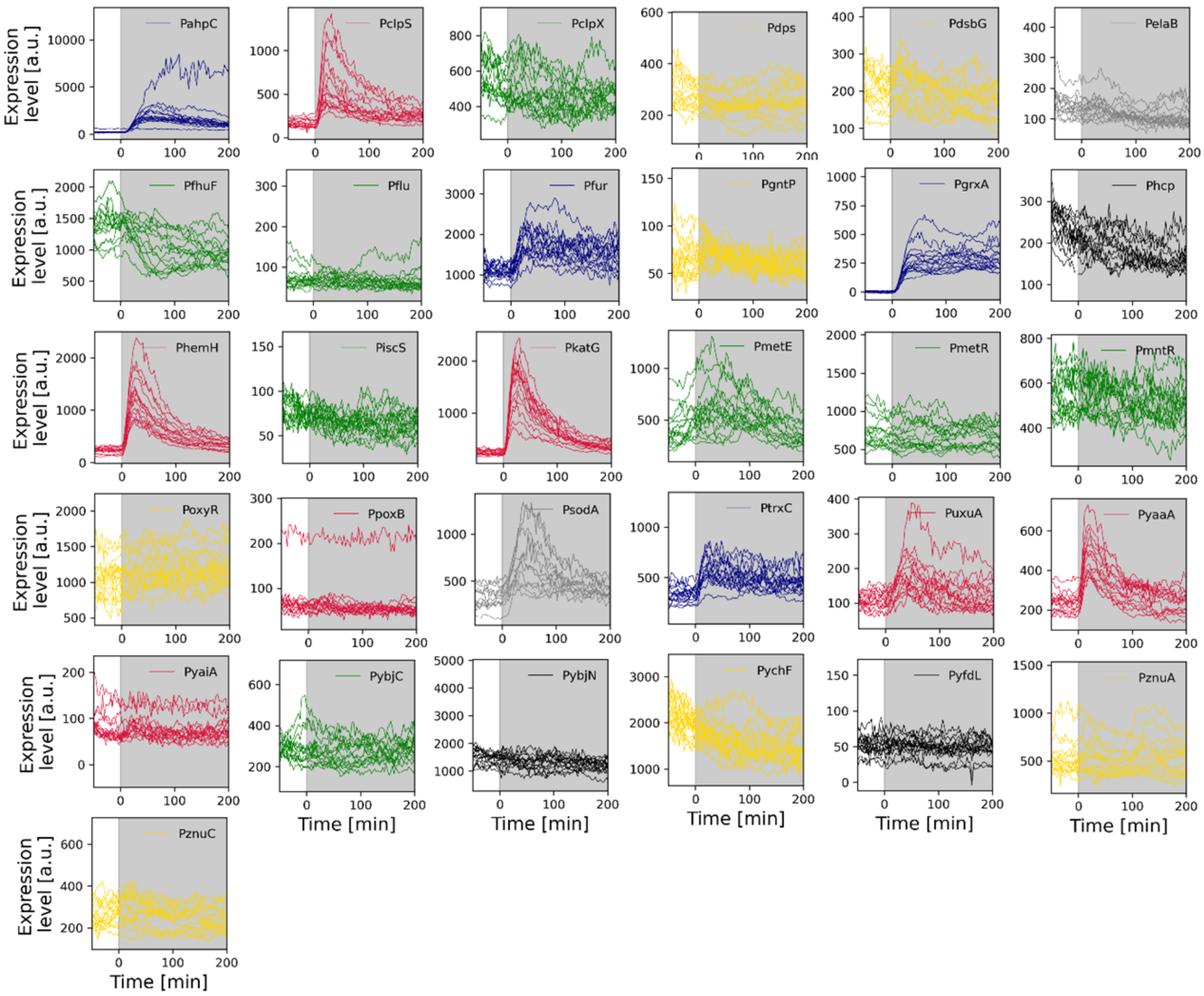

Figure 5.5 Single cell expression traces of oxidative stress response genes display the cell-cell variability:

Single cell expression levels of mother cells for 31 transcriptional reporters with constant 100 µM H_2O_2 *treatment from t = 0 minutes (shaded region). Line colours correspond to the gene regulation categories as explained in Figure 5.3B (pulsatile: pink, gradual: blue, down-regulated: green, transiently up-(grey) or down- (yellow) regulated post treatment, no change in promoter activity: black). n = 15 representative traces per reporter.*

analysis shows has a similar expression pulse but constant promoter activity [Figure 5.3C]. That is, we find that the growth arrest-dependent accumulation of proteins is a global genome-wide effect and not specific to oxidative stress response genes. 13 genes displayed upregulation and 3 genes (P*hcp*, P*yfdL*, P*ybjN*) showed no significant change in promoter activity at any time [Figure 5.3B, C]. 8 of the 15 downregulated genes, and 11 of the 13 upregulated genes showed significantly lower and higher promoter activity respectively, at steady-state after prolonged treatment compared to untreated cells, while other (7 downregulated and 2 upregulated) genes only showed a transient down- and up-regulation during the first ~100 minutes of treatment.

5.5 Upregulated genes exhibit pulsatile or gradual induction dynamics

We next focused on the 11 genes whose gene expression increases and promoter activity shows significant upregulation of different magnitudes with H_2O_2 treatment [Figure 5.3B, 5.5]. We analysed the expression levels during the transient and steady state by analysing the extent of pulsing in a plot of the reporter expression level during the transient peak versus the level at steady-state [Figure 5.4A]. This analysis reveals that the upregulated genes cluster on 2 distinct slopes. The clustering was performed using K-means clustering from the ckwrap library in Python. Seven of the upregulated genes (P*katG*, P*yaaA*, P*clpS*, P*hemH*, P*uxuA*, P*poxB*, P*yaiA*) genes all have a high ratio of peak/steady-state ~ 3, while the other upregulated genes (P*grxA*, P*trxC*, P*fur*, P*ahpC*) share a lower ratio of peak/steady-state ~ 1.5 [Figure 35.4B]. The former class of genes showed a strong initial expression pulse that decays rapidly after its peak and stabilises at a low steady-state level (hence termed "pulsatile"). In contrast, the genes with lower peak/steady-state ratioshowed a gradual induction to an elevated steady-state level (hence termed "gradually induced") [Figure 5.4C, D]. After classifying the up-regulated genes into two groups based on the peak/steady-state ratio, we also noticed that the pulsatile genes are generally activated earlier after the onset of H_2O_2 stress than the non-pulsatile genes [Figure 5.4E, 5.5].

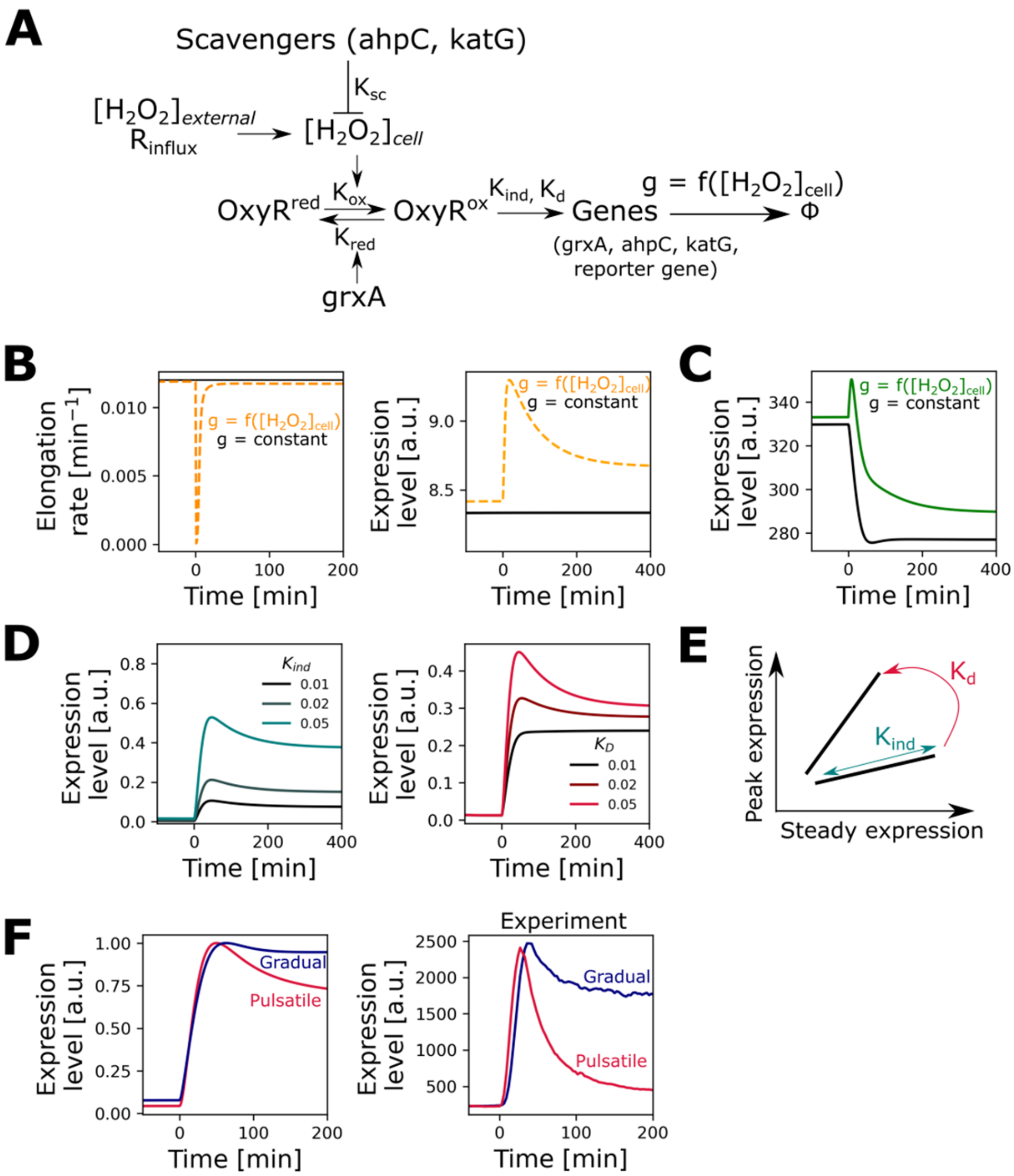

Figure 5.6 A model of the oxidative stress response predicts the molecular basis of the different categories of gene regulation:

*(**A**) Schematic represents the oxidative stress response model. The cells experience influx of H_2O_2 at R_{influx} rate, causing OxyR oxidation and induction of stress response genes. GrxA (glutaredoxin-1) converts oxidised OxyR back to its reduced form and scavenging enzymes AhpC and KatG lower the intracellular H_2O_{2cell} concentration. The expression of the proteins is balanced by dilution due to cell growth, where the cell elongation rate g is a function of H_2O_{2cell}. OxyR also regulates a transcriptional*

*reporter gene which has no function in the response itself. (**B**) Effect of growth inhibition by H_2O_2 on gene expression dynamics. (left) Cell elongation rate affected by intracellular H_2O_2 concentration (orange dashed) compared to constant growth rate unaffected by H_2O_2 (black). H_2O_2 treatment provided at t = 0 min. (right) Expression level of a constitutively-expressed reporter gene (not regulated by OxyR) shows a passive induction pulse in the case where H_2O_2 inhibits cell elongation (orange) and no induction effect when the elongation rate is unaffected by H_2O_2 (black). (**C**) Expression dynamics of a negatively regulated reporter gene in the case where cell elongation rate is affected (green) or unaffected (black) by H_2O_2. (**D**) Induction of positively-regulated reporter genes for varying values of induction rate (K_{ind}, left) and promoter dissociation constant of oxidised OxyR (K_d, right) with H_2O_2 treatment from t = 0 min. K_{ind}/K_d ratio was kept constant for curves with varying K_d. (**E**) Schematic represents the effect of K_{ind} (teal) and K_d (pink) on the gene expression dynamics. Pulsatile genes with high peak/steady ratio are characterised by a higher K_d value, while K_{ind} determines the overall magnitude of the induction without affecting the peak/steady ratio. (**F**) Mean gene expression levels from model (left) and experiments (right) of representative genes for the two categories of positive regulation – PkatG (pink, pulsatile gene) and PahpC (blue, gradually induced gene) of frontier cells treated with 100 µM treatment from t = 0 min (n≥3 repeats).*

5.6 Modelling explains the different regulation patterns

What are the mechanisms generating these different regulatory patterns? Oxidative stress tolerance entails the regulation of genes involved in ROS scavenging, redox balance, and metal ion homeostasis, the expression of which is linked via feedbacks with various metabolic pathways[33,84,85,97,159,160,163–166,168,173,270–284]. Furthermore, several genes in the OxyR regulon are co-regulated by more than one transcription factor[109,270,286–289]. It is therefore unsurprising that these genes can show a range of expression patterns. To understand the specific role of OxyR in this, we constructed a minimal mathematical model, as described in Chapter 4, based on the ordinary differential equations to describe changes in gene expression over time. Here, H_2O_2 permeates through the cell membrane and oxidises OxyR, which leads to the induction of genes of the oxidative stress response regulon[290][Figure 5.6A]. For simplicity, we reduced the operon to include only *grxA* (glutaredoxin-1) that converts OxyR back to its reduced form, the genes *ahpCF* (alkylhydroperoxidase) and *katG* (catalase) that scavenge intracellular H_2O_2, and a ‘reporter gene’ that is induced by OxyR but does not have a functional role (to mimic the GFP reporters used in experiments). Gene expression increases on induction by OxyR and decreases due to dilution by cell growth. The growth rate slows down with increasing H_2O_2 concentration.

In Chapter 4, we showed that this model recapitulates many aspects of the gene regulatory response and growth dynamics of *E. coli* with H_2O_2 treatment. We here focus on probing the mechanism behind the different expression patterns seen across the genes in the OxyR regulon. We first tested if the model can explain the passive gene induction due to growth arrest-dependent accumulation of proteins. Indeed, when the expression of the reporter gene was uncoupled from OxyR regulation in the model, the gene still showed the expression pulse during the transient growth arrest while the promoter activity stayed constant [Figure 5.6B]. Next, for a reporter gene that is downregulated by OxyR, we observed a similar induction pulse followed by a decrease in expression [Figure 5.6C].

We devised a simple model for OxyR-dependent gene regulation that involves only two parameters: K_{ind} reflects the maximal expression rate when the promoter is fully occupied by oxidised OxyR, and K_D reflects the dissociation constant of oxidised OxyR from the promoter. Varying these two parameters allowed us to shift expression dynamics from gradual to pulsatile. Specifically, changing K_D affected the *peak/steady-state* ratio of the gene, with pulsatile genes being characterised by a high K_D value [Figure 5.6D]. K_{ind} determined the position of the gene along the slope in a *peak vs steady-state* plot. Hence, the two categories of genes, pulsatile and gradual, which fall on two separate slopes, can be explained by two distinct promoter dissociation constants of OxyR [Figure 5.6D, E]. This

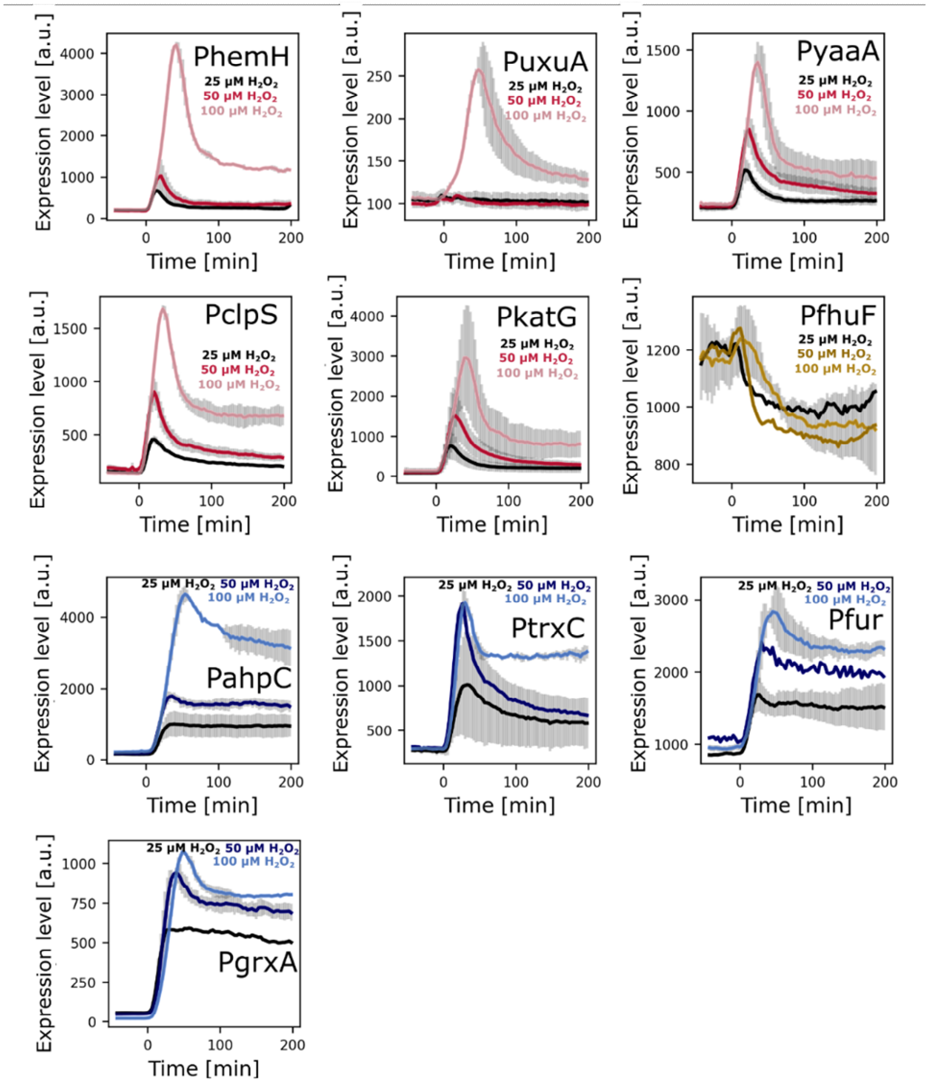

Figure 5.7 Pulsatile genes exhibit higher expression sensitivity to H_2O_2 stress intensity:
Mean expression of frontier cells for the indicated transcriptional reporters under 25 µM, 50 µM and 100 µM H_2O_2 provided at t = 0 min (red: pulsatile induced, blue: gradual induced, yellow: downregulated). Error bars: standard deviation (n ≥ 2 repeats per gene).

prediction matches prior measurements for some of the genes[156]. For example, the dissociation constant of oxidised OxyR from the pulsatile gene promoter P*katG* is an order of magnitude higher than for the gradually induced P*ahpC* promoter[156] [Figure 5.6F]. More broadly, the model demonstrates that coupling the simple OxyR redox switch with cell

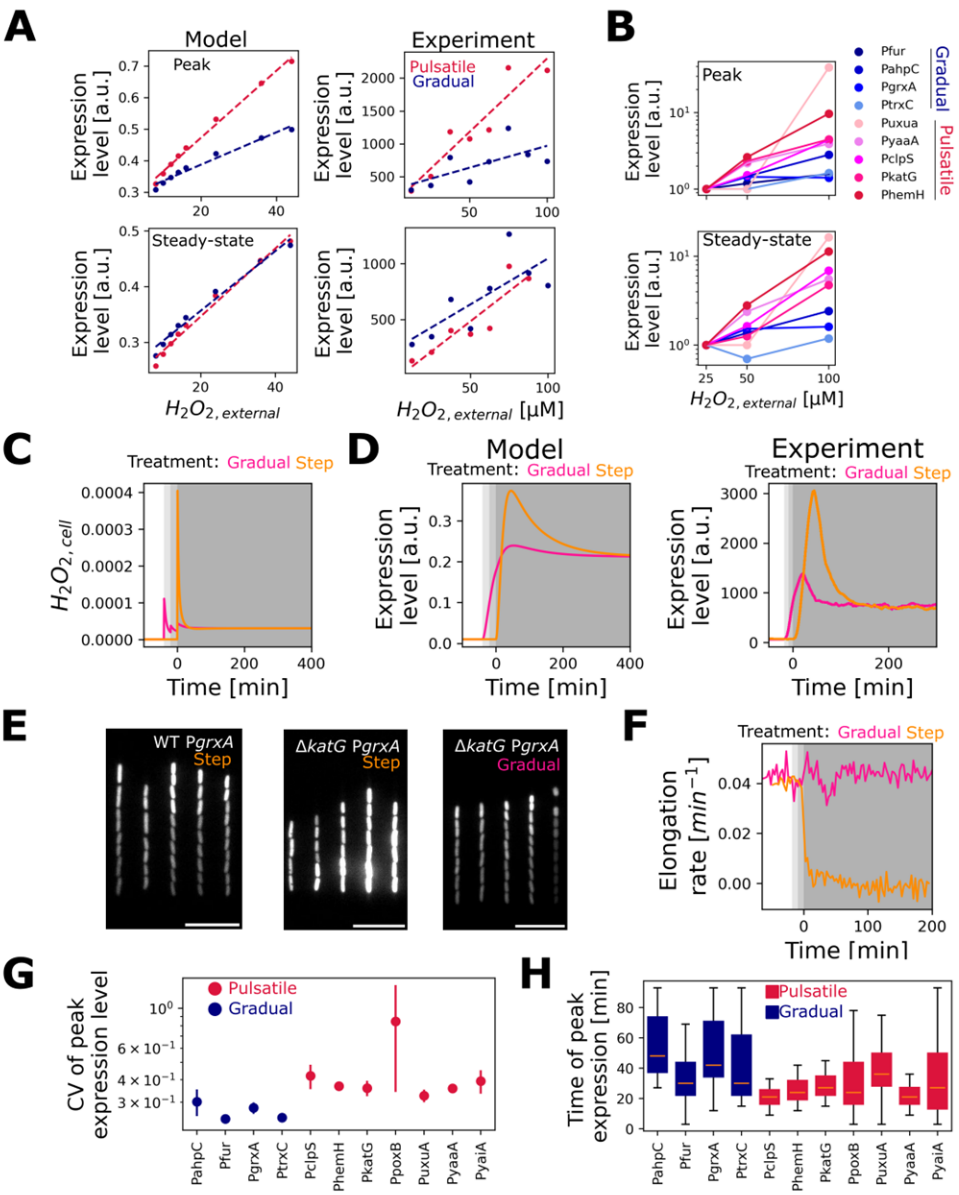

Figure 5.8 Pulsatile genes respond quickly to bridge the adaptation lag after H_2O_2 treatment: *(**A**) The response of pulsatile genes is more sensitive to changes in H_2O_2 concentration than gradually induced genes. Model outputs (left) and experimental data (right) for peak (top) and steady state (bottom) expression level of PkatG (pulsatile gene, pink) and PgrxA (gradual, blue) across a range of external H_2O_2 concentrations. Dashed lines show linear fits. (**B**) Relative changes in gene expression at peak (top) and steady-state (bottom) of frontier cells with H_2O_2 treatment ranging from 25 μM to 100 μM H_2O_2. Pulsatile genes (pink) show higher dose-sensitivity compared to gradual induced genes (blue)(n≥2 repeats per gene per H_2O_2 concentration). (**C**) Model results of intracellular $H_2O_{2,cell}$ concentration with step treatment (100 μM H_2O_2, orange) from t= 0 minutes or gradual treatment (from 25 to 50 to 100 units H_2O_2, pink). (**D**) Mean expression levels for model (left) and experiments (right) of pulsatile gene PkatG for step (orange) or gradual H_2O_2 treatments (from*

*25 μM to 50 μM to 100 μM H_2O_2, pink) as depicted in panel C (n≥2 repeats). (**E**) Snapshot of PgrxA expression at steady state for step (left and middle) or gradually (right, as shown in panel C-D) treated wild-type (left) cells and ΔkatG cells (middle and right) after 120 min of treatment with 100 μM H_2O_2. (**F**) Gradual treatment enables adaptation of ΔkatG cells. Mean elongation rate for ΔkatG cells (located at a position with 3 barrier cells) treated with 100 μM H_2O_2 in a step (orange) or gradual (pink) manner (as depicted in panel C-E, n≥2 repeats). (**G**) Coefficient of variation (C.V.) for peak gene expression values of frontier cells showing cell-to-cell heterogeneity under 100 μM H_2O_2 treatment (blue: gradual, pink: pulsatile genes, error bars represent standard deviation, n≥3 repeats per gene). (**H**) Boxplots indicate the median of time taken to reach the peak gene expression for individual mother cells under 100 μM H_2O_2 treatment (gradual: blue, pulsatile: pink; box length extends to the lower and upper quartile with error bars representing the range, n≥3 repeats per gene).*

growth is sufficient for explaining the different gene expression dynamics we observed in experiments.

5.7 Model predictions suggest functional differences between pulsatile and gradually induced genes

Differences in the dissociation constant of OxyR should affect the sensitivity of the promoter activity to changes in H_2O_2 concentration. Specifically, promoters with a high K_D for OxyR are expected to show an approximately proportional increase in activity with H_2O_2 concentration, whereas the activity of promoters with a low K_D should saturate and show little dependence on H_2O_2. Indeed, experiments and model outputs showed that rising H_2O_2 concentration caused a much steeper increase for the pulsatile P*katG* promoter activity compared to the gradually induced P*grxA* promoter [Figure 5.7, 5.8A]. Similarly, other pulsatile genes showed a higher sensitivity to H_2O_2 compared to gradually induced genes [Figure 5.7, 5.8B]. The model further predicts that the pulsatile gene induction is a consequence of response to a transient spike in intracellular H_2O_2 which accumulates until the increased level of scavenging enzymes tips the balance [Figure 5.8C]. Consistent with this interpretation, experiments showed that the expression pulse of P*katG* was much reduced

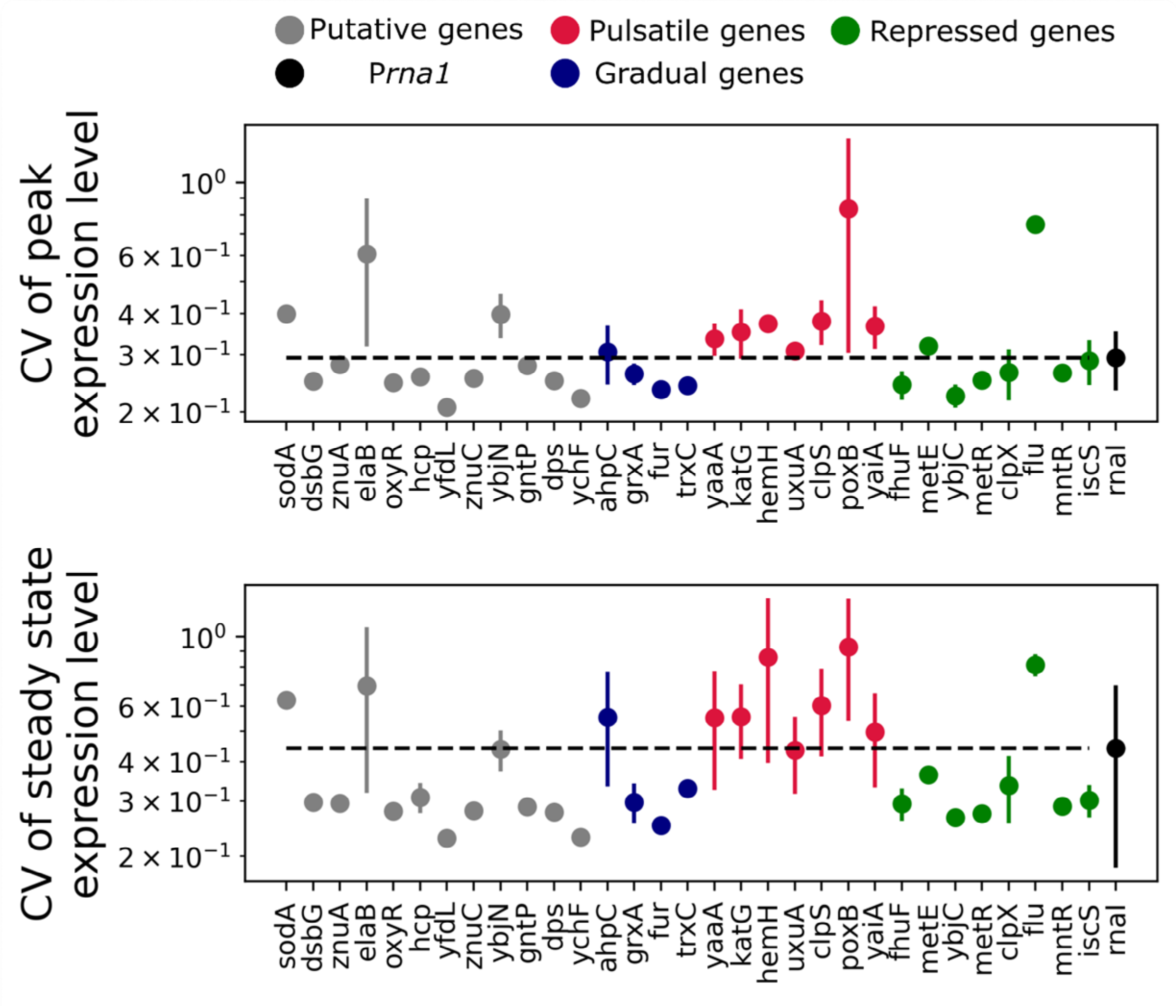

Figure 5.9 Cell-cell variability in gene expression magnitude for oxidative stress response genes in different regulation categories:

Coefficient of variation for peak (top) and steady state (bottom) expression values of frontier cells under 100 µM H_2O_2 treatment (pulsatile genes: red, gradual: blue, negative: green, putative: grey, constitutive Prna1: black). Error bars represent standard deviation (n ≥ 3 repeats per gene).

when cells responded to a gradually increasing dose of H_2O_2 instead of a step treatment [Figure 5.8D].

What is the benefit of pulsatile expression of some genes and gradual induction of others? We suggest that the functions of the pulsatile genes must be particularly important in response to sudden stress, whereas gradually induced genes may be more important during prolonged stress exposure. Consistent with this notion, deletion of the pulsatile *katG* gene made cells extremely sensitive to sudden H_2O_2 treatment, but these cells were still able to survive a gradually increasing dose of H_2O_2 reaching the same final concentration [Figure 5.8E, F]. This suggests that the expression pulse of *katG* is critical for the rapid production of catalase enzymes to counteract the transient spike in intracellular H_2O_2 but *katG* expression becomes dispensable after the initial adaptation delay[188]. H_2O_2 tolerance during prolonged exposure is then provided by the gradually upregulated AhpCF (alkylhydroperoxidase), which scavenges lower concentrations of H_2O_2 efficiently[85]. In agreement with these observations, expression dynamics in *P. aeruginosa* were also variable across oxidative stress response genes[291]. In *Mycobacterium tuberculosis*, induction of *katG* showed higher sensitivity to H_2O_2 than *ahpC* [292], matching the pulsatile behaviour of *katG* and gradual induction of *ahpC* in *E. coli*.

5.8 Pulsatile genes show higher cell-to-cell expression heterogeneity

Our single-cell data allowed us to assess if there are any differences in cell-to-cell expression heterogeneity between pulsatile and gradually induced genes. We found that the amplitude of the expression peak reached by individual cells was more variable for pulsatile genes compared to gradually induced genes, indicating that a rapid response comes at the cost of lower precision at a single-cell level [Figure 5.5, 5.8G, 5.9]. Indeed, the time of induction after the onset of stress was shorter and less variable for the pulsatile genes [Figure 5H]. Regulation of pulsatile genes, therefore, appears to prioritise control of the timing over the magnitude of the response [Figure 5.8G-H, 5.9].

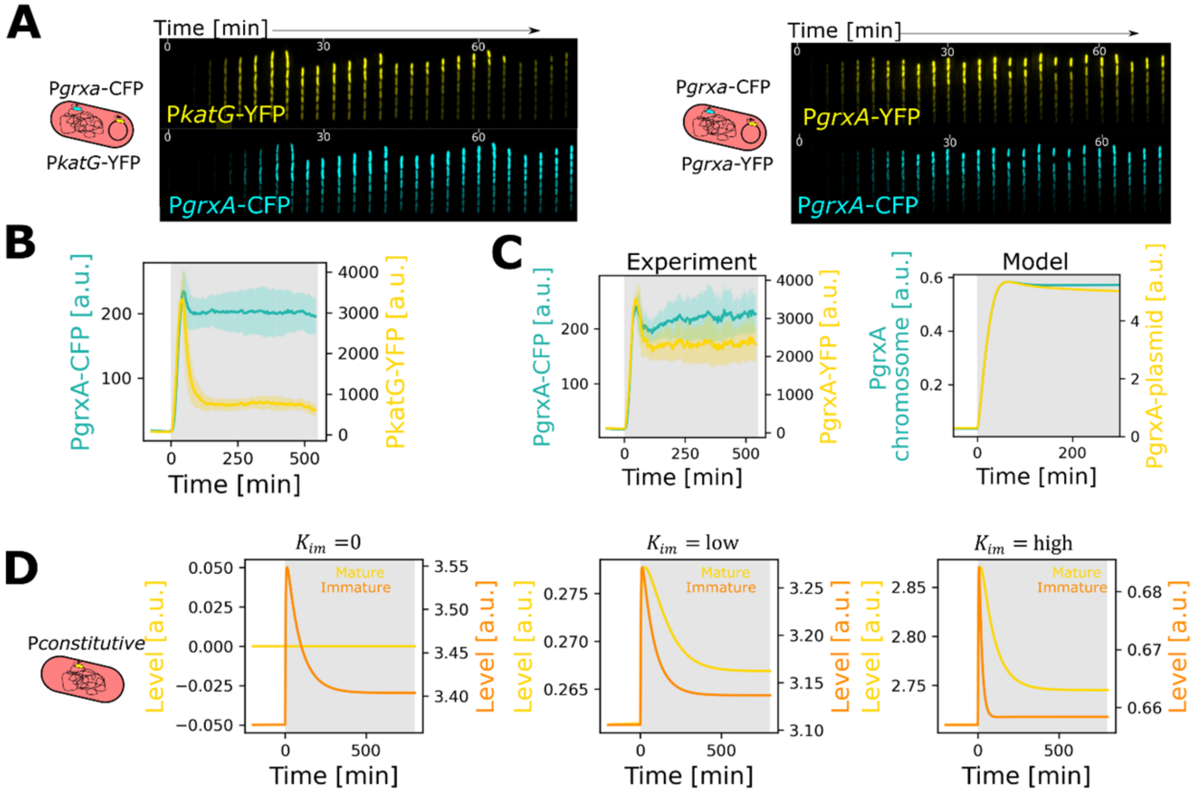

Figure 5.10 Model to account for differences in reporters to follow gene expression dynamics: ***(A)*** *E. coli dual reporter strains with PkatG-YFP on plasmid + PgrxA-CFP on chromosome (left) and PgrxA-YFP on plasmid + PgrxA-CFP on chromosome (right, control strain). Kymographs represent gene expression levels for both reporters in cells treated with 100 µM H_2O_2.* ***(B)*** *Mean expression of PgrxA-CFP and PkatG-YFP for frontier cells under 100 µM H_2O_2 provided at t = 0 min (n= 3 repeats, error bars: standard deviation).* ***(C)*** *Mean expression of PgrxA-CFP (cyan) and PgrxA-YFP (yellow) for frontier cells under 100 µM H_2O_2 provided at t = 0 min from experiments (left) and model output (right) (n= 3 repeat, error bars: standard deviation).* ***(D)*** *Levels of immature (orange) and mature (yellow) reporter proteins produced by constitutively expressed gene for varying K_{im} (rates of conversion of immature to mature protein; no conversion (left), low rate (middle), high rate (right)) treated with H_2O_2 provided at t = 0 min from model output.*

We next asked to what extent the expression of pulsatile and gradually induced genes is coordinated within the same cell. To this end, we constructed a dual-reporter strain with two fluorescently labelled transcriptional reporters: the pulsatile P*katG*-YFP reporter expressed from a plasmid and the gradually induced P*grxA*-CFP reporter inserted on the chromosome [Figure 5.10A]. We also constructed a control strain with two P*grxA* reporters, one marked

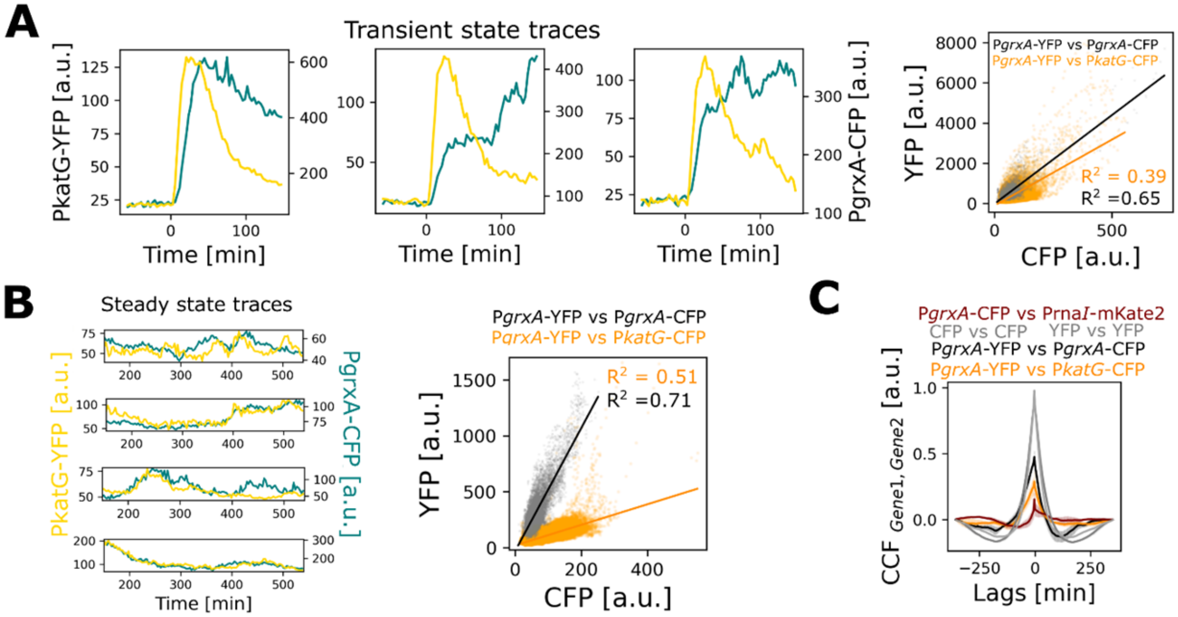

Figure 5.11 Coordination of pulsatile and gradual gene regulation in single cells:
*(**A**) (left) Representative expression of PkatG-YFP (yellow) and PgrxA-CFP (cyan) for individual mother cells after treatment with 100 µM H_2O_2 from t = 0 min. (right) Peak expression of PgrxA-YFP vs. PgrxA-CFP (black) and PgrxA-YFP vs. PkatG-CFP (orange) for mother cells after treatment with 100 µM H_2O_2. The lines represent linear fits. (**B**) (left) Representative expression traces of PkatG-YFP (yellow) and PgrxA-CFP (teal) for individual mother cells during steady state with 100 µM H_2O_2 treatment from t = 0 min. (right) PgrxA-YFP vs. PgrxA-CFP (black) and PgrxA-YFP vs. PkatG-CFP (orange) expression for mother cells during steady-state with 100 µM H_2O_2 treatment. The lines represent the linear regression fit to the data sets. (**C**) Mean temporal cross-correlation of steady-state expression dynamics between PgrxA-YFP and PrnaI-mKate2 (red), PgrxA-YFP and PgrxA-YFP or PgrxA-CFP and PgrxA-CFP (dashed grey), PgrxA-YFP and PgrxA-CFP (black), PgrxA-YFP and PkatG-CFP (orange) for mother cells under 100 µM H_2O_2 treatment.*

with CFP on the chromosome and one marked with YFP on the plasmid, to account for variability due to differences in fluorescent proteins (YFP versus CFP) and the difference in gene copy numbers of the reporters (chromosomal versus multi-copy plasmid) [Figure 5.10A]. The mean expression dynamics of the dual reporter strains matched our previous analysis for P*katG* and P*grxA* in single reporter strains [Figure 5.10B]. Interestingly, for the control strain, the plasmid-expressed P*grxA* displayed a higher expression pulse compared to the P*grxA* reporter on the chromosome, even after normalising for differences in the steady-

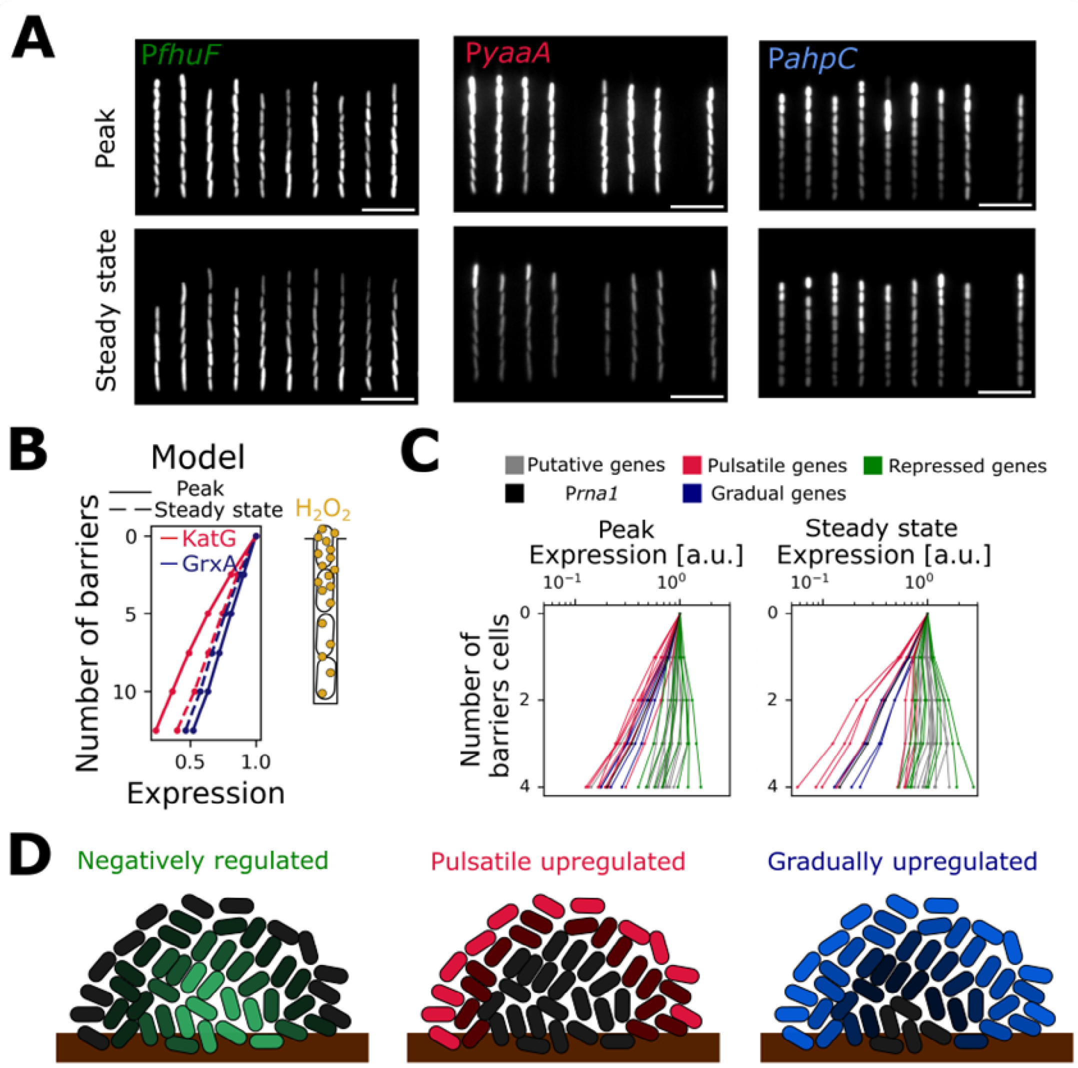

Figure 5.12 Spatio-temporal expression patterns across the OxyR regulon:
*(**A**) Snapshots of cells with representative reporters for the three categories of gene regulation: PfhuF (left, downregulated), PyaaA (middle, pulsatile induced) and PahpC (right, gradual induced) during peak expression (top) and at steady-state (bottom) with 100 µM H_2O_2 treatment. (**B**) Scavenging of H_2O_2 by bacteria creates $H_2O_{2,external}$ gradients in the growth trench from the source of treatment at the open end to the mother cell at the closed end. Model output for the expression of KatG (pulsatile, red) and GrxA (gradual., blue) across the growth trench (increasing number of barrier cells) relative to the expression of frontier cells. Peak expression (solid lines) and steady-state expression (dashed lines). (**C**) Mean expression of 31 transcriptional reporters in cells with different number of barrier cells with 100 µM H_2O_2 treatment relative to the expression of frontier cells during peak expression (left) and steady-state (right) (pulsatile: pink, gradual: blue, negative: green, constitutive Prna1: black, putative: grey; n≥3 repeats per gene). (**D**) Schematic depicting the spatial variation across a bacterial population in the expression of OxyR-controlled genes that are downregulated (left), pulsatile induced (center) and gradually induced (right) under H_2O_2 treatment.*

state level [Figure 5.10C]. This is explained by our model, which showed that the plasmid copy number increases transiently when the cell growth rate slows during the onset of H_2O_2 treatment [Figure 5.10C]. This effective increase in gene dosage leads to an additional expression boost for the plasmid-based promoter. The effect of plasmid copy number variation is considered by modifying the equation for reporter gene expression (Eq 5.1) such that the gene induction is proportional to the plasmid copy number n. The change in plasmid copy number is computed as a constitutive expression R_n diluted by cellular growth (Eq 5.2).

$$\frac{d[reporter]}{dt} = R_{reporter,basal} + K_{reporter,act} \cdot \left(\frac{[OxyR]_{total}-[OxyR]_{Red}}{([OxyR]_{total}-[OxyR]_{Red})+Kd_{reporter}}\right) - g \cdot [Reporter] \qquad \{\text{Eq } 5.1\}$$

$$\frac{dn}{dt} = R_n - g \cdot n \qquad \{\text{Eq } 5.2\}$$

Together, the reporter gene expression on a plasmid is quantified as follows:

$$\frac{d[Plasmidreporter]}{dt} = R_{reporter,basal} + K_{reporter,act} \cdot \left(\frac{[OxyR]_{total}-[OxyR]_{Red}}{([OxyR]_{total}-[OxyR]_{Red})+Kd_{reporter}}\right) . n - g \cdot [Reporter] \qquad \{\text{Eq } 5.3\}$$

In this study, we utilise fluorescence intensity of fast maturing fluorescent proteins (such as GFP and CFP) to assess gene promoter activity. Since different fluorescent proteins exhibit distinct maturation kinetics, we account for maturation lag by introducing a model of a constitutively expressed protein. We formulate the equations to describe the levels of immature (C_{im}) and mature (C_m) fluorescent protein levels as follows: Immature proteins are constitutively expressed at a rate of $R_{C_{im}}$ and convert to mature proteins at a rate of K_{im}. For slow maturing fluorescent reporters like RFP, K_{im} is higher than that of fast-maturing GFP and CFP.

$$\frac{dC_{im}}{dt} = R_{C_{im}} - (g + K_{im}) \cdot [C_{im}]$$

$$\frac{dC_m}{dt} = K_{im} \cdot [C_{im}] - g \cdot [C_m]$$

For slow maturing proteins, the dynamics would proceed at a slower pace, resulting in a flattened peak following H_2O_2 treatment during the dip in elongation rate. Conversely, fast maturing proteins exhibit a quicker onset of expression and a peakier expression [Figure 5.10D].

Focusing on the dual reporter strain, we found that P*katG* and P*grxA* expression showed relatively little correlation during the transient expression pulse [Figure 5.11A]. However, both promoters exhibited substantial fluctuations in gene expression during prolonged treatment, and we found that these fluctuations were closely correlated [Figure 5.11B]. This was evident from gene expression levels at discrete time points and from temporal cross-correlation analysis [Figure 5.11C]. Together, our single-cell analysis revealed that pulsatile and gradually induced genes are tightly coordinated during prolonged stress, but appear to be uncoupled in regulation during the transient response to sudden stress.

5.9 Downregulated, pulsatile, and gradually induced genes show different spatial patterns in cell populations

Cellular uptake and scavenging of H_2O_2 causes collective detoxification of the environment within cell populations. This phenomenon is remarkably effective, with each individual cell reducing the local H_2O_2 concentration by around 30% in its vicinity in a 1D growth channel, leading to steep spatial H_2O_2 gradients from the edge to the interior of bacterial colonies as shown in Chapter 3. The genes in the OxyR regulon are marked by different sensitivities to changes in H_2O_2 concentration. Do the genes differ not only in the temporal expression dynamics but also show different spatial patterns of gene expression? Indeed, quantifying expression levels from the frontier cells located at the open end of the growth channel to the mother cell at the closed end revealed clear differences. We find a steeper decay for pulsatile genes compared to the gradually induced genes in our model and experiments [Figure 5.12]. Conversely, downregulated genes exhibited an inverse gradient with the lowest expression seen in the frontier cells that are closest to the H_2O_2 source [Figure 5.12A, C]. Notably, even passively induced genes that are not part of the OxyR regulon showed a spatial gradient in expression level that was driven by a more pronounced inhibition of growth for cells that are located closer to the H_2O_2 source, especially during the initial adaptation lag [Figure 5.12C].

5.10 Discussion

Gene regulation in response to environmental changes is essential for cellular adaptation[293]. Recent studies at the single cell level and high-throughput temporal studies have identified serial induction of genes[74,262,263,265–267], which remained elusive in bulk assays. In this study, we investigate the bacterial oxidative stress response to continuous H_2O_2 treatment, where the expression of tens of genes is controlled by a single transcription factor - OxyR [294]. We observed different regulation dynamics across 31 oxidative stress response genes. Our classification of genes as induced or repressed after H_2O_2 treatment is broadly coherent with previous studies[173,270,275]. Our results differ for several genes that were previously shown to exhibit a small increase change in expression, which we find are in fact negatively regulated after accounting for the apparent increase in expression due to the slow-down of growth with stress. Our model suggests that the dissociation constant of OxyR to the promoters (K_d) and the gene induction rate (K_{ind}) together with the effects of the cell growth rate on gene expression can explain the multiple different gene regulation patterns. In particular, we observed two categories of positively regulated genes: pulsatile and gradual, where the former has a high K_d and show a strong transient expression pulse after H_2O_2 treatment, whilst the latter have a lower K_d and activate more slowly and sustain elevated expression rates throughout the treatment. At a single-cell level, expression of pulsatile and gradual genes is highly variable and uncoordinated during the initial expression pulse post H_2O_2 treatment. However, the expression fluctuations of both types of genes become temporally correlated at steady-state during prolonged treatment. Previously in Chapter 4, we demonstrated that fluctuations in the oxidative stress response of a single cell arise deterministically, driven by the changes in the external environment. The dynamic surroundings act as a common extrinsic source of fluctuations for both genes within individual cells, leading to the correlated gene expression, as opposed to being a result of noise.

Model and experiments show that a higher sensitivity of pulsatile genes to H_2O_2 dose is important for rapid defence against the sudden burst of intracellular H_2O_2 upon stress exposure. The pulsatile genes are more sensitive to local H_2O_2 fluctuations and therefore display high cell-cell variability in expression magnitude. The varied sensitivity of genes in different categories to changes in H_2O_2 results in spatial stratification of gene expression within a population. Pulsatile genes are expressed only by a small fraction of cells close to the H_2O_2 source, creating steep expression gradients and protecting a larger proportion of the population. By contrast, the gradually and negatively regulated genes show a more consistent response both in space and time, with more cells contributing to protection at the steady state. Gradually induced thioredoxins (grxA[153], trxC[272]) regulate the redox status of proteins, including OxyR. These genes showed a lower expression sensitivity to changes in H_2O_2 levels and hence display more uniform induction across the population. Curiously, many of the pulsatile genes including *yaaA*[164], *clpS*[165], and *hemH*[168], are involved in iron regulation to counter the rapid lethality of H_2O_2 experienced due to the Fenton reaction[106,120,153,188,295]. Therefore, the quick regulation of iron levels by pulsatile genes may aid the cells to adapt before cellular damages accumulate. The ferric iron reductase FhuF[274] is down regulated[173,275] to keep ferrous iron concentrations low. The cells away from the H_2O_2 source exhibit a higher expression of *fhuF* and consistent spatio-temporal dynamics. Interestingly, the two H_2O_2 scavenging enzymes catalase (*katG*) and alkylhydroperoxidase (*ahpCF*) fall into different categories of regulation. Pulsatile k*atG* is important against sudden stress and primarily expressed by frontier cells under continuous H_2O_2 treatment, whereas *ahpCF* efficiently degrades low H_2O_2 levels that reach the rest of the population. Together, our results suggest that the promoter binding affinities of OxyR are tuned to orchestrate a defined programme of gene activation and repression in single cells. This translates to a spatio-temporal gene expression pattern in cell groups, which likely benefits population fitness.

Table 5.1: Genes chosen for this study along with their characteristics.

#	Gene	Function	Implicated in oxidative stress	Regulation in this study (peak /steady-state)	Promoter activity significance value (peak /steady-state)
1	*sodA*	Superoxide dismutase	P [273]	P/-	1.72e^{-06}/n.s.
2	*fhuF*	Ferric iron reductase	N[173,274,275]	N/N	2.21e^{-18}/2.46e^{-10}
3	*trxC*	Thioredoxin 2	P[97,159,173,270,272,274,275]	P/P	2.83e^{-23}/2.65e^{-24}
4	*yaaA*	Suppress intracellular iron levels	P[164,173,274]	P/P	2.23e^{-09}/2.0e^{-12}
5	*dps*	Fe-binding & storage	P[163,173,270,275,277]	N/-	4.9e^{-05}/n.s.
6	*ahpC*	Akylhydroperoxidase	P[84,108,173,270,274,275]	P/P	1.45e^{-17}/4.36e^{-06}
7	*katG*	Catalase	P[84,85,173,270,274,275]	P/P	5.24e^{-22}/2.65e^{-24}
8	*grxA*	Glutaredoxin-1	P[97,159,173,270,275]	P/P	7.029e^{-18}/1.18e^{-18}
9	*dsbG*	Sulfenic acid reductase	P[173,275,278,296]	N/-	1.912e^{-09}/n.s.
10	*znuA*	Zinc transport	P[270]	N/-	7.61e^{-06}/n.s.
11	*metE*	methionine synthase	P/N[270,279]	N/N	3.73e^{-09}/2.31e^{-06}
12	*oxyR*	OxyR	N[160,173,275]	N/-	1.512e^{-09}/n.s.
13	*hemH*	Ferrochelatase	P[168,173,274,275]	P/P	7.029e^{-18}/1.18e^{-18}
14	*mntR*	Mn^{2+} regulator [280]	N[173,275]	N/N	1.359e^{-10}/0.015
15	*gntP*	gluconate permease	N[173,274,275]	N/-	1.512e^{-09}/n.s.
16	*uxuA*	Mannonate hydrolase	N[173,274,275]	P/P	3.36e^{-05}/0.016
17	*iscS*	Iron-sulfur cluster assemby	N[166,274]	N/-	1.29e^{-09}/n.s.
18	*hcp*	Hybrid cluster proteins of Fe/S	P[173,275,281]	-/-	n.s./ n.s.
19	*flu*	surface adhesin	N/P[173,270,275,282]	N/N	0.0076/0.00545
20	*ybjC*	Unknown	N[173,270,274,275]	N/N	1.39e^{-09}/0.00036
21	*ychF*	ATPase	N[173,275,283]	N/-	2.77e^{-06}/n.s.
22	*yfdL*	Putative ligase	-[296]	-/-	n.s./ n.s.
23	*metR*	methionine biosynthesis [297]	P [173,270]	N/N	6.046e^{-09}/3.73e^{-06}
24	*znuC*	Zinc transport [298]	P [173,270]	N/-	1.34e^{-06}/n.s.
25	*ybjN*	Unknown	N[173,275]	-/-	n.s./ n.s.
26	*elaB*	Membrane integrity	P[173,284]	P/P	2.05e^{-05}/n.s.
27	*fur*	iron-homeostatic control protein	P[173,271,274,275]	P/P	2.44e^{-12}/5.60e^{-13}
28	*poxB*	pyruvate:quinoneoxido reductase[299]	P[173,274]	P/P	8.58e^{-07}/6.17e^{-05}
29	*yaiA*	Unknown	P[173,274]	P/P	0.00015/0.00279
30	*clpS*	Iron sequestration	P [165]	P/P	1.3877e^{-13}/1.18e^{-18}
31	*clpX*	Iron sequestration	P [165]	N/N	1.738e^{-05}/3.67e^{-06}

P: positive regulation, N: negative regulation, -: no significant regulation detected, n.s.: p-value>0.05

Chapter 6

Discussion

Bacteria surround us everywhere and constantly experience changes in their environment. In the face of these changes, bacteria get stressed and exploit their complex regulatory networks to respond. Under stress cellular damages are repaired in individual cells, and within populations, cells may interact together to provide collective protection. In this thesis, we investigated bacterial response to oxidative stress – one of the major stresses important in shaping microbial community interactions and impacting host-pathogen interactions[89,141,142,300–303]. Moreover, bacteria frequently experience oxidative stress due to aerobic growth[85,108] and exposure to external agents like antibiotics[5,144,145], radiations[136].

In particular, we studied the response of *E. coli* to H_2O_2, which is a reactive oxygen species. We performed experiments in microfluidic mother machine devices to observe cellular behavior at the single cell level at high temporal resolution and complemented them with quantitative tools including machine learning models, mathematical modelling, and simulations.

6.1 Bacterial stress responses: random or deterministic?

Genetically identical cells often exhibit phenotypic heterogeneity even when they reside in the same external environment[10,11,25] but the sources and consequences of this variability are not well understood. In Chapter 3, we observed a heterogeneous response of a clonal *E. coli* population to H_2O_2. Interestingly, we also observed steep micro-scaled spatial gradients in the stress response across cells. These gradients are formed due to diffusion limitation, where scavenging by individual cells creates sinks of H_2O_2, such that there is a reduction of ~30% H_2O_2 per cell from its surroundings in a 1D growth channel. Previous studies have observed that a population of bacteria exposed to H_2O_2 shows spatial gradients in the expression of catalase enzyme that degrade H_2O_2[91]. While the gradient in H_2O_2 concentrations has been inferred from these studies, the implications at single cell level, especially in terms of phenotypic heterogeneity remained elusive. Stress responses are inherently noisy, and spatial variation of stress penetrance into a population adds another level of complexity that makes it difficult to determine the source of heterogeneity in the responses of cells. To overcome this problem, we used a machine learning (ML) algorithm to search for 'hidden variables' that underlie the cell-cell variability under oxidative stress. Surprisingly, the ML model predicted the variable responses of individual cells with good accuracy solely based on variables that relate to the environment of each cell. This was unexpected because the variability in cellular behaviour observed in the constant environment of microfluidic growth channels is usually attributed to intracellular stochastic molecular processes[11,22–25]. Instead, we found that the spatial structure of neighboring cells is the most important predictor of the oxidative stress response of a focal cell. In particular, an increase in the cumulative volume and surface-area-to-volume ratio of neighbors provides a higher protection to a focal cell. The morphology of neighboring cells changes over time as they grow and divide, modulating the H_2O_2 gradients and hence the local concentration experienced by a focal cell. Therefore, what we observe as a noisy population response is in fact a very precise response of individual cells to the dynamic H_2O_2 concentration in their immediate environment. The steep stressor gradients provide population protection such that only a few cells close to the source sponge up a substantial proportion of the incoming stress agent. Further, this population of cells close to the treatment source displays higher rates of DNA mismatches and a larger reduction in growth rate due to the mutagenic and growth inhibiting effects of H_2O_2. Therefore, this results in variability in cellular growth rate and DNA damage rates within a population under oxidative stress. Our results are in line with bulk mutation rate measurements that show the inverse relation between mutation rates and population densities, which impacts cellular response to environmental variation by modulation of mutagenesis rates[208]. Green *et al.* suggested that density-dependent detoxification of peroxide can modify mutagenesis, which influences community composition as a dynamic trait[304]. Our study suggests that within a community mutagenesis rates are diversified where a small proportion of the population close to oxidative stress source shows higher mutagenesis.

The majority of studies that used mother machine microfluidic devices have explored solely the response of mother cells-i.e. cells at the bottom of the growth channels. This study, however, highlights that bacterial phenotypes can be extremely sensitive to subtle environmental changes even within optimally controlled microfluidic growth chambers. In particular, cell-cell interactions should be considered as a source of phenotypic heterogeneity not only in large populations such as dense cultures and biofilms but also in small populations of only a few cells. We expect our combination of ML and single-cell imaging to be broadly applicable for understanding sources of heterogeneity and population adaptations of bacteria against diverse types of stressors. These approaches can be extended not only to predict the sources of response heterogeneity but causes of other variable behaviors of cells like their fates – survival vs death, which is especially important in the context of stress caused by antibiotics. Further, our approach should be useful for studying other microbiological phenomena related to cell-cell interactions like quorum sensing[41] and division of labor[46,48]. The strong spatial gradients for clonal populations under stress as observed in our study and their impact on cell-cell variability could have implications for bacterial interactions in multi-species communities. Here, production and consumption of metabolites, and the formation of redox and toxin gradients are known to shape bacterial interactions[45,48,305,306], and hence it is important to understand the mechanisms of these processes at a single-cell level. We found in our experiments that mutant cells incapable of scavenging excessive amounts of oxidative stress are protected by wild-type cells with high oxidative stress tolerance. For the mammalian gut, a hypoxic environment is important for nutrient absorption and innate immunity[307]. *E. coli* reside in the large intestine lumen, which lies beneath the epithelial cells. The oxygen levels drop quickly towards the interior of the gut and an oxygen barrier is created[89]. Moreover, at the barrier interface, sulphate-reducing bacteria residing in anaerobic regions produce large amounts of hydrogen sulphide, which on reacting with oxygen produces H_2O_2[89]. Our results would suggest that at these interfaces of dynamic oxygen levels, aerobic cells can protect anaerobic cells in their close vicinity. Hence, the population protection effect and modulation of cellular behavior by levels of ROS in the external environment can be an important predictor of microbial community interactions in the gut. Many such examples exist in natural communities, where nutrients and other metabolites in the environment change temporally and in space affecting the composition and structure of microbial communities[44,45].

The rapid and efficient scavenging activity generates stress gradients within bacterial populations, as observed across various concentrations of H_2O_2 in Chapter 3. This heterogeneity arises due to diffusion limitation, with no discernible differences in growth rates among cells exposed to H_2O_2 concentrations of $\leq 50\mu M$. However, at concentrations exceeding this threshold, cells encounter growth inhibition attributed to elevated intracellular levels of H_2O_2, particularly for those in close proximity to the stress source. In a mixed community, we would anticipate that cells exposed to local H_2O_2 concentrations exceeding

50μM would exhibit lower growth rates, not necessarily due to the cost of diversification, but rather as a consequence of the inhibitory effects of H_2O_2. Such growth inhibitions can be particularly significant for anaerobes or cells with lower H_2O_2 scavenging efficiency, such as Δ*oxyR* cells. Within mixed communities, these strains may find protection through stress scavenging by neighboring cells that have a higher scavenging capacity. In ecological niches characterized by sharp oxygen gradients, these mechanisms and interactions could undergo selection. Examples include environments like the gut or oxic-anoxic interfaces in thermal vents. The bulk studies have informed the global interaction patterns between bacterial strains. However, to uncover the local cell-cell interaction, especially, in a spatially structured community against varying environments, we need to investigate cellular behaviour through a single cell perspective.

6.2 Deterministic chaos in cellular response

In Chapter 4, we built a mathematical model to predict the behaviour of a bacterial population at the single cell level to understand the mechanisms that underlie the heterogenous response to oxidative stress. We simulated bacterial growth in microfluidic channels. The simple 1D growth geometry allowed us to parametrise the model with experiments performed in 'mother machine' devices and generate experimentally testable predictions. The output recapitulated H_2O_2 and stress response gradients in the cell population. It further predicted periodic fluctuations in gene expression which correlated with the cell cycle time of individual cells. This is in line with our observations described in Chapter 3, where we found that the fluctuations in the response of individual cells are anticorrelated with changes in the number of neighbouring cells that fluctuate according to the cell cycle. Surprisingly, when we added the inhibition effect of H_2O_2 on growth rate in our model, the oxidative stress response traces of single cells no longer displayed periodic fluctuations but seemingly random dynamics. Moreover, an infinitesimal change in the spatial structure of the cells at the start of the simulation resulted in diverging response traces, prompting us to consider that chaos may play a role in the system. Chaotic systems are characterised by a set of deterministic rules that result in dramatic differences in output for infinitesimal changes in initial conditions[243]. The amplification of changes in initial conditions over time renders it impossible to forecast the dynamics over longer time scales. Many studies have suggested that chaos is common in biology[210,211,227] but it has been a controversial topic. Considering that biological systems are noisy; it remains uncertain if the observed fluctuations are random or follow deterministic chaos. While many studies have relied on modelling data that supports chaos[191,211,212,220,221,226,230], the predictions are usually not testable experimentally because most biological systems cannot be monitored for sufficiently long times under constant external conditions. Our study system provided an opportunity to do so. We used the Grassberger-Proccacia algorithm[193] and a recently introduced chaos detection algorithm[191] and found that the experimentally observed oxidative stress response dynamics have deterministic drivers. We show that the response of a focal cell is determined by the feedback between cellular growth rate, cell-cell interaction, and stress response. The small differences in the initial conditions of a cell are amplified by this feedback generating divergent outputs, resulting in chaos. To rigorously demonstrate chaos and its emergence, we identified the parameters of our model to make or break chaos and found close correspondence between experiments and simulations. We found that a strong stress response results in chaos, suggesting that under high stress conditions, chaotic gene regulation can generate variability in bacterial responses without the requirement of noise. Stochasticity can diversify the response of individual bacteria under stress but a noisier response may compromise accuracy. Deterministic chaos driven dynamics could overcome this such that the population is diversified by individual cells precisely responding to their dynamic environment.

Our approach and findings motivate further research into the existence of chaos in bacterial responses to different stresses. Chaos may be widespread, especially in cases where cell-cell interactions modify the external environment and cellular growth rates are affected. Further, a recent study by Karkaria *et al.* suggested the potential for chaos in small microbial communities that might interact for resources, communication, or warfare[211]. Hence, our model and experimental approach could test the existence of chaos and probe the underlying mechanisms that could shift community interactions towards or away from chaos. Moreover, Sella *et al.* pointed towards the existence of chaos in host-microbiome interactions that might aid the short-term predictability of infections, for instance[308]. Cell-cell variability is often observed in stress responses but cells exhibit variability during normal growth as well, for instance, in their cell-cycle duration. Sandler *et al.*, found that the variability in cell-cycle duration stems from deterministic factors[194]. They suggest that probing these factors can reduce heterogeneity in cancer cells or in cells responding to antibiotics, making treatment strategies more successful.

Under lethal levels of stress or environmental cues of cell lysis, cells cease to survive. The death of cells impacts cellular interaction, thereby affecting population response dynamics. Here, we explored chaotic dynamics generated by the strong responses of living bacterial cells, it would be important to investigate how cell death impacts chaos. Moreover, it would be interesting to investigate if there are deterministic factors underlying cell fate. This would allow the forecasting of cell death events, which can inspire the design of more impactful cancer and bacterial infection treatment therapies.

6.3 Gene regulation coordination in bacterial oxidative stress response

In Chapter 5, we investigate how bacteria manage the regulation of gene networks in the face of stressful conditions. Many stress responses have one master transcription factor regulating multiple target genes that form its regulon. Many population-average studies have shown that regulatory dynamics are complex where genes within the same regulon show differential regulation. Here, we asked how differential gene expressions under continuous H_2O_2 stress are regulated to provide individual and collective protection as observed in Chapters 3 and 4. We characterised the transcriptional regulation of thirty-one genes implicated in oxidative stress response. As expected, the regulation was multiplexed with each gene exhibiting unique magnitude, induction rates, and up- versus down-regulation. A few genes were regulated only transiently upon stress, whereas others showed a negative or positive regulation throughout the treatment. We identified two categories of positively regulated genes: pulsatile and gradual genes, where the former pulsed transiently after H_2O_2 treatment was provided, whilst the latter sustained a higher expression throughout the treatment. Gene expressions of both categories of positively regulated genes are temporally correlated in individual cells during steady state but they transiently diverged after the treatment. Using a mathematical model, we found that OxyR binding kinetics and growth dynamics can explain the regulation categorisation. The pulsatile genes are very sensitive protecting against sudden H_2O_2 stress and expressed by only a few cells closer to stress with a high cell-cell variability, while the gradually induced genes are expressed consistently by a larger number of cells. Altogether, we uncover that a simple redox switch of the OxyR transcription factor generates a defined gene expression program for tens of genes in response to H_2O_2 and creates characteristic spatio-temporal gene expression patterns across cells that benefit population adaptation.

This approach can be applied to understand the mechanisms underlying gene expression changes to map the regulation dynamics with cellular phenotypes against changing environments. Our study can be applied to other stresses to understand the origins of population level gene expression patterns, especially under antibiotic stress where multiple stress responses are induced and both primary and secondary responses implicate lethality[43]. Further, our technique can unravel underlying regulatory dynamics that give rise to a temporally programmed cellular response to antibiotics, as suggested in studies[263], and its significance in the context of antibiotic stress tolerance.

As demonstrated in this thesis, the implementation of a Machine learning model with microfluidic microscopy experiments (Chapter 3) can uncover the hidden variables of phenotypic heterogeneity in multicellular systems. Subsequently, the effect of the important predictors of heterogeneity can be studied using the simulations probing population behavior at a single cell level (Chapter 4). Implementing these techniques, we demonstrate how bacteria respond to oxidative stress at a population (Chapter 3), and the single cell level (Chapter 4), and how that response is coordinated at the molecular level in individual cells (Chapter 5). We determine that the population level dynamics emerge from cell-cell interactions (Chapters 3 and 4) that are orchestrated by transcription factor binding at the molecular level (Chapter 5).

6.4 Outlook

Cellular populations respond to environmental cues at the single cell and population level[1]. An individual cell responds to changes in immediate surroundings. Collectively, cells interact with each other in multicellular systems, either due to direct contact (contact dependent toxin[309], quorum sensing[41,310]) or indirectly by modulating external environments (division of labor[46], cross-protection against stress). The impact of environmental variation and individual cellular responses on the emergence of collective population behaviour is not well understood. The hierarchical complexity of dynamics at the population, individual and molecular levels prompts the advancement of analysing cellular responses at the single cell level in conjunction with modeling approaches. Other biological systems that could be explored in the context of our findings would, for example, include cellular differentiation in the development of multi-cellular organisms and during tumour development[311,312]. The behaviour of cells during development involves specialisation that occurs at variable spatial scales and through multiplexed regulation of genes[312]. These processes are sensitive to environmental cues, cell-cell interactions, and intracellular responses. Although there are substantial differences in the underlying biological mechanisms, there are many parallels with the bacterial stress response that is the focus of this dissertation. The effects of oxidative stress and mechanisms of oxidative stress tolerance are broadly conserved. In cancer cells, the creation of oxygen gradients impacts oxidative stress levels across cells in a tumour[313]. A similar application of single-cell imaging and ML could provide insights into the influence of local cell-cell interactions on cellular fates and phenotypic heterogeneity in this context.

Whilst oxidative stress has been studied for decades, our observations open many questions about the effects of oxidative stress and the functions of the bacterial responses to it, in general. Our results provide insights about (1) generalised principles that drive variability in cellular responses under stress, challenging the notion that intracellular molecular noise is the ultimate source of phenotypic heterogeneity and (2) understanding the impact of local cell-cell interactions on population protection against stress. Finally, (3) the tools and approaches developed here provide systematic ways to predict cellular response against an array of external perturbations.

Bibliography

1. Gottesman, S. Trouble is coming: Signaling pathways that regulate general stress responses in bacteria. *J Biol Chem* **294**, 11685 (2019).
2. Imlay, J. A. The molecular mechanisms and physiological consequences of oxidative stress: lessons from a model bacterium. *Nature Reviews Microbiology 2013 11:7* **11**, 443–454 (2013).
3. Zhu, M. & Dai, X. Maintenance of translational elongation rate underlies the survival of Escherichia coli during oxidative stress. *Nucleic Acids Res* **47**, 7592–7604 (2019).
4. Cheng-Guang, H. & Gualerzi, C. O. The Ribosome as a Switchboard for Bacterial Stress Response. *Front Microbiol* **11**, 619038 (2021).
5. Dwyer, D. J., Collins, J. J. & Walker, G. C. Unraveling the physiological complexities of antibiotic lethality. *Annu Rev Pharmacol Toxicol* **55**, 313–332 (2015).
6. Tipping, M. J. & Gibbs, K. A. Biofilms: Managing Stress to Navigate Group Dynamics. *Current Biology* **30**, R324–R326 (2020).
7. McAdams, H. H., Srinivasan, B. & Arkin, A. P. The evolution of genetic regulatory systems in bacteria. *Nature Reviews Genetics 2004 5:3* **5**, 169–178 (2004).
8. Hartwell, L. H., Hopfield, J. J., Leibler, S. & Murray, A. W. From molecular to modular cell biology. *Nature 1999 402:6761* **402**, C47–C52 (1999).
9. Bintu, L., Buchler, N. E., Garcia, H. G., Gerland, U., Hwa, T., Kondev, J., & Phillips, R. Transcriptional regulation by the numbers: models. *Curr Opin Genet Dev* **15**, 116–124 (2005).
10. Raj, A. & van Oudenaarden, A. Nature, Nurture, or Chance: Stochastic Gene Expression and Its Consequences. *Cell* **135**, 216–226 (2008).
11. Rosenfeld, N., Young, J. W., Alon, U., Swain, P. S. & Elowitz, M. B. Gene regulation at the single-cell level. *Science* **307**, 1962–1965 (2005).
12. Novick, A. & Weiner, M. Enzyme induction as an all-or-none phenomenon. *Proceedings of the National Academy of Sciences* **43**, 553–566 (1957).
13. Spudich, J. L. & Koshland, D. E. Non-genetic individuality: chance in the single cell. *Nature 1976 262:5568* **262**, 467–471 (1976).
14. Kærn, M., Elston, T. C., Blake, W. J. & Collins, J. J. Stochasticity in gene expression: from theories to phenotypes. *Nature Reviews Genetics 2005 6:6* **6**, 451–464 (2005).
15. Berg, O. G. A model for the statistical fluctuations of protein numbers in a microbial population. *J Theor Biol* **71**, 587–603 (1978).
16. Eldar, A. & Elowitz, M. B. Functional roles for noise in genetic circuits. *Nature 2010 467:7312* **467**, 167–173 (2010).
17. Alnahhas, R. N. & Dunlop, M. J. Advances in linking single-cell bacterial stress response to population-level survival. *Curr Opin Biotechnol* **79**, 102885 (2023).
18. Balaban, N. Q., Merrin, J., Chait, R., Kowalik, L. & Leibler, S. Bacterial persistence as a phenotypic switch. *Science (1979)* **305**, 1622–1625 (2004).
19. Hardo, G. & Bakshi, S. Challenges of analysing stochastic gene expression in bacteria using single-cell time-lapse experiments. *Essays Biochem* **65**, 67–79 (2021).
20. Raser, J. M. & O’Shea, E. K. Molecular biology - Noise in gene expression: Origins, consequences, and control. *Science (1979)* **309**, 2010–2013 (2005).
21. Geiler-Samerotte, K. A., Bauer, C. R., Li, S., Ziv, N., Gresham, D., & Siegal, M. L. The details in the distributions: why and how to study phenotypic variability. *Curr Opin Biotechnol* **24**, 752–759 (2013).

22. Elowitz, M. B., Levine, A. J., Siggia, E. D. & Swain, P. S. Stochastic gene expression in a single cell. *Science* **297**, 1183–1186 (2002).
23. Silander, O. K., Nikolic, N., Zaslaver, A., Bren, A., Kikoin, I., Alon, U., & Ackermann, M. A Genome-Wide Analysis of Promoter-Mediated Phenotypic Noise in Escherichia coli. *PLoS Genet* **8**, e1002443 (2012).
24. Pedraza, J. H. & Van Oudenaarden, A. Noise propagation in gene networks. *Science* **307**, 1965–1969 (2005).
25. Golding, I., Paulsson, J., Zawilski, S. M. & Cox, E. C. Real-time kinetics of gene activity in individual bacteria. *Cell* **123**, 1025–1036 (2005).
26. Okumus, B., Landgraf, D., Lai, G. C., Bakshi, S., Arias-Castro, J. C., Yildiz, S., Huh, D., Fernandez-Lopez, R., Peterson, C. N., Toprak, E., El Karoui, M., & Paulsson, J. Mechanical slowing-down of cytoplasmic diffusion allows in vivo counting of proteins in individual cells. *Nature Communications 2016 7:1* **7**, 1–11 (2016).
27. Uphoff, S., Lord, N. D., Okumus, B., Potvin-Trottier, L., Sherratt, D. J., & Paulsson, J. Stochastic activation of a DNA damage response causes cell-to-cell mutation rate variation. *Science (1979)* **351**, 1094–1097 (2016).
28. Azpeitia, E. & Wagner, A. Short Residence Times of DNA-Bound Transcription Factors Can Reduce Gene Expression Noise and Increase the Transmission of Information in a Gene Regulation System. *Front Mol Biosci* **7**, 67–67 (2020).
29. Huh, D. & Paulsson, J. Random partitioning of molecules at cell division. *Proc Natl Acad Sci U S A* **108**, 15004–15009 (2011).
30. Jaramillo-Riveri, S., Broughton, J., McVey, A., Pilizota, T., Scott, M., & El Karoui, M. Growth-dependent heterogeneity in the DNA damage response in Escherichia coli. *Mol Syst Biol* **18**, e10441 (2022).
31. Patange, O., Schwall, C., Jones, M., Villava, C., Griffith, D. A., Phillips, A., & Locke, J. C. W. Escherichia coli can survive stress by noisy growth modulation. *Nature Communications 2018 9:1* **9**, 1–11 (2018).
32. Sampaio, N. M. V., Blassick, C. M., Andreani, V., Lugagne, J. B. & Dunlop, M. J. Dynamic gene expression and growth underlie cell-to-cell heterogeneity in Escherichia coli stress response. *Proc Natl Acad Sci U S A* **119**, e2115032119 (2022).
33. De Martino, M., Ershov, D., van den Berg, P. J., Tans, S. J. & Meyer, A. S. Single-Cell Analysis of the Dps Response to Oxidative Stress. *J Bacteriol* **198**, 1662–1674 (2016).
34. Mathis, R. & Ackermann, M. Response of single bacterial cells to stress gives rise to complex history dependence at the population level. *Proc Natl Acad Sci U S A* **113**, 4224–4229 (2016).
35. Wolf, D. M., Fontaine-Bodin, L., Bischofs, I., Price, G., Keasling, J., & Arkin, A. P. Memory in Microbes: Quantifying History-Dependent Behavior in a Bacterium. *PLoS One* **3**, e1700 (2008).
36. Veening, J. W., Stewart, E. J., Berngruber, T. W., Taddei, F., Kuipers, O. P., & Hamoen, L. W. Bet-hedging and epigenetic inheritance in bacterial cell development. *Proc Natl Acad Sci U S A* **105**, 4393–4398 (2008).
37. Kiviet DJ, Nghe P, Walker N, Boulineau S, Sunderlikova V, & Tans SJ. Stochasticity of metabolism and growth at the single-cell level. *Nature* **514**, 376–379 (2014).
38. Ojkic, N., Serbanescu, D. & Banerjee, S. Antibiotic Resistance via Bacterial Cell Shape-Shifting. *mBio* **13**, (2022).

39. Łapińska, U., Voliotis, M., Lee, K. K., Campey, A., Stone, M. R. L., Tuck, B., Phetsang, W., Zhang, B., Tsaneva-Atanasova, K., Blaskovich, M. A. T., & Pagliara, S. Fast bacterial growth reduces antibiotic accumulation and efficacy. *Elife* **11**, (2022).
40. Smith, A., Kaczmar, A., Bamford, R. A., Smith, C., Frustaci, S., Kovacs-Simon, A., O'Neill, P., Moore, K., Paszkiewicz, K., Titball, R. W., & Pagliara, S. The culture environment influences both gene regulation and phenotypic heterogeneity in Escherichia coli. *Front Microbiol* **9**, 370108 (2018).
41. van Gestel, J., Bareia, T., Tenennbaum, B., Dal Co, A., Guler, P., Aframian, N., Puyesky, S., Grinberg, I., D'Souza, G. G., Erez, Z., Ackermann, M., & Eldar, A. Short-range quorum sensing controls horizontal gene transfer at micron scale in bacterial communities. *Nature Communications 2021 12:1* **12**, 1–11 (2021).
42. Dal Co, A., van Vliet, S., Kiviet, D. J., Schlegel, S. & Ackermann, M. Short-range interactions govern the dynamics and functions of microbial communities. *Nature Ecology & Evolution 2020 4:3* **4**, 366–375 (2020).
43. Snoussi, M., Talledo, J. P., Del Rosario, N. A., Mohammadi, S., Ha, B. Y., Košmrlj, A., & Taheri-Araghi, S. Heterogeneous absorption of antimicrobial peptide LL37 in escherichia coli cells enhances population survivability. *Elife* **7**, (2018).
44. van Vliet, S., Dal Co, A., Winkler, A. R., Spriewald, S., Stecher, B., & Ackermann, M. Spatially Correlated Gene Expression in Bacterial Groups: The Role of Lineage History, Spatial Gradients, and Cell-Cell Interactions. *Cell Syst* **6**, 496-507.e6 (2018).
45. Jo, J., Price-Whelan, A. & Dietrich, L. E. P. Gradients and consequences of heterogeneity in biofilms. *Nat Rev Microbiol* **20**, 593–607 (2022).
46. Dal Co, A., Brannon, C. & Ackermann, M. Division of labor in bacteria. *Elife* **7**, (2018).
47. Giri, S., Waschina, S., Kaleta, C. & Kost, C. Defining Division of Labor in Microbial Communities. *J Mol Biol* **431**, 4712–4731 (2019).
48. Co, A. D., Van Vliet, S. & Ackermann, M. Emergent microscale gradients give rise to metabolic cross-feeding and antibiotic tolerance in clonal bacterial populations. *Philosophical Transactions of the Royal Society B* **374**, (2019).
49. Serra, D. O. & Hengge, R. Stress responses go three dimensional – the spatial order of physiological differentiation in bacterial macrocolony biofilms. *Environ Microbiol* **16**, 1455–1471 (2014).
50. Zoheir, A. E., Sobol, M. S., Meisch, L., Ordoñez-Rueda, D., Kaster, A. K., Niemeyer, C. M., & Rabe, K. S. A three-colour stress biosensor reveals multimodal response in single cells and spatiotemporal dynamics of biofilms. *npj Biofilms and Microbiomes 2023 9:1* **9**, 1–10 (2023).
51. Brameyer, S., Schumacher, K., Kuppermann, S. & Jung, K. Division of labor and collective functionality in Escherichia coli under acid stress. *Communications Biology 2022 5:1* **5**, 1–14 (2022).
52. Kleijn, I. T., Krah, L. H. J. & Hermsen, R. Noise propagation in an integrated model of bacterial gene expression and growth. *PLoS Comput Biol* **14**, (2018).
53. St-Pierre, F. & Endy, D. Determination of cell fate selection during phage lambda infection. *Proc Natl Acad Sci U S A* **105**, 20705–20710 (2008).
54. Snijder, B. & Pelkmans, L. Origins of regulated cell-to-cell variability. *Nat Rev Mol Cell Biol* **12**, 119–125 (2011).
55. Golding, I. Infection by bacteriophage lambda: an evolving paradigm for cellular individuality. *Curr Opin Microbiol* **43**, 9–13 (2018).

56. Lavi, I., Piel, M., Lennon-Duménil, A. M., Voituriez, R. & Gov, N. S. Deterministic patterns in cell motility. *Nature Physics 2016 12:12* **12**, 1146–1152 (2016).
57. Rossi, N. A., El Meouche, I. & Dunlop, M. J. Forecasting cell fate during antibiotic exposure using stochastic gene expression. *Commun Biol* **2**, (2019).
58. Yang, Y., Karin, O., Mayo, A., Song X., Chen P., Santos A. L., Lindner A. B., & Alon U. Damage dynamics and the role of chance in the timing of E. coli cell death. *Nature Communications 2023 14:1* **14**, 1–11 (2023).
59. Thattai, M. & Van Oudenaarden, A. Stochastic Gene Expression in Fluctuating Environments. *Genetics* **167**, 523–530 (2004).
60. Martins, B. M. C. & Locke, J. C. W. Microbial individuality: how single-cell heterogeneity enables population level strategies. *Curr Opin Microbiol* **24**, 104–112 (2015).
61. Kussell, E. & Leibler, S. Ecology: Phenotypic diversity, population growth, and information in fluctuating environments. *Science (1979)* **309**, 2075–2078 (2005).
62. Losick, R. & Desplan, C. Stochasticity and cell fate. *Science (1979)* **320**, 65–68 (2008).
63. Acar, M., Mettetal, J. T. & Van Oudenaarden, A. Stochastic switching as a survival strategy in fluctuating environments. *Nature Genetics 2008 40:4* **40**, 471–475 (2008).
64. Morawska, L. P., Hernandez-Valdes, J. A. & Kuipers, O. P. Diversity of bet-hedging strategies in microbial communities—Recent cases and insights. *WIREs Mechanisms of Disease* **14**, e1544 (2022).
65. Maamar, H., Raj, A. & Dubnau, D. Noise in gene expression determines cell fate in Bacillus subtilis. *Science (1979)* **317**, 526–529 (2007).
66. Bar-Even, A., Paulsson, J., Maheshri, N., Carmi, M., O'Shea, E., Pilpel, Y., & Barkai, N. Noise in protein expression scales with natural protein abundance. *Nature Genetics 2006 38:6* **38**, 636–643 (2006).
67. Gefen, O. & Balaban, N. Q. The importance of being persistent: heterogeneity of bacterial populations under antibiotic stress. *FEMS Microbiol Rev* **33**, 704–717 (2009).
68. el Meouche, I., Siu, Y. & Dunlop, M. J. Stochastic expression of a multiple antibiotic resistance activator confers transient resistance in single cells. *Scientific Reports 2016 6:1* **6**, 1–9 (2016).
69. Vincent, M. S. & Uphoff, S. Bacterial phenotypic heterogeneity in DNA repair and mutagenesis. *Biochemical Society Transactions* vol. 48 451–462 (2020).
70. Veening, J. W., Smits, W. K. & Kuipers, O. P. Bistability, epigenetics, and bet-hedging in bacteria. *Annu Rev Microbiol* **62**, 193–210 (2008).
71. Ackermann, M. A functional perspective on phenotypic heterogeneity in microorganisms. *Nature Reviews Microbiology 2015 13:8* **13**, 497–508 (2015).
72. Vincent, M. S. & Uphoff, S. Cellular heterogeneity in DNA alkylation repair increases population genetic plasticity. *Nucleic Acids Res* **49**, 12320–12331 (2021).
73. Bigger, J. W. Treatment of Staphyloeoeeal Infections with Penicillin by Intermittent Sterilisation. *Lancet* 497–500 (1944).
74. Mitosch, K., Rieckh, G. & Bollenbach, T. Noisy Response to Antibiotic Stress Predicts Subsequent Single-Cell Survival in an Acidic Environment. *Cell Syst* **4**, 393-403.e5 (2017).
75. Ozbudak, E. M., Thattai, M., Kurtser, I., Grossman, A. D. & Van Oudenaarden, A. Regulation of noise in the expression of a single gene. *Nature Genetics 2002 31:1* **31**, 69–73 (2002).
76. Sánchez, Á. & Kondev, J. Transcriptional control of noise in gene expression. *Proc Natl Acad Sci U S A* **105**, 5081–5086 (2008).

77. Blake, W. J., Balázsi, G., Kohanski, M. A., Isaacs, F. J., Murphy, K. F., Kuang, Y., Cantor, C. R., Walt, D. R., & Collins, J. J. Phenotypic Consequences of Promoter-Mediated Transcriptional Noise. *Mol Cell* **24**, 853–865 (2006).
78. Raser, J. M. & O'Shea, E. K. Control of stochasticity in eukaryotic gene expression. *Science (1979)* **304**, 1811–1814 (2004).
79. Lan, G., Sartori, P., Neumann, S., Sourjik, V. & Tu, Y. The energy-speed-accuracy tradeoff in sensory adaptation. *Nat Phys* **8**, 422–428 (2012).
80. Meyerovich, M., Mamou, G. & Ben-Yehuda, S. Visualizing high error levels during gene expression in living bacterial cells. *Proc Natl Acad Sci U S A* **107**, 11543–11548 (2010).
81. Van Boxtel, C., Van Heerden, J. H., Nordholt, N., Schmidt, P. & Bruggeman, F. J. Taking chances and making mistakes: non-genetic phenotypic heterogeneity and its consequences for surviving in dynamic environments. *J R Soc Interface* **14**, (2017).
82. van Heerden, J. H., Wortel, M. T., Bruggeman, F. J., Heijnen, J. J., Bollen, Y. J., Planqué, R., Hulshof, J., O'Toole, T. G., Wahl, S. A., & Teusink, B. Lost in transition: Start-up of glycolysis yields subpopulations of nongrowing cells. *Science (1979)* **343**, (2014).
83. Wolf, L., Silander, O. K. & van Nimwegen, E. Expression noise facilitates the evolution of gene regulation. *Elife* **4**, (2015).
84. Mishra, S. & Imlay, J. Why do bacteria use so many enzymes to scavenge hydrogen peroxide? *Archives of Biochemistry and Biophysics* vol. 525 145–160 (2012).
85. Seaver, L. C. & Imlay, J. A. Hydrogen peroxide fluxes and compartmentalization inside growing Escherichia coli. *J Bacteriol* **183**, 7182–7189 (2001).
86. Kümmerli, R. & Frank, S. A. Evolutionary explanations for heterogeneous behavior in clonal bacterial populations. *Trends Microbiol* **31**, 665–667 (2023).
87. Storz, G. & Imlay, J. A. Oxidative stress. *Curr Opin Microbiol* **2**, 188–194 (1999).
88. O'Connell, D. Stress relief... *Nature Reviews Microbiology 2007 5:4* **5**, 247–247 (2007).
89. Imlay, J. A. Where in the world do bacteria experience oxidative stress? *Environ Microbiol* **21**, 521–530 (2019).
90. Ma, M. & Eaton, J. W. *Multicellular oxidant defense in unicellular organisms*. vol. 89 (1992).
91. Cochran, W. L., McFeters, G. A. & Stewart, P. S. Reduced susceptibility of thin Pseudomonas aeruginosa biofilms to hydrogen peroxide and monochloramine. *J Appl Microbiol* **88**, 22–30 (2000).
92. Holland, M., Farinella, D. N., Cruz-Lorenzo, E., Laubscher, M. I., Doakes, D. A., Ramos, M. A., Kubota, N., & Levin, T. C. L. pneumophila resists its self-harming metabolite HGA via secreted factors and collective peroxide scavenging. *mBio* (2023).
93. Stewart, P. S. Diffusion in biofilms. *Journal of Bacteriology* vol. 185 1485–1491 (2003).
94. Åslund, F., Zheng, M., Beckwith, J. & Storz, G. Regulation of the OxyR transcription factor by hydrogen peroxide and the cellular thiol-disulfide status. *Proc Natl Acad Sci U S A* ***96*,*6161*** (1999).
95. Baker, C. J., Orlandi, E. W. & Anderson, A. J. Oxygen metabolism in plant cell culture/bacteria interactions: Role of bacterial concentration and H2O2-scavenging in survival under biological and artificial oxidative stress. *Physiol Mol Plant Pathol* **51**, 401–415 (1997).
96. Imlay, J. A. Diagnosing oxidative stress in bacteria: not as easy as you might think. *Current Opinion in Microbiology* vol. 24 124–131 (2015).
97. Kiley, P. J. & Storz, G. Exploiting Thiol Modifications. *PLoS Biol* **2**, e400 (2004).

98. Seaver, L. C. & Imlay, J. A. Are Respiratory Enzymes the Primary Sources of Intracellular Hydrogen Peroxide? *Journal of Biological Chemistry* **279**, 48742–48750 (2004).
99. Korshunov, S. & Imlay, J. A. Two sources of endogenous hydrogen peroxide in Escherichia coli. *Mol Microbiol* **75**, 1389–1401 (2010).
100. Maisch, T., Baier, J., Franz, B., Maier, M., Landthaler, M., Szeimies, R. M., & Bäumler, W. The role of singlet oxygen and oxygen concentration in photodynamic inactivation of bacteria. *Proc Natl Acad Sci U S A* **104**, 7223 (2007).
101. McCord, J. M. & Fridovich, I. The utility of superoxide dismutase in studying free radical reactions. I. Radicals generated by the interaction of sulfite, dimethyl sulfoxide, and oxygen. *Journal of Biological Chemistry* **244**, 6056–6063 (1969).
102. Fenton, H. J. H. LXXIII.—Oxidation of tartaric acid in presence of iron. *Journal of the Chemical Society, Transactions* **65**, 899–910 (1894).
103. Fridovich, I. Biological effects of the superoxide radical. *Arch Biochem Biophys* **247**, 1–11 (1986).
104. Messner, K. R. & Imlay, J. A. The Identification of Primary Sites of Superoxide and Hydrogen Peroxide Formation in the Aerobic Respiratory Chain and Sulfite Reductase Complex of Escherichia coli. *Journal of Biological Chemistry* **274**, 10119–10128 (1999).
105. Zhao, X. & Drlica, K. Reactive oxygen species and the bacterial response to lethal stress. *Curr Opin Microbiol* **0**, 1 (2014).
106. Imlay, J. A. Pathways of Oxidative Damage. *Annual Rev Microbiol.* **57**, 395–418 (2003).
107. Sen, A. & Imlay, J. A. How Microbes Defend Themselves From Incoming Hydrogen Peroxide. *Frontiers in Immunology* vol. 12 (2021).
108. Seaver, L. C. & Imlay, J. A. Alkyl hydroperoxide reductase is the primary scavenger of endogenous hydrogen peroxide in Escherichia coli. *J Bacteriol* **183**, 7173–7181 (2001).
109. Chiang, S. M. & Schellhorn, H. E. Regulators of oxidative stress response genes in Escherichia coli and their functional conservation in bacteria. *Archives of Biochemistry and Biophysics* vol. 525 161–169 (2012).
110. Ezraty, B., Gennaris, A., Barras, F. & Collet, J. F. Oxidative stress, protein damage and repair in bacteria. *Nature Reviews Microbiology 2017 15:7* **15**, 385–396 (2017).
111. Wagner, A. F. V., Frey, M., Neugebauer, F. A., Schafer, W. & Knappe, J. The free radical in pyruvate formate-lyase is located on glycine-734. *Proc Natl Acad Sci U S A* **89**, 996–1000 (1992).
112. Carlioz, A. & Touati, D. Isolation of superoxide dismutase mutants in Escherichia coli: is superoxide dismutase necessary for aerobic life? *EMBO J* **5**, 623–630 (1986).
113. Benov, L. & Fridovich, I. Why Superoxide Imposes an Aromatic Amino Acid Auxotrophy on Escherichia coli: The transketolase connection. *Journal of Biological Chemistry* **274**, 4202–4206 (1999).
114. Flint, D. H., Tuminello, J. F. & Emptage, M. H. The inactivation of Fe-S cluster containing hydro-lyases by superoxide. *Journal of Biological Chemistry* **268**, 22369–22376 (1993).
115. Andrés, C. M. C., Pérez de la Lastra, J. M., Andrés Juan, C., Plou, F. J. & Pérez-Lebeña, E. Superoxide Anion Chemistry—Its Role at the Core of the Innate Immunity. *Int J Mol Sci* **24**, (2023).
116. Knapp, H. R. & Melly, M. A. Bactericidal effects of polyunsaturated fatty acids. *J Infect Dis* **154**, 84–94 (1986).

117. Kobayashi, Y., Hayashi, M., Yoshino, F., Tamura, M., Yoshida, A., Ibi, H., Lee, M. C., Ochiai, K., & Ogiso, B. Bactericidal effect of hydroxyl radicals generated from a low concentration hydrogen peroxide with ultrasound in endodontic treatment. *J Clin Biochem Nutr* **54**, 161 (2014).
118. Winterbourn, C. C. The Biological Chemistry of Hydrogen Peroxide. *Methods Enzymol* **528**, 3–25 (2013).
119. Farr, S. B., Touati, D. & Kogomal, T. Effects of Oxygen Stress on Membrane Functions in Escherichia coli: Role of HPI Catalase. *Journal of bacteriology vol. **170,4*** (1988).
120. Park, S., You, X. & Imlay, J. A. Substantial DNA damage from submicromolar intracellular hydrogen peroxide detected in Hpx- mutants of Escherichia coli. *Proc Natl Acad Sci U S A* **102**, 9317–9322 (2005).
121. Buxton, G. V., Greenstock, C. L., Helman, W. P. & Ross, A. B. Critical Review of rate constants for reactions of hydrated electrons, hydrogen atoms and hydroxyl radicals (·OH/·O− in Aqueous Solution. *J Phys Chem Ref Data* **17**, 513–886 (1988).
122. Imlay, J. A., Chin, S. M., & Linn, S. Toxic DNA Damage by Hydrogen Peroxide Through the Fenton Reaction in Vivo and in Vitro. *Science (1979)* **240**, 640–642 (1988).
123. Cadet, J. & Richard Wagner, J. DNA Base Damage by Reactive Oxygen Species, Oxidizing Agents, and UV Radiation. *Cold Spring Harb Perspect Biol* **5**, (2013).
124. Fasnacht, M. & Polacek, N. Oxidative Stress in Bacteria and the Central Dogma of Molecular Biology. *Front Mol Biosci* **8**, 671037 (2021).
125. Candeias, L. P. & Steenken, S. Electron Transfer in Di(deoxy)nucleoside Phosphates in Aqueous Solution: Rapid Migration of Oxidative Damage (via Adenine) to Guanine. *J Am Chem Soc* **115**, 2437–2440 (1993).
126. Cadet, J., Ravanat, J.-L., Martinez, G. R., Medeiros, M. H. G. & Mascio, P. D. Singlet Oxygen Oxidation of Isolated and Cellular DNA: Product Formation and Mechanistic Insights. *Photochem Photobiol* **82**, 1219–1225 (2006).
127. Cadet, J., Douki, T. & Ravanat, J. L. Oxidatively generated base damage to cellular DNA. *Free Radic Biol Med* **49**, 9–21 (2010).
128. Cheng, K. C., Cahill, D. S., Kasai, H., Nishimura, S. & Loeb, L. A. 8-Hydroxyguanine, an abundant form of oxidative DNA damage, causes G-T and A-C substitutions. *Journal of Biological Chemistry* **267**, 166–172 (1992).
129. Hsu, G. W., Ober, M., Carell, T. & Beese, L. S. Error-prone replication of oxidatively damaged DNA by a high-fidelity DNA polymerase. *Nature 2004 431:7005* **431**, 217–221 (2004).
130. Liu, M., Gong, X., Alluri, R. K., Wu, J., Sablo, T., & Li, Z. Liu, M. *et al.* Characterization of RNA damage under oxidative stress in Escherichia coli. *Biol Chem* **393**, 123–132 (2012).
131. Seixas, A. F., Quendera, A. P., Sousa, J. P., Silva, A. F. Q., Arraiano, C. M., & Andrade, J. M. Bacterial Response to Oxidative Stress and RNA Oxidation. *Front Genet* **12**, (2021).
132. Leichert, L. I., Gehrke, F., Gudiseva, H. V., Blackwell, T., Ilbert, M., Walker, A. K., Strahler, J. R., Andrews, P. C., & Jakob, U. Quantifying changes in the thiol redox proteome upon oxidative stress in vivo. *Proc Natl Acad Sci U S A* **105**, 8197–8202 (2008).
133. Khademian, M., Imlay, J. A. & Khademian, M. How Microbes Evolved to Tolerate Oxygen. *Trends Microbiol* **29**, 428–440 (2021).
134. Hassan, H. M. & Fridovich, I. Superoxide radical and the oxygen enhancement of the toxicity of paraquat in Escherichia coli. *Journal of Biological Chemistry* **253**, 8143–8148 (1978).

135. Lesser, M. P. Oxidative stress in marine environments: Biochemistry and Physiological Ecology. A*nnual Rev Physiol.* **68**, 253–278 (2006).
136. Meslé M. M., Beam J. P., Jay Z. J., Bodle B., Bogenschutz E., & Inskeep W. P. Hydrogen peroxide cycling in high-temperature acidic geothermal springs and potential implications for oxidative stress response. *Front Mar Sci* **4**, 130 (2017).
137. Ogino, T., Maegawa, S., Shigeno, S., Fujikura, K. & Toyohara, H. Highly sensitive avoidance plays a key role in sensory adaptation to deep-sea hydrothermal vent environments. *PLoS One* **13**, e0189902 (2018).
138. Pitcher, M. C. L., Beatty, E. R. & Cummings, J. H. The contribution of sulphate reducing bacteria and 5-aminosalicylic acid to faecal sulphide in patients with ulcerative colitis. *Gut* **46**, 64–72 (2000).
139. Tong, H., Chen, W., Merritt, J., Qi, F., Shi, W., & Dong, X. Streptococcus oligofermentans inhibits Streptococcus mutans through conversion of lactic acid into inhibitory H2O2: a possible counteroffensive strategy for interspecies competition. *Mol Microbiol* **63**, 872–880 (2007).
140. Dong, T. G., Dong, S., Catalano, C., Moore, R., Liang, X., & Mekalanos, J. J. Generation of reactive oxygen species by lethal attacks from competing microbes. *Proc Natl Acad Sci U S A* **112**, 2181–2186 (2015).
141. Slauch, J. M. How does the oxidative burst of macrophages kill bacteria? Still an open question. *Mol Microbiol* **80**, 580 (2011).
142. Passo, S. A. & Weiss, S. J. Oxidative Mechanisms Utilized by Human Neutrophils to Destroy Escherichia coli. *Blood* **63**, 1361–1368 (1984).
143. Mittal, M., Siddiqui, M. R., Tran, K., Reddy, S. P. & Malik, A. B. Reactive Oxygen Species in Inflammation and Tissue Injury. *Antioxid Redox Signal* **20**, 1126 (2014).
144. Kohanski, M. A., DePristo, M. A. & Collins, J. J. Sublethal Antibiotic Treatment Leads to Multidrug Resistance via Radical-Induced Mutagenesis. *Mol Cell* **37**, 311–320 (2010).
145. Kohanski, M. A., Dwyer, D. J. & Collins, J. J. How antibiotics kill bacteria: from targets to networks. *Nat Rev Microbiol* **8**, 423–435 (2010).
146. Ezraty, B., Vergnes, A., Banzhaf, M., Duverger, Y., Huguenot, A., Brochado, A. R., Su, S. Y., Espinosa, L., Loiseau, L., Py, B., Typas, A., & Barras, F. Fe-S cluster biosynthesis controls uptake of aminoglycosides in a ROS-less death pathway. *Science (1979)* **340**, 1583–1587 (2013).
147. Keren, I., Wu, Y., Inocencio, J., Mulcahy, L. R. & Lewis, K. Killing by bactericidal antibiotics does not depend on reactive oxygen species. *Science (1979)* **339**, 1213–1216 (2013).
148. Liu, Y. & Imlay, J. A. Cell death from antibiotics without the involvement of reactive oxygen species. *Science* **339**, 1210–1213 (2013).
149. Lynch, R. E. & Fridovich, I. Permeation of the erythrocyte stroma by superoxide radical. *Journal of Biological Chemistry* **253**, 4697–4699 (1978).
150. Korshunov, S. S. & Imlay, J. A. A potential role for periplasmic superoxide dismutase in blocking the penetration of external superoxide into the cytosol of Gram-negative bacteria. *Mol Microbiol* **43**, 95–106 (2002).
151. Imlay, J. A. Transcription Factors That Defend Bacteria Against Reactive Oxygen Species. *Annual Rev Microbiol.* **69**, 93–108 (2015).

152. Winterbourn, C. C., Hampton, M. B., Livesey, J. H. & Kettle, A. J. Modeling the Reactions of Superoxide and Myeloperoxidase in the Neutrophil Phagosome: Implications for microbial killing. *Journal of Biological Chemistry* **281**, 39860–39869 (2006).
153. Åslund, F., Zheng, M., Beckwith, J. & Storz, G. Regulation of the OxyR transcription factor by hydrogen peroxide and the cellular thiol-disulfide status. *Proc Natl Acad Sci U S A* **96**, 6161–6165 (1999).
154. Zheng, M., Åslund, F. & Storz, G. Activation of the OxyR transcription factor by reversible disulfide bond formation. *Science (1979)* **279**, 1718–1721 (1998).
155. Choi, H., Kim, S., Mukhopadhyay, P., Cho, S., Woo, J., Storz, G., & Ryu, S. E. Structural basis of the redox switch in the OxyR transcription factor. *Cell* **105**, 103–113 (2001).
156. Tartaglia, L. A., Gimeno, C. J., Storz, G. & Ames, B. N. Multidegenerate DNA recognition by the OxyR transcriptional regulator. *Journal of Biological Chemistry* **267**, 2038–2045 (1992).
157. Toledano, M. B., Kullik, I., Trinh, F., Baird, P. T., Schneider, T. D., & Storz, G. Redox-dependent shift of OxyR-DNA contacts along an extended DNA-binding site: A mechanism for differential promoter selection. *Cell* **78**, 897–909 (1994).
158. Kim, S. O., Merchant, K., Nudelman, R., Beyer, W. F., Jr, Keng, T., DeAngelo, J., Hausladen, A., & Stamler, J. S. OxyR: A molecular code for redox-related signaling. *Cell* **109**, 383–396 (2002).
159. Dubbs, J. M. & Mongkolsuk, S. Peroxide-sensing transcriptional regulators in bacteria. *J Bacteriol* **194**, 5495–5503 (2012).
160. Storz, G. & Tartaglia, L. A. OxyR: a regulator of antioxidant genes. *J Nutr* **122**, 627–630 (1992).
161. González-Flecha, B. & Demple, B. Role for the oxyS gene in regulation of intracellular hydrogen peroxide in Escherichia coli. *J Bacteriol* **181**, 3833–3836 (1999).
162. Barshishat, S., Elgrably-Weiss, M., Edelstein, J., Georg, J., Govindarajan, S., Haviv, M., Wright, P. R., Hess, W. R., & Altuvia, S. OxyS small RNA induces cell cycle arrest to allow DNA damage repair. *EMBO J* **37**, 413–426 (2018).
163. Chiancone, E. & Ceci, P. The multifaceted capacity of Dps proteins to combat bacterial stress conditions: Detoxification of iron and hydrogen peroxide and DNA binding. *Biochim Biophys Acta* **1800**, 798–805 (2010).
164. Liu, Y., Bauer, S. C. & Imlay, J. A. The YaaA protein of the Escherichia coli OxyR regulon lessens hydrogen peroxide toxicity by diminishing the amount of intracellular unincorporated iron. *J Bacteriol* **193**, 2186–2196 (2011).
165. Sen, A., Zhou, Y. & Imlay, J. A. During Oxidative Stress the Clp Proteins of Escherichia coli Ensure that Iron Pools Remain Sufficient To Reactivate Oxidized Metalloenzymes. *J Bacteriol* **202**, (2020).
166. Jang, S. & Imlay, J. A. Hydrogen peroxide inactivates the Escherichia coli Isc iron-sulphur assembly system, and OxyR induces the Suf system to compensate. *Mol Microbiol* **78**, 1448–1467 (2010).
167. Anjem, A., Varghese, S. & Imlay, J. A. Manganese import is a key element of the OxyR response to hydrogen peroxide in Escherichia coli. *Mol Microbiol* **72**, 844–858 (2009).
168. Mancini, S. & Imlay, J. A. The induction of two biosynthetic enzymes helps Escherichia coli sustain heme synthesis and activate catalase during hydrogen peroxide stress. *Mol Microbiol* **96**, 744–763 (2015).

169. Kim, S., Bang, Y. J., Kim, D., Lim, J. G., Oh, M. H., & Choi, S. H. Distinct characteristics of OxyR2, a new OxyR-type regulator, ensuring expression of Peroxiredoxin 2 detoxifying low levels of hydrogen peroxide in Vibrio vulnificus. *Mol Microbiol* **93**, 992–1009 (2014).
170. Schellhorn, H. E. Regulation of hydroperoxidase (catalase) expression in Escherichia coli . *FEMS Microbiol Lett* **131**, 113–119 (1995).
171. Kukurba, K. R. & Montgomery, S. B. RNA Sequencing and Analysis. *Cold Spring Harb Protoc* **2015**, 951 (2015).
172. Bhatia, R. P., Kirit, H. A., Predeus, A. V. & Bollback, J. P. Transcriptomic profiling of Escherichia coli K-12 in response to a compendium of stressors. *Scientific Reports 2022 12:1* **12**, 1–14 (2022).
173. Roth, M., Jaquet, V., Lemeille, S., Bonetti, E. J., Cambet, Y., François, P., & Krause, K. H. Transcriptomic Analysis of E. coli after Exposure to a Sublethal Concentration of Hydrogen Peroxide Revealed a Coordinated Up-Regulation of the Cysteine Biosynthesis Pathway. *Antioxidants (Basel)* **11**, (2022).
174. Zhu, Z., Surujon, D., Ortiz-Marquez, J. C., Huo, W., Isberg, R. R., Bento, J., & van Opijnen, T. Entropy of a bacterial stress response is a generalizable predictor for fitness and antibiotic sensitivity. *Nature Communications 2020 11:1* **11**, 1–15 (2020).
175. Ma, P., Amemiya, H. M., He, L. L., Gandhi, S. J., Nicol, R., Bhattacharyya, R. P., Smillie, C. S., & Hung, D. T. Bacterial droplet-based single-cell RNA-seq reveals antibiotic-associated heterogeneous cellular states. *Cell* **186**, 877-891.e14 (2023).
176. Tang, F., Barbacioru, C., Wang, Y., Nordman, E., Lee, C., Xu, N., Wang, X., Bodeau, J., Tuch, B. B., Siddiqui, A., Lao, K., & Surani, M. A. mRNA-Seq whole-transcriptome analysis of a single cell. *Nature Methods 2009 6:5* **6**, 377–382 (2009).
177. Taniguchi, Y., Choi, P. J., Li, G. W., Chen, H., Babu, M., Hearn, J., Emili, A., & Xie, X. S. Quantifying E. coli proteome and transcriptome with single-molecule sensitivity in single cells. *Science (1979)* **329**, 533–538 (2010).
178. Zaslaver, A., Bren, A., Ronen, M., Itzkovitz, S., Kikoin, I., Shavit, S., Liebermeister, W., Surette, M. G., & Alon, U. A comprehensive library of fluorescent transcriptional reporters for Escherichia coli. *Nat Methods* **3**, 623–628 (2006).
179. Young, J. W., Locke, J. C., Altinok, A., Rosenfeld, N., Bacarian, T., Swain, P. S., Mjolsness, E., & Elowitz, M. B. Measuring single-cell gene expression dynamics in bacteria using fluorescence time-lapse microscopy. *Nat Protoc* **7**, 80 (2012).
180. Padron, G. C., Shuppara, A. M., Sharma, A., Koch, M. D., Palalay, J. S., Radin, J. N., Kehl-Fie, T. E., Imlay, J. A., & Sanfilippo, J. E. Shear rate sensitizes bacterial pathogens to H2O2 stress. *Proc Natl Acad Sci U S A* **120**, e2216774120 (2023).
181. Hartmann, R., Jeckel, H., Jelli, E., Singh, P. K., Vaidya, S., Bayer, M., Rode, D. K. H., Vidakovic, L., Díaz-Pascual, F., Fong, J. C. N., Dragoš, A., Lamprecht, O., Thöming, J. G., Netter, N., Häussler, S., Nadell, C. D., Sourjik, V., Kovács, Á. T., Yildiz, F. H., & Drescher, K. Quantitative image analysis of microbial communities with BiofilmQ. *Nature Microbiology 2021 6:2* **6**, 151–156 (2021).
182. O'Connor, O. M., Alnahhas, R. N., Lugagne, J. B. & Dunlop, M. J. DeLTA 2.0: A deep learning pipeline for quantifying single-cell spatial and temporal dynamics. *PLoS Comput Biol* **18**, e1009797 (2022).
183. Warren, M. R., Sun, H., Yan, Y., Cremer, J., Li, B., & Hwa, T. Spatiotemporal establishment of dense bacterial colonies growing on hard agar. *Elife* **8**, (2019).

184. Ullman, G., Wallden, M., Marklund, E. G., Mahmutovic, A., Razinkov, I., & Elf, J.High-throughput gene expression analysis at the level of single proteins using a microfluidic turbidostat and automated cell tracking. *Philosophical Transactions of the Royal Society B: Biological Sciences* **368**, (2013).
185. Wang, P., Robert, L., Pelletier, J., Dang, W. L., Taddei, F., Wright, A., & Jun, S. Robust growth of Escherichia coli. *Curr Biol* **20**, 1099 (2010).
186. Long, Z., Nugent, E., Javer, A., Cicuta, P., Sclavi, B., Cosentino M. L., & and Dorfman, K. D. Microfluidic chemostat for measuring single cell dynamics in bacteria. *Lab Chip* **13**, 947–954 (2013).
187. Uphoff, S. Real-time dynamics of mutagenesis reveal the chronology of DNA repair and damage tolerance responses in single cells. *Proc Natl Acad Sci U S A* **115**, E6516–E6525 (2018).
188. Lagage, V., Chen, V. & Uphoff, S. Adaptation delay causes a burst of mutations in bacteria responding to oxidative stress. *EMBO Rep* **24**, (2023).
189. Ollion, J., Elez, M. & Robert, L. High-throughput detection and tracking of cells and intracellular spots in mother machine experiments. *Nat Protoc* **14**, 3144–3161 (2019).
190. Sliusarenko, O., Heinritz, J., Emonet, T. & Jacobs-Wagner, C. High-throughput, subpixel precision analysis of bacterial morphogenesis and intracellular spatio-temporal dynamics. *Mol Microbiol* **80**, 612–627 (2011).
191. Toker, D., Sommer, F. T. & D'Esposito, M. A simple method for detecting chaos in nature. *Communications Biology 2020 3:1* **3**, 1–13 (2020).
192. Breiman, L. Random Forests. *Machine Learning 2001 45:1* **45**, 5–32 (2001).
193. Grassberger, P. & Procaccia, I. Characterization of Strange Attractors. *Phys Rev Lett* **50**, 346 (1983).
194. Sandler, O., Mizrahi, S. P., Weiss, N., Agam, O., Simon, I., & Balaban, N. Q. Lineage correlations of single cell division time as a probe of cell-cycle dynamics. *Nature 2015 519:7544* **519**, 468–471 (2015).
195. Uhl, L. & Dukan, S. Hydrogen Peroxide Induced Cell Death: The Major Defences Relative Roles and Consequences in E. coli. *PLoS One* **11**, (2016).
196. Pillay, C. S., Eagling, B. D., Driscoll, S. R. E. & Rohwer, J. M. Quantitative measures for redox signaling. *Free Radic Biol Med* **96**, 290–303 (2016).
197. Schindelin, J., Arganda-Carreras, I., Frise, E., Kaynig, V., Longair, M., Pietzsch, T., Preibisch, S., Rueden, C., Saalfeld, S., Schmid, B., Tinevez, J. Y., White, D. J., Hartenstein, V., Eliceiri, K., Tomancak, P., & Cardona, A. Fiji: an open-source platform for biological-image analysis. *Nature Methods 2012 9:7* **9**, 676–682 (2012).
198. Schwall, C. P., Loman, T. E., Martins, B. M. C., Cortijo, S., Villava, C., Kusmartsev, V., Livesey, T., Saez, T., & Locke, J. C. W. Tunable phenotypic variability through an autoregulatory alternative sigma factor circuit. *Mol Syst Biol* **17**, e9832 (2021).
199. Imlay, J. A. Cellular defenses against superoxide and hydrogen peroxide. *Annu Rev Biochem* **77**, 755–776 (2008).
200. Rodríguez-Rojas, A., Kim, J. J., Johnston, P. R., Makarova, O., Eravci, M., Weise, C., Hengge, R., & Rolff, J. Non-lethal exposure to H2O2 boosts bacterial survival and evolvability against oxidative stress. *PLoS Genet* **16**, (2020).
201. Uphoff, S. Super-Resolution Microscopy and Tracking of DNA-Binding Proteins in Bacterial Cells. *Methods Mol Biol* **1431**, 221–234 (2016).

202. Pribis, J. P., García-Villada, L., Zhai, Y., Lewin-Epstein, O., Wang, A. Z., Liu, J., Xia, J., Mei, Q., Fitzgerald, D. M., Bos, J., Austin, R. H., Herman, C., Bates, D., Hadany, L., Hastings, P. J., & Rosenberg, S. M. Gamblers: An Antibiotic-Induced Evolvable Cell Subpopulation Differentiated by Reactive-Oxygen-Induced General Stress Response. *Mol Cell* **74**, 785-800.e7 (2019).
203. Robert, L., Ollion, J., Robert, J., Song, X., Matic, I., & Elez, M. Mutation dynamics and fitness effects followed in single cells. *Science (1979)* **359**, 1283–1286 (2018).
204. Hong, Y., Li, Q., Gao, Q., Xie, J., Huang, H., Drlica, K., & Zhao, X. Reactive oxygen species play a dominant role in all pathways of rapid quinolone-mediated killing. *J Antimicrob Chemother* **75**, 576–585 (2020).
205. Lee, C., Lee, S. M., Mukhopadhyay, P., Kim, S. J., Lee, S. C., Ahn, W. S., Yu, M. H., Storz, G., & Ryu, S. E. Redox regulation of OxyR requires specific disulfide bond formation involving a rapid kinetic reaction path. *Nature Structural & Molecular Biology 2004 11:12* **11**, 1179–1185 (2004).
206. Alon, U. Network motifs: theory and experimental approaches. *Nature Reviews Genetics 2007 8:6* **8**, 450–461 (2007).
207. Krašovec, R., Belavkin, R. V., Aston, J. A., Channon, A., Aston, E., Rash, B. M., Kadirvel, M., Forbes, S., & Knight, C. G.Mutation rate plasticity in rifampicin resistance depends on Escherichia coli cell–cell interactions. *Nature Communications 2014 5:1* **5**, 1–8 (2014).
208. Krašovec, R., Richards, H., Gifford, D. R., Hatcher, C., Faulkner, K. J., Belavkin, R. V., Channon, A., Aston, E., McBain, A. J., & Knight, C. G. Spontaneous mutation rate is a plastic trait associated with population density across domains of life. *PLoS Biol* **15**, e2002731 (2017).
209. Strogatz, S.H. *Nonlinear Dynamics and Chaos: With Applications to Physics, Biology, Chemistry, and Engineering* (2018).
210. Rogers, T. L., Johnson, B. J. & Munch, S. B. Chaos is not rare in natural ecosystems. *Nature Ecology & Evolution 2022 6:8* **6**, 1105–1111 (2022).
211. Karkaria, B. D., Manhart, A., Fedorec, A. J. H. & Barnes, C. P. Chaos in synthetic microbial communities. *PLoS Comput Biol* **18**, e1010548 (2022).
212. Allen, J. C., Schaffer, W. M. & Rosko, D. Chaos reduces species extinction by amplifying local population noise. *Nature 1993 364:6434* **364**, 229–232 (1993).
213. Cenci, S. & Saavedra, S. Non-parametric estimation of the structural stability of non-equilibrium community dynamics. *Nature Ecology & Evolution 2019 3:6* **3**, 912–918 (2019).
214. Doebeli, M. & Ispolatov, I. Chaos and unpredictability in evolution. *Evolution (N Y)* **68**, 1365–1373 (2014).
215. Pearce, M. T., Agarwala, A., Agarwala, A. & Fisher, D. S. Stabilization of extensive fine-scale diversity by ecologically driven spatiotemporal chaos. *Proc Natl Acad Sci U S A* **117**, 14572–14583 (2020).
216. de la Fuente, M., Martinez, L., Veguillas, J. & Aguirregabiriatm, J. M. Quasiperiodicity Route to Chaos in a Biochemical System. *Biophys J* **71**, (1996).
217. Zhdanov, V. P. Periodic perturbation of the bistable kinetics of gene expression. *Physica A: Statistical Mechanics and its Applications* **390**, 57–64 (2011).
218. Bi, P., Ruan, S. & Zhang, X. Periodic and chaotic oscillations in a tumor and immune system interaction model with three delays. *Chaos: An Interdisciplinary Journal of Nonlinear Science* **24**, 023101 (2014).

219. Heltberg, M., von Borries, M., Bendix, P. M., Oddershede, L. B. & Jensen, M. H. Temperature Controls Onset and Period of NF-κB Oscillations and can Lead to Chaotic Dynamics. *Front Cell Dev Biol* **10**, (2022).
220. Hirata, Y. & Aihara, K. Typical Chaotic Dynamics in Squid Giant Axons. *Procedia IUTAM* **5**, 54–58 (2012).
221. Iasemidis, L. D. & Sackellares, J. C. Chaos theory and epilepsy. *Neuroscientist* **2**, 118–126 (1996).
222. Hirata, Y., Oku, M. & Aihara, K. Chaos in neurons and its application: Perspective of chaos engineering. *Chaos: An Interdisciplinary Journal of Nonlinear Science* **22**, 047511 (2012).
223. Schweighofer, N., Doya, K., Fukai, H., Chiron, J. V., Furukawa, T., & Kawato, M. Chaos may enhance information transmission in the inferior olive. *Proc Natl Acad Sci U S A* **101**, 4655–4660 (2004).
224. Heltberg, M. L., Krishna, S., Kadanoff, L. P. & Jensen, M. H. A tale of two rhythms: Locked clocks and chaos in biology. *Cell Syst* **12**, 291–303 (2021).
225. Gonze, D., Halloy, J., Leloup, J. C. & Goldbeter, A. Stochastic models for circadian rhythms: Effect of molecular noise on periodic and chaotic behaviour. *C R Biol* **326**, 189–203 (2003).
226. Glass, L. Introduction to Controversial Topics in Nonlinear Science: Is the Normal Heart Rate Chaotic? *Chaos: An Interdisciplinary Journal of Nonlinear Science* **19**, 028501 (2009).
227. Lloyd, A. L. & Lloyd, D. Chaos: Its significance and detection in biology (2008).
228. Olsen, L. F., & Degn, H. Chaos in an enzyme reaction. *Nature 1977 267:5607* **267**, 177–178 (1977).
229. Kaity, B., Sarkar, R., Chakrabarti, B. & Mitra, M. K. Reprogramming, oscillations and transdifferentiation in epigenetic landscapes. *Scientific Reports 2018 8:1* **8**, 1–12 (2018).
230. Zhang, Z., Ye, W., Qian, Y., Zheng, Z., Huang, X., & Hu, G. Chaotic Motifs in Gene Regulatory Networks. *PLoS One* **7**, e39355 (2012).
231. Glass, D. S., Jin, X. & Riedel-Kruse, I. H. Nonlinear delay differential equations and their application to modeling biological network motifs. *Nature Communications 2021 12:1* **12**, 1–19 (2021).
232. Chen, L., Hamarash, I. I., Jafari, S., Rajagopal, K. & Hussain, I. Various bifurcations in the development of stem cells. *Eur. Phys. J. Spec. Top* **231**, 1015–1021 (2022).
233. Ahamed, T., Costa, A. C. & Stephens, G. J. Capturing the continuous complexity of behaviour in Caenorhabditis elegans. *Nature Physics 2020 17:2* **17**, 275–283 (2020).
234. Becks, L., Hilker, F. M., Malchow, H., Jürgens, K. & Arndt, H. Experimental demonstration of chaos in a microbial food web. *Nature 2005 435:7046* **435**, 1226–1229 (2005).
235. Poon, C. S. & Barahona, M. Titration of chaos with added noise. *Proc Natl Acad Sci U S A* **98**, 7107 (2001).
236. Storz, G. & Hengge, R. *Bacterial stress responses*. (2010).
237. Dawan, J. & Ahn, J. Bacterial Stress Responses as Potential Targets in Overcoming Antibiotic Resistance. *Microorganisms* **10**, (2022).
238. Wakamoto, Y., Dhar, N., Chait, R., Schneider, K., Signorino-Gelo, F., Leibler, S., & McKinney, J. D. Dynamic persistence of antibiotic-stressed mycobacteria. *Science (1979)* **339**, 91–95 (2013).
239. Balázsi, G., Van Oudenaarden, A. & Collins, J. J. Cellular decision making and biological noise: from microbes to mammals. *Cell* **144**, 910–925 (2011).

240. Mukhopadhyay, P., Zheng, M., Bedzyk, L. A., LaRossa, R. A. & Storz, G. Prominent roles of the NorR and Fur regulators in the Escherichia coli transcriptional response to reactive nitrogen species. *Proc Natl Acad Sci U S A* **101**, 745–750 (2004).
241. Susman, L., Kohram, M., Vashistha, H., Nechleba, J. T., Salman, H., & Brenner, N. Individuality and slow dynamics in bacterial growth homeostasis. *Proc Natl Acad Sci U S A* **115**, E5679–E5687 (2018).
242. Yang, D., Jennings, A. D., Borrego, E., Retterer, S. T. & Männik, J. Analysis of factors limiting bacterial growth in PDMS mother machine devices. *Front Microbiol* **9**, 871 (2018).
243. May, R. M. Biological Populations with Nonoverlapping Generations: Stable Points, Stable Cycles, and Chaos. *Science (1979)* **186**, 645–647 (1974).
244. Lagage, V. & Uphoff, S. Pulses and delays, anticipation and memory: seeing bacterial stress responses from a single-cell perspective. *FEMS Microbiol Rev* **44**, 565–571 (2020).
245. Murray, J. D. Mathematical Biology I. An introduction. *Interdisciplinary Applied Mathematics* **17**, 551 (2002).
246. Bower J. M., & Bolouri, H. *Computational Modeling of Genetic and Biochemical Networks* (2001).
247. Angelova, M. & Ben-Halim, A. Dynamic model of gene regulation for the lac operon. *J Phys Conf Ser* **286**, 012007 (2011).
248. Stark, H. & Woods, J. W. Probability and Random Processes with Applications to Signal Processing. *Prentice Hall* 706 (2002).
249. Kloeden, P. E. & Platen, E. Numerical Solution of Stochastic Differential Equations. *Numerical Solution of Stochastic Differential Equations* (1992).
250. Shaikhet, L. Lyapunov Functionals and Stability of Stochastic Difference Equations. *Lyapunov Functionals and Stability of Stochastic Difference Equations* (2011).
251. Deangelis, D. L. & Waterhouse, J. C. Equilibrium and nonequilibrium concepts in ecological models. *Ecol Monogr* **57**, 1–21 (1987).
252. Heltberg, M. L., Krishna, S. & Jensen, M. H. On chaotic dynamics in transcription factors and the associated effects in differential gene regulation. *Nature Communications 2019 10:1* **10**, 1–10 (2019).
253. Perez, J. C. & Groisman, E. A. Evolution of transcriptional regulatory circuits in bacteria. *Cell* **138**, 233 (2009).
254. Gunasekera, T. S., Csonka, L. N. & Paliy, O. Genome-Wide Transcriptional Responses of Escherichia coli K-12 to Continuous Osmotic and Heat Stresses. *J Bacteriol* **190**, 3712 (2008).
255. Li, Y. *et al.* Transcriptomic analysis by RNA-seq of Escherichia coli O157:H7 response to prolonged cold stress. *LWT* **97**, 17–24 (2018).
256. Tucker, D. L., Tucker, N. & Conway, T. Gene Expression Profiling of the pH Response in Escherichia coli. *J Bacteriol* **184**, 6551 (2002).
257. Wolfram-Schauerte, M., Pozhydaieva, N., Viering, M., Glatter, T. & Höfer, K. Integrated Omics Reveal Time-Resolved Insights into T4 Phage Infection of E. coli on Proteome and Transcriptome Levels. *Viruses 2022, Vol. 14, Page 2502* **14**, 2502 (2022).
258. Ma, P., Amemiya, H. M., He, L. L., Gandhi, S. J., Nicol, R., Bhattacharyya, R. P., Smillie, C. S., & Hung, D. T. Bacterial droplet-based single-cell RNA-seq reveals antibiotic-associated heterogeneous cellular states. *Cell* **186**, (2023).

259. Stanford, B. C. M., Clake, D. J., Morris, M. R. J. & Rogers, S. M. The power and limitations of gene expression pathway analyses toward predicting population response to environmental stressors. *Evol Appl* **13**, 1166 (2020).

260. Bervoets, I. & Charlier, D. Diversity, versatility and complexity of bacterial gene regulation mechanisms: opportunities and drawbacks for applications in synthetic biology. *FEMS Microbiol Rev* **43**, 304–339 (2019).

261. Wang, T., Shen, P., He, Y., Zhang, Y. & Liu, J. Spatial transcriptome uncovers rich coordination of metabolism in E. coli K12 biofilm. *Nature Chemical Biology 2023 19:8* **19**, 940–950 (2023).

262. Mark Kim, J., Garcia-Alcala, M., Balleza, E. & Cluzel, P. Stochastic transcriptional pulses orchestrate flagellar biosynthesis in Escherichia coli. *Sci Adv* **6**, (2020).

263. Mitosch, K., Rieckh, G. & Bollenbach, T. Temporal order and precision of complex stress responses in individual bacteria. *Mol Syst Biol* **15**, 8470 (2019).

264. Gasch, A. P., Spellman, P. T., Kao, C. M., Carmel-Harel, O., Eisen, M. B., Storz, G., Botstein, D., & Brown, P. O. Genomic expression programs in the response of yeast cells to environmental changes. *Mol Biol Cell* **11**, 4241–4257 (2000).

265. Zaslaver, A., Mayo, A. E., Rosenberg, R., Bashkin, P., Sberro, H., Tsalyuk, M., Surette, M. G., & Alon, U. Just-in-time transcription program in metabolic pathways. *Nature Genetics 2004 36:5* **36**, 486–491 (2004).

266. Courcelle, J., Khodursky, A., Peter, B., Brown, P. O. & Hanawalt, P. C. Comparative gene expression profiles following UV exposure in wild-type and SOS-deficient Escherichia coli. *Genetics* **158**, 41 (2001).

267. Culyba, M. J., Kubiak, J. M., Mo, C. Y., Goulian, M. & Kohli, R. M. Non-equilibrium repressor binding kinetics link DNA damage dose to transcriptional timing within the SOS gene network. *PLoS Genet* **14**, e1007405 (2018).

268. Klumpp, S., Zhang, Z. & Hwa, T. Growth-rate dependent global effects on gene expression in bacteria. *Cell* **139**, 1366 (2009).

269. Deris, J. B., Kim, M., Zhang, Z., Okano, H., Hermsen, R., Groisman, A., & Hwa, T. The innate growth bistability and fitness landscapes of antibiotic-resistant bacteria. *Science (1979)* **342**, (2013).

270. Seo, S. W., Kim, D., Szubin, R. & Palsson, B. O. Genome-wide Reconstruction of OxyR and SoxRS Transcriptional Regulatory Networks under Oxidative Stress in Escherichia coli K-12 MG1655. *Cell Rep* **12**, 1289–1299 (2015).

271. Varghese, S., Wu, A., Park, S., Imlay, K. R. C. & Imlay, J. A. Submicromolar hydrogen peroxide disrupts the ability of Fur protein to control free-iron levels in Escherichia coli. *Mol Microbiol* **64**, 822 (2007).

272. Ritz, D., Patel, H., Doan, B., Zheng, M., Aslund, F., Storz, G., & Beckwith, J. Thioredoxin 2 Is Involved in the Oxidative Stress Response in Escherichia coli. *Journal of Biological Chemistry* **275**, 2505–2512 (2000).

273. Manchado, M., Michán, C. & Pueyo, C. Hydrogen Peroxide Activates the SoxRS Regulon In Vivo. *J Bacteriol* **182**, 6842 (2000).

274. Zheng, M., Wang, X., Templeton, L. J., Smulski, D. R., LaRossa, R. A., & Storz, G. DNA microarray-mediated transcriptional profiling of the Escherichia coli response to hydrogen peroxide. *J Bacteriol* **183**, 4562–4570 (2001).

275. Gama-Castro, S., Rinaldi, F., López-Fuentes, A., Balderas-Martínez, Y. I., Clematide, S., Ellendorff, T. R., Santos-Zavaleta, A., Marques-Madeira, H., & Collado-Vides, J. Assisted curation of regulatory interactions and growth conditions of OxyR in E. coli K-12. *Database (Oxford)* **2014**, (2014).

276. Müller, K., Matzanke, B. F., Schünemann, V., Trautwein, A. X. & Hantke, K. FhuF, an iron-regulated protein of Escherichia coli with a new type of [2Fe-2S] center. *Eur J Biochem* **258**, 1001–1008 (1998).

277. Zhao, G., Ceci, P., Ilari, A., Giangiacomo, L., Laue, T. M., Chiancone, E., & Chasteen, N. D. Iron and Hydrogen Peroxide Detoxification Properties of DNA-binding Protein from Starved Cells: A ferritin-like DNA-binding protein of Escherichia coli. *Journal of Biological Chemistry* **277**, 27689–27696 (2002).

278. Kumar, S. R. & Imlay, J. A. How Escherichia coli Tolerates Profuse Hydrogen Peroxide Formation by a Catabolic Pathway. *J Bacteriol* **195**, 4569 (2013).

279. Hondorp, E. R. & Matthews, R. G. Oxidative Stress Inactivates Cobalamin-Independent Methionine Synthase (MetE) in Escherichia coli. *PLoS Biol* **2**, e336 (2004).

280. Patzer, S. I. & Hantke, K. Dual repression by Fe2+-Fur and Mn2+-MntR of the mntH gene, encoding an NRAMP-like Mn2+ transporter in Escherichia coli. *J Bacteriol* **183**, 4806–4813 (2001).

281. Almeida, C. C., Romão, C. V., Lindley, P. F., Teixeira, M. & Saraiva, L. M. The role of the hybrid cluster protein in oxidative stress defense. *J Biol Chem* **281**, 32445–32450 (2006).

282. Schembri, M. A., Hjerrild, L., Gjermansen, M. & Klemm, P. Differential Expression of the Escherichia coli Autoaggregation Factor Antigen 43. *J Bacteriol* **185**, 2236 (2003).

283. Wenk, M., Ba, Q., Erichsen, V., MacInnes, K., Wiese, H., Warscheid, B., & Koch, H. G. A universally conserved ATPase regulates the oxidative stress response in Escherichia coli. *J Biol Chem* **287**, 43585–43598 (2012).

284. Guo, Y., Li, Y., Zhan, W., Wood, T. K. & Wang, X. Resistance to oxidative stress by inner membrane protein ElaB is regulated by OxyR and RpoS. *Microb Biotechnol* **12**, 392 (2019).

285. Visick, J. E. & Clarke, S. RpoS- and OxyR-independent induction of HPI catalase at stationary phase in Escherichia coli and identification of rpoS mutations in common laboratory strains. *J Bacteriol* **179**, 4158–4163 (1997).

286. Ivanova, A., Miller, C., Glinsky, G. & Eisenstark, A. Role of rpoS (katF) in oxyR-independent regulation of hydroperoxidase I in Escherichia coli. *Mol Microbiol* **12**, 571–578 (1994).

287. Becker-Hapak S', M. & Eisenstark, A. Role of rpoS in the regulation of glutathione oxidoreductase (gor) in Escherichia coli. *FEMS Microbiol Lett* **134**, 39–44 (1995).

288. Faulkner, M. J. & Helmann, J. D. Peroxide Stress Elicits Adaptive Changes in Bacterial Metal Ion Homeostasis. *Antioxid Redox Signal* **15**, 175 (2011).

289. Cornelis, P., Wei, Q., Andrews, S. C. & Vinckx, T. Iron homeostasis and management of oxidative stress response in bacteria. *Metallomics* **3**, 540–549 (2011).

290. Choudhary, D., Foster, K. R. & Uphoff, S. Chaos in a bacterial stress response. *Curr Biol* (2023).

291. Wei, Q., Minh, P. N., Dötsch, A., Hildebrand, F., Panmanee, W., Elfarash, A., Schulz, S., Plaisance, S., Charlier, D., Hassett, D., Häussler, S., & Cornelis, P. Global regulation of gene expression by OxyR in an important human opportunistic pathogen. *Nucleic Acids Res* **40**, 4320–4333 (2012).

292. Wu, M., Shan, W., Zhao, G. P. & Lyu, L. D. H2O2 concentration-dependent kinetics of gene expression: linking the intensity of oxidative stress and mycobacterial physiological adaptation. *Emerg Microbes Infect* **11**, 573–584 (2022).

293. Ireland, W. T., Beeler, S. M., Flores-Bautista, E., McCarty, N. S., Röschinger, T., Belliveau, N. M., Sweredoski, M. J., Moradian, A., Kinney, J. B., & Phillips, R. Deciphering the regulatory genome of Escherichia coli, one hundred promoters at a time. *Elife* **9**, 1–76 (2020).

294. Semchyshyn, H. Hydrogen peroxide-induced response in E. coli and S. cerevisiae: Different stages of the flow of the genetic information. *Cent Eur J Biol* **4**, 142–153 (2009).

295. Imlay, J. A. & Linn, S. DNA damage and oxygen radical toxicity. *Science* **240**, 1302–1309 (1988).

296. Zheng, M., Wang, X., Doan, B., Lewis, K. A., Schneider, T. D., & Storz, G. Computation-Directed Identification of OxyR DNA Binding Sites in Escherichia coli. *J Bacteriol* **183**, 4571 (2001).

297. Maxon, M. E., Redfield, B., Cai, X. Y., Shoeman, R., Fujita, K., Fisher, W., Stauffer, G., Weissbach, H., & Brot, N. Regulation of methionine synthesis in Escherichia coli: effect of the MetR protein on the expression of the metE and metR genes. *Proc Natl Acad Sci U S A* **86**, 85–89 (1989).

298. Graham, A. I., Hunt, S., Stokes, S. L., Bramall, N., Bunch, J., Cox, A. G., McLeod, C. W., & Poole, R. K. Severe Zinc Depletion of Escherichia coli: Roles for high affinity zinc binding by ZinT, Zinc transport and zinc-independent proteins. *J Biol Chem* **284**, 18377 (2009).

299. Moreau, P. L. Regulation of phosphate starvation-specific responses in Escherichia coli. *REVIEW Moreau, Microbiology* **169**, 1312 (2023).

300. Martino, R. Di, Picot, A. & Mitri, S. Oxidative stress changes interactions between two bacterial species. *bioRxiv* 2023.05.24.542164 (2023).

301. Shandilya, S., Kumar, S., Kumar Jha, N., Kumar Kesari, K. & Ruokolainen, J. Interplay of gut microbiota and oxidative stress: Perspective on neurodegeneration and neuroprotection. *J Adv Res* **38**, 223–244 (2022).

302. da Silva Dantas, A. Reactive oxygen species at the interface of host-pathogen interactions. *Cell Microbiol* **23**, (2021).

303. Baker, C. J., Deahl, K., Domek, J. & Orlandi, E. W. Oxygen Metabolism in Plant/Bacteria Interactions: Effect of DPI on the Pseudo-NAD(P)H Oxidase Activity of Peroxidase. *Biochem Biophys Res Commun* **252**, 461–464 (1998).

304. Green, R., Wang, H., Botchey, C., Zhang, N., Wadsworth, C., McBain, A. J., Paszek, P., Krašovec, R., & Knight, C. G. Working together to control mutation: how collective peroxide detoxification determines microbial mutation rate plasticity. *bioRxiv* 2023.09.27.557722 (2023).

305. Piccardi, P., Vessman, B. & Mitri, S. Toxicity drives facilitation between 4 bacterial species. *Proc Natl Acad Sci U S A* **116**, 15979–15984 (2019).

306. Hammarlund, S. P. & Harcombe, W. R. Refining the stress gradient hypothesis in a microbial community. *Proc Natl Acad Sci U S A* **116**, 15760 (2019).

307. Singhal, R. & Shah, Y. M. Oxygen battle in the gut: Hypoxia and hypoxia-inducible factors in metabolic and inflammatory responses in the intestine. *J Biol Chem* **295**, 10493 (2020).

308. Sella, Y., Broderick, N. A., Stouffer, K., McEwan, D. L., Ausubel, F. M., Casadevall, A., & Bergman, A. Chaotic signatures in host-microbe interactions. *bioRxiv* (2022).

309. Granato, E. T., Meiller-Legrand, T. A. & Foster, K. R. The Evolution and Ecology of Bacterial Warfare. *Current Biology* **29**, R521–R537 (2019).

310. Pena, R. T., Blasco, L., Ambroa, A., González-Pedrajo, B., Fernández-García, L., López, M., Bleriot, I., Bou, G., García-Contreras, R., Wood, T. K., & Tomás, M. Relationship between quorum sensing and secretion systems. *Front Microbiol* **10**, 455464 (2019).

311. Smith, E. A. & Hodges, H. C. The spatial and genomic hierarchy of tumor ecosystems revealed by single-cell technologies. *Trends Cancer* **5**, 411 (2019).

312. Adler, M., Korem Kohanim, Y., Tendler, A., Mayo, A. & Alon, U. Continuum of Gene-Expression Profiles Provides Spatial Division of Labor within a Differentiated Cell Type. *Cell Syst* **8**, 43-52.e5 (2019).

313. Pandkar, M. R., Dhamdhere, S. G. & Shukla, S. Oxygen gradient and tumor heterogeneity: The chronicle of a toxic relationship. *Biochimica et Biophysica Acta (BBA) - Reviews on Cancer* **1876**, 188553 (2021).

Appendix

Table A.1 Machine learning regressor model: Predicted and experimental P*grxA* peak values for test data output by the regressor model

[Found as Data S1B on https://doi.org/10.1016/j.celrep.2023.112168]

Table A.2 Machine learning regressor model feature importance list

[Found as Data S1A on https://doi.org/10.1016/j.celrep.2023.112168]

Table A.3 Machine learning classifier model: Predicted and experimental H_2O_2 concentration values for test data output by the classification model

[Found as Data S1C on https://doi.org/10.1016/j.celrep.2023.112168]

Table A.4 Machine learning classifier model feature importance list

[Found as Data S1D on https://doi.org/10.1016/j.celrep.2023.112168]

Table A.5 Machine learning regressor model trained only on barrier cell features: Predicted and experimental P*grxA* peak values for test data output by the regressor model trained only on barrier cell features

[Found as Data S1E on https://doi.org/10.1016/j.celrep.2023.112168]

Table A.6 Machine learning regressor model feature importance list for model trained only on barrier cell features [Found as Data S1F on https://doi.org/10.1016/j.celrep.2023.112168]

Table A.7 Simulation input

[Found as Methods S1 on https://doi.org/10.1016/j.cub.2023.11.002]

Table A.8 Strain list

	Strain
1	AB1157, Δ*flhD*, PRNAI-mKate2, mutL-mYpet (SU178)
2	AB1157, Δ*flhD*, PRNAI-mKate2, mutL-mYPet, carrying pUA139 P*grxA*-SCFP3A Kan (SU777)
3	AB1157, Δ*flhD*, PRNAI-mKate2, mutL-mYpet, Δ*oxyR*, carrying pUA139 P*grxA*-SCFP3A kan (PSU044) (SU802)
4	AB1157, Δ*flhD*, PRNAI-mKate2, mutL-mYpet, carrying pUA066-P*katG*-SCFP3A kan (SU620)
5	AB1157, Δ*flhD*, PRNAI-mKate2, mutL-mYpet, carrying pUA066-P*ahpC*-SCFP3A kan (SU948)
6	AB1157, Δ*flhD*, PRNAI-mKate2, MutL-mYPet carrying P*katE*-SCFP3A kan (SU945)
7	AB1157, Δ*flhD*, PRNAI-mKate2 P*grxA*-SCFP3A kan (SU880)
8	AB1157, Δ*flhD*, mKate2, MutL-mYPet, Δ*oxyR,* pUA P*grxA*-SCFP3A kan + pUC18 amp encodes YPet preceeded by 11 aa linker followed by a kan cassette flanked by frt sites. (SU882)
9	AB1157, Δ*flhD*, PRNAI-mKate2, (SU069)
10	AB1157, Δ*flhD*, PRNAI-mKate2, (SU069) carrying pUA066-P*fhuF*-GFPmut2 kan (SU1226)
11	AB1157, Δ*flhD*, PRNAI-mKate2, (SU069) carrying pUA066-P*trxC*-GFPmut2 kan (SU1221)
12	AB1157, Δ*flhD*, PRNAI-mKate2, (SU069) carrying pUA066-P*yaaA*-GFPmut2 kan (SU1195)
13	AB1157, Δ*flhD*, PRNAI-mKate2, (SU069) carrying pUA066-P*dps*-GFPmut2 kan (SU1193)
14	AB1157, Δ*flhD*, PRNAI-mKate2, (SU069) carrying pUA066-P*katG*-GFPmut2 kan (SU1189)
15	AB1157, Δ*flhD*, PRNAI-mKate2, (SU069) carrying pUA066-P*dsbG*-GFPmut2 kan (SU1194)
16	AB1157, Δ*flhD*, PRNAI-mKate2, (SU069) carrying pUA066-P*znuA*-GFPmut2 kan (SU1227)
17	AB1157, Δ*flhD*, PRNAI-mKate2, (SU069) carrying pUA066-P*metE*-GFPmut2 kan (SU1218)
18	AB1157, Δ*flhD*, PRNAI-mKate2, mutL-mYpet, carrying pUA066-P*sodA*-SCFP3A kan (SU1121)
19	AB1157, Δ*flhD*, PRNAI-mKate2, (SU069) carrying pUA066-P*oxyR*-GFPmut2 kan (SU1217)

20	AB1157, Δ*flhD*, P_{RNAI}-mKate2, (SU069) carrying pUA066-P*hemH*-GFPmut2 kan (SU1188)
21	AB1157, Δ*flhD*, P_{RNAI}-mKate2, (SU069) carrying pUA066-P*mntR*-GFPmut2 kan (SU1223)
22	AB1157, Δ*flhD*, P_{RNAI}-mKate2, (SU069) carrying pUA066-P*gntP*-GFPmut2 kan (SU1219)
23	AB1157, Δ*flhD*, P_{RNAI}-mKate2, (SU069) carrying pUA066-P*uxuA*-GFPmut2 kan (SU1228)
24	AB1157, Δ*flhD*, P_{RNAI}-mKate2, (SU069) carrying pUA066-P*iscS*-GFPmut2 kan (SU1225)
25	AB1157, Δ*flhD*, P_{RNAI}-mKate2, (SU069) carrying pUA066-P*hcp*-GFPmut2 kan (SU1305)
26	AB1157, Δ*flhD*, P_{RNAI}-mKate2, (SU069) carrying pUA066-P*flu*-GFPmut2 kan (SU1308)
27	AB1157, Δ*flhD*, P_{RNAI}-mKate2, (SU069) carrying pUA066-P*ybjC*-GFPmut2 kan (SU1307)
28	AB1157, Δ*flhD*, P_{RNAI}-mKate2, (SU069) carrying pUA066-P*ychF*-GFPmut2 kan (SU1306)
29	AB1157, Δ*flhD*, P_{RNAI}-mKate2, (SU069) carrying pUA066-P*yfdL*-GFPmut2 kan (SU1304)
30	AB1157, Δ*flhD*, P_{RNAI}-mKate2, (SU069) carrying pUA066-P*metR*-GFPmut2 kan (SU1220)
31	AB1157, Δ*flhD*, P_{RNAI}-mKate2, (SU069) carrying pUA066-P*znuC*-GFPmut2 kan (SU1224)
32	AB1157, Δ*flhD*, P_{RNAI}-mKate2, (SU069) carrying pUA066-P*ybjN*-GFPmut2 kan (SU1303)
33	AB1157, Δ*flhD*, P_{RNAI}-mKate2, (SU069) carrying pUA066-P*elaB*-GFPmut2 kan (SU1311)
34	AB1157, Δ*flhD*, P_{RNAI}-mKate2, (SU069) carrying pUA066-P*fur*-GFPmut2 kan (SU1192)
35	AB1157, Δ*flhD*, P_{RNAI}-mKate2, (SU069) carrying pUA066-P*poxB*-GFPmut2 kan (SU1310)
36	AB1157, Δ*flhD*, P_{RNAI}-mKate2, (SU069) carrying pUA066-P*yaiA*-GFPmut2 kan (SU1309)
37	AB1157, Δ*flhD*, P_{RNAI}-mKate2, (SU069) carrying pUA066-P*clpS*-GFPmut2 kan (SU1345)
38	AB1157, Δ*flhD*, P_{RNAI}-mKate2, (SU069) carrying pUA066-P*clpX*-GFPmut2 kan (SU1346)
39	AB1157, Δ*flhD*, P_{RNAI}-mKate2, mutL-mYPet (SU178)
40	AB1157, Δ*flhD*, P_{RNAI}-mKate2, mutL-mYPet, carrying pUA139 P*grxA*-SCFP3A Kan (SU777)
41	AB1157, Δ*flhD*, P_{RNAI}-mKate2, mutL-mYPet, carrying pUA066-P*katG*-SCFP3A kan (SU620)
42	AB1157, Δ*flhD*, P_{RNAI}-mKate2, mutL-mYPet, carrying pUA066-P*ahpC*-SCFP3A kan (SU948)
43	AB1157, Δ*flhD*, P_{RNAI}-mKate2, mutL-mYPet ΔKatG (SU590) carrying pUA066-P*katG*-SCFP3A kan (SU1325)
44	AB1157, Δ*flhD*, P_{RNAI}-mKate2, mutL-mYPet ΔKatG (SU590) carrying pUA066-P*grxA*-SCFP3A kan (SU778)
45	DH5α lambda red chromosomal P*grxA*-SCFP3A kan (aslA site) (SU1409)
46	AB1157, Δ*flhD*, P_{RNAI}-mKate2, (SU069) P*grxA*-SCFP3A kan (aslA site) (P1 transduction of SU1409) (SU1410)
47	DH5α carrying pUA066-P*katG*-SCFP3 amp (SU1390)
48	DH5α carrying pUA066-P*grxA*- SCFP3 amp (SU1392)
49	DH5α carrying pUA066-P*katG*-mYPet amp (SU1395)
50	DH5α carrying pUA066-P*grxA*-mYPet amp (SU1394)
51	AB1157, Δ*flhD*, P_{RNAI}-mKate2,P*grxA*-SCFP3A-kan (chr) (SU1410) carrying pUA066-P*katG*-mYPet-amp(SU1411)
52	AB1157, Δ*flhD*, P_{RNAI}-mKate2, P*grxA*-SCFP3A kan (chr) (SU1410) carrying pUA066-P*grxA*-mYPet-amp(SU1412)

Table A.9: Reagents and software

REAGENT or RESOURCE	**SOURCE**	**IDENTIFIER**
M9 minimal salts 5x	Sigma	Product Number: M9956
MEM amino acids	Gibco	Catalog number: 11130-036
L-Proline	Biochemica	Reference Number: A3453,0100
Thiamine	Biochemica	Reference Number: A0955,0050
Pluronic F-127	Sigma	Product Number: P2443-250G
Propidium iodide	Sigma	Product Number: P4170
30% W/W solution of H_2O_2	Sigma	Product Number: H1009-100mL
Kanamycin	Sigma	Product Number: A1493
Agarose	Bio-Rad	Product Number: 1613100
PDMS	Univar Specialty Consumables Ltd	Dowsil / Dow Corning Sylgard 184 Kit 1.1kg
Software and Algorithms		
MATLAB	Mathworks	Mathworks.com
BACMMAN	Fiji [311], Ollion et al. [311]	github.com/jeanollion/bacmman
Python	Spyder	anaconda.com